Electronic excitations in light absorbers for photoelectrochemical energy conversion

By

Yuan Ping
B.S. (University of Science and Technology of China) 2007
M.A. (University of California, Davis) 2009

DISSERTATION

Submitted in partial satisfaction of the requirements for the degree of

DOCTOR OF PHILOSOPHY

in

CHEMISTRY

in the

OFFICE OF GRADUATE STUDIES

of the

UNIVERSITY OF CALIFORNIA

DAVIS

Approved:

Giulia Galli (Chair)

Susan Kauzlarich

Gergely T. Zimanyi

Committee in Charge
2013

To my husband Marc Alexander

Contents

Acknowledgments

I am grateful to my supervisor Professor Giulia Galli for her supervision, guidance, support and patience during my entire PhD. She provided me with tremendous opportunities and invaluable assistance in developing my expertise in computational solid state physics/chemistry. She also introduced me to a very exciting research field- solar energy research and gave me the opportunity to be part of the CCI-Power The Planet project. During my PhD, I am not only excited by the scientific discoveries I have been fortunate to make, but also by the prospect of bridging my theoretical studies with real life energy problems. Besides research, Professor Galli also taught me how to face difficulties in work and stay positive and optimistic. She told me, "Never, never give up!" whenever I faced a challenge or felt stuck in my research. This built up my confidence and persistence and serves as a lesson that I've carried to my personal life as well.

I also would like to thank Professor Dario Rocca who was formerly a postdoc in our group. He helped me immensely at the start of my research and explained fundamental knowledge and technical details very carefully and patiently whenever I asked him. Dario also inspired and guided me on many difficult problems and always encouraged me to move forward. There are also a lot of my collaborators and colleagues I am thankful to: Dr. Yan Li and Dr. Deyu Lu who were former postdocs in our group and helped me understand the fundamentals of electronic structure and provided many useful guidance on my research and life; my Angstrom Group colleagues who had many useful discussions with me, and my experimental collaborators at Caltech and University of Wisconsin-Madison.

Chapter 1

Overview

The production of hydrogen and oxygen from water through photo-electrochemical energy conversion is a promising strategy to take advantage of the Earth's main energy source, the Sun [1, 2]. For example, upon absorption of sunlight by a semiconducting electrode (e.g. a solid oxide) interfaced with liquid water, electron-hole pairs may be formed, leading to coupled electron-proton transfers at the interface and eventually to water splitting. One of the challenges in the optimization of this process is to find Earth abundant and stable materials that are at the same time efficient absorbers of sunlight (e.g. direct band gap semiconductors absorbing mostly in the visible), and have band edges appropriately aligned with water reduction and oxidation potentials to permit efficient proton-coupled electron transfer reactions. Therefore, from a theoretical standpoint, an essential prerequisite to predict materials

Table 1.1 : Electronic excitations discussed in this thesis (first row), together with experimental (second row) and theoretical (third row) approaches used to probe them. The fundamental equations of the theory described here are given in the fourth row of the table and will be discussed in chapter 2.

Processes of interest	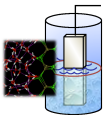 Band edge alignment between electrodes and water	 Light absorption by electrodes
Experiments	Photoemission spectroscopy	UV-vis and ellipsometry spectroscopy
Theory	Single particle Green's functions $G^{(1)}$: poles represent energies to add or remove an electron from a solid or molecule	Two particle correlation function L: poles correspond to neutral excitation energies of interacting electrons
Equations	Dyson's equation: relates $G^{(1)}$ to self energy Σ (effective potential of interacting electrons)	Bethe Salpeter equation: relates L to the variation of Σ with respect to $G^{(1)}$

for photoelectrochemical energy conversion is the development of efficient methods

to describe electronic excitation in solids and molecules.

Desirable methods to study electronic excitations should allow one to tackle condensed and molecular systems on the same footing, and be applicable to broad classes of materials with various compositions. Indeed, depending on the desired design of the photoelectrochemical cell, one may need to describe interfaces between liquid water and a solid surface with a molecular catalyst attached to it, or between water and a complex, possibly disordered and defective solid with a thin film acting as a catalyst deposited on top. In addition, it is necessary to have a general theoretical framework to handle both charged and neutral electronic excitations; the prediction of band edge alignments between photoelectrodes and water, requires the ability to describe charge excitations, that is photoemission and inverse photoemission processes, through which one determines the energy of valence and conduction bands. The optimization of photoelectrodes for light absorption involves instead the description of neutral electron hole pair excitations formed upon the interaction of the material with light, and the description of the subsequent formation of a bound exciton.

Given the breadth of materials which are interesting to explore for photoelectrochemical research, and the complexity of electronic excitations involved, the choice of theoretical methods naturally falls on first principles approaches. First principles (or ab initio) calculations do not require any fit to experimental data and are thus not limited to specific classes of systems nor to predetermined morphologies of materials. Density Functional Theory [3](DFT) is one of the most successful ab initio theories adopted in the last thirty years by chemists and physicists alike, to compute ground state properties of molecules and solids [4]. It is in principle an exact theory which however requires approximations for the exchange-correlation potential (V_{xc}) of the electrons in practical calculations (the exact V_{xc} is unknown). While used mostly by condensed matter physicists until the early 1990s, within the so called local density approximation [5] (LDA) of V_{xc}, DFT was also adopted by chemists in the last 20 years. The adoption of DFT by the quantum chemistry community came after the development of generalized gradient corrected approximations [6, 7, 8] (GGA) to V_{xc}. Such approximations yield reasonably accurate results for ground state properties of many solids and molecules, unlike the LDA which overall appears to work better for condensed than for molecular phases.

Within DFT, a set of self-consistent independent-electron Schrödinger equations is solved, for a given, approximate V_{xc}, to obtain the density of interacting electrons within a solid or a molecule. These equations are named after Kohn and Sham (KS) [5]. The density uniquely determines all properties of the system. The eigenvalues of the KS equations cannot be interpreted as excitation energies involving addition (electron affinity) or removal (ionization potential) of an electron, unlike the eigenvalues of the Hartree Fock Hamiltonian for which the Koopman's theorem [9] holds. Therefore KS eigenvalues should not be used to describe photoemission pro-

cesses, nor, for example, to compute band offsets and band edges in solids. However, in solids electronic gaps obtained as the difference between the KS energies of the top of the valence band and the bottom of the conduction band, are often compared to experimental data, and likewise the difference between HOMO and LUMO energies in molecules. In many cases it was found that trends within given classes of solids or molecules are well reproduced by KS electronic gaps; however absolute values often show large errors compared to experiments (e.g. a factor of approximately two in the case of the band gap of Si). An alternative method to compute excitation energies of molecules and clusters, called the Δ self-consistent approach [10], consists in performing DFT ground-state calculations for neutral and charged systems (i.e. with an electron either removed or added to the system) and in obtaining the first electron affinity or first ionization potential as differences of total energies. Recently this method was generalized to treat periodic solids [11].

Furthermore, DFT is not suitable for describing electronic excitations probed by optical absorption experiments. In the simplest linear optical process, an electron undergoes a transition from the ground to an excited state upon interaction with an external electromagnetic field; in a semiconductor or insulator, the excited electron may then bind to the corresponding hole, forming an exciton. In order to describe such an excitation, an extension of DFT to include time dependent perturbations, i.e. the electromagnetic field impinging upon a solid or molecule, is required. Such generalization was developed in the 1980s, and goes by the name of time-dependent density functional theory (TDDFT) [12]. The performance of TDDFT in describing absorption processes and exciton binding energies depends again on the choice of the (time dependent) exchange correlation potential. When using adiabatic local or GGA-based approximations, the results of TDDFT for semi-conducting solids and insulators are usually rather poor [13]; they appear to be in better agreement with experiments for several classes of molecules, although notable failures were observed, e.g. in the description of charge transfer excitations [14, 15].

An alternative approach to compute electronic excitations of solids and molecules is based on many-body perturbation theory (MBPT) and the Green's function formalism [16, 17]. In the last two decades single-particle Green's functions have been widely used in the calculations of photoemission spectra, band offsets and band edges of solids [18, 19, 20, 21] and they are now applied to the calculation of ionization potentials and electron affinities of molecules as well [22, 23, 24, 25]. In a similar fashion, two-particle Green's functions, obtained through approximate solutions of the Bethe-Salpeter equation [26, 16] (BSE) have been employed for the calculation of neutral excitations involved in optical absorption experiments of solids [27, 28, 29, 30]. Recently the BSE has also been used to compute optical excitations in molecules and clusters [31, 32, 33, 29]. The calculation of Green's functions requires first the determination of the ground state of the electronic system. This may be accomplished in different manners. In most of the condensed matter physics literature, Green's

functions are built from single-particle states obtained by solving the KS equations.

Computational difficulties have long limited the application of MBPT to realistic systems of interest for photo-electrochemical energy conversion. However recent algorithmic advances in the computation of quasi-particle energies [23, 24] and in the solution of the BSE [33, 30] are permitting considerable progress in the application of MBPT to photoelectrode materials, including complex semi-conducting oxides. In this thesis we describe MBPT and Green's function based techniques, for first principle calculations of electronic excitation processes in solids and molecules (see Table 1.1); we include a discussion of recent algorithms allowing for the application of MBPT to realistic materials. One of our goals is to introduce the formalism of MBPT to the quantum chemistry community and to specify in detail the theoretical and numerical approximations used in ab initio calculations, so as to facilitate accurate comparisons with experiments.

The rest of the thesis is organized as follows: we summarize the general concepts and equations of MBPT in Section 2.1, and in Section 2.2 we describe algorithms to solve, in approximate forms, the key equations of MBPT to obtain electronic excitation energies and spectra. We then give some examples of predictions of band alignments and absorption spectra of promising photoeletrode materials in Section 3 and Section 4. We focus on silicon based materials (bulk silicon and silicon nanowires) and oxides (WO_3, WO_3 clathrates and $CuW_xMo_{1-x}O_4$) for photocathode and photoanode materials,respectively. Finally we give our conclusions and outlook in Section 5.

Chapter 2

Theoretical background

2.1 First-principles methods to compute photoemission and absorption spectra within many body perturbation theory

In this section we discuss the basic concept of MBPT, that of single-particle many body Green's functions [17]. For the purpose of this thesis, the term "particle" refers to an electron but the Green's function formalism is not restricted to electrons or fermions (for example, it can be applied to describe phonons).

2.1.1 Single-particle Green's functions

Single-particle Green's functions are useful concepts to compute electronic excitations involving the addition or the removal of an electron and thus to describe photoemission experiments (see Table 1.1). The time-ordered single-particle Green's function is defined as

$$G^{(1)}(1,2) = -i\langle \Psi_0^N | \hat{T}\hat{\psi}(1)\hat{\psi}^\dagger(2) | \Psi_0^N \rangle, \tag{2.1.1}$$

where $1 \equiv (\mathbf{r}_1, t_1)$ and $2 \equiv (\mathbf{r}_2, t_2)$ are compact notations to indicate space coordinates $\mathbf{r}$ and time t (for simplicity the spin variable is not included in our discussion); ${\Psi_0}^N$ is the normalized many body ground-state wavefunction of a system containing N electrons, $\hat{T}$ is the time-ordering operator, and $\hat{\psi}^\dagger(\mathbf{r},t)$ ($\hat{\psi}(\mathbf{r},t)$) is an operator in the Heisenberg representation that creates (destroys) an electron at position $\mathbf{r}$ at time t. In Eq. 2.1.1 and hereafter, the hat "$\hat{}$" indicates quantum-mechanical operators. Atomic units ($\hbar = m = e = 1$) are used throughout the thesis. Symbols frequently used in this thesis are summarized in Table 2.1.

In Eq. 2.1.1 if $t_1 > t_2$ the Green's function $G^{(1)}$ gives the probability amplitude that a particle added to the system at time t_2 in position $\mathbf{r_2}$ be detected in position $\mathbf{r_1}$ at time t_1. Similarly, if $t_2 > t_1$ a particle is removed from the system and the Green's

Table 2.1 : Summary of symbols frequently used in this thesis.

$G^{(1)}$	Single-particle Green's function
$G_0^{(1)}$	Non-interacting single-particle Green's function
$G^{(2)}$	Two-particle Green's function
$\hat{\psi}^\dagger$	Creation field operator
$\hat{\psi}$	Annihilation field operator
Ψ_j^N, E_j^N	Wavefunctions and energies of a interacting N electron system $j = 0$ corresponds to the ground-state
Φ_0^N	Ground state wavefunctions of a non-interacting N electron system
φ_j, ϵ_j^{ind}	Independent-electron Hartree orbitals and energies
ϕ_j, ϵ_j^{KS}	Kohn-Sham orbitals and energies
f_j	Lehmann amplitudes
ε	Dielectric matrix

function describes the time-evolution of the corresponding hole. From the single-particle Green's function it is possible to obtain the expectation value of any single-particle operator (e.g. the density) on the interacting ground-state, and to obtain the ground-state energy by using the Galitskii-Migdal formula [34]. The physical interpretation of the Green's function as propagator of a state with an additional electron or a hole intuitively suggests that Green's function theory may be used to describe experiments that measure electron affinities or ionization potentials.

If the Hamiltonian that describes the time evolution of the field operators $\hat{\psi}(1)$ and $\hat{\psi}^\dagger(2)$ does not explicitly depend on time, the time-ordered Green's function in Eq. 2.1.1 depends only on the difference $(t_1 - t_2)$. In this case, by inserting a complete set of eigenstates of the system $\{\Psi_j^{N+1}\}$ and $\{\Psi_j^{N-1}\}$ with (N+1) and (N-1) particles, respectively, in Eq. 2.1.1, and by applying a Fourier transform (from time t to energy ω), one obtains the so-called Lehmann representation of the Green's function:

$$G^{(1)}(\mathbf{r}_1, \mathbf{r}_2, \omega) = \sum_j \frac{f_j(\mathbf{r}_1) f_j^*(\mathbf{r}_2)}{\omega - \epsilon_j + i\eta sgn(\epsilon_j - \mu)} \tag{2.1.2}$$

where η is a positive infinitesimal.

$$\left.\begin{aligned} f_j(\mathbf{r}) &= \langle \Psi_0^N | \hat{\psi}(\mathbf{r}) | \Psi_j^{N+1} \rangle \\ \epsilon_j &= E_j^{N+1} - E_0^N \end{aligned}\right\} \quad \text{for } \epsilon_j > \mu, \tag{2.1.3}$$

and

$$\left.\begin{aligned} f_j(\mathbf{r}) =& \langle \Psi_j^{N-1} | \hat{\psi}(\mathbf{r}) | \Psi_0^N \rangle \\ \epsilon_j =& E_0^N - E_j^{N-1} \end{aligned}\right\} \quad \text{for } \epsilon_j < \mu. \tag{2.1.4}$$

In Eqs. 2.1.3-2.1.4 μ is the chemical potential, E_0^N is the ground-state energy of the N electrons system and E_j^{N-1} and E_j^{N+1} are the energies of the system in which an electron is removed or added, respectively. Within the Lehmann representation, the poles of the time-ordered single-particle Green's function represent the energies necessary to add or remove an electron. In general the calculation of these energies is far from trivial, since when an electron is added or removed from the system, all the other electrons readjust in a correlated manner. The Green's function $G^{(1)}$ (Eqs. 2.1.1-2.1.2) accounts for all these correlation effects.

2.1.2 The Dyson's equation

The calculation of the full single-particle Green's function is a difficult task for any system of interacting electrons, in principle as difficult as determining the full many body wavefunction. Perturbation theory may be used to approximate the many body Green's function by considering the Coulomb interaction between electrons, v, as a perturbation acting on the non-interacting system. This approach is called Feynman-Dyson perturbation theory [17]. The perturbation v is adiabatically "switched on" from $t = -\infty$ (when the perturbation is absent) to $t = 0$, when the interacting Hamiltonian is obtained. The Gell-Mann and Low theorem [17] ensures that the non-interacting ground-state Φ_0^N of the system at $t = -\infty$ (that can be easily computed) evolves, upon adiabatic application of v, to an eigenstate of the fully interacting Hamiltonian. Similarly, the perturbation can be adiabatically "switched off" from $t = 0$ to $t = +\infty$, bringing back the system to the non-interacting ground-state Φ_0^N.

Within this framework the single-particle Green's function is expressed in terms of an expectation value on the non interacting ground-state Φ_0^N. By using Wick's theorem [17] the Green's function can then be expanded in a perturbative series whose terms depend only on the non-interacting single-particle Green's function $G_0^{(1)}$ and the Coulomb interaction v. Feynman diagrams are a convenient way of representing the integrals involved in this perturbative expansion. The analysis of the diagrammatic expansion of the Green's function $G^{(1)}$ leads to the definition of the Dyson's equation [35, 17]

$$\begin{aligned} G^{(1)}(1,2) =& G_0^{(1)}(1,2) \\ &+ \int G_0^{(1)}(1,3)\Sigma(3,4)G^{(1)}(4,2)d(34) \end{aligned} \tag{2.1.5}$$

where Σ is the self-energy, whose physical meaning will be discussed in detail in the next section. The Dyson's equation is a concise way of expressing the summation

over an infinite number of diagrams (within the perturbative expansion).

If an accurate approximation of Σ were known, the Dyson's equation would provide a way to compute the interacting Green's function G from the non-interacting G_0. The Green's function G_0 can be obtained by setting $\Psi_0^N = \Phi_0^N$ in Eq. 2.1.1, where Φ_0^N is an independent-particle ground-state wavefunction (it corresponds to a Slater determinant within the first quantization formalism). The non-interacting G_0 can be written explicitly as:

$$G_0^{(1)}(1,2) = -i \sum_j \varphi_j(\mathbf{r}_1)\varphi_j^*(\mathbf{r}_2)e^{-i\epsilon_j^{ind}(t_1-t_2)} \times \left[\theta(t_1-t_2)\theta(\epsilon_j^{ind}-\mu) - \theta(t_2-t_1)\theta(\mu-\epsilon_j^{ind})\right], \quad (2.1.6)$$

where θ is the Heaviside function. The independent single-particle orbitals φ_j and energy levels ϵ_j^{ind} are obtained from the independent electron equation

$$\hat{H}^{ind}\varphi_j = \left[-\frac{1}{2}\nabla^2 + \hat{V}_{e-I} + \hat{V}_H\right]\varphi_j = \epsilon_j^{ind}\varphi_j, \quad (2.1.7)$$

where $\hat{V}_{e-I}$ is the Coulomb potential due to the nuclei, $\hat{V}_H$ is the Hartree potential $\int v(\mathbf{r}_1,\mathbf{r}_2)\rho(\mathbf{r}_2)d\mathbf{r}_2$, and ρ is the electron density. By Fourier transforming Eq. 2.1.6, the Lehmann representation of the independent electron Green's function is obtained:

$$G_0^{(1)}(\mathbf{r_1},\mathbf{r_2},\omega) = \sum_j \frac{\varphi_j(\mathbf{r}_1)\varphi_j^*(\mathbf{r}_2)}{\omega - \epsilon_j^{ind} + i\eta sgn(\epsilon_j^{ind}-\mu)}. \quad (2.1.8)$$

where η is a positive infinitesimal introduced to perform the Fourier transform from the time to the frequency domain.

By expressing Eq. 2.1.8 as $G_0^{(1)} = 1/(\omega - \hat{H}^{ind})$ and using Eq. 2.1.2, the Fourier transform of Eq. 2.1.5 leads to the following eigenvalue equation:

$$\hat{H}^{ind}(\mathbf{r}_1)f_j(\mathbf{r}_1) + \int \Sigma(\mathbf{r}_1,\mathbf{r}_2,\epsilon_j)f_j(\mathbf{r}_2)d\mathbf{r}_2 = \epsilon_j f_j(\mathbf{r}_1) \quad (2.1.9)$$

If Σ is known, this equation determines the Lehmann amplitudes and energies defined in Eqs. 2.1.3-2.1.4.

2.1.3 The concepts of self-energy and quasi-particle

Eq. 2.1.9 is an independent-particle Schrödinger-like equation in which the electrons move in a mean-field determined by the self-energy Σ, which thus plays the role of an effective potential. However, there are a few differences between Eq. 2.1.9 and a single-particle Schrödinger equation, (e.g. the KS equations of DFT): The self-energy Σ depends on the single-particle energy and is a non-local and non-Hermitian

operator. Hence the functions $\{f_j(\mathbf{r})\}$ are not an orthonormal set and the eigenvalues of Eq. 2.1.9 are not real; therefore it is not straightforward to interpret them in terms of single-particle energies. However, when the imaginary part of ϵ_j is small (i.e. the lifetime of the state is long), the corresponding spectral peak is narrow and exhibits a strong intensity; in this case ϵ_j and $f_j(\mathbf{r})$ define a quasi-particle state. The condition of long lifetimes is usually best fulfilled by electronic states near the Fermi energy [36].

As already mentioned, the self-energy in Eq. 2.1.5 and Eq. 2.1.9 may be approximated through a diagrammatic expansion, within the Feynman-Dyson perturbation theory. The simplest approximation yields the exchange self-energy [17]:

$$\Sigma_x(1,2) = iG^{(1)}(1,2)\upsilon(1^+,2) \tag{2.1.10}$$

Here $\upsilon(1,2) \equiv \upsilon(\mathbf{r}_1,\mathbf{r}_2)\delta(t_1^+ - t_2)$ and $1^+ = (\mathbf{r}_1, t_1^+) \equiv (\mathbf{r}_1, t_1 + \gamma)$ where γ is a positive infinitesimal. Since Σ_x depends explicitly on the Green's function G, the Dyson's equation and Eq. 2.1.9 must be solved self-consistently. By performing a Fourier transform from t to ω and computing the corresponding integrals in the frequency domain, Eq. 2.1.10 becomes:

$$\Sigma_x(\mathbf{r}_1,\mathbf{r}_2) = -\sum_{j=1}^{N_{occ}} f_j(\mathbf{r}_1) f_j^*(\mathbf{r}_2)\upsilon(\mathbf{r}_1 - \mathbf{r}_2) \tag{2.1.11}$$

where N_{occ} is the number of occupied states. By using the definition of the exchange self-energy (Eq. 2.1.11) in Eq. 2.1.9, one recovers the Hartree-Fock (HF) equations. Within the HF approximation, the self-energy Σ does not depend on the energy ω, is Hermitian and the self-consistent solution of Eq. 2.1.9 is straightforward. For practical purposes the HF approximation may be accurate to treat some excitation energies in molecules [37] but it is not reliable for solids [38, 39]. In a first quantization framework the HF ground-state wavefunction is a single Slater determinant, namely the electrons are independent particles. In Sec. 2.1.6 we will discuss the GW approximation to the self-energy, which introduces correlation effects. We now turn to the definition of the two particle Green's function.

2.1.4 Two-particle Green's function and the Bethe-Salpeter equation

As mentioned in 2.1.1, single-particle Green's functions may be used to model photoemission experiments. However, these Green's functions cannot describe the excitations involved in optical absorption experiments. Indeed the simplest linear optical process involves two quasi-particles, an electron and an hole, interacting with each other to form an exciton. The description of such a bound excitation requires a Green's function that represents at the same time the propagation of a hole and of an electron (see Table 1.1). To describe absorption spectra, we define the two-particle

Green's function [17]:

$$G^{(2)}(1,2;1',2') = -\langle \Psi_0^N | \hat{T}\hat{\psi}(1)\hat{\psi}(2)\hat{\psi}^\dagger(2')\hat{\psi}^\dagger(1')|\Psi_0^N\rangle. \tag{2.1.12}$$

Eq. 2.1.12 can be interpreted as a propagator of a state with two additional particles. Depending on the time ordering, these two particles can be two holes, two electrons or an electron-hole pair (i.e. the case of interest to this thesis). Within this formalism it is convenient to introduce the two-particle correlation function

$$iL(1,2;1',2') = -G^{(2)}(1,2;1',2') + G^{(1)}(1,1')G^{(1)}(2,2'), \tag{2.1.13}$$

where the product of the single-particle Green's functions $G^{(1)}(1,1')$ and $G^{(1)}(2,2')$ (second term on the right hand side) represents the independent evolution of two quasi-particles. The two-particle correlation function satisfies the following form of the Bethe-Salpeter equation [40, 17]:

$$\begin{aligned} L(1,2;1',2') &= L_0(1,2;1',2') \\ &+ \int d3456 L_0(1,4;1',3)\Xi(3,5;4,6)L(6,2;5,2') \end{aligned} \tag{2.1.14}$$

where $iL_0(1,2;1',2') = G^{(1)}(1,2')G^{(1)}(2,1')$; the kernel Ξ is an effective two-particle interaction that can be expressed as the sum of the derivatives of the Hartree potential and of the self-energy (see Eq. 2.1.5 and Eq. 2.1.9) with respect to the single-particle Green's function:

$$\Xi(3,5;4,6) = v(3,6)\delta(3,4)\delta(5,6) + i\frac{\delta\Sigma(3,4)}{\delta G^{(1)}(6,5)} \tag{2.1.15}$$

In order to obtain the two-particle correlation function L from Eq. 2.1.14, approximations of the single-particle Green's function $G^{(1)}$ and of the kernel Ξ are required. As apparent from Eq. 2.1.5 and Eq. 2.1.15, the evaluation of the self-energy Σ is crucial to compute both $G^{(1)}$ and Ξ. If one uses the exchange self-energy (Eq. 2.1.10) in Eqs. 2.1.14-2.1.15, an equation equivalent to the time-dependent Hartree-Fock (TDHF) equation is recovered [41].

We note that in Eq. 2.1.12 the two-particle Green's function contains more information than actually necessary to model any optical absorption experiment and, in general, any neutral excitation involving an electron-hole pair. To model optical absorption, it is sufficient to consider the Green's function [17]

$$G^{(2)}(1,2;1,2) = -\langle \Psi_0^N | \hat{T}\hat{\psi}^\dagger(1)\hat{\psi}(1)\hat{\psi}^\dagger(2)\hat{\psi}(2)|\Psi_0^N\rangle, \tag{2.1.16}$$

obtained by setting $1' = 1^+$ and $2' = 2^+$ in Eq. 2.1.12. In Eq. 2.1.16, $G^{(2)}$ determines the time-evolution of an electron-hole pair, described by the operator $\hat{\psi}^\dagger\hat{\psi}$ (where $\hat{\psi}$

creates a hole and $\hat{\psi}^\dagger$ a particle). Similar to the case of single-particle Green's functions, one may introduce the Lehmann representation for the two-particle correlation function L corresponding to $G^{(2)}$ in Eq. 2.1.16:

$$L(\mathbf{r}_1,\mathbf{r}_2;\mathbf{r}_1,\mathbf{r}_2,\omega) \equiv L(\mathbf{r}_1,\mathbf{r}_2,\omega) = \sum_{j\neq 0}\left[\frac{\langle\Psi_0^N|\hat{\psi}^\dagger(\mathbf{r}_1)\hat{\psi}(\mathbf{r}_1)|\Psi_j^N\rangle\langle\Psi_j^N|\hat{\psi}^\dagger(\mathbf{r}_2)\hat{\psi}(\mathbf{r}_2)|\Psi_0^N\rangle}{\omega-(E_j^N-E_0^N)+i\eta} - \frac{\langle\Psi_0^N|\hat{\psi}^\dagger(\mathbf{r}_2)\hat{\psi}(\mathbf{r}_2)|\Psi_j^N\rangle\langle\Psi_j^N|\hat{\psi}^\dagger(\mathbf{r}_1)\hat{\psi}(\mathbf{r}_1)|\Psi_0^N\rangle}{\omega+(E_j^N-E_0^N)-i\eta}\right] \tag{2.1.17}$$

where $\{\Psi_j^N\}$ represents excited state wavefunctions of the system with N electrons and E_j^N the corresponding energies. Since the application of the operator $\hat{\psi}^\dagger(1)\hat{\psi}(1)$ (or $\hat{\psi}^\dagger(2)\hat{\psi}(2)$) to the ground state Ψ_0^N does not change the total number of electrons, only the states Ψ_j^N with N electrons yield non-zero matrix elements in Eq. 2.1.17. Because of the product $G^{(1)}(1,1')G^{(1)}(2,2')$ entering the definition of L (Eq. 2.1.13), the term $j=0$ does not contribute to the summation in Eq. 2.1.17.

The physical meaning of L in Eq. 2.1.17 will be discussed further in the next section; we note here that the poles of L correspond to the neutral excitation energies of the many body system. In Sec. 2.2.3 we will show that the calculation of neutral excitations through the solution of the Bethe-Salpeter equation (Eq. 2.1.14) can be reformulated in terms of an eigenvalue problem.

2.1.5 Two-particle correlation functions and linear response theory

Given a many-particle system, one may use linear response theory to study the first order variation of the ground-state expectation value of any physical observable (described by an operator $\hat{A}$) due to the application of a weak external perturbation $V_{ext}(\mathbf{r},t)$. Our interest in linear response theory is twofold: (i) we wish to describe optical absorption experiments, where the electric field of the incident light (the perturbation) is small compared to the internal field of the system (see Sec. 2.2.3); (ii) the definition of response functions, such as the dielectric matrix, is necessary to introduce the screened Coulomb interaction and the GW approximation (see Sec. 2.1.6). Below we relate the two-particle correlation function introduced in the previous section to the first order response (ρ') of the density of a multi-electron system to an applied perturbation.

Consider the ground-state electronic density $\hat{\rho}$ (namely $\hat{A}=\hat{\rho}$); the first order

response to an external perturbation V_{ext} is:

$$\rho'(1) = \int L^R(1,2)V_{ext}(2)d(2) \tag{2.1.18}$$

Here we use the prime symbol $'$ to indicate a perturbed quantity. The first-order response of any other observable represented by an operator $\hat{B}$ can be obtained as $\delta\langle B\rangle(t) = \int B(\mathbf{r})\rho'(\mathbf{r},t)d\mathbf{r}$. In Eq. 2.1.18 we have introduced the retarded two-particle correlation function L^R, that by definition is the response function of the system. At variance with the time-ordered case, retarded correlation functions fulfill the requirement of causality, which is necessary in linear response theory, where a response is obtained only after a perturbation is applied. However, we note that the use of time-ordered Green's functions is necessary to develop Feynman-Dyson perturbation theory and to derive Hedin's equations discussed in the next section.

In Eq. 2.1.18 $L^R(1,2)$ is a particular case of the full (four indexes) retarded correlation function and its Fourier transform to the frequency domain (Lehmann representation) may be easily defined from the time-ordered correlation function of Eq. 2.1.17:

$$L^R(\mathbf{r_1},\mathbf{r_2},\omega) = Re[L(\mathbf{r_1},\mathbf{r_2},\omega)] + i\ sgn(\omega)Im[L(\mathbf{r_1},\mathbf{r_2},\omega)], \tag{2.1.19}$$

where *sgn* denotes the sign function. This relation shows how L^R may be obtained from L. Furthermore, for $\omega \geq 0$ L and L^R coincide. Eq. 2.1.19 represents the formal link between the two-particle correlation function L defined in Sec. 2.1.4 within a Green's function formalism, and linear response theory; in particular, it links L to the first order response of the charge density due to an external perturbation (Eq. 2.1.18).

In the following, we introduce the notation used in the literature of many body perturbation theory (MBPT) applied to solids and we relate such notation to that of linear response theory. We define:

$$\chi(1,2) \equiv L(1,2) \qquad \text{and} \qquad \chi_r(1,2) \equiv L^R(1,2), \tag{2.1.20}$$

where χ is often called time-ordered reducible polarizability and χ_r is the retarded reducible polarizability. For the purpose of this thesis it is also convenient to define the retarded dielectric matrix ε_r and its inverse ε_r^{-1}:

$$V'_{scr}(1) \;=\; \int \varepsilon_r^{-1}(1,2)V_{ext}(2)d(2) \tag{2.1.21}$$

Within linear response Eq. 2.1.21 defines the total screened potential V'_{scr} induced in the system by the external perturbation V_{ext}. By considering $V'_{scr} = V_{ext} + V'_H$, where the second term is the linear response of the Hartree potential induced by V_{ext}, Eq. 2.1.21 can be written as $V'_{scr} = V_{ext} + \upsilon \cdot \chi_r \cdot V_{ext}$ (where we have used Eq. 2.1.18

and the integrals are implicit), and we obtain the relation:

$$\varepsilon_r^{-1}(1,2) = \delta(1,2) + \int v(1,3)\chi_r(3,2)d(3). \tag{2.1.22}$$

Using the definition of V'_{scr} in Eq. 2.1.21, one can alternatively define an irreducible polarizability $\tilde{\chi}_r$, which relates the induced density response to the screened potential V'_{scr}:

$$\rho'(1) = \int \tilde{\chi}_r(1,2)V'_{scr}(2)d(2). \tag{2.1.23}$$

Through Eq. 2.1.19, the definitions of ε_r and relations between ε_r, χ_r and $\tilde{\chi}_r$ may be extended to the corresponding time-ordered quantities ε, χ and $\tilde{\chi}$. From the next section, we drop the subscript "r" for simplicity.

A summary of response functions introduced in this thesis is given in Table 2.2. In the next section we use the concept of dielectric matrix to define an effective

Table 2.2 : Response functions (first column) used in this thesis are defined in the second column. The reducible polarizability (χ) is related to the two particle correlation function (L) (see Eq. 2.1.19 and 2.1.20); the irreducible polarizability ($\tilde{\chi}$) can be expressed by the product of single particle Green's functions (see Eq. 2.1.32) within the Random Phase Approximation (RPA); the dielectric matrix (ε) defines the screened Coulomb interaction (Eq. 2.1.24).

Response Function	Definition
Reducible Polarizability χ	Response of the charge density to the external perturbation V_{ext} $\rho' = \chi V_{ext}$
Irreducible Polarizability $\tilde{\chi}$	Response of the charge density to the screened potential V'_{scr} $\rho' = \tilde{\chi} V'_{scr}$
Dielectric Matrix ε	Screened potential V'_{scr} induced by the external perturbation V_{ext} $V'_{scr} = \varepsilon^{-1} V_{ext}$

(screened) Coulomb interaction W, a basic quantity entering the GW approximation.

2.1.6 Hedin's equations and the GW approximation to the self-energy

In principle, electronic removal and addition energies, necessary to model photoemission measurements, can be computed by solving Eq. 2.1.9; however, the exact self-energy is unknown. As discussed in Sec. 2.1.2, an approximation of Σ may be found by applying Feynman-Dyson perturbation theory to the Coulomb interaction v. In the simplest case this approach leads to the Hartree-Fock approximation, which by definition does not account for any correlation effect. In order to introduce correlation effects Hedin proposed an approach [42, 36] based on the Schwinger's functional derivative method [43, 44]. Instead of expressing Σ in terms of the bare Coulomb potential v, one expresses the self-energy in terms of the dynamically screened Coulomb potential defined by:

$$W(1,2) = \int \varepsilon^{-1}(1,3)v(3,2)d(3). \tag{2.1.24}$$

Here ε^{-1} is the inverse time-ordered dielectric matrix, which describes the screening of the bare Coulomb potential due to all other electrons in the system. Eq. 2.1.24 is a specific case of Eq. 2.1.21 in time-ordered form; all the response functions used in this section will be considered in their time-ordered form.

One may view the screened Coulomb potential W as the Coulomb interaction attenuated by ε^{-1}; hence in principle a perturbative expansion of the self-energy in powers of W may lead to a more rapid convergence than Feynman-Dyson perturbation theory, which is based on the bare v.

Using the polarizabilities defined in Sec. 2.1.5, the screened Coulomb potential can be expressed as

$$\begin{aligned} W(1,2) &= v(1,2) + \int v(1,3)\chi(3,4)v(4,2)d(34) \\ &= v(1,2) + \int v(1,3)\tilde{\chi}(3,4)W(4,2)d(34) \end{aligned} \tag{2.1.25}$$

Hedin [36] introduced a closed set of equations determining Σ and $G^{(1)}$ in terms of

W:

$$\Sigma(1,2) = i \int G^{(1)}(1,3)\Gamma(3,2;4)W(4,1)d(34), \tag{2.1.26}$$

$$\tilde{\chi}(1,2) = -i \int G^{(1)}(1,3)G^{(1)}(4,1)\Gamma(3,4;2)d(34), \tag{2.1.27}$$

$$\Gamma(1,2;3) = \delta(1,2)\delta(1,3) \tag{2.1.28}$$
$$+ \int \frac{\delta\Sigma(1,2)}{\delta G^{(1)}(4,5)} G^{(1)}(4,6)G^{(1)}(7,5)\Gamma(6,7;3)d(4567)$$

where $G^{(1)}$ is given by Eq. 2.1.5 and W by Eq. 2.1.25. Here $v(1,2) = v(\mathbf{r}_1,\mathbf{r}_2)\delta(t_1-t_2)$ and $\Gamma(1,2;3)$ is the so-called vertex function. In principle, the set of Eqs. 2.1.5, 2.1.25-2.1.29 must be solved self-consistently to obtain the exact self-energy and the exact many body single-particle Green's function $G^{(1)}$. However, from a computational standpoint the full self-consistent solution of Hedin's equations is a formidable task. Following Hedin [36], by setting the self-energy Σ to 0 in Eq. 2.1.29, one obtains:

$$\Gamma(1,2;3) = \delta(1,2)\delta(1,3) \tag{2.1.29}$$

which provides a first order expansion of Σ in terms of W, through Eqs 2.1.26-2.1.27:

$$\Sigma(1,2) = iG^{(1)}(1,2)W(1,2) \tag{2.1.30}$$

$$W(1,2) = v(1,2) + \int d(34)v(1,3)\chi_0(3,4)W(4,2) \tag{2.1.31}$$

$$\tilde{\chi}(1,2) = \chi_0(1,2) = -iG^{(1)}(1,2)G^{(1)}(2,1). \tag{2.1.32}$$

Eq. 2.1.32 defines χ_0 which is the random-phase approximation (RPA) to the irreducible polarizability; this approximation treats quasi-particles as independent entities. Eq. 2.1.30 defines the GW approximation to the self-energy. By comparison with Eq. 2.1.10, a formal analogy between the GW and the Hartree-Fock approximation is evident: In the GW approximation instead of the bare Coulomb potential v, used within HF, one uses the dynamically screened Coulomb potential W. Since the self-energy (Eq. 2.1.30) depends on the Green's function, Eq. 2.1.5 or Eq. 2.1.9 must be solved self-consistently. However, in most practical implementations the self-consistent procedure is avoided and the GW self-energy is approximated starting from DFT orbitals and energies (see Secs. 2.2.2.1-2.2.2.2).

By performing a Fourier transform, Eq. 2.1.30 can be expressed as a convolution:

$$\Sigma(\mathbf{r}_1,\mathbf{r}_2,\omega) = \frac{i}{2\pi} \int e^{i\omega'\eta} G^{(1)}(\mathbf{r}_1,\mathbf{r}_2,\omega+\omega')W(\mathbf{r}_1,\mathbf{r}_2,\omega')d\omega'; \tag{2.1.33}$$

this expression is often used in numerical calculations, and its evaluation is a challenging task. To simplify such a task, Hedin introduced the Coulomb-hole plus screened

exchange (COHSEX) approximation to the GW self-energy [42]:

$$\Sigma_{COHSEX}(\mathbf{r}_1,\mathbf{r}_2) = \Sigma_{COH}(\mathbf{r}_1,\mathbf{r}_2) + \Sigma_{SEX}(\mathbf{r}_1,\mathbf{r}_2) = \frac{1}{2}\delta(\mathbf{r}_1,\mathbf{r}_2)W_p(\mathbf{r}_1,\mathbf{r}_2,0) - \sum_{j=1}^{N_{occ}} f_j(\mathbf{r}_1)f_j^*(\mathbf{r}_2)W(\mathbf{r}_1,\mathbf{r}_2,0), \tag{2.1.34}$$

where $W_p = W - v$ and W is the statically screened Coulomb interaction. The term Σ_{COH} describes the interaction of a quasi-particle with the potential induced by the quasi-particle itself. The term Σ_{SEX} represents a statically screened Hartre-Fock exchange operator (see Eq. 2.1.11). The COHSEX self-energy presents several practical advantages over the full GW self-energy (Eq. 2.1.33). The operator Σ_{COHSEX} is Hermitian, static, (i.e. it does not depend on ω) and requires only a summation up to N_{occ} (the number of occupied electronic states); instead the use of the GW approximation (see the definition of the Greens function $G^{(1)}$ in Eq. 2.1.2), requires a summation over all the states (occupied and empty). However, the COHSEX approximation is known to overestimate the electronic gaps of several materials [18], despite some recent improvements [45]. We note that in most computational applications [46, 28, 29], a static approximation to the self-energy is used to approximate the kernel of the Bethe-Salpeter equation (see Eq. 2.1.15), as discussed in Sec. 2.2.

As mentioned in Sec.1.1, in first-principles calculations the KS energy levels and orbitals are often used to build approximations to the Green's functions and response functions and hence to W. The screened Coulomb potential W is a fundamental ingredient both for the solution of the Dyson's equation in the GW approximation, and for the solution of the Bethe-Salpeter equation. Therefore in the next section we describe in detail how W is evaluated in practical calculations starting from KS orbitals. (see Table 2.3 for a summary).

2.1.7 Dielectric matrices and polarizabilities

The key quantity entering the definition of the screened Coulomb potential (Eq. 2.1.24) is the dielectric matrix ε. The main purpose of this section is to discuss how ε is approximated in first-principles calculations based on MBPT. These approximations will then be used in Sec. 2.2, where we describe practical implementations of the GW approximation and the Bethe-Salpeter equation. We first discuss the calculation of the static ε ($\omega = 0$) and later we will illustrate practical approaches adopted to introduce dynamical effects. The response functions discussed here are retarded response functions (see Sec. 2.1.5); however, in order to simplify the notation the subscript "$_r$" is not included. We emphasize again that in the static limit ($\omega = 0$) there is no difference between time-ordered and retarded Green's functions.

In most first-principles MBPT calculations the dielectric matrix ε is computed us-

ing KS single-particle orbitals and energies [18, 47, 46, 28, 48]. Hence before discussing ε, we summarize the definition of polarizabilities within DFT. The Kohn-Sham equations of DFT have the following form [5]:

$$\left[-\frac{1}{2}\nabla^2 + V_{KS}(\mathbf{r})\right]\phi_j(\mathbf{r}) = \epsilon_j^{KS}\phi_j(\mathbf{r}). \tag{2.1.35}$$

where ϕ_j and ϵ_j are KS orbitals and KS single particle energies, respectively, and we have defined the KS effective potential:

$$\begin{aligned} V_{KS}(\mathbf{r}) &= V_H(\mathbf{r}) + V_{xc}(\mathbf{r}) + V_{e-I}(\mathbf{r}) \\ &= \int \frac{\rho(\mathbf{r}')}{|\mathbf{r}-\mathbf{r}'|}d\mathbf{r}' + \frac{\delta E_{xc}[n]}{\delta n(\mathbf{r})} + V_{e-I}(\mathbf{r}). \end{aligned} \tag{2.1.36}$$

In Eq. 2.1.36 $\rho(\mathbf{r})$ is the electronic density, V_H is the Hartree potential, V_{xc} is the functional derivative with respect to the density of the exchange-correlation (xc) energy functional E_{xc}, and V_{e-I} is the external Coulomb potential due to the atomic nuclei. If the exact V_{xc} were known, the self-consistent solution of Eq. 2.1.36 would give the exact density of the many-electron system. The density is expressed as:

$$\rho(\mathbf{r}) = \sum_{j=1}^{N_{occ}} \phi_j^*(\mathbf{r})\phi_j(\mathbf{r}), \tag{2.1.37}$$

where the sum is over the number of occupied orbitals N_{occ}. In practice, approximations are used for E_{xc}. Even simple approximations, such as the local density approximation (LDA), may lead to accurate results for several ground state properties of realistic materials [4].

As a consequence of fundamental theorems [3] of DFT, the response of the KS density to a static perturbation V_{ext} is the same as that of the full many body system. The response of the electronic density can be written as

$$\rho'(\mathbf{r}) = \int \chi_0(\mathbf{r},\mathbf{r}')V'_{KS}(\mathbf{r}')d\mathbf{r}', \tag{2.1.38}$$

where

$$V'_{KS}(\mathbf{r}) = V_{ext}(\mathbf{r}) + V'_H(\mathbf{r}) + V'_{xc}(\mathbf{r}), \tag{2.1.39}$$

and we assumed that the position of atomic nuclei is not modified by the application of the perturbation ($V'_{e-I} = 0$); χ_0 is the static RPA irreducible polarizability, which has the following explicit form:

$$\chi_0(\mathbf{r},\mathbf{r}') = \sum_{jk}(n_k - n_j)\frac{\phi_k^*(\mathbf{r})\phi_j(\mathbf{r})\phi_j^*(\mathbf{r}')\phi_k(\mathbf{r}')}{\epsilon_k^{KS} - \epsilon_j^{KS} + i\eta}. \tag{2.1.40}$$

Here ϕ_j and ϕ_k are KS orbitals and ϵ_j^{KS} and ϵ_k^{KS} are KS energies (see Eq. 2.1.35); n_j and n_k are the occupation numbers of the states j and k, respectively. If j an k are both occupied or both empty states, their contribution to χ_0 vanishes. Note that in the static limit ($\omega = 0$) and within an approximation of $G^{(1)}$ based on DFT (i.e. when approximating the Lehmann amplitudes and energies of Eq. 2.1.2 by ϕ_j and ϵ_j^{KS}, respectively), Eq. 2.1.32 and Eq. 2.1.40 are equivalent. In Eq. (2.1.39) we have introduced the first-order response of the Hartree and xc potential induced by the application of V_{ext}:

$$\begin{aligned} V'_{Hxc}(\mathbf{r}) &= V'_H(\mathbf{r}) + V'_{xc}(\mathbf{r}) \\ &= \int v(\mathbf{r},\mathbf{r}')\rho'(\mathbf{r}')d\mathbf{r}' + \int K^{xc}(\mathbf{r},\mathbf{r}')\rho'(\mathbf{r}')d\mathbf{r}' \end{aligned} \tag{2.1.41}$$

where $K^{xc} = \delta V_{xc}/\delta\rho$ is the functional derivative of the xc potential with respect to the density, evaluated at the ground-state density. By comparing the density response expressed by Eq. 2.1.38 to the definition of Eq. 2.1.18 (with $\omega = 0$, and using $\chi = L^R$), we obtain the following relation, by means of Eq. 2.1.41:

$$\chi = \chi_0 + \chi_0(v + K^{xc})\chi. \tag{2.1.42}$$

Here the coordinate dependence and the integrals over space coordinates are implicit. The term $(v + K^{xc})$ describes correlation effects, absent in the non-interacting KS polarizability χ_0. Indeed, by setting $v + K^{xc}$ to zero, in Eq. 2.1.42 we obtain $\chi = \chi_0$. Eq. 2.1.42 may be used to express χ in terms of χ_0:

$$\chi = (1 - \chi_0 v - \chi_0 K^{xc})^{-1}\chi_0. \tag{2.1.43}$$

Having derived an explicit expression for χ, we finally determine the inverse dielectric matrix entering Eq. 2.1.21 and defining the screened Coulomb interaction. By interpreting the KS response potential V'_{KS} in Eq. 2.1.39 as the effective potential V'_{scr} acting on the electrons, we can easily derive the result

$$\varepsilon^{-1} = 1 + (v + K^{xc})\chi; \tag{2.1.44}$$

this expression of ε is obtained for the case in which the electrons themselves are the probe of the system response [49]. In most practical implementations of first-principles many body perturbation theory the random-phase approximation (RPA) is used for ε^{-1} instead of the full DFT expression of Eq. 2.1.42. The RPA consists in discarding the term K^{xc} in Eq. 2.1.42 and leads to the following expression of ε^{-1}:

$$\varepsilon^{-1}_{RPA} = 1 + v\chi = 1 + v(1 - \chi_0 v)^{-1}\chi_0 \tag{2.1.45}$$

that can also be written in the more common form:

$$\varepsilon_{RPA} = 1 - v\chi_0. \tag{2.1.46}$$

In several first-principles MBPT calculations the frequency dependence of ε is described by using models, such as the plasmon-pole model [20, 50], which will be discussed in detail in Sec. 2.2.1.1. Alternatively, by defining the RPA independent electron dynamical polarizability

$$\chi_0(\mathbf{r}, \mathbf{r}', \omega) = \sum_{jk} (n_k - n_j) \frac{\phi_k^*(\mathbf{r})\phi_j(\mathbf{r})\phi_j^*(\mathbf{r}')\phi_k(\mathbf{r}')}{\omega + (\epsilon_k^{KS} - \epsilon_j^{KS}) + i\eta}, \tag{2.1.47}$$

an equation formally identical to Eq. 2.1.42 may be derived for the frequency dependent ε. However, in this case the derivation must be carried out within the time-dependent density functional theory framework, and the kernel K^{xc} depends explicitly on the energy ω [12]. For practical purposes the adiabatic approximation $K^{xc} \approx K^{xc}(\omega = 0)$ is adopted in most cases [51]. The definition of the RPA dielectric matrix given in Eqs. 2.1.45-2.1.46 are valid also in the dynamical case. The solution of Eq. 2.1.42 or the analogous RPA equation ($K^{xc} = 0$) could be used to describe the optical spectra at the TDDFT and DFT-RPA levels of theory.

2.2 Algorithms to compute quasi-particle energies and optical spectra

Having established the theoretical framework of MBPT, we discuss below the main algorithms used in first principles calculations to compute photoemission and absorption spectra (see Table 2.3). Our discussion is split into three parts and includes algorithms to compute the dielectric matrix, the self-energy, and to solve approximate forms of the BSE.

2.2.1 Calculation of dielectric matrices

The algorithms discussed in this section are divided into methods where explicit summations on empty states are performed (Sec. 2.2.1.1) and methods that avoid these explicit summations (Sec. 2.2.1.2) by using, e.g. density functional perturbation theory.

2.2.1.1 Direct calculation of dielectric matrices

Most calculations of dielectric matrices are based on a plane wave(PW) representation [52, 20, 49, 53] of the orbitals and density, although calculations using localized

Table 2.3 : Theoretical approximations (second row) and algorithmic challenges (fourth row) involved in the calculation of photoemission and absorption spectra. Quasiparticle energies and absorption spectra are defined in the third row of the table.

Physical observables	Photoemission spectra	Absorption spectra
Theoretical Approximations	GW approximation: 1st order, perturbative expansion of the self energy Σ in terms of the screened Coulomb interaction W: $\Sigma \sim iGW$; $W = \varepsilon^{-1} v$	Solution of the BSE: approximate self energy (e.g. using GW) in two particle Hamiltonian ($\mathcal{L}$) , defined within 1st order perturbation theory
Practical calculations	Ground state single particle orbitals from KS equations; Quasi-particle energy corrections to KS eigenvalues from the expectation value of Σ on KS orbitals	Frequency dependent polarizability (molecules) or macroscopic dielectric function (solids) from iterative diagonalization of two-particle Hamiltonian
Algorithmic Challenges	Evaluate sums on virtual states for G and W Frequency dependence and inversion of ε	Evaluate sums on virtual states for $\mathcal{L}$ and W inversion of ε

orbitals have been proposed in the literature [54, 55, 56]. With PW basis sets, both periodic systems and molecules can be treated in a straightforward way, by using a supercell approach. Here we discuss practical calculations of dielectric matrices using a plane-wave basis set for the KS orbitals and charge density. However, our discussion is general and valid irrespective of the basis set chosen.

Within a plane-wave representation,

$$\varepsilon^{-1}(\mathbf{r},\mathbf{r}') = \frac{1}{\Omega}\sum_{\mathbf{q},\mathbf{G},\mathbf{G}'} e^{i(\mathbf{q}+\mathbf{G})\cdot\mathbf{r}}\varepsilon^{-1}_{\mathbf{G},\mathbf{G}'}(\mathbf{q})e^{-i(\mathbf{q}+\mathbf{G}')\cdot\mathbf{r}'}, \tag{2.2.1}$$

where Ω denotes the crystal volume, $\mathbf{q}$ is the transferred momentum and $\mathbf{G}$ and $\mathbf{G}'$ are the reciprocal lattice vectors. The limit $q \to 0$ is well defined, as discussed in Refs. [49, 53], but for $G' = G = 0$ the calculation of ε^{-1} requires a special treatment. For a homogeneous system, ε depends only on $|\mathbf{r} - \mathbf{r}'|$ and is diagonal in reciprocal space ($\varepsilon(\mathbf{G},\mathbf{G}') = 0$ for $\mathbf{G} \neq \mathbf{G}'$). For an inhomogeneous system, the off-diagonal elements $\varepsilon(\mathbf{G},\mathbf{G}')$ yield the so called local field effects.

The first step to compute $\varepsilon^{-1}_{\mathbf{G},\mathbf{G}'}$ is the evaluation of the irreducible polarizability χ_0 (Eq. 2.1.40):

$$(\chi_0)_{\mathbf{G},\mathbf{G}'}(\mathbf{q}) = \frac{4}{\Omega}\sum_{c,v,\mathbf{k}} \frac{\langle\phi_{v\mathbf{k}}|e^{-i(\mathbf{q}+\mathbf{G})\cdot\mathbf{r}}|\phi_{c\mathbf{k}+\mathbf{q}}\rangle\langle\phi_{c\mathbf{k}+\mathbf{q}}|e^{i(\mathbf{q}+\mathbf{G}')\cdot\mathbf{r}'}|\phi_{v\mathbf{k}}\rangle}{\epsilon^{KS}_{v\mathbf{k}} - \epsilon^{KS}_{c\mathbf{k}+\mathbf{q}}} \tag{2.2.2}$$

where a factor 2 has been introduced to account for spin degeneracy and the indexes v and c label valence and conduction states, respectively, in the case of a solid. (In the case of molecules, v and c represent occupied and virtual states, respectively). Eq. 2.2.2 is the Adler-Wiser formulation [57, 58] of χ_0. The evaluation of χ_0 using Eq. 2.2.2 requires the explicit calculation of the conduction states ϕ_c. In principle all the empty states of the KS Hamiltonian should be included in the summation. In practical calculations only a finite number of them is included and the convergence of the sum is systematically tested. In addition, the expression of Eq. 2.2.2 requires the evaluation of all possible combinations of c, v, $\mathbf{k}$, and $\mathbf{q}$. The calculation of the integrals $\int \phi^*_{v\mathbf{k}}(\mathbf{r}) e^{-i(\mathbf{q}+\mathbf{G})\cdot\mathbf{r}} \phi_{c\mathbf{k}+\mathbf{q}}(\mathbf{r}) d\mathbf{r}$ scales has $N^2_{pw} N_c N_v N_k N_q$ where N_{pw} is the number of basis functions (plane-waves) used to represent the single particle states; N_c and N_v is the number of conduction and valence states, respectively and N_k and N_q are the number of k and q points (defined as the difference between k points) included in the BZ summation. (For calculations of molecules and clusters one uses only the $k = (0, 0, 0)$ point and $N_k = N_q = 1$). Once χ_0 is obtained, ε^{-1} is computed through Eq. 2.1.45, which requires the inversion of the matrix $(1 - \chi_0 v)$ and a subsequent matrix multiplication. The number of reciprocal $\mathbf{G}$ vectors (that determines the dimension of χ_0) used in first-principles calculations is often large (many thousands) even for systems with a relatively small number of electrons, and the direct inversion of ε becomes very demanding. If the dielectric matrix is computed for multiple frequencies, the inversion must be repeated for each frequency.

For example, in the calculation of quasi-particle energies within the GW approximation, dynamical effects are included in the screened Coulomb potential by evaluating the inverse dynamical dielectric matrix $\varepsilon^{-1}(\omega)$, which thus needs to be inverted for each ω. Furthermore ε^{-1} has poles on the real ω axis. To overcome these difficulties several numerical implementations use a plasmon-pole model (PPM), where the dependence on ω of ε^{-1} is described by a single plasmon-pole:

$$\begin{aligned}\varepsilon^{-1}_{\mathbf{G}\mathbf{G}'}(\mathbf{q},\omega) \approx & \delta_{\mathbf{G}\mathbf{G}'} + \frac{R_{\mathbf{G}\mathbf{G}'}(\mathbf{q})}{\omega - \tilde{\omega}_{\mathbf{G}\mathbf{G}'}(\mathbf{q}) + i\eta} \\ & - \frac{R_{\mathbf{G}\mathbf{G}'}(\mathbf{q})}{\omega + \tilde{\omega}_{\mathbf{G}\mathbf{G}'}(\mathbf{q}) - i\eta},\end{aligned} \tag{2.2.3}$$

where $R_{\mathbf{G}\mathbf{G}'}$ and $\tilde{\omega}_{\mathbf{G}\mathbf{G}'}$ are parameters to be determined for each specific system. Once Eq. 2.1.45 is solved, the value of $\varepsilon^{-1}_{\mathbf{G}\mathbf{G}'}(\mathbf{q}, \omega = 0)$ can be used to fix one of the two parameters in Eq. 2.2.3 (this operation is required for each value of $\mathbf{G}, \mathbf{G}'$, and $\mathbf{q}$). In the plasmon-pole approximation proposed by Hybertsen and Louie [20] the f-sum rule is used as a constraint for the determination of the remaining parameter. In the approach proposed by Godby and Needs [50] the remaining parameter is determined by computing ε^{-1} for an additional imaginary frequency ($i\omega$). The PPM approach considerably simplifies the numerical workload necessary to include dynamical effects in quasi-particle calculations. However, the accuracy of the PPM to compute GW

quasi-particle energies is difficult to assess, and the results may considerably depend on the choice of the specific model [59, 21].

Alternatively, one may solve Eq. 2.1.45 starting from the dynamical polarizability χ_0 defined in Eq. 2.1.47. Since χ_0 and the inverse dielectric matrix ε^{-1} have poles on the real axis, they are usually computed on the imaginary axis ($\omega \to i\omega$) [19, 47]. On the imaginary axis ε^{-1} is a smooth function of ω and the integrals necessary to evaluate the self-energy Σ are easier to compute. The expectation value of the self-energy on the imaginary axis is then fitted to a multipole function, which is used to evaluate the final result for real energies.

2.2.1.2 Projective dielectric eigenpotential method

Recently an alternative approach was introduced for the calculation of the dielectric matrix ε [60, 61] called projective dielectric eigenpotential method (PDEP). Applied so far within the RPA approximation, this approach is based on the iterative diagonalization of the dielectric matrix and is of general validity beyond the RPA. At each iterative step, the dielectric matrix is applied to an approximate set of eigenvectors using density-functional perturbation theory (DFPT) [53]. The method was first used to compute ε for the evaluation of ground-state correlation energies [62, 63], and more recently it was incorporated in many body perturbation theory calculations [33, 30, 23].

The dielectric matrix ε is not Hermitian and it is convenient to introduce the following symmetrized form:

$$\bar{\varepsilon}_{\mathbf{G},\mathbf{G}'}(\mathbf{q}) = \frac{|\mathbf{q}+\mathbf{G}|}{|\mathbf{q}+\mathbf{G}'|}\varepsilon_{\mathbf{G},\mathbf{G}'}(\mathbf{q}). \tag{2.2.4}$$

The matrix $\bar{\varepsilon}$ is easier to handle from a numerical point of view, since iterative algorithms to diagonalize Hermitian matrices, such as the Davidson algorithm [64], are in general more stable and efficient than those used for non-Hermitian matrices. Within PDEP one considers a spectral decomposition of $\bar{\varepsilon}$:

$$\bar{\varepsilon} = \sum_{i=1}^{N_{eig}} \lambda_i |U_i\rangle\langle U_i| = \sum_{i=1}^{N_{eig}} (\lambda_i - 1)|U_i\rangle\langle U_i| + I. \tag{2.2.5}$$

where the eigenvectors (or eigenpotentials) U_i and eigenvalues λ_i are obtained iteratively.

A number N_{eig} of random trial potentials U_i^0 is first generated and then orthonormalized. Starting from this guess, an iterative algorithm, such as Davidson [64] or Ritz acceleration, is used to diagonalize $\bar{\varepsilon}$. At each iteration (*iter*) the dielectric matrix is applied to the current approximation of the eigenpotentials U_i^{iter}:

$(\bar{\varepsilon} - I)U_i^{iter} = -v^{\frac{1}{2}}\chi_0 v^{\frac{1}{2}}U_i^{iter} = -v^{\frac{1}{2}}\rho'$, where ρ' is determined from:

$$\rho'(\mathbf{r}) = 4Re\sum_{j=1}^{N_{occ}} \phi_j^*(\mathbf{r})\phi_j'(\mathbf{r}), \tag{2.2.6}$$

and

$$(\hat{H}_{KS} - \varepsilon_j^{KS})|\phi_j'\rangle = -\hat{Q}V_{KS}'|\phi_j\rangle \tag{2.2.7}$$

by setting $V_{KS}' = v^{\frac{1}{2}}U_i^{iter}$. In Eq. 2.2.6 and 2.2.7 $\hat{Q}$ is the projector onto the virtual state subspace, V_{KS}' is defined in Eq. 2.1.39, and ϕ_i' represents the linear response of KS orbitals. Once the required accuracy in the diagonalization is reached, the iterative procedure is stopped.

The eigenvalue decomposition of Eq. 2.2.5 is useful for practical purposes only if the number of eigenpotentials N_{eig} necessary to approximate $\bar{\varepsilon}$ is much smaller than the dimension of the full matrix [65]. The eigenvalues λ_i are larger than or equal to 1 and for many systems [60, 61] they rapidly decay to 1 as a function of the index i. This finding implies that $(\lambda_i - 1)$ rapidly goes to 0 as a function of i and the summation in Eq. 2.2.5 can be truncated to a small number N_{eig}. Recent GW and BSE calculations [33, 30, 23] demonstrated that the number N_{eig} is indeed much smaller than the size of the full matrix $\bar{\varepsilon}$ for several classes of systems.

The use of Eq. 2.2.5 to represent the dielectric matrix has several advantages: a small number of eigenpotentials needs to be stored in memory instead of the full matrix $\bar{\varepsilon}$; the size of $\bar{\varepsilon}$ as function of the number of PWs does not need to be truncated, and the inversion of the dielectric matrix is avoided. Furthermore, the eigenvalue decomposition of $\bar{\varepsilon}$ is obtained within DFPT and does not require the explicit inclusion of virtual (empty) states in any summation: all the virtual states described by the chosen basis set are automatically included.

The PDEP procedure may also be applied to compute the frequency dependent dielectric function. In the case of imaginary frequencies, the operator on the left hand side of Eq. 2.2.7 is $(\hat{H}_{KS} - \epsilon_i^{KS} - i\omega)$. The corresponding linear problem is no longer Hermitian and can be solved by a biconjugate gradient algorithm. The eigenvalue decomposition is carried out [62] for each value of ω.

An alternative, more efficient approach consists in using the eigenpotentials $\{U_i\}$ at $\omega = 0$ as a basis set for $\bar{\chi}_0(i\omega) = v^{\frac{1}{2}}\chi_0(i\omega)v^{\frac{1}{2}}$; the definition of $\bar{\chi}_0$ is computationally more convenient than that of χ_0 as it is similar to the definition of $\bar{\varepsilon}$. The expansion coefficients $\bar{\chi}_0^{ij}(i\omega) = \int U_i(\mathbf{r})\bar{\chi}_0(\mathbf{r},\mathbf{r}';i\omega)U_j(\mathbf{r}')d\mathbf{r}d\mathbf{r}'$ are expressed in the form [23]:

$$\begin{aligned}\bar{\chi}_0^{ij}(i\omega) = & 2\sum_{k=1}^{N_{occ}}\{\langle\phi_k(v^{\frac{1}{2}}U_i)|\hat{Q}(\hat{H}_{KS} - \epsilon_k^{KS} - i\omega)^{-1}\hat{Q}|\phi_k(v^{\frac{1}{2}}U_j)\rangle \\ & + c.c.\}\end{aligned} \tag{2.2.8}$$

and they can be efficiently computed by using the Lanczos algorithm [66]. By introducing $\bar{\chi}(i\omega) = v^{\frac{1}{2}}\chi(i\omega)v^{\frac{1}{2}}$ from Eq. 2.1.42 in the RPA approximation ($K^{xc} = 0$) we have $\bar{\chi} = (1 - \bar{\chi}_0)^{-1}\bar{\chi}_0$. This equation can be easily solved to compute $\bar{\chi}$ and the reducible polarizability, and the basis set $\{U_i\}$ is usually much smaller than that used for the wavefunctions and density.

2.2.2 Calculation of the self-energy

Similar to the previous section we first discuss methods where explicit summations on empty states are performed (Sec. 2.2.2.1) and then methods that avoid these summations (Sec. 2.2.2.2). Recent developments beyond the G_0W_0 approximation are presented in Sec. 2.2.2.3.

2.2.2.1 G_0W_0 calculations based on direct summations

Calculations of quasi-particle energies of realistic systems within the GW approximation have been performed both in the time domain (Eq. 2.1.30) [67] and in the frequency domain (Eq. 2.1.33) [20, 19]. In particular, the time domain approach [67] takes advantage of the simple multiplicative form of the self-energy (Eq. 2.1.30) and of the polarizability in Eq. 2.1.32, within a real space and (imaginary) time representation. However, it includes FFT transforms of ϵ from imaginary frequencies and reciprocal space to real time and space, and summations over empty states are not avoidable in any straightforward way.

The solution of Eq. 2.1.9 with the self-energy approximated at the GW level of theory (Eq. 2.1.33) is numerically challenging for several reasons: the GW self-energy depends on the solution of the Dyson's equation, and explicitly on the energy; in addition, it is non-local in space. Most of practical implementations are based on the G_0W_0 approach [18, 20]. Within this scheme the Green's function (Eq. 2.1.2) is evaluated by approximating the quasi-particle amplitudes with KS orbitals and the quasi-particle energies with KS energy levels:

$$G^{(1)}(\mathbf{r}_1, \mathbf{r}_2, \omega) \approx \sum_j \frac{\phi_j(\mathbf{r}_1)\phi_j^*(\mathbf{r}_2)}{\omega - \epsilon_j^{KS} + i\eta sgn(\epsilon_j^{KS} - \varepsilon_F)}. \tag{2.2.9}$$

The screened Coulomb potential is approximated by using the inverse dielectric matrix in Eq. 2.1.45; when using the KS orbitals to evaluate the screened Coulomb potential, one uses the notation W_0 instead of W. The effects of the dynamical screening are often introduced by a plasmon-pole model (Eq. 2.2.3) or by evaluating ε on the imaginary axis. The quasi-particle energies are then computed as corrections to KS eigenvalues by using first order perturbation theory:

$$\epsilon_j^{GW} = \epsilon_j^{KS} + \langle\phi_j|\Sigma(\epsilon_j^{GW}) - V_{xc}|\phi_j\rangle. \tag{2.2.10}$$

Eq. 2.2.10 must be solved self-consistently in ϵ_j^{GW}; alternatively, using a Taylor expansion one has $\epsilon_j^{GW} \approx \epsilon_j^{KS} + Z_j\langle\phi_j|\Sigma(\epsilon_j^{KS}) - V_{xc}|\phi_j\rangle$ with $Z_j = [1 - \langle\phi_j|\partial\Sigma/\partial\epsilon|_{\epsilon=\epsilon_j^{KS}}|\phi_j\rangle]^{-1}$.

The G_0W_0 approximation implicitly assumes that KS orbitals are a reasonably accurate representation of quasi-particle wavefunctions. In principle there is no sound theoretical justification for this assumption. In practice the G_0W_0 approximation has been shown to work reasonably well for a variety of periodic solids [18, 19, 20]. For molecules the use of this approximation is more controversial [68] but overall it has given accurate results for the ionization potentials of several systems [24, 25, 23].

For computational convenience, one normally writes $iG\cdot W = iG\cdot\upsilon + iG\cdot\upsilon\cdot\chi\cdot\upsilon \equiv \Sigma_x + \Sigma_c$, where the term $iG\cdot\upsilon$ is the Hartree-Fock self-energy Σ_x (Eq. 2.1.10). The evaluation of the expectation value of Σ_x is equivalent to evaluating the exchange term in the Hartree-Fock theory but using DFT orbitals instead of self-consistent HF orbitals. In quantum chemistry codes, this operation is efficiently performed with localized basis, but it is not straightforward in a plane wave representation; in particular care must be exercised to integrate divergences [62, 69]. The most expensive component of G_0W_0 calculations is the evaluation of Σ_c, which requires summations over virtual states of the KS Hamiltonian. These sums are necessary to evaluate both Eq. 2.2.9 and Eq.2.1.40 (or equivalently Eq.2.2.2). In particular it has been shown that the convergence of G_0W_0 can be extremely slow both for some bulk materials, e.g. ZnO [70, 59] and molecular systems, e.g. benzene [24].

Unless a PPM is used, the sum over states in the screened Coulomb potential must be evaluated for each value of ω'; in the case of $G^{(1)}$ it must be evaluated for each value of $(\omega + \omega')$ (namely on a mesh twice as large as that of the ω domain). The convolution in Eq. 2.1.33 can then be computed through a direct integration or a Fourier transform.

2.2.2.2 G_0W_0 calculations based on the spectral decomposition of the dielectric matrix

To avoid the explict summations over a large number of virtual states required for the calculation of the GW self-energy Σ_c, one may use the PDEP technique. We rewrite Eq. 2.2.9 as:

$$G^{(1)}(i\omega) \approx \frac{1}{\hat{H}_{KS} - i\omega}. \tag{2.2.11}$$

We then use the definition of the GW self-energy in the frequency domain (Eq 2.1.33) and the expansion of the dielectric matrix in terms of the static eigenpotentials (see Sec. 2.2.1.2); we arrive at the following expression for the expectation value of Σ_c for

imaginary frequencies:

$$\langle\phi_k|\Sigma_c(i\omega)|\phi_k\rangle = \frac{i}{2\pi}\sum_{i,j=1}^{N_{eig}}\int d\omega' \bar{\chi}_{ij}(i\omega') \times$$
$$\langle\phi_k(v^{\frac{1}{2}}U_i)|[\hat{H}_{KS} - i(\omega+\omega')]^{-1}|\phi_k(v^{\frac{1}{2}}U_j)\rangle; \quad (2.2.12)$$

the coefficients $\bar{\chi}_{ij}$ are computed from Eq. 2.2.8 by using the definition $\bar{\chi} = (1 - \bar{\chi}_0)^{-1}\bar{\chi}_0$. In Eq. 2.2.12 the matrix element can be computed with the Lanczos algorithm proposed in Refs. [66, 25]. Such algorithm has the advantage that only a single iterative Lanczos chain is performed for all the frequencies $(\omega + \omega')$. Within this approach all summations over the virtual states are avoided, and all the virtual states described by the chosen basis set are implicitly included. In addition the convergence of the calculation is controlled by a single parameter: N_{eig} (Eq. 2.2.5).

The computational workload[60, 61, 62] to generate the dielectric matrix with N_{eig} eigenvectors scales as $N_{iter} \times N_{eig} \times N_{pw} \times N_v^2$, with N_{iter} being the number of iterations needed to converge the dielectric eigenvectors in the iterative diagonalization procedure (N_{iter} is typically not more than 10 for systems with tens to several hundreds electrons). In addition, the cost of Lanczos chains generation to compute $\bar{\chi}_0^{ij}$ and Σ_c is $N_{Lanczos} \times N_{eig} \times N_{pw} \times N_v^2$ where $N_{Lanczos}$ is the number of Lanczos iterations, which is typically just a few tens. Therefore the total workload of our approach is $(N_{iter} + N_{Lanczos}) \times N_{eig} \times N_{pw} \times N_v^2$, and it is proportional to the fourth power of the system size.

This workload represents a substantial improvement over that of conventional approaches (which sum over all the conduction states explicitly), $N_{pw\bar{\chi}}^2 \times N_v \times N_c$, which is also proportional to the fourth power of the system size, but with a substantially larger prefactor. In particular, N_{pw} is much smaller than the number of basis function $N_{pw\bar{\chi}}$, used to represent density responses and perturbing potentials; the corresponding kinetic-energy cutoff is four times as large as that needed to represent wavefunctions, in the case of norm-conserving pseudopotentials. Furthermore, the number of occupied states N_v is often an order of magnitude smaller than the number of unoccupied states N_c required to converge summations in the dielectric matrix and Green's function. Finally, the number of eigenvectors N_{eig} is usually several orders of magnitude smaller than the size of the response function $N_{pw\bar{\chi}}$.

Recently, in addition to PDEP several other techniques were proposed, to improve the efficiency of GW calculations by removing the explicit summations over empty states entering the expression of Σ_c. For example, the approach of Refs. [24, 25] uses an optimal basis set to represent the polarizability; a Lanczos algorithm is then adopted to numerically compute an expression similar to Eq. 2.2.12. In order to eliminate the summation over virtual states necessary to compute the optimal basis set, in Ref. [25] the projector onto the virtual state subspace $\hat{Q}$ is approximated by an expansion in plane-waves orthogonalized to the occupied state subspace. DFPT was

also used in Ref. [71] to avoid the calculation of empty states: the inverse dielectric matrix $\varepsilon^{-1}_{\mathbf{G},\mathbf{G}'}(\mathbf{q},\omega)$ is computed by solving Eq. 2.2.7 for each perturbation, namely for each set of parameters $[\mathbf{q},\mathbf{G},\omega]$. The solution of such equation for all possible perturbations is computationally very demanding with PW basis sets, but it can be efficiently implemented in a localized basis set approach [72]. In Ref. [73, 74] the summation over empty states in the GW self-energy was avoided by defining and systematically approximating an effective energy that takes into account the contribution of all empty states. Finally we would like to mention that other approaches were proposed that, while retaining summations over empty states, attempt to reduce the number of unoccupied states needed [75] to reach convergence, or to approximate them by a combination of plane-waves and resonant orbitals [76].

2.2.2.3 Self-consistent GW calculations and vertex corrections

The G_0W_0 approach was used in most implementations appeared so far in the literature. However, fully or partially self-consistent calculations were performed either using the full energy dependent GW self-energy [68, 77] or a static approximation [78, 79]. In some cases partial self-consistency was included, by approximating the quasi-particle wavefuntions at the DFT level of theory and performing a self-consistent calculation only on the energy levels (in G, in W, or in both) [80, 81]. In Ref. [82], it was suggested that GW quasi-particle wavefunctions can be accurately approximated by those obtained in self-consistent COHSEX calculations (Eq. 2.1.34); this approach was applied to bulk silicon, aluminum, and argon and gave reasonable estimates of self-consistent GW results, at a much lower computational cost. The usefulness of the GW self-consistent approach is still controversial; in some cases it was proven to decrease significantly the dielectric screening and to worsen the agreement between theory and experiment [83], with respect to G_0W_0.

Some implementations also attempted to go beyond the GW approximation and introduce vertex corrections by improving the approximation of Γ in Eq. 2.1.29. A possible practical way to proceed consists in approximating the initial self-energy by the DFT (LDA) exchange and correlation potential $\Sigma(1,2) = V_{xc}(1)\delta(1,2)$ [84]. After an iterative step of the Hedin's equations, one obtains an expression formally similar to the GW approximation (Eq. 2.1.33). However, in this case the reducible polarizability χ is approximated through Eq. 2.1.42 and the screened Coulomb potential is obtained by using the inverse dielectric matrix in Eq. 2.1.44. This formalism, called GWΓ, was applied to compute the quasi-particle spectrum of silicon and it was suggested that, although the computed quasi-particle gap is similar to that of the G_0W_0 approach, the vertex corrections might introduce substantial changes in the absolute position of the energy levels [84, 85]. In Ref. [86] it was shown that the GWΓ method improves the agreement with experiment for the values of the ionization potentials and electron affinities of several molecules (e.g. benzene and naphthalene) and it was also applied to the study of silicon nanoparticle electronic properties as a function of

diameter.

2.2.3 Solution of the Bethe-Salpeter equation and calculation of optical spectra

In this section we first define the physical quantities related to optical absorption measurements in molecules and solids (Sec. 2.2.3.1) and we then present algorithms to solve the BSE and compute absorption spectra (Sec. 2.2.3.2). We close this section by comparing time dependent DFT and the BSE (Sec. 2.2.3.3).

2.2.3.1 Macroscopic polarizability and macroscopic dielectric function

In optical absorption or reflectivity experiments, for example by UV-Vis spectrometry or ellipsometry, the intensity of the electromagnetic field of the incident light is much weaker than that of internal fields, and it can be treated within linear response theory. Here we discuss how the response functions that describe optical absorption experiments are calculated.

In molecules the macroscopic polarizability tensor α_{ij} relates the induced dipole ($\mathbf{d}'$) and the applied field $\mathbf{E}$:

$$d'_i(\omega) = \sum_j \alpha_{ij}(\omega) E_j(\omega), \tag{2.2.13}$$

where i and j indicate Cartesian coordinates; α is related to the retarded reducible polarizability (Eq. 2.1.20), by the equation $\alpha = \int \mathbf{r}\chi(\mathbf{r},\mathbf{r}')\mathbf{r}' d\mathbf{r} d\mathbf{r}'$, where the external perturbing potential is $V_{ext} = -\mathbf{E}(\omega)\cdot\mathbf{r}'$, and $\mathbf{r}$ is proportional to the dipole induced in the system. The absorption coefficient $I(\omega)$ is proportional to the imaginary part of the trace of the dynamical polarizability tensor: $I(\omega) \propto \omega \mathrm{Im}\left(\mathrm{Tr}(\alpha(\omega))\right)$. For an isolated molecule there is no preferred orientation and one averages over the diagonal components of the macroscopic polarizability.

In the case of solids the optical absorption spectrum is given by the imaginary part of the macroscopic dielectric function, which is related to the dielectric matrix (a microscopic quantity) by [57, 58]:

$$\varepsilon^M = \lim_{\mathbf{q}\to 0} \frac{1}{\varepsilon^{-1}_{\mathbf{G}=0,\mathbf{G}'=0}(\mathbf{q},\omega)}. \tag{2.2.14}$$

In principle Eq. 2.2.14 requires the calculation of the full dielectric matrix and its inversion to obtain the single matrix element in the denominator. In practice, as shown in Ref. [16], the value of ε_M (or α) may be obtained by computing the matrix element of the resolvent of an effective two-particle operator (the operator $\mathcal{L}$ that will be discussed below in Sec. 2.2.3.2); the eigenvalues of this operator correspond to the excitation energies of the system.

2.2.3.2 Formulation of the Bethe-Salpeter equation based on density matrix perturbation theory

Here we derive a specific form of the BSE using linear response theory applied to density matrices, and we present practical ways of computing neutral two-particle excitation energies as eigenvalues of an effective two-particle operator. The approach presented below may be considered as equivalent to solving a time-dependent Dyson's equation. We note that the formalism presented here may not be used to solve the full BSE of Eq. 2.1.14; indeed only the response function χ of Eq. 2.1.20 is considered, instead of the full (four-indexes) correlation function of Eq. 2.1.13. As discussed in Secs. 2.1.4-2.1.5, the response function χ is sufficient to describe optical absorption experiments. The starting point of our derivation is the quantum-Liouville equation (for simplicity we omit k-point labeling of states):

$$i\frac{d\hat{\rho}(t)}{dt} = \left[\hat{H}(t), \hat{\rho}(t)\right], \tag{2.2.15}$$

where the square brackets indicate commutators. Within a real space representation, we have $\rho(\mathbf{r}, \mathbf{r}', t) = \sum_{j=1}^{N_{occ}} \phi_j(\mathbf{r}, t)\phi_j^*(\mathbf{r}', t)$; here we use ϕ to indicate time-dependent orbitals and ϕ° to indicate unperturbed ground-state orbitals. The time-dependent quasi-particle Hamiltonian is:

$$\begin{aligned}
&\int \hat{H}(\mathbf{r}, \mathbf{r}', t)\phi(\mathbf{r}', t)\, d\mathbf{r}' = \\
&\left(-\frac{1}{2}\nabla^2 + V_H(\mathbf{r}, t) + V_{e-I}(\mathbf{r}) + V_{ext}(\mathbf{r}, t)\right)\phi(\mathbf{r}, t) \\
&+ \int \Sigma(\mathbf{r}, \mathbf{r}', t)\phi(\mathbf{r}', t)d\mathbf{r}',
\end{aligned} \tag{2.2.16}$$

where we assumed that the electron-ion potential is left unchanged by the external potential $V_{ext}(\mathbf{r}, t)$. We consider a static approximation to the self-energy, hence Σ depends on time only through the dependence on $\hat{\rho}(t)$. The static approximation is justified in the case of the COHSEX self-energy (Eq. 2.1.34) but not for the GW self-energy (Eq. 2.1.33), that includes dynamical effects and depends explicitly on $G^{(1)}$. The quasi-particle amplitudes f_j in Eqs. 2.1.3-2.1.4 are approximated by KS orbitals, as usually done in practical implementations to solve the BSE [87, 46, 28, 88]. However, the derivation below is valid in general as long as the $\{f_j(\mathbf{r})\}$ are an orthonormal basis set.

By considering $\hat{V}_{ext}$ in Eq. 2.2.16 as a small perturbation, the linearization of Eq. (4.1.1) leads to:

$$
\begin{aligned}
i\frac{d\hat{\rho}'(t)}{dt} &= \mathcal{L}\cdot\hat{\rho}'(t) + \left[\hat{V}_{ext}(t),\hat{\rho}^{\circ}\right], && (2.2.17)\\
\mathcal{L}\cdot\hat{\rho}'(t) &= \left[\hat{H}^{\circ},\hat{\rho}'(t)\right] + \left[\hat{V}'_{H}[\hat{\rho}'](t),\hat{\rho}^{\circ}\right] \\
&\quad + \left[\hat{\Sigma}'[\hat{\rho}'](t),\hat{\rho}^{\circ}\right], && (2.2.18)
\end{aligned}
$$

where variables with superscript "$\circ$" represent unperturbed quantities, and those with prime denote linear variations; specifically in this case $\hat{\rho}' = \hat{\rho} - \hat{\rho}^{\circ}$ denotes the linear variation of the charge density. Note the dependence of $\hat{V}_H$ and $\hat{\Sigma}$ on the linear-response of the density matrix $\hat{\rho}'$. In Eq. 4.1.9 a non-Hermitian operator $\mathcal{L}$ acting on $\hat{\rho}'$ has been defined, which is known as Liouvillian super-operator [89, 66], as its action is defined on a space of operators (the density matrices). By Fourier transforming Eq. 4.1.9 into the frequency domain, one obtains

$$(\omega - \mathcal{L})\cdot\hat{\rho}'(\omega) = \left[\hat{V}_{ext}(\omega),\hat{\rho}^{\circ}\right]. \tag{2.2.19}$$

The solution of this equation yields $\hat{\rho}'(\omega)$. If in Eq. 2.2.19 the external perturbation is set to $V_{ext}(\mathbf{r},\omega) = -\mathbf{E}(\omega)\cdot\mathbf{r}$, the response of the i-th component of the dipole in Eq. 2.2.13 can be obtained as $d'_i(\omega) = \mathrm{Tr}\left(\hat{r}_i\hat{\rho}'(\omega)\right)$, where Tr indicates the trace operator. By solving explicitly Eq. 2.2.19, we have that the components of the polarizability tensor are:

$$\alpha_{ij}(\omega) = -\left\langle\hat{r}_i|(\omega - \mathcal{L} + i\eta)^{-1}\cdot[\hat{r}_j,\hat{\rho}^{\circ}]\right\rangle, \tag{2.2.20}$$

where η is a positive infinitesimal, and we wrote the scalar product of two operators A and B as $\langle\hat{A}|\hat{B}\rangle \equiv Tr(\hat{A}^{\dagger}\hat{B})$. The excitations energies of the system are obtained by diagonalizing $\mathcal{L}$ (indeed the excitations energies correspond to the poles of the response function).

The formalism introduced here can be applied to any approximation of the non-local and static self-energy operator $\Sigma(\mathbf{r},\mathbf{r}',\omega=0)$(see Table 2.4).

If $\Sigma(\mathbf{r},\mathbf{r}') = V_{xc}(\mathbf{r})\delta(\mathbf{r}-\mathbf{r}')$ the adiabatic TDDFT formalism is recovered [89, 66]. Here we consider the COHSEX self-energy given in Eq. 2.1.34 and we call the corresponding Hamiltonian H_{COHSEX}. Since this self-energy depends explicitly on the density matrix, it can be easily linearized and inserted in Eq. (4.1.9). This approach can be considered as a time-dependent COHSEX method and the corresponding equations are equivalent to the BSE with static screening in the electron-hole interaction.

2.2.3.2.1 Electron-hole representation

The practical solution of Eq. (2.2.20) requires a basis set for $\hat{\rho}'$. A commonly used one is the ensemble of occupied and virtual states of the unperturbed Hamiltonian,

Table 2.4 : The choice of the self energy (first column) in the solution of the quantum Liouville equation within first order perturbation theory (see Eq.63) , determines the level of theory used in the calculation of absorption spectra (second column), including time dependent (TD) Hartree Fock (HF) and density functional theory (DFT) and the Bethe Salpeter Equation (BSE) (see text).

Self energy	Level of theory
$\Sigma(r,r') = v_{xc}(r)\delta(r-r')$	TD-DFT in the adiabatic approximation
$\Sigma = \Sigma_{HF}$ $\Sigma_{HF}(r,r',t) = -\sum_v \phi_v(r,t)\phi_v^*(r',t)v(r,r')$	TD-HF
$\Sigma = \Sigma_{COH} + \Sigma_{SEX}$ $\Sigma_{COH}(r,r') = \frac{1}{2}\delta(r-r')(W(r,r') - v(r,r'))$ $\Sigma_{SEX}(r,r',t) = -\sum_v \phi_v(r,t)\phi_v^*(r',t)W(r,r')$	Statically screened BSE

as the only non zero matrix elements of $\hat{\rho}'$ are those between unperturbed occupied and virtual orbitals [66]: $\langle\phi_c^\circ|\rho'|\phi_v^\circ\rangle$ and $\langle\phi_v^\circ|\rho'|\phi_c^\circ\rangle$. Note that $\langle\phi_v^\circ|\left[\hat{r}_j,\hat{\rho}^\circ\right]|\phi_{v'}^\circ\rangle = \langle\phi_c^\circ|\left[\hat{r}_j,\hat{\rho}^\circ\right]|\phi_{c'}^\circ\rangle = 0$, $\forall\ v,v'$ and c,c'; $\langle\phi_v^\circ|\hat{r}_i|\phi_{v'}^\circ\rangle \neq 0$ and $\langle\phi_c^\circ|\hat{r}_i|\phi_{c'}^\circ\rangle \neq 0$, however one needs only the matrix elements $\langle\phi_c^\circ|\hat{r}_i|\phi_v^\circ\rangle$ and $\langle\phi_v^\circ|\hat{r}_i|\phi_c^\circ\rangle$ when computing [66] the scalar product (trace) in Eq. 2.2.20.

This so called electron-hole basis set is used in most current implementations to solve the BSE [46, 28, 29, 90, 91, 92]. Within this framework, for spin singlet excitations the operator $\mathcal{L}$ takes the form [29]:

$$\mathcal{L} = \begin{pmatrix} \mathcal{D} + 2\mathcal{K}^{1x} - \mathcal{K}^{1d} & 2\mathcal{K}^{2x} - \mathcal{K}^{2d} \\ -2\mathcal{K}^{2x*} + \mathcal{K}^{2d*} & -\mathcal{D} - 2\mathcal{K}^{1x*} + \mathcal{K}^{1d*} \end{pmatrix}, \tag{2.2.21}$$

where $\mathcal{D}$, the exchange terms $\mathcal{K}^{1x}$ and $\mathcal{K}^{2x}$ and the direct terms $\mathcal{K}^{1d}$ and $\mathcal{K}^{2d}$ are

defined as

$$\mathcal{D}_{vc,v'c'} = (\epsilon_c^{QP} - \epsilon_v^{QP})\delta_{vv'}\delta_{cc'}, \tag{2.2.22}$$

$$\mathcal{K}^{1x}_{vc,v'c'} = \int \phi_c^{\circ *}(\mathbf{r})\phi_v^{\circ}(\mathbf{r})\frac{1}{|\mathbf{r}-\mathbf{r}'|}\phi_{v'}^{\circ *}(\mathbf{r}')\phi_{c'}^{\circ}(\mathbf{r}')d\mathbf{r}d\mathbf{r}', \tag{2.2.23}$$

$$\mathcal{K}^{2x}_{vc,v'c'} = \int \phi_c^{\circ *}(\mathbf{r})\phi_v^{\circ}(\mathbf{r})\frac{1}{|\mathbf{r}-\mathbf{r}'|}\phi_{c'}^{\circ *}(\mathbf{r}')\phi_{v'}^{\circ}(\mathbf{r}')d\mathbf{r}d\mathbf{r}', \tag{2.2.24}$$

$$\mathcal{K}^{1d}_{vc,v'c'} = \int \phi_c^{\circ *}(\mathbf{r})\phi_{c'}^{\circ}(\mathbf{r})W(\mathbf{r},\mathbf{r}')\phi_{v'}^{\circ *}(\mathbf{r}')\phi_v^{\circ}(\mathbf{r}')d\mathbf{r}d\mathbf{r}', \tag{2.2.25}$$

$$\mathcal{K}^{2d}_{vc,v'c'} = \int \phi_c^{\circ *}(\mathbf{r})\phi_{v'}^{\circ}(\mathbf{r})W(\mathbf{r},\mathbf{r}')\phi_{c'}^{\circ *}(\mathbf{r}')\phi_v^{\circ}(\mathbf{r}')d\mathbf{r}d\mathbf{r}', \tag{2.2.26}$$

and W is the statically screened Coulomb interaction (namely the static limit of the Fourier transform of Eq. 2.1.24). In Eq. 2.2.22 ϵ_c^{QP} (conduction) and ϵ_v^{QP} (valence) are quasi-particle energies. In principle these energies should be approximated at the COHSEX level of theory, for consistency with the choice of the Hamiltonian; in practice a more accurate approximation may be chosen and usually the GW approximation is adopted to evaluate the term $\mathcal{D}$ in Eq. 2.2.22.

The matrix form of the operator $\mathcal{L}$, as defined by Eqs. 2.2.22-2.2.26, can be diagonalized to obtain the excitation energies of the system. Alternatively, a linear system involving $\mathcal{L}$ can be solved in order to compute the macroscopic polarizability defined by Eq. 2.2.20. Note that the operator $\mathcal{L}$ in Eq. 2.2.20 is non-Hermitian and thus the solution of the corresponding eigenvalue problem may not be achieved by using iterative solvers adopted for Hermitian problems. For this reason Hermiticity is often enforced by neglecting the off-diagonal blocks of $\mathcal{L}$; this approximation is known as the Tamm-Dancoff approximation (TDA) [93]. The TDA greatly reduces the computational complexity of the BSE solution and has successfully predicted the absorption spectra of several solids [28, 46, 94, 95, 29, 96]. However, the TDA does not always hold: for example it does not account for plasmons in solids [97] and it breaks down for some confined systems [98, 99, 33], such as carbon nanotubes [99] and silicon clusters [33].

The definition of $\mathcal{L}$ through Eqs. 2.2.22-2.2.26 requires the calculation of the unoccupied single particle states (virtual orbitals) of the unperturbed Hamiltonian and the corresponding matrix must be explicitly evaluated and stored. A large number of virtual orbitals ϕ_c° is usually necessary for calculations that require the evaluation of a spectrum in a large energy range and/or involve large systems; even for small molecules, obtaining converged spectra may be challenging, in cases where the inclusion of many virtual states is necessary [100].

2.2.3.2.2 Use of Density functional perturbation theory

The explicit inclusion of virtual orbitals ϕ_c° may be avoided with the use of DFPT [53].

In this framework the projector operator onto the unperturbed empty state subspace is introduced $\hat{Q} = \hat{I} - \hat{P} = \hat{I} - \sum_{j=1}^{N_{occ}} |\phi_j^\circ\rangle\langle\phi_j^\circ|$, where $\hat{P}$ is the projector onto the occupied state subspace and $\hat{I}$ is the identity operator; the evaluation of $\hat{Q}$ only requires the evaluation of the occupied states ϕ_v°. At variance from the electron-hole representation, the operators entering Eq. 2.2.19 (ρ', $\hat{r}_i$ and $[\hat{r}_j, \hat{\rho}^\circ]$) are expressed in the so-called *batch* representation [66, 33], and Eqs. 2.2.22- 2.2.26 become:

$$\mathcal{D}_{v,v'} |a_{v'}\rangle = (\hat{H}^\circ_{COHSEX} - \epsilon_{v'})\, \delta_{vv'} |a_{v'}\rangle, \tag{2.2.27}$$

$$\mathcal{K}^{1x}_{v,v'} |a_{v'}\rangle = \hat{Q} \left(\int \frac{1}{|\mathbf{r} - \mathbf{r}'|} \phi^{\circ *}_{v'}(\mathbf{r}') a_{v'}(\mathbf{r}') d\mathbf{r}' \right) |\phi^\circ_v\rangle, \tag{2.2.28}$$

$$\mathcal{K}^{2x}_{v,v'} |b_{v'}\rangle = \hat{Q} \left(\int \frac{1}{|\mathbf{r} - \mathbf{r}'|} b^*_{v'}(\mathbf{r}') \phi^\circ_{v'}(\mathbf{r}') d\mathbf{r}' \right) |\phi^\circ_v\rangle, \tag{2.2.29}$$

$$\mathcal{K}^{1d}_{v,v'} |a_{v'}\rangle = \hat{Q} \left(\int W(\mathbf{r}, \mathbf{r}') \phi^{\circ *}_{v'}(\mathbf{r}') \phi^\circ_v(\mathbf{r}') d\mathbf{r}' \right) |a_{v'}\rangle, \tag{2.2.30}$$

$$\mathcal{K}^{2d}_{v,v'} |b_{v'}\rangle = \hat{Q} \left(\int W(\mathbf{r}, \mathbf{r}') b^*_{v'}(\mathbf{r}') \phi^\circ_v(\mathbf{r}') d\mathbf{r}' \right) |\phi^\circ_{v'}\rangle. \tag{2.2.31}$$

where for a generic operator $\hat{A}$, the so called "batch "components $|a_{v'}\rangle$ and $|b_{v'}\rangle$ are defined as:

$$|a_v\rangle = \hat{Q}\, \hat{A}\, |\phi^\circ_v\rangle, \tag{2.2.32}$$

$$\langle b_v| = \langle \phi^\circ_v|\, \hat{A}\, \hat{Q}. \tag{2.2.33}$$

The index v runs over the number N_{occ} of occupied states. Hence in this representation no calculation of virtual orbitals is necessary. As a result the required computational workload is comparable to that of a ground state HF calculation. Specifically, in a plane wave (PW) representation, the evaluation of $\mathcal{K}^{1d}$ and $\mathcal{K}^{1d}$ scales as $\alpha[N_v^2 \times N_{pw} \times lnN_{pw}]$, where α is constant with respect to system size (i.e. the number of Lanczos iterations); however, within a electron-hole approach, the evaluation of $\mathcal{K}^{1d}$ and $\mathcal{K}^{1d}$ scales as $\alpha[N_c \times N_v \times N_{pw} \times lnN_{pw}]$, where N_c is in general much larger than N_v.

As mentioned in the previous section, quasi-particle corrections to the unoccupied states are introduced either through the COHSEX Hamiltonian of Eq. 2.2.27 or through more accurate quasi-particle corrections (i.e., GW corrections), as discussed in Refs. [33, 30].

In principle, the evaluation of the statically screened Coulomb potential W entering Eqs. 2.2.30-2.2.31 requires summations over empty states; these are avoided by computing the dielectric matrix as described in Sec. 2.2.1.2.

Although in general the size of the operator $\mathcal{L}$ in the DFPT-based representation (see Eqs. 2.2.27-2.2.31) is larger than in the electron-hole representation, the full matrix does not need to be built explicitly. Indeed iterative techniques, that require

only matrix by vector multiplications, are used to diagonalize $\mathcal{L}$ or to solve the corresponding linear system in Eq. 2.2.20. The operator $\mathcal{L}$ can be efficiently applied to a vector by exploiting techniques developed for ground-state calculations, such as fast Fourier transforms used in plane-wave implementations of ground state DFT calculations. The DFPT-based approach described in this section has been applied to the calculation of the optical properties of molecules (an example is shown in Fig.2.1) and solids without relying on the Tamm-Dancoff approximation [93]; either the non-Hermitian Lanczos algorithm developed in Refs. [66, 33], was used or diagonalization was carried out with the algorithm of Ref. [101].

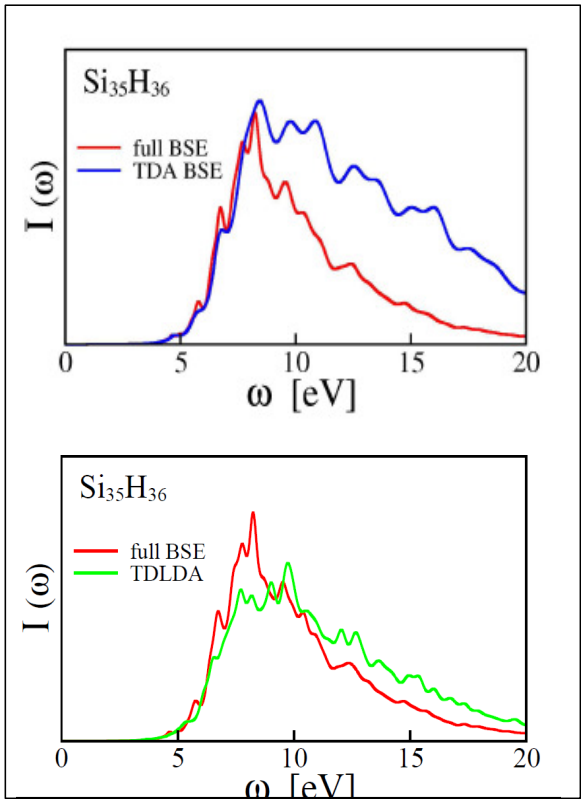

Fig.2.1 : Absorption spectra of a 1 nm hydrogenated Si cluster ($Si_{35}H_{36}$) as obtained by using many body perturbation theory and the techniques to solve the Bethe-Salpeter equation (BSE) described in Sec.3.3.2.2 and in Ref. [33]. Results without (full BSE) and with the Tamm-Damcoff approximation (TDA) are presented in the upper panel. The lower panel compares the full BSE results with time dependent DFT results obtained using the LDA approximation (TDLDA).

2.2.3.3 Comparison between calculations using time dependent DFT and the Bethe-Salpeter equation

TDDFT is an alternative approach to the Bethe-Salpeter equation to compute neutral excitations of materials. In principle TDDFT is a formally exact theory [12]. However, in practical calculations it is necessary to approximate the exchange-correlation potential $V_{xc}(\mathbf{r},\omega)$ and, within the linear response regime, the corresponding kernel $K^{xc}(\mathbf{r},\mathbf{r}',\omega) \equiv \delta V_{xc}(\mathbf{r},\omega)/\delta\rho(\mathbf{r}',\omega)$ (see Eq. 2.1.41). The most commonly used forms of the TDDFT kernel rely on the adiabatic approximation [51]. The latter consists in using local, semi-local or hybrid functionals commonly adopted in ground-state calculations, to approximate the TDDFT kernel by discarding memory effects ($\omega = 0$). This approximation accurately reproduced the excitation energies of molecules but it is known to fail to describe excitons in extended systems [102]. In contrast, the Bethe-Salpeter equation appears to describe more accurately the electron-hole interaction in extended systems [46, 28, 88].

Recently, there have been several attempts to improve the accuracy of TDDFT for extended systems. For example the approximate long-range kernel $K^{xc} = -\alpha/|\mathbf{q}+\mathbf{G}|^2$ was found accurate for the calculation of the absorption spectra of several solids [102, 103]. The final result depends on the parameter α, which is system dependent. A more systematic way to find an approximation of K^{xc} for solids relies on the comparison between the BSE and the TDDFT equations [104]. Since K^{xc} depends only on two indexes (Eq. 2.1.42) and Ξ depends on four indexes (Eq. 2.1.14), this comparison is possible by considering a symmetrized version of Eq. 2.1.42, in its dynamical form. This approach requires the calculation of GW quasi-particle corrections and the same matrix elements involved in the solution of the BSE equation in the electron-hole representation (Eqs. 2.2.22-2.2.26). In Refs. [105, 106] an xc kernel was developed by requiring TDDFT reproduce the perturbative expansion of the BSE in terms of the screened Coulomb interaction; at the first order this approach is equivalent to the one of Ref. [104]. In general the TDDFT kernels derived from the BSE are dynamical ones (K^{xc} depends on ω) and include the correct long-range limit $1/|\mathbf{q}+\mathbf{G}|^2$. Many of the absorption spectra of solids computed by BSE-based kernels are in excellent agreement with experimental spectra; the computational cost of this method is comparable to that of solving the full BSE.

Recently, Sharma et al [107] proposed a new approximation for K^{xc}, that gives accurate results for the optical properties of solids within TDDFT. This kernel, called bootstrap kernel, takes the form

$$K^{xc}_{boot}(\mathbf{q},\omega) = \frac{\varepsilon^{-1}(\mathbf{q},\omega=0)}{\chi_0^{00}(\mathbf{q},\omega=0)}, \tag{2.2.34}$$

where χ_0^{00} indicates the $G = G' = 0$ component of the independent-particle polarizability in Eq. 2.2.2, while ε^{-1} is the static inverse dielectric matrix. The bootstrap

kernel (Eq. 2.2.34) is designed to reproduce the correct asymptotic behavior $1/|\mathbf{q}+\mathbf{G}|^2$ necessary to describe the optical spectra of extended systems. Since the kernel itself depends on ε^{-1}, the numerical solution of the TDDFT equations must be performed self-consistently. At the first iteration K^{xc} is set to 0, Eq. 2.1.42 (in its dynamical form) is solved to determine χ, which is then used to compute the inverse dielectric matrix ε^{-1} through Eq. 2.1.22; by inserting ε^{-1} in Eq. 2.2.34, one can compute a new approximation for K^{xc} and the procedure is repeated until self-consistency is achieved. Since local or semi-local functionals are known to underestimate electronic gaps, the independent-electron polarizability χ_0 used in the bootstrap kernel is approximated starting from GW or LDA+U [108, 109, 110] calculations. The bootstrap kernel was applied to different systems including small to medium band gap bulk semiconductors and materials with strongly bound excitons, such as LiF and noble gas solids [107]; for the cases considered so far a good agreement with experiments was found.

We now turn to the application of the many body techniques described in Section 2.1 and 2.2 to the calculations of electronic excitations in materials used as photocathodes and photoanodes in photoelectrochemical cells.

Chapter 3

Structral and electronic properties of light absorbers

In this chapter we first recall the basic steps involved in photoelectrochemical(PEC) energy conversion and we introduce the excitation processes of interest to our study; we then focus on specific materials. In each case we will point out the effects on the final results, of the numerical approximations described in Section 2. The main goal of this section is to illustrate what we could compute using MBPT, which physical properties we can predict and how calculations may contribute to interpret specific measurements of interest for PEC cells.

The photoelectrochemical path to water splitting involves separating the oxidation and reduction processes into half reactions. Photoelectrolysis, or semiconductor-based PEC water splitting, can be accomplished by following two main strategies [111, 2]: one uses photovoltaic (PV) modules connected directly to electrolyzers and/or catalytic electrodes; another one uses semiconductor/liquid junctions, where water splitting occurs at the semiconductor surface. The latter has several advantages over the former approach, e.g. it avoids significant fabrication and systems costs involved in the use of separate electrolyzers wired to p-n junction solar cells [112]; in addition it is relatively straightforward to create an electric field at a semiconductor/liquid junction [113]. One promising photoelectrolysis cell is based on two semiconductor-liquid junctions: a n-type semiconductor is used for the evolution of O_2 (photoanode) and a p-type one for the evolution of H_2 (photocathode). In this way two semiconductors with band gaps smaller than those used in wired cells can be utilized, and each one needs only to provide part of the water splitting potential. A smaller band gap implies an increased absorption in the visible region of the solar spectrum, where the sun has a greater photon flux, and thus a higher maximum theoretical efficiency [111].

The desirable properties of water-splitting photoanode and/or photocathode materials are the following [114]: (i) Efficient absorption of visible light. The minimum required band gap is determined by the energy necessary to split water (1.23 eV) plus the thermodynamic losses [115] (0.3–0.4eV) and the overpotential necessary to ensure

sufficiently fast reaction kinetics [116, 117] (0.4 –0.6 eV). As a result, the optimum value of the band gap should be equal to or larger than ∼1.9 eV and smaller than 3.1 eV, so as to fall within the visible range of the solar spectrum. (ii) High chemical stability in the dark and under illumination. Metal oxide semiconductors are more stable than most non-oxide semiconductors and in this respect they appear to be promising materials. (iii) Band edge positions that straddle the water reduction and oxidation potentials. The band edges of non-oxide semiconductors tend to be better suited to reduce water and produce H_2, whereas those of oxide semiconductors are often more appropriate for water oxidation and the production of O_2. We recall that for an efficient reaction, the conduction band minimum (CBM) of the photocathode must be higher than the water reduction potential H^+/H_2O, and the valence band maximum (VBM) of the photoanode lower (more positive in potential) than the water oxidation potential O_2/H_2O. (iv) Efficient charge transport: efficiency is determined by intrinsic factors such as mobilities and extrinsic factors such as defects that may act as recombination centers [114]. So far no single material has been found that meets all requirements listed above.

In this thesis we focus on the description of optical absorption and photoemission processes and hence on requirements (i) and (iii). This chapter discusses band edges and the next chapter describes absorption spectra.

Water reduction and oxidation reactions occur at the interface with a photoelectrode, hence surface band edges determine the alignment of the photoelectrode energy levels with the water redox potential. Several procedures have been proposed in the literature to determine band alignments at water/photoelectrode interfaces [118, 119, 120]; for example the authors of Ref [119] computed the alignments between the CBM of TiO_2 and the water reduction potential by computing the free energy change in proton-coupled redox reactions occurring at the interface, from ab initio molecular dynamics. They also determined the shift of the TiO_2 band edges and found results in agreement with experimental Volta potential shift [120]. However, all water/photoelectrode interface calculations appeared so far were carried out at the local or semi-local DFT level and no MBPT calculation has yet been reported. In general, due to the complexity of surface and interface structures, many studies of band edge alignments with the water redox potential are based on bulk systems (for example see Fig. 3.0.1, from Ref[121]).

Within this framework one determines the absolute positions of the VBM and CBM energies of the photoelectrode and the absolute positions of the O_2/H_2O oxidation and H^+/H_2O reduction potential relative to the vacuum level E_{Vacuum}. The measured O_2/H_2O oxidation and H^+/H_2O reduction potentials are 1.23 eV and 0 eV, respectively, relative to the normal hydrogen electrode (E_{NHE}) at $pH = 0$ and their corresponding values relative to vacuum are $-E_{NHE} - 4.44eV = E_{Vacuum}$, as recommended by the International Union of Pure and Applied Chemistry [125, 126]. Experimentally the value of the CBM and VBM of a photoelectrode relative to vac-

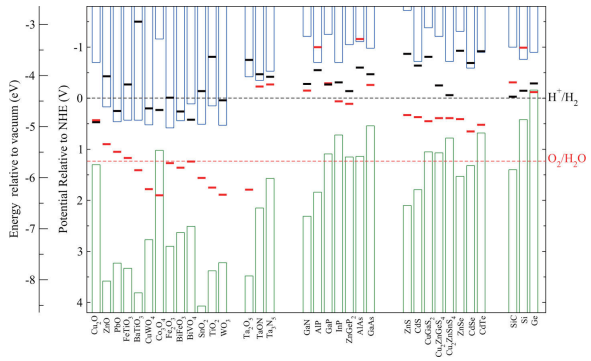

Figure 3.0.1: The water redox potentials $\Phi(O_2/H_2O)$ and $\Phi(H^+/H_2)$ (dashed lines) and the valence (green columns) and conduction (blue columns) band edge positions at pH = 0 of several semiconductors . The valence and conduction band edges are collected from Ref [122] for most metal oxides, from Ref [123] for most non-oxides, and from Ref [124] for Ta_2O_5, Ta_3N_5, and TaON. Calculated oxidation potential Φ_{ox} (red bars) and reduction potential Φ_{re} (black bars) relative to the NHE and vacuum level for a series of semiconductors in solution at pH = 0, the ambient temperature 298.15 K, and pressure 1 bar are also plotted. Reprinted with permission from Ref.[121]. Copyright 2012 American Chemical Society.

uum can be measured by PES (photoemission spectroscopy)-IPES (inverse photoemission spectroscopy). Computationally the determination of the CBM and VBM for a homogeneous solid is relatively straightforward, following two separate steps: first one determines the difference between the VBM and CBM energies (quasiparticle band gap) using a supercell calculation for a periodic system; then the difference between the average potential in the bulk of the solid and in a slab (composed of a portion of the bulk plus vacuum) is used to refer the computed energies to the vacuum level. An alternative procedure was proposed in Ref. [127], where one determines the band gap center (BGC) relative to the vacuum first, then obtain the VBM(CBM) energy from the BGC minus(plus) one half of the band gap [127]. The calculations of the VBM and CBM energies is more complex in the case of surfaces, as a determination of the surface structure needs to be carried out which, depending on the surface morphology, may require the use of large super cells.

In the following, we discuss the computation of quasi particle gaps and band alignment for tungsten trioxide based materials. We focus on WO_3 and $CuWO_4$ as promising photoanode materials. We recall that tungsten trioxide (WO_3) is a promising oxide for use in photo-electrochemical water-splitting systems [128, 129, 130, 131, 132]: it is stable against photocorrosion; its optical gap (2.6-2.7 eV) is smaller than that of TiO_2 and it may absorb sufficient visible light to generate modest photocurrents. Furthermore WO_3 electrochromism has additional applications, in e.g. building smart windows [133, 134, 135].

3.1 Structral properties of WO_3 solids

The structure of WO_3 is best described as a three-dimensional network of corner-sharing WO_6 octahedra. The connectivity is identical to the ABO_3 perovskite structure in the absence of an A cation. The BO_3 structure is unstable, because the decrease in size of the A ion of ABX_3 perovskite increases the instability of the crystal and this structural instability reaches its maximum in BO_3, where the A ion is completely missing. In general, the cubic perovskite structure is unstable to energy-lowering distortions, the most common being tilting of octahedra and displacement of the B cation from the center of its octahedra.

In the case of tungsten trioxide, six different phases have been identified as a function of P and T. When the temperature is decreased from its melting point (1700K) the crystallographic symmetry of the solid changes as follows: tetragonal to orthorhombic to monoclinic to triclinic to monoclinic. Simple cubic WO_3 has been prepared at 0.66 GPa, 700℃and then stablized at the ambient conditions [136]. The energy-lowering distortions result in ferroelectricity in many compounds, such as $BaTiO_3$, $PbTiO_3$ and $KNbO_3$. Similarly, the low temperature monoclinic phase (ε-WO_3) has been confirmed to be ferroelectric.

The simple cubic phase has the smallest unit cell with one WO_3 unit; the unit cell is doubled only along the c direction in tetragonal phase; then doubled along a,b,c three directions (eight units) in orthorombic, RT-monoclinic phase and triclinic phase, but four units in LT-monoclinic phase. The geometric details has been modified progressively in different phases (summarized in Table 3.1 and Table 3.3): the simple cubic phase has no distortions; the W atom moves off center along c in tetragonal phase, which cause alternatingly long and short W-O bonds in an "antiferroelectric" fashion; the W off-center occurs along both b and c directions for orthorombic phase and the WO_6 octahedra are slighly tilted as well along these two directions; for RT-monoclinic, triclinic and LT-monoclinic phases, the W atom off-center and octahedra tile occur along a,b,c three directions. Difference of geometric details of the last three phases has been discussed in Ref. [137]. The averaged tilt angles between RT-monoclinic and triclinic phase have similar magnitude 156-161°, but different octahedra tilt patterns ($a^-b^+c^-$ for the former, $a^-b^-c^-$ for the latter [138]). The change of octahedral tilt patterns drives the RT-monoclinic-triclinic phase transition. On the other hand, the triclinic phase and LT-monoclinic phase have similar tilt patterns but the magnitude of tilt angles is different:154-157°for LT-monoclinic phase. Another important difference between the last three phases is that LT-monoclinic phase does not have an inversion center and owns unequal W off center shifts along c and a axis, which causes a net spontaneous polariztation and is directly related to the ferroelectricity of LT-monoclinic WO_3 [137] and dielectric anomaly with giant dielectric constant [139, 140].

Table 3.1: Structural properties of different phases of WO_3. Z is the number of WO_3 units in the unit cell, BLS is short and long bond length splitting along the directions of lattice vectors; tilting is the tilt between two WO_6 octrahedra and tilt system is the tilt patterns of octrahedra [138, 137].

	Z	space group	BLS	tilting	tilt system
Simple Cubic	1	$Pm3\bar{m}$	no	no	-
Tetragonal	2	P4/nmm	c	no	-
Orthorombic	8	Pnmb	b,c	yes	tilt angles around a
RT-monoclinic	8	$P2_1/n$	a,b,c	yes	$a^-b^+c^-$
Triclinic	8	$P\bar{1}$	a,b,c	yes	$a^-b^-c^-$
LT-monoclinic	4	Pc	a,b,c	yes	$a^-b^-c^-$

3.1.1 Ab-initio calculations of the structral properties of WO_3 solid phases

We studied the structral and electronic properties of the various WO_3 phases by performing first-principles calculations within the framework of density functional theory (DFT) using the Quantum Espresso package [141] and the Qbox code [142], and different levels of theory (the local density approximation (LDA), the generalized gradient approximation (GGA) using the PBE [143] functional, the hybrid functional PBE0 [144], non local van der Waals functional vdW-DF2 [145, 146, 147, 148, 149] and the modified self-consistent field method proposed in Ref. [150]). Our LDA results for the structural properties of cubic and monoclinic WO_3 are in agreement with previous calculations [151, 152, 153, 154, 155] (see Table S1 and S2 in the Appendix1). The LDA predicted equilibrium volume deviates from experiment by less than 1%, whereas PBE and the functional vdW-DF2 [145, 146, 147, 148, 149] overestimate the equilibrium volume by $\sim 5\%$. In the calculations of the intercalated systems reported in section 3.3, we primarily used the LDA, as we focus on discussing trends in computed properties rather than on absolute values of computed gaps and total energies. We also used G_0W_0 calculations to compute the band alignment between different phases of WO_3. Computational details of G_0W_0 can be found in the Appendix II.

Consistent with previous results [151, 152, 153, 154, 155], we found that LDA and PBE calculations underestimate the band gap of monoclinic WO_3 by about 50%, when both the lattice constants and the internal geometry are optimized, while vdW-DF2 yields a larger gap than both LDA and PBE. We note that DFT geometry optimizations yielded reduced structural distortions in monoclinic WO_3, relative to those reported experimentally; in turn this leads to, e.g. at the LDA (vdW-DF2) level a moderate decrease of the band gap from 1.87(2.04) eV at the experimental geometry to 1.46(2.01) eV when computed at the experimental lattice parameters (V_{exp}) but allowing for internal structural relaxations, and finally to 1.30(1.80) eV when

evaluated at the fully optimized DFT geometry. To obtain a quantitative estimate of the band gap, we used the modified self-consistent field (SCF) approach recently proposed for solids in Ref.[150] (hereafter referred to as modified ΔSCF approach): we found that the band gap of monoclinic WO_3 is 2.90 eV at the experimental geometry, and 2.39 eV at the LDA relaxed geometry; these values are much closer to the measured room temperature band gap of 2.60 eV than those obtained within LDA, PBE or vdW-DF2. We also carried out calculations at the PBE0 level of theory, using the LDA optimized geometry. The computed band gap is 3.28 eV, higher than in experiments, and consistent with the value of 3.67 eV reported in Ref. [156] [157].

The lattice parameters of six different phases of WO_3 are listed in Table 3.2, including our LDA and HSE06 in Ref [156] optimized results and experimental values. Overall, our LDA equilibrium volume deviates from experiment by 1-2%, which is at the similar (or better) level of accuracy with published HSE06 [156] results.

We calculated the vibrational properties of WO_3 with different phases using density functional perturbation theory (DFPT), in the harmonic approximation and at the LDA level. We found that a plane wave cutoff of 140 Ry is sufficient to converge the vibrational frequencies within 5 cm^{-1}.

3.1.2 Connection between Structural Properties and Electronic Structure

With the progressive lattice distortions from simple cubic phase to LT-monoclinic phase as shown in Table 3.3, the band gaps increase dramatically with a color change of the sample observed experimentally, from "ruby red" in simple cubic to "pale yellow" in RT-monoclinic and "bluish white" in LT-monoclinic phase. A consistent trend of the band gap increases from simple cubic to LT-monoclinic is reproduced by our calculations, at the LDA, G_0W_0 and HSE06 [156] levels of theory, as shown in Table 3.4.

The LDA computed band gap of the simple cubic structure is 0.53 eV, and it is indirect from R (0.5,0.5,0.5) to Γ. The valence band maximum (VBM) is mainly composed of O nonbonding $2p$ states (p_x, p_y, p_z are degenerate), whereas the conduction band minimum (CBM) is composed of W $5d$ t_{2g} states (d_{xy}, d_{yz}, d_{xz} are degenerate) and O $2p$ states. The metal d orbitals are split by the octahedral field of oxygen ligands, with t_{2g} levels at lower energy than e_g levels. There is a considerable amount of hybridization between O $2p$ and W $5d$ bands, which can be clearly seen from the Projected Density of States (PDOS) reported in Fig. 3.1.1(c). The mixing of W $5d$ and O $2p$ yields bonding states belonging to the valence band, and anti-bonding states contributing to the conduction band.

The VBM of RT monoclinic WO_3 is located at B (0.5, 0, 0), as shown in the band structure computed within the LDA in Fig. 3.1.2(b). From Γ to B, the band is nearly dispersionless, implying a very high effective hole mass perpendicular to the

Table 3.2: Equilibrium lattice parameters of different phases of WO_3 obtained by ab initio calculations, with HGH pseudopotentials [158] and the LDA exchange correlation functional, compared with the results obtained with the HSE06 functional in Ref. [156] and experimental results (EXP).a_0,b_0,c_0 denote the lattice constants; β denotes the angle between the a and c axes; α denotes the angle between b and c; and γ denotes the angle between a and b. V is the volume of the primitive cell.

	lattice parameters (Å)			angles (°)			V($Å^3$/cell)
	Simple Cubic						
	a_0						
LDA	3.78						54.4
HSE06	3.80						54.7
EXP [136]	3.77						53.7
	Tetragonal						
	a_0		c_0				
LDA	5.30		3.88				55.6
HSE06	5.31		3.97				55.9
EXP [159]	5.25		3.91				54.0
	Orthorombic						
	a_0	b_0	c_0				
LDA	7.47	7.60	7.71				54.7
HSE06	7.46	7.70	7.80				56.0
EXP [160]	7.24	7.57	7.75				53.9
	RT-monoclinic						
	a_0	b_0	c_0		β		
LDA	7.35	7.45	7.66		90.6		52.5
HSE06	7.39	7.64	7.75		90.3		54.7
EXP [161]	7.306	7.54	7.692		90.88		53.0
	Triclinic						
	a_0	b_0	c_0	α	β	γ	
LDA	7.36	7.45	7.58	88.8	90.9	90.9	52.0
HSE06	7.44	7.58	7.75	89.4	90.3	90.3	54.6
EXP [162]	7.31	7.53	7.69	88.8	90.9	90.9	52.9
	LT-monoclinic						
	a_0	b_0	c_0		β		
LDA	5.25	5.18	7.62		91.5		51.9
HSE06	5.31	5.27	7.67		91.2		53.6
EXP [137]	5.28	5.16	7.66		91.8		52.1

W-O-W chain in the x direction [163]. The CBM is located at the Γ point and the computed band gap is 1.3 eV (at the LDA level). Note that the PDOS of monoclinic

Table 3.3: Octahedra tilt angles ∠W-O-W and W-O bond length $d_{W-O}(\AA)$ in different phases of WO_3 as measured (EXP) in Refs [136, 159, 160, 161, 162, 137] and obtained in our calculations with the LDA functional. "x,y,z" denote the bond lengths or tilt angles along the x,y,z directions, respectively. As α,β,γ are close or equal to 90°(within 1°), the x,y,z directions are roughly parallel to the a,b,c lattice vectors. Hence W-O chains are almost parallel to each of the three Cartesian axes.

	∠W-O-W (LDA)	∠W-O-W (EXP)	d_{W-O} (LDA)	d_{W-O} (EXP)
		Simple Cubic		
x	180	180	1.890	1.89
y	180	180	1.890	1.89
z	180	180	1.890	1.89
		Tetragonal		
x	180	180	1.89	1.89
y	180	180	1.89	1.89
z	180	180	1.76-2.12	1.68-2.25
		Orthorombic		
x	180	180	1.89	1.86
y	180	166-168	1.80-2.02	1.82-2.03
z	173	169-173	1.78-2.08	1.80-2.10
		RT-monoclinic		
x	157-158	153-159	1.83-1.97	1.85-1.95
y	161	159-160	1.82-1.98	1.74-2.12
z	167-168	154-166	1.78-2.07	1.73-2.18
		Triclinic		
x	157	156-157	1.84-1.97	1.82-1.97
y	158-163	157-162	1.82-2.00	1.71-2.12
z	156-163	155-161	1.77-2.08	1.65-2.30
		LT-monoclinic		
x	154-161	151-157	1.83-1.97	1.77-2.05
y	154-161	150-162	1.83-1.97	1.78-2.03
z	161	155	1.77-2.09	1.80-2.14

WO_3, shown in Fig. 3.1.2(c), is similar to that of simple cubic WO_3: in both cases the onset of W 5d and O 2p hybridization in the valence band occurs about 1 eV below the VBM; the pure oxygen states at the VBM arise from unshared oxygen electrons occupying orbitals oriented perpendicular to the W-O bonds, and the CBM is composed of hybridized W $5d$ and O $2p$ states.

Both the off-center distortion of W sites and the tilting of octahedra could affect the band gap of WO_3. The W off center distortion causes long and short bond

Table 3.4: Band gaps of different phases of WO_3 as obtained by first-principles calculations using the LDA and HSE06 functional and MBPT within the G_0W_0 approximation. EXP denotes experimental results.

	LDA	HSE06 [156]	G_0W_0 [1]	G_0W_0 [2]	EXP
Simple Cubic	0.54	1.67	1.78	1.78	
Tetragonal	0.52	1.71	1.74	1.82	1.8(opt.)
Orthorombic	1.01	2.57	2.39	1.54	
RT-monoclinic	1.30	2.80	2.59	3.26	2.6(opt.)
Triclinic	1.55	2.94	2.86	3.38	
LT-monoclinic	1.68	3.14	3.05	3.66	

[a] G_0W_0 calculations performed at the LDA optimized geometry
[b] G_0W_0 calculations performed at the experimental geometry

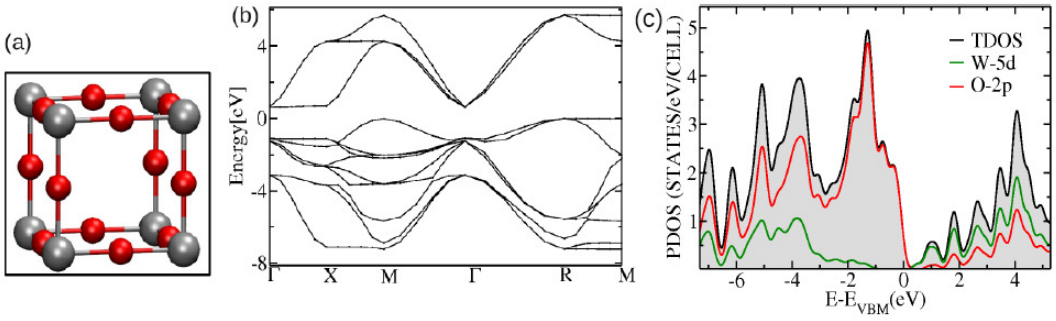

Figure 3.1.1: Band structure (b) and projected density of states (PDOS) and total density of states (TDOS) (c) of simple cubic WO_3 as obtained with DFT/LDA calculations. In panel (c), the zero of energy has been chosen at the VBM (E_{VBM}). The crystal structure is shown in (a).

length splittings, which in turn could possibly affect W-O bonding and (W-5d, O-2p) hybridization, eventually increasing the band gap, as discussed in several references [151, 155]. Ref [151] suggested that it is only when the bond length splitting (BLS) occurs in more than one direction that the band gap will increase; for example, the tetragonal and cubic phase have similar band gaps, as the bond length splitting is only in the z direction. However, the correlation between BLS and the band gap is not straightforward in the case of the RT-monoclinic and LT-monoclinic phases: RT-monoclinic has larger BLS than LT along y and z but smaller BLS along x at the experimental geometry (no substantial difference between the two phases appears at the LDA optimized geometry); however, the LT-monoclinic phase has a

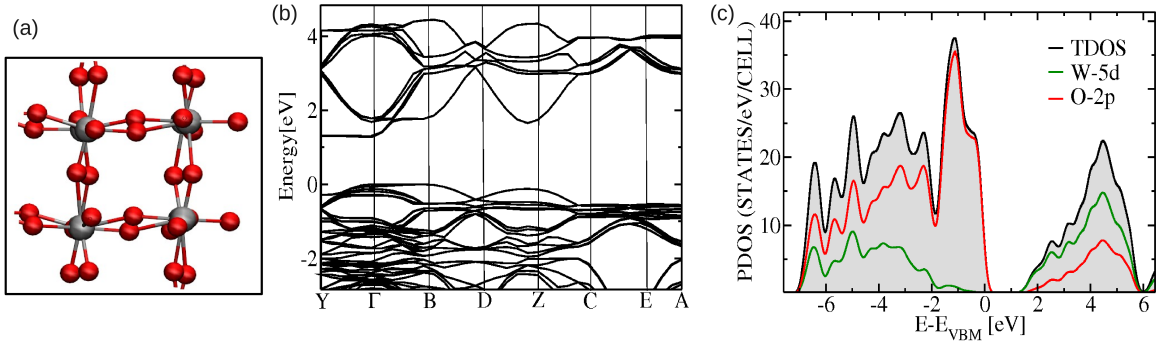

Figure 3.1.2: Band structure (b) and projected density of states (PDOS) and total density of states (TDOS) (c) of monoclinic WO_3 as obtained with DFT/LDA calculations. In panel (c), the zero of energy has been chosen at the VBM (E_{VBM}). The crystal structure is shown in (a).

larger gap than the RT at both the experimental and theoretically optimized structure. The correlation between octahedra tilt angles and band gaps is clearer than that of BLS: no octahedra tilting in simple cubic and tetragonal phases, resulting in smallest band gaps; the octahedra tilt angle increases gradually from orthorombic to the LT-monoclinic phase, along with an increased band gap; the LT-monoclinic phase has a larger band gap than the RT-monoclinic one because LT has octahedra tilt angles 2-10°smaller than the RT one. Tilting of octahedra can possibly decrease the orbital overlap between the W 5d and O 2p which destablize the hybridized W 5d-O 2p states at the conduction band minumum (CBM) of WO_3 band structure(see Fig. 3.1.1 and 3.1.2), shifting up the CBM and thus increasing the band gaps.

The transformations from the RT-monoclinic phase to the high temperature tetrogonal or simple cubic phases are accompanied by a volume expansion of 2∼3% [161, 159] and by a band gap reduction from 2.6 eV (monoclinic WO_3) to 1.8 eV (tetragonal WO_3). To further identify the main geometrical factors responsible for the band gap reduction upon volume expansion, we compared the variation of the gap (E_g) with volume (V) in monoclinic and cubic WO_3. The slope dE_g/dV found experimentally is 0.2-0.3 eV/Å^3/WO_3 [164, 165], higher than our computed value using the LDA functional, 0.09 eV/Å^3/WO_3, which is similar to those of other DFT calculations [151, 156](dE_g/dV=0.1 eV/Å^3 in the LDA calculation of Ref. [151] and 0.085 eV/Å^3 in the B3LYP calculation of Ref. [156], see Fig. 3.1.3). In contrast, the computed slope of simple cubic WO_3 is much smaller (0.02 eV/Å^3/WO_3).

Fig. 3.1.4 shows the variation of bond length splitting (BLS) and octahedra tilt angles upon lattice expansion. The W-O BLS increases less than 1% along x and y and 2∼3% along the z direction; the tilt angles (∠W-O-W) increase by 10° ∼15°. These results indicate that the variation of tilt angles, i.e. the relative rotation angles of the almost rigid octahedra, is mainly responsible for the band gap reduction during

the lattice expansion of monoclinic WO_3. Indeed, the linear coefficient between the band gap and the volume is rather small in the simple cubic phase, where the tilt angle is always 180°.

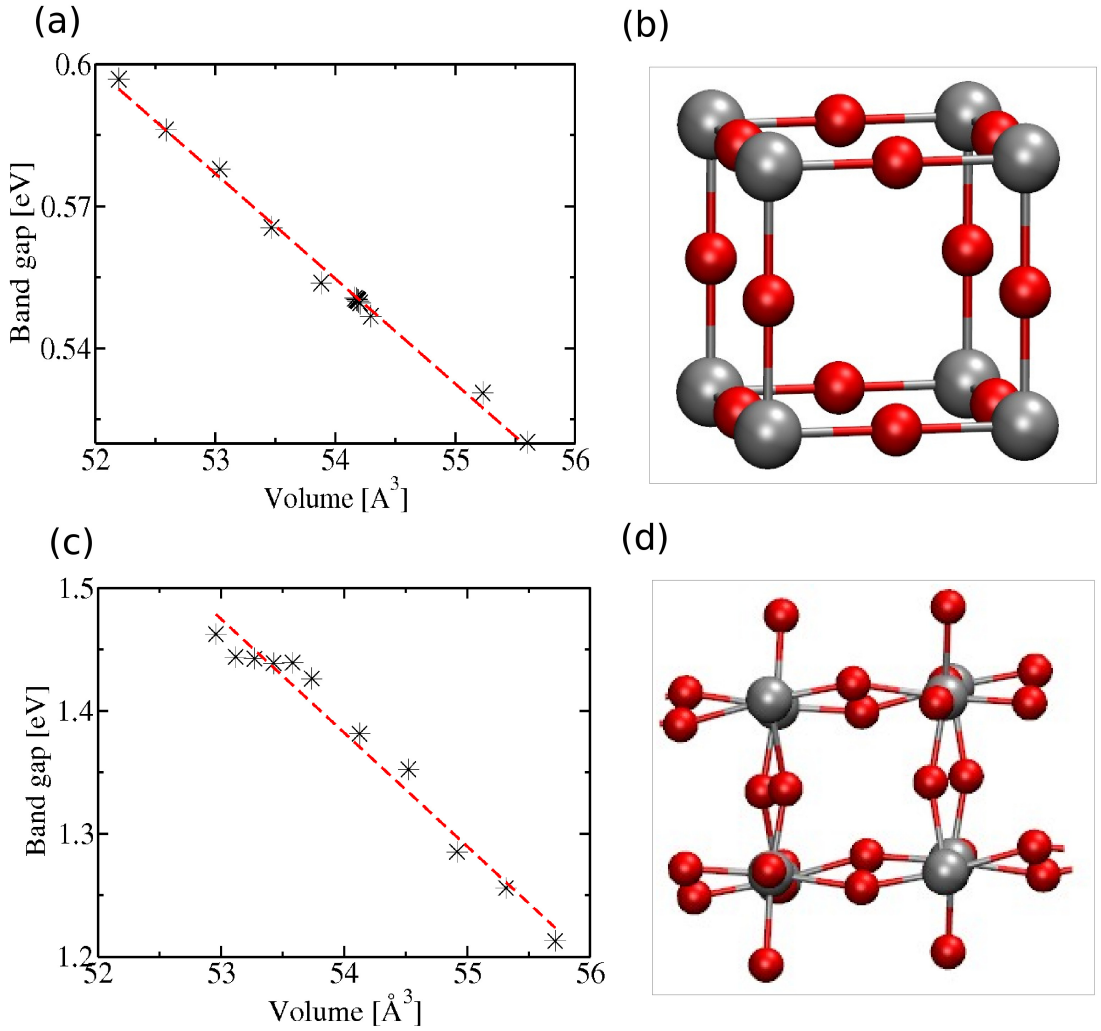

Figure 3.1.3: Band gap of simple cubic (a) and monoclinic (c) WO_3 as a function of volume, as obtained from LDA calculations; the simple cubic and monoclinic WO_3 unit cells are shown in (b) and (d), respectively. In our calculations the monoclinic WO_3 internal geometries are fully relaxed at each lattice constant. The lattice constants corresponding to the volumes between $53 \sim 54$ Å^3/WO_3 are taken from experiments [164, 165]; those corresponding to larger volumes are calculated by keeping the $a/b/c$ ratio fixed to that found experimentally at 53Å^3.

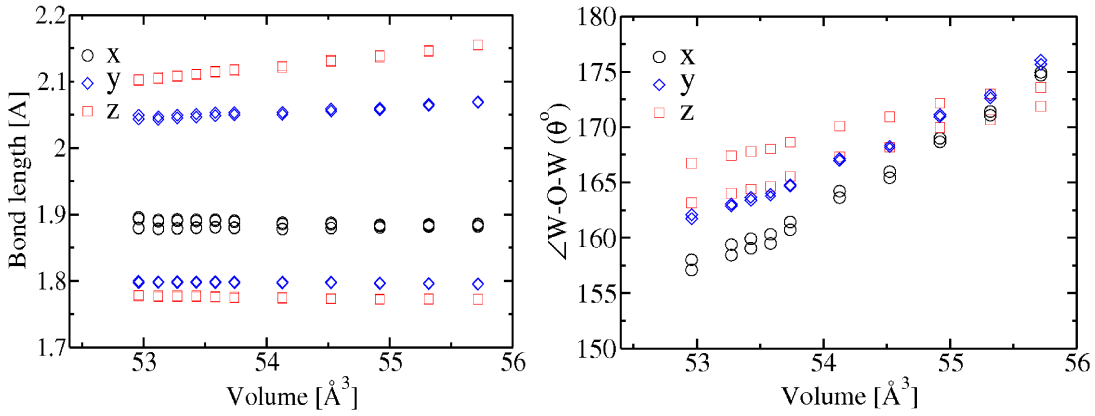

Figure 3.1.4: W-O bond lengths (left panel) and tilt angles (right panel) of monoclinic WO_3 at different volumes (see Fig. 3.1.3(c)). In each panel "x,y,z" denote the bond lengths or tilt angles along the x,y,z directions, respectively.

The effect of tilt angles on the band gap was further investigated by using different functionals. Despite the fact that LDA and PBE generally give reasonable lattice contants with errors within 1-2% (see Table 3.2 and Table S1), both approximations underestimate the octahedra tilt angles by over 5°compared with experiments (see Table 3.3 and Table 3.5). Interestingly, vdW-DF2 gives the octahedra tilt angles much closer to experiments than PBE and LDA (see Table 3.5). As discussed before, larger tilting of octahedra can destablize (W-5d, O-2p) hybrized states and shift up the CBM, while the VBM is composed by O nonbonding states which are less sensitive to the octahedra tilting than the CBM. Fig. 3.1.5 shows the band structure of monoclinic WO_3 computed with PBE and vdW-DF2 fully optimized geometry, respectively. The two band structures are aligned by the W 5s and 5p semicore states since the same pseudopotentials were used in both cases. We can see that the CBM of the vdW-DF2 band strucutre shifts up compared with the PBE one, possibly due to the fact that vdW-DF2 yields an optimized structure with larger octahedra tilt angles. The band gap of vdW-DF2 is 1.80 eV, considerably larger than that obtained with both LDA(1.30 eV) and PBE(1.53 eV). We note that the larger band gap obtained by vdW-DF2 mostly originates from the geometry optimization; i.e. by using the LDA functional but the vdW-DF2 optimized geometry, we obtained a value of 1.73 eV. This value is close to the one obtained with LDA at the experimental geometry (1.87 eV).

Table 3.5: Octahedra tilt angles ∠W-O-W and W-O bond length $d_{W-O}(\mathring{A})$ in RT-monoclinic WO_3 obtained using ab-initio calculations with LDA, PBE and vdW-DF2 functionals. "x,y,z" denote the bond lengths or tilt angles along the x,y,z directions, respectively.

	LDA	PBE	vdW-DF2	EXP
		∠ W-O-W tilt angle		
x	157-158	173	156-159	153-159
y	161	174	160	159-160
z	167-168	172	158-164	154-165
		W-O distance ($\mathring{A}$)		
x	1.827-1.973	1.887-1.899	1.822-2.061	1.855-1.948
y	1.820-1.982	1.780-2.082	1.821-2.057	1.741-2.119
z	1.780-2.074	1.760-2.148	1.782-2.167	1.732-2.186

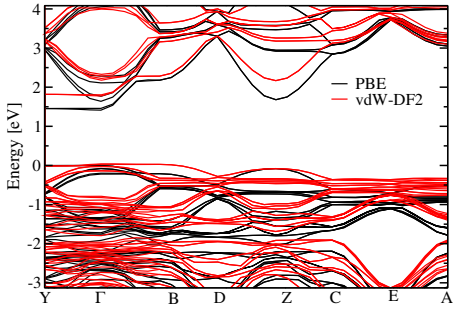

Figure 3.1.5: Band structure of RT-monoclinic WO_3 obtained by using the PBE functional, at the fully optimized geometry (black) and by using the vdW-DF2 at the fully optimized geometry (red)

3.1.3 Connection between Structural Properties and Vibrational Properties

We calculated the vibrational properties of six phases of WO_3 using density functional perturbation theory (DFPT) [53], in the harmonic approximation and at the LDA level. We found that a plane wave cutoff of 140 Ry is sufficient to converge the vibrational frequencies within 10 cm^{-1} for all phases; except simple cubic and tetrogonal for which we used a 280 Ry plane wave cutoff. We employed a $(12 \times 12 \times 12)$ Monkhorst-Pack k-point grid [166] for the BZ sampling of the simple cubic phase and $(6 \times 6 \times 6)$ for the other phases.

A large TO-LO phonon splitting of over 300 cm^{-1} was found for simple cubic WO_3, as shown in Table 3.6, the splitting and phonon frequencies were obtained by

Table 3.6: Theoretical (LDA) and experimental frequencies [167] (in cm^{-1}) at the Γ point of phonon modes for the simple cubic, tetragonal and RT-monoclinic phases of WO_3. "-I" denotes IR active modes and "-R" denotes Raman active modes. "Irrep" denotes irreducible representations.

Irrep	LDA	EXP
	Cubic	
$T_{1u} - LO$	392-I	
T_{2u}	260	
$T_{1u} - TO$	619-I	
$T_{1u} - LO$	938-I	
	Tetragonal	
A_{1g}	129-R	
E_g	254-R	
E_g	370-R	
A_{1g}	773-R	
	RT-Monoclinic	
A_g	48	33-R
A_g	60	60-R
A_g	74	73-R
B_g	90	93-R
A_g	123	133-R
B_u	240	230-I
B_g	273	275-R
A_u	288	285-I
B_u	316	310-I
B_g	331	330-R
A_u	337	335-I
B_u	365	370-I
A_u	659	665-I
B_g	725	719-R
B_u	756	765-I
A_g	811	808-R
B_u	812	825-I
A_u	950	920-I

computing from the dynamical matrix in the form:

$$D_{mn\mu\nu}(\mathbf{q}) = D^{(0)}_{mn\mu\nu}(\mathbf{q}) + \frac{4\pi e^2}{\Omega}\frac{(Z^*_m.\hat{\mathbf{q}})_\mu (Z^*_n.\hat{\mathbf{q}})_\nu}{\varepsilon_\infty(\mathbf{q})} \tag{3.1.1}$$

where $\mathbf{q}$ is the wave vector, ε_∞ is the high frequency dielectric function, and $D^{(0)}_{mn\mu\nu}$ is an analytic function of $\mathbf{q}$. For an ionic crystal, the difference between LO and TO frequencies arises from the last term in Eq. 3.1.1, which accounts for the coupling between LO phonons and a macroscopic electric field. As discussed for perovskite ferroelectrics, large dynamical effective charges give rise to "giant LO-TO splittings" [168], as observed in the case of WO_3. We note that, as in Refs [168] discussed, in a simple polar solid such as NaCl with a single optical branch, the LO splitting refers to the splitting of the transverse optical (TO) and longitudinal optical (LO) frequencies, as described by the Lyddane-Sachs-Teller relation; in a perovskite solid such as WO_3, the three polar modes are mixed by nonanalytic terms in the dynamical matrix, and there is no longer a one-to-one correspondence between individual TO and LO phonon modes.

The structrual phase transitions occuring in WO_3 has been interpreted by the condensations of soft phonon modes at the points Γ, X, M and R of the Brillouin zone of the hypothetical cubic prototype structure [169]. For example, the antiferrodistortive $M_3^{'z}$ mode (tungsten and oxygen atoms displaced only along the z axis) leads to the cubic-tetragonal transition; the octahedra rotation(tilt) modes are connected with the orthorhombic-RT-monoclinic as well as the RT-monoclinic to triclinic phase transition; the z displacement of W atoms (Γ^z_{15}) which is connected with the ferroelectricity of WO_3, leads to the triclinic to LT-monoclinic phase transition. The octahedra tilting in most phases of WO_3 is larger than those observed in $SrTiO_3$, $KMnF_3$, due to the instability of the WO_3 structure with a missing A ion of ABX_3 perovskite.

We have computed the phonon frequencies of different phases of WO_3 partly (see in Table 3.6). Interestingly, the simple cubic phase has soft modes with imaginary frequencies, not only at the zone center, but also at other high symmetric points, such as the M point ($133icm^{-1}$) and the X point ($97icm^{-1}$). These results agree with the experimental observations that several types of low symmetry distortions drive WO_3 phase transitions away from the simple cubic phase. The tetragonal phase also has a soft mode with imaginary frequency 120 cm^{-1} associated with the oxygen shifting approximately along the $\langle 111 \rangle$ direction. Soft modes with large imaginary frequency indicate that the simple cubic and tetragonal phases are highly unstable, indeed they only exsit at high temperatures over 740℃(tetragonal) and 700℃and 0.66 GPa pressure (simple cubic).

For orthorhombic, RT-monoclinic and triclinic phases, more than ten phonon modes have vibrational frequencies less than $100cm^{-1}$; in contrast, the LT-monoclinic phase only has four such low frequency modes, which can be understood by the fact that the LT-monoclinic phase is the stablest one at 0 K. We note that in the RT-monoclinic WO_3 the vibrational mode with the lowest frequency (19cm^{-1}) is related to the titling of octahedra, as shown in Fig 3.1.6. As we discussed in the section 1.1, the octahedra tilt pattern has changed from $(a^-b^+c^-)$ in the RT-monoclinic phase to

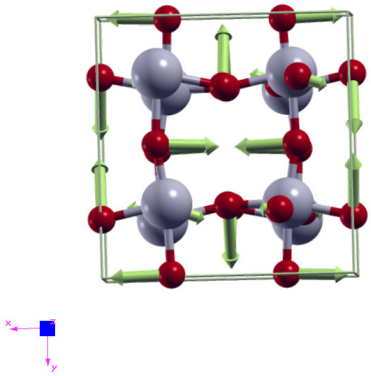

Figure 3.1.6: The green arrows represent the direction of the atom movements. Soft octahedra tilt mode in RT-monoclinic WO_3

$(a^-b^-c^-)$ in the triclinic phase, which has been considered as the driving force of the RT-monoclinic-triclinic phase transtion [137, 169].

3.2 Optical properties and band edges of WO_3

Despite many experimental studies devoted to WO_3, its optical properties are not well understood. Several measurements by UV-vis spectroscopy [170] and photoelectrolysis [171] yielded an indirect optical gap of 2.6 eV at room temperature(T), while Salje et al [172], who measured transmission spectra at room temperature, reported a direct gap of 2.58 eV. Similar to the case of TiO_2 [173, 174, 175], direct and inverse photoemission measurements of the fundamental gap of WO_3 led to a value much larger (0.6∼0.7 eV) [176, 126] than that of its optical gap, and this difference cannot be accounted for by the exciton binding energy. We note that optical and photoemission experiments were both conducted on the phase stable at room T. On the theoretical side, a coherent and consistent interpretation of experiments has not yet been formulated and the level of theory necessary to describe photoemission and absorption experiments of WO_3 is yet unclear. This lack of fundamental understanding of optical properties is common to several other oxides, and it has negatively impacted our ability to predict materials with desired properties for solar energy conversion.

In this section we report ab initio calculations of the fundamental photoemission and optical gap of RT-monoclinic-WO_3, carried out using many body perturbation theory(MBPT) [16, 177]. We close the section by discussing band edge alignment in various phases of WO_3.

We carried out calculations of the band structure within the G_0W_0 approximation [90, 23, 20] and we solved the Bethe-Salpeter Equation (BSE) [16, 177] to obtain

the optical spectra and exciton binding energy, using the method of Refs. [33, 30]. The electron phonon renormalization of the band gap was obtained by means of a Fröhlich Hamiltonian [178, 179, 180], where the high frequency and static dielectric functions and longitudinal optical phonon frequency were computed from first principles, using Density Functional Perturbation Theory (DFPT) [53]. Spin orbit interaction was included using fully relativistic pseudopotentials [158].

We show below that multiple effects need to be taken into account, in order to correctly predict the experimental optical gap, including spin-orbit and electron-phonon interaction, and exciton binding. Our computed quasi-particle gap including spin-orbit and electron-phonon interaction is smaller (∼0.4 eV) than that obtained from photoemission experiments, which most likely probed surface instead of bulk electronic gaps.

3.2.1 Photoemission gap of WO_3 at room temperature

We first computed the electronic gap of WO_3 at several levels of theory and we compared our results with photoemission data (see Table 3.7 and Table 3.8). We used the Quantum Espresso package [141] for all ground state calculations without spin orbit (SO) and the ABINIT code [181, 182] for those including SO; we used the Yambo code [90] for G_0W_0 calculations.

We considered both the RT-monoclinic phase (see Fig. 3.2.1) and the simple cubic (SC) phase (unstable at atmospheric pressure but stable at 0.66 Gpa and 700℃ [136]). At room T, WO_3 has a perovskite structure that differs from that of the simple cubic lattice only by the location of the W atoms, that are off the octahedra centers; the tilt angles between octahedra deviate from 180°by 15°∼25°in the RT-monoclinic phase. As a result, the electronic structure of simple cubic and RT-monoclinic WO_3 are similar: the top of the valence band consists of the O 2p states and the bottom of the conduction band is composed of W 5d states (slightly hybridized with O 2p states).

All band gap calculations for RT-monoclinic WO_3 were carried out at the experimental geometry, which is well established. At present there is a lack of consensus in optimized structures [130] using Density Functional Theory (DFT) with local density (LDA) [183, 184], PBE [8], or Van der Waals density functionals [148] as shown in Section 3.3. Calculations for SC were instead carried out at optimized geometries (Table 3.7).

We used DFT/LDA, the modified ΔSCF method proposed in Ref [11], and MBPT within the G_0W_0 approximation. The computational details of the ΔSCF and G_0W_0 calculations are given in the Appendix A and B, respectively. The computed G_0W_0 band gap is converged within 0.1 eV with respect to all numerical parameters. In Table 3.8 we also report results of previous band gap calculations [153, 151, 156].

All DFT calculations with local or semi-local functionals greatly underestimate the measured gap, as expected, while the hybrid functional PBE0 [144] overestimates it. The HSE06 functional [185, 186] and the ΔSCF method yield very similar results

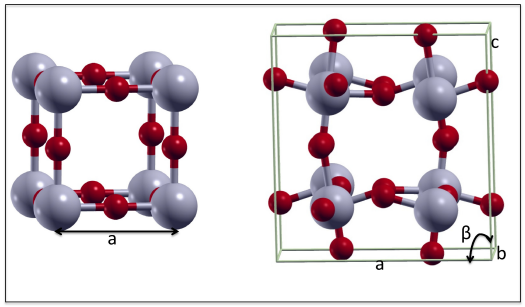

Figure 3.2.1: The crystal structure of simple cubic WO_3(left) and RT-monoclinic WO_3(right). WO_3 has the perovskite structure (ABO_3) where the central "A" site is not occupied.

Table 3.7: Electronic band gap of simple cubic WO_3 computed at different levels of theory: LDA, ΔSCF and G_0W_0 and using the hybrid functional HSE06 [185, 186]. All band gaps were computed at the LDA optimized geometry. In Ref [156], the geometry was optimized at the HSE06 level of theory.

	LDA	ΔSCF	HSE06	G_0W_0
Indirect($R \rightarrow \Gamma$)	0.55	1.57	1.54, 1.67 [156]	1.78
Direct(Γ)	1.56	-	2.69	2.90

for both RT-monoclinic WO_3 and simple cubic WO_3, and they appear to moderately underestimate photoemission experiments; analogous findings were reported for rutile TiO_2, whose gap computed with the HSE06 functional, 3.05 eV [187], underestimates the measured photoemission gap (3.3-3.6 eV [174, 175]). The computed G_0W_0 band gap of RT-monoclinic WO_3 is 3.26 eV, in apparent, excellent agreement with photoemission experiments (3.38±0.2 in Ref [176], and 3.28±0.14 in Ref [126]).

However additional, important effects need to be taken into account, before carrying out a meaningful comparison with experiment, e.g. spin-orbit (SO) effects and corrections to the computed gap due to electron phonon interaction.

We discuss SO interaction first.The effect of spin orbit (SO) interaction on the band structure of solids containing W was so far examined only for bulk bcc W [189]. Large SO splittings up to 0.8 eV were found for some of the bands. In Table 3.9, we compare the lattice constants and band gaps of simple cubic and RT-monoclinic WO_3 (see Fig. 3.2.1) computed without and including SO coupling. In the former case we used non relativistic pseudopotentials (PP), while in the latter we used fully relativistic PP of the HGH form [158] which were generated from fully relativistic all electron calculations, i.e. by solving the two-component Dirac equation.

When including SO effects self-consistently in our LDA band structure calcula-

Table 3.8: Electronic band gap (eV) of RT-monoclinic WO_3 computed using different levels of theory (acronyms are defined in the text). The first five rows of the table report results from the literature, while the remaining ones report results of this work. E_g^{opt} denotes the optical gap. The last column indicates whether the gap is direct (D), indirect (I) or pseudodirect (PD). In our calculations I and D gaps differ by less than $\sim$0.05 eV.

Theory	Band Gaps [eV]	Type
LDA	1.87[3],1.31 [153]	D,PD
PW91	0.90 [151],1.19 [156][2]	D
	1.36 [156][2],1.57 [156][2]	
RPBE	1.73 [155]	ID
B3LYP	3.13 [156]	D
HSE06	2.80 [156]	D
PBE0	3.94[3],3.67 [156]	D
ΔSCF	2.92[3]	-
G_0W_0	3.26[3]	D
G_0W_0(w/SO[1])	3.16[3]	D
G_0W_0(w/SO/e-ph[1])	2.86[3]-2.96[3]	D
Exp(UPS-IPES)	3.38$\pm$0.2 [176],3.28$\pm$0.14 [126]	-
E_g^{opt}	2.71[3]-2.81[3]	D
E_g^{opt}(exp) [171, 172, 188]	2.6-2.7(300K),2.8-2.9(0K)	ID,D

[a]SO: spin orbit; e-ph: electron phonon.

[b]Ref [156](**PW91**):1.19 eV computed by ultrasoft pseudopotentials; 1.36 eV computed by PAW pseudopotentials; 1.57 eV computed by Gaussian-type basis sets with a linear combination of atomic orbitals approach.

[c]All band gaps were computed at the experimental geometry; the other calculations shown in the table were carried out at the optimized geometries of the corresponding functionals.

tions (see Fig. 3.2.2 and Fig. 3.2.3), we found a decrease of 0.1 eV in the band gap of RT-monoclinic WO_3 obtained without SO (0.2 eV decrease in the case of simple cubic; see Table 3.9). Such a reduction comes from the lowering of the conduction band minimum (CBM): the CBM states have mostly W 5d characters and are thus more affected than the O 2p states at the valence band maximum (VBM). We assumed that the magnitude of SO effects on the band gap is similar at the LDA and G_0W_0 level of theory (similar SO splittings, within 0.1 eV, were reported in LDA and GW calculations of several systems with heavy elements [190, 191]).

Next we consider the effect of electron phonon (e-ph) interaction on the band gap of WO_3; such an effect was discussed in several papers for numerous semiconductors and insulators [192, 193, 194, 195, 196, 197]. In general, including e-ph interaction decreases the value of the fundamental gap (E_g) even at zero temperature, due to zero point motion [192]. In principle, the e-ph renormalization of E_g may be obtained

Table 3.9: Equilibrium lattice parameters [lattice constants (Å), and angle (°), see Fig. 3.2.1] and direct (D) and indirect (I) band gaps (eV, fifth and sixth column) of simple cubic and RT-monoclinic WO_3 computed with (w/SO) and without spin orbit interaction (wo/SO), using Density Functional Theory, and the local density approximation.

		Simple Cubic			
	a				
wo/SO	3.79				0.54(ID)1.62(D)
w/SO	3.79				0.34(ID)1.35(D)
		RT-monoclinic WO_3			
	a	b	c	β	
wo/SO	7.35	7.45	7.66	90.6	1.30(D)(1.87(D)[1])
w/SO	7.38	7.45	7.66	90.4	1.20(D)(1.79(D)[1])

[a]Computed at the experimental geometry

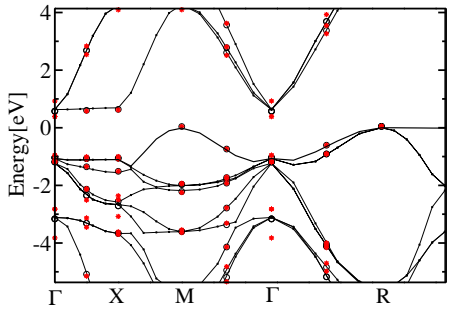

Figure 3.2.2: Band structure of simple cubic WO_3 computed by including spin orbit (SO) interaction (black circles) and without SO (red stars).

from ab initio calculations, as recently reported, e.g. for carbon diamond (8 valence electrons per unit cell) [193]. However these calculations are computationally very demanding, and they are still prohibitive for a system such as WO_3, with 256 electrons per unit cell. Therefore, following previous work on ionic crystals [198, 199, 200], we adopted a model Fröhlich Hamiltonian (FH)[178, 179, 180], assuming that the interaction of electrons with optical phonons is the dominant effect contributing to e-ph interaction. We note that the CBM of WO_3 is at Γ and thus the use of a FH is a reasonably accurate approximation. We also note that we did not consider small (Holstein) polaron formation (as, e.g. done in Refs. [201] and [202]) as these polarons do not affect the value of the optical gap, although they may affect photoluminescence.

The renormalization of the lowest conduction band (ΔE) due to electron-optical phonon interaction can be evaluated by Rayleigh-Schrödinger(RS) perturbation the-

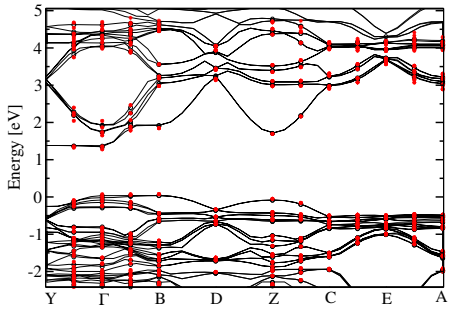

Figure 3.2.3: Band structure of RT-monoclinic WO_3 computed by including SO interaction (black circles) and without SO (red stars).

ory and following Smondyrev [203] we have:

$$\Delta E = -\omega_{LO}[\alpha + 0.0159\alpha^2 + 0.000806\alpha^3 + O(\alpha^4)] \tag{3.2.1}$$

where ω_{LO} is the frequency of the longitudinal optical phonon, m_b is the conduction band effective mass, and α is a dimensionless coupling constant defined as:

$$\alpha = \frac{e^2}{\hbar}(\frac{m_b}{2\hbar\omega_{LO}})^{1/2}(\frac{1}{\epsilon_\infty} - \frac{1}{\epsilon_0}). \tag{3.2.2}$$

Here ϵ_∞ and ϵ_0 are the high frequency and static dielectric constants, respectively, and a large difference between the two constants may be responsible for a large electron-phonon coupling.

We computed the optical phonon frequency and the dielectric constants of RT-monoclinic WO_3 at different levels of theory using DFPT [53], and we fixed the values of m_b to that reported by experiments by fitting Hall mobility values [204]. Our results are shown in Table 3.10: overall we found a downward shift of the CBM of 0.2-0.3 eV due to electron-phonon interaction. This value represents a lowerbound to the e-ph renormalization of the gap, since we did not include possible couplings of phonons with the valence band.

The coupling constant α computed at the LDA optimized geometry (1.74) is lower than the previously reported ones (approximately 3$\sim$5) based on experimental data [205, 206]. The difference comes, at least in part, from the larger value of ϵ_∞ (6.53) obtained within LDA, compared to experimental data, varying between 3.2 and 6 [207, 208]. As pointed out in Ref [206], this variability probably stems from a great sensitivity of ϵ_∞ to small structural differences. Indeed we found that our results for ϵ_∞ are extremely sensitive to geometrical details. For example, the ϵ_∞ obtained as $\frac{1}{3}Tr(\varepsilon_\infty)$ (where ε_∞ is the macroscopic dielectric tensor) at the experimental geometry is 5.57, substantially smaller than the LDA optimized value of 6.53. The latter higher value originates from an underestimate of lattice distortions at the DFT/LDA level

Table 3.10: Energy shift (ΔE) of the conduction band minumum of RT-monoclinic WO_3 due to electron-phonon interaction, obtained from Eq. 3.2.1. The effective mass of the lowest conduction band (1.75), was taken from Ref [204]. All other parameters (the high frequency, ϵ_∞, and static, ϵ_0, dielectric constants and longitudinal phonon frequency ω_{LO}) were computed from first principles (see text).

ϵ_∞	ϵ_0	ω_{LO}(eV)	α	ΔE(eV)
6.53[1]	44.67[1]	0.134[2]	1.74	-0.241
6.53[1]	44.67[1]	0.070[3]	2.41	-0.176
5.57[4]	44.67[1]	0.134[2]	2.09	-0.291
5.57[4]	44.67[1]	0.070[3]	2.90	-0.214
5.63[5]	31.33[5]	0.125[5]	2.01	-0.260

[a]Optimized LDA geometry; averaged diagonal value.
[b]Optimized LDA geometry; highest optical phonon.
[c]From Ref [205]
[d]Experimental geometry; averaged diagonal value.
[e]Optimized vdW-DF2 geometry.

of theory, which in turn leads to a gap 0.5 eV lower than that computed at the experimental geometry. We note that using $\omega_{LO} = 70$ meV[1] and ϵ_∞ computed at the experimental geometry, we obtained a coupling constant of 2.90, close to that reported by Refs. [205, 206]. However, the use of $\omega_{LO} = 70$ meV does not appear to have a robust justification. Interestingly, with the vdW-DF2 functional we obtained [130] results in better agreement with experiments for ϵ_∞ (5.63), ω_{LO} (125 meV) [206] and ϵ_0 (31) [139, 140].

When we included both SO and electron phonon interaction in the calculation of the RT-monoclinic WO_3 quasiparticle gap we obtained a value of 2.9$\sim$3.0 eV (see the value G_0W_0 (w/SO/e-ph) in Table 3.8), which appears to underestimate the UPS-IPES gap measurements [126, 176]. We note that these measurements were performed using He I(21 eV) and He II(41 eV) sources and they have great surface sensitivity; hence the measured gap is most likely that of the surface, while we computed a bulk electronic gap. Higher photon energies (e.g. hard X-ray [210]) would be required to measure the bulk gap. Ref [126] noted that in a polycrystalline semiconductor a surface gap larger than that of the bulk is not unusual [211], due to possible structural and/or compositional differences between bulk and surface. Further studies are clearly necessary to clarify the difference between surface and bulk WO_3 quasiparticle gaps.

[1]Our computed ω_{LO} frequency (134 meV) at the fully optimized LDA geometry is in relatively good agreement with recent experiments by Gunnar [206], who reported longitudinal peaks at 50 and 123 meV. However Ref. [205] reported a single ω_{LO} value at 70 meV, which is close to the average, 75 meV, obtained using Gunnar's data: $\omega_{LO}^{-0.5} = \omega_{LO1}^{-0.5} + \omega_{LO2}^{-0.5}$. A much higher value (164 meV) was instead given in Ref. [209].

3.2.2 Optical gap of WO_3 at room temperature

Here we discuss the optical gap (E_g^{opt}) of RT-monoclinic WO_3, which was measured by UV-vis transmission spectroscopy and photoelectrolysis, yielding a well accepted experimental value of 2.6-2.7 eV [171, 172, 170] at room T. These measurements probed bulk properties. Data were analyzed using a Tauc plot(a power-law fitting of the absorption edge [212]): $\alpha h\nu = A(h\nu - E_g)^{\beta}$, with β =2 (1/2) for an indirect (direct) gap [213]; α is the absorption coefficient and A a constant. The direct or indirect nature of the fundamental optical gap of RT-monoclinic WO_3 is still controversial. Several authors [171, 170] claimed the optical gap is indirect, because $\alpha(h\nu)$ is better fitted by a Tauc plot with $\beta = 2$; however, Saljie et al [172] fitted the absorption edge to a direct gap formula ($\beta = 1/2$) and obtained results (2.58 eV) similar to those with $\beta = 2$. We found (see Table B1 of appendix B) that the direct and indirect electronic gaps computed within G_0W_0 differ by less than 0.05 eV. We computed the optical gap of RT-monoclinic WO_3 by subtracting the exciton binding energy from the G_0W_0 gap, evaluated by including SO and e-ph interaction. The exciton binding (ϵ_b) was calculated as the difference between the first excitation energy of the optical spectrum (obtained by solving the BSE [33, 30]) and the G_0W_0 gap[2]. We found $\epsilon_b = 0.15$ eV and a value of the optical gap of 2.7$\sim$2.8 eV (see Table 3.8), in accord with the value measured as a function of T with in the region of stability of RT-monoclinic WO_3, extrapolated to 0 K, i.e. 2.8-2.9 eV[188].

In summary, in this section we showed that several effects need to be taken into account in order to correctly predict the optical gap of WO_3, including spin-orbit and electron-phonon interaction, and exciton binding. We interpreted the difference between computed quasiparticle gaps and photoemission data (0.3-0.4 eV) as originating, at least in part, from the difference between measured surface gaps and computed bulk values. We also found minor differences ($\sim$0.05 eV) between indirect and direct minimum gap of RT-monoclinic WO_3, which may explain why different experiments [171, 172, 170] appeared to disagree on the character of the lowest gap of WO_3. We expect that the detailed comparison between theory and experiments achieved here for WO_3 will serve as a guide to carry out similar comparisons for other materials of interest for solar energy conversion.

3.2.3 Band edge alignment between different phases of WO_3

Here we turn to the discussion of the band edge alignment between different phases of WO_3 [214]. Fig. 3.2.4 and 3.2.5 shows the band edge alignment between different phases of WO_3 obtained at the LDA optimized geometry and at the experimental geometry, respectively, computed using the G_0W_0 approximation. As we discussed in section 3.2, due to the flat octahedra tilt angles of the simple cubic and tetragonal

[2]We note that a dense k point sampling is essential to obtain the well converged exciton binding energy. We used a 8x8x8 k point mesh.

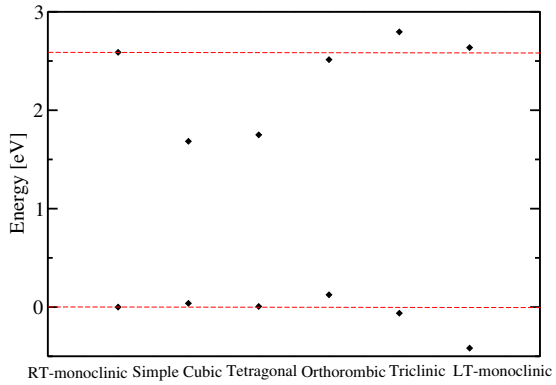

Figure 3.2.4: Band edge alignment between different phases of WO_3 computed at the G_0W_0 level of theory, at the LDA optimized geometry. The band edges are aligned at the energy of the W 5s, 5p core states.

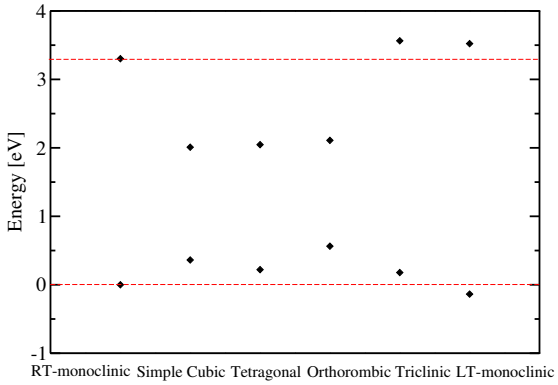

Figure 3.2.5: Band edge alignment between different phases of WO_3 computed at G_0W_0 level of theory, at the experimental geometry. The band edges are aligned at the energy of the W 5s, 5p core states.

phases, their CBM are the lowest among all the phases; on the other hand, the triclinic and LT-monoclinic phases have slightly larger octahedra tilt angles (or smaller W-O-W angles) than the RT-monoclinic phase, which is responsible for a shift up of the CBM of these two phases compared with that of a RT-monoclinic one. However, the relative position of the VBM between different phases does not follow the same trend as the CBM, due to its non-bonding nature, being mainly composed of O 2p states. The variation of the VBM positions between different phases is not as significant as that of the CBM.

3.3 WO_3 Clathrates

As mentioned earlier in the chapter, tungsten oxide (WO_3) has been extensively studied for its potential use as an anode material in photovoltaic and photoelectrochemical cells [215, 216, 217, 131, 218, 219, 220, 132]; however its band gap far exceeds 1.23 eV, the minimum energy per electron required for water oxidation at standard conditions, and a number of investigations have been focused on lowering the band gap of this material either by doping or structural modifications [153, 221, 222, 223, 224, 225]. As described in section 3.1.1, tungsten oxide has the perovskite structure (ABO_3) where the central "A" site is not occupied. The "A" position may be filled by dopants (e.g. H, Li, or Na) leading to intricate structural changes, e.g. to cubic structures for $H_{0.5}WO_3$, Li_xWO_3 ($0.1 < x < 0.4$) and Na_xWO_3 ($0.3 < x < 1$). Doping WO_3 with alkali metals changes both the crystal structure and the electronic and optical properties. For example, the color of Na_xWO_3 may be tuned from greenish to yellow as x is increased from 0 to 1 [226], and the WO_3 unit cell volume expands by 7.3% at $x = 1$ [152, 227]. The incorporation of alkali ions results in the formation of an s-band high above the Fermi level and to the formation of a metallic conductor [152, 228].

Recently much effort was devoted to N-doping of oxides which are promising photoanodes, including WO_3 and TiO_2. Nitrogen substitution of O was shown to extend the light absorption onset from 380 nm to visible light (above 500 nm) in TiO_2, thus offering possible photocatalytic activity under visible light irradiation [229, 230, 231]. However, N-doping usually yielded a lower photocurrent under a full spectrum and a lower quantum yield in the UV region than pure TiO_2. The reason for the photocurrent decrease is under debate: it was proposed [232, 230, 233] that substitutional N leads to isolated mid-gap states which are highly localized and act as recombination centers. An alternative explanation is based on the hybridization of N and O 2p orbitals, which is expected to shift the valence band edge of the oxide to more negative potentials, thus providing a less favorable alignment with the water redox potential [234]. Atomic N doping of WO_3 was studied in several recent papers [221, 153]. It was found that N substitution leads to a significant decrease of the band gap of WO_3 [221] for N concentrations larger than 2%. Unfortunately, this high concentration of N gives rise to charged defects [235, 236, 153] and increases carrier recombination rates, thus leading to a poor photocurrent density.

It was shown by our experimental collaborators [129] that doping (or intercalation) of N_2 into WO_3 leads to the formation of stable clathrates without adding charged defects to the system, thus avoiding the formation of undesired carrier recombination centers. By intercalating N_2 into WO_3, the band gap was reduced by $\sim$0.8 eV, compared to that of room temperature (RT) monoclinic WO_3. This observation suggests that the formation of clathrates is a promising route to improve the absorption efficiency of WO_3 and it is interesting to search for other small molecules or atoms that may induce a desired gap decrease upon intercalation in WO_3. We note that N_2 intercalation was reported in several (Ba)-Ti-O systems with the per-

ovskite structure [237, 238], where the presence of dinitrogen was characterized using X-ray Photoelectron (XPS) and Raman spectroscopy. A slight increase in the unit cell volume upon nitrogen molecules intercalation was observed in several cases [237] and all reactions were found to be endothermic [238].

In this section, we present first principles calculations of tungsten oxide compounds intercalated with molecular nitrogen, which were used to interpret experimental results [129, 130] and with CO and rare gas atoms; we show that both structural changes, and electronic interactions between the matrix and the guest species lead to a lowering of the band gap. Structural changes are the major effect. Our results provide a detailed interpretation of experiments in the case of N_2, and predictions on other stable clathrates with promising properties for water oxidation.

3.3.1 N_2-intercalated WO_3

3.3.1.1 Structural Properties

We first discuss the structural modifications occurring in WO_3 upon N_2 insertion. We showed that the top of the valence band of WO_3 is mostly composed of O nonbonding $2p$ orbitals, which are hardly affected by the coordination environment; nevertheless, an element less electronegative than O, e.g. N, may help raise the VB edge. However, doping WO_3 by N substitution of O is likely to form electron-hole recombination centers which then have a negative effect on the photocatalytic activity of the material, as discussed in the introduction. A different way of lowering the band gap was recently proposed, by doping WO_3 with molecular nitrogen. Stable clathrate compounds with composition $xN_2{\cdot}WO_3$, x =0.034–0.039 were prepared by trapping N_2 in WO_3 [129]. The incorporation of N_2 significantly reduced the band gap of the monoclinic phase WO_3, up to 0.8 eV, the exact value depending on the annealing temperature.

Assuming the absence of other defects in the N_2-intercalated WO_3, our calculations showed that the band gap reduction may be attributed to two factors. One is the orbital coupling between N_2 and WO_3, accompanied by a small charge overlap. In addition, N_2 exerts an effective stress on the WO_3 lattice, causing a structural change. We first discuss the structural changes occurring in WO_3 upon N_2 insertion, which are mostly responsible for the gap decrease, and then we examine the modification of the electronic structure of the host oxide in the presence of N_2.

Fig. 3.3.1 shows the bond lengths and tilt angles of the octahedra of pure monoclinic WO_3 and N_2-intercalated WO_3 ($1N_2$:$8WO_3$) as a function of the structural parameters varied in our geometry optimizations (internal coordinates and cell volume) at the LDA level. The left panel shows that N_2 doping causes slightly larger bond length splitting (BLS) (on average by $0.017\mathring{A}$) than those found in pure WO_3 in all the three directions, for both internally and fully optimized N_2-doped WO_3. Fig. 3.3.1 also shows that the bond angle $\angle$W-O-W exhibits small variations when

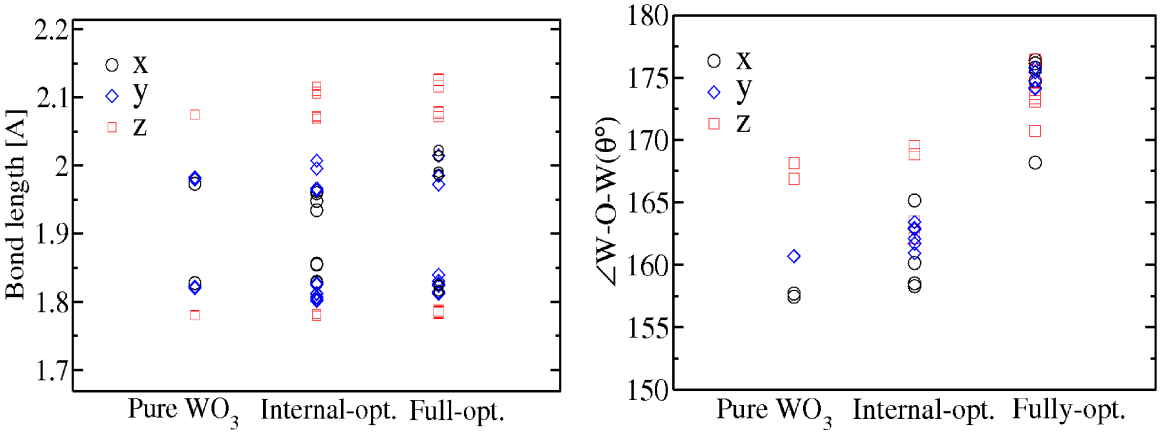

Figure 3.3.1: Bond length (left panel) and tilt angle (right panel) of pure monoclinic WO_3 and N_2-intercalated WO_3 with concentration $1N_2$:$8WO_3$ optimized using the LDA functional. In each panel, the first column (Pure-WO_3) corresponds to the optimized geometry of pure monoclinic WO_3; the second column (Internal-opt.) to the geometry of N_2-intercalated WO_3 where only the internal coordinates were optimized while keeping the same cell parameters as those of pure monoclinic WO_3; the third column (Fully-opt.) to the geometry of N_2-intercalated WO_3 where both the internal coordinates and the cell parameters were optimized. In each panel "x,y,z" denote the bond lengths or tilt angles along the x,y,z directions, respectively. As β is close to 90°(within 1°), the x,y,z directions are roughly parallel to the a,b,c lattice vectors. Hence W-O chains are almost parallel to each of the three Cartesian axes.

only internal coordinates are optimized in N_2-intercalated WO_3; in contrast, upon full optimization including the cell parameters, the volume of N_2-intercalated WO_3 increases by 5% and the ∠W-O-W increases from 155∼165°to 170∼175°. The structural changes obtained by fully optimizing N_2-intercalated WO_3 are similar to those observed in the lattice expansion of monoclinic WO_3 (see Fig.S2 in the Appendix1) where ∠W-O-W increased by 10∼15° with 5% volume expansion.

To investigate the stability of N_2 in the oxide, we computed the energy change for incorporation of N_2 into WO_3 as ΔE in Table 3.12 shows. For all N_2 intercalated configurations studied here, we found that the energy change is about +1.6 eV; the positive value indicates that the intercalation process is endothermic. This result is consistent with those of N_2-containing perovskite compounds (La-Ba-Ti systems) reported in Ref [238]: calorimetric experiments have shown that incorporation of N_2 in these compounds is an endothermic reaction. However, N_2-containing perovskite compounds(La-Ba-Ti systems), are stable under ambient conditions, indicating that N_2 molecules are kinetically trapped into the oxide lattices. This is again similar to what was found here in the case of N_2 in WO_3. By using nudge elastic band calculations [239], we found that the kinetic barrier for N_2 to diffuse from a hollow

center of the WO_3 crystal to a neighboring hollow center is 2.6 eV, indicating that $xN_2.WO_3$ is kinetically stable (thermal energy RT=0.067 eV at 750 °C) although not thermodynamically stable.

Experimentally [129], Raman and NMR spectroscopies were used to characterize N_2 into WO_3 and to better understand the structural properties of the clathrate. In the measured Raman spectra of $xN_2{\cdot}WO_3$, x =0.034–0.039, the maximum corresponding to the N−N stretching frequency was found to split into two peaks around the gas phase value: a sharp one red-shifted by 4 cm^{-1} and a broad one blue-shifted by 8 cm^{-1}. We carried out a series of calculations at the LDA level to interpret the observed vibrational signatures. We first computed the frequency of gas phase N_2 and obtained a value of 2383 cm^{-1}, which is 25 cm^{-1} higher than the experimental one (2330 cm^{-1}) after anharmonic corrections, $\nu_{\text{exp.}}^{\text{corrected}} = 2358.6$ cm^{-1}.

As the errors caused by the use of approximate exchange-correlation approximations and the neglect of anharmonic effects are most likely systematic [240], we expect the use of such approximations to yield the correct trend of the frequency shift within different environments, e.g. in the gas phase or within WO_3. When computing the N_2 frequency in the oxide, we carried out two sets of calculations: one where the WO_3 lattice was kept frozen and one where all atoms were allowed to move. The results of the two sets of calculations for the vibrational frequencies of N_2 differed by at most 1 cm^{-1}, confirming that the vibrational properties of the guest molecule are not affected by those of the host oxide.

Table 3.11 and Table 3.12 list the structural, vibrational and bonding properties of interstitial N_2 in simple cubic and monoclinic WO_3, respectively. We note that the frequency (ν) and bond distance ($d_{\text{N-N}}$) of a N_2 molecule placed in a monoclinic unit cell of WO_3 in the absence of the oxide (configuration e in Table 3.12), are almost identical to those of the gas phase, indicating that the interaction between N_2 molecules in different unit cells is negligible.

In the case of N_2-intercalated simple cubic WO_3, we found that ν always increases regardless of the molecular orientation, and the bond length is decreased by about 0.4-0.5%. Instead the frequency of N_2 in intercalated monoclinic WO_3 exhibits a

Table 3.11: Structural, bonding and vibrational properties of an interstitial N_2 molecule in simple cubic WO_3, oriented along different directions, at the "A" site of the "ABO_3" structure. ΔE is the change of total energy obtained after the insertion of N_2 ($\Delta E = E(8WO_3.N_2) - E(8WO_3) - E(N_2)$), and positive values indicate that such process is endothermic. "d" indicates distances and "ν" frequencies.

	$d_{\text{N-N}}$ (Å)	$d_{\text{N-W}}$ (Å)	$d_{\text{N-O}}$ (Å)	ΔE (eV)	ν (cm^{-1})
$\langle 100 \rangle$	1.090	3.018	2.437	1.648	2397
$\langle 111 \rangle$	1.090	3.044	2.381	1.496	2408
gas phase	1.094	–	–	–	2383

strong orientation dependence (see Table 3.12): Configurations *a*, *b*, *c* have higher frequencies whereas configuration *d* has a lower frequency than gas phase N_2. The total energy difference between configurations *a*, *b* and *c* is rather small (within 0.1 eV), which implies that all these geometrical arrangements may exist with similar probability at room temperature, thus explaining the broadening of the blue shifted peak found in experiments [129]. In Table 3.11 and 3.12, we also list the shortest distances between an N atom and either W or O atoms for both simple cubic and monoclinic WO_3. These distances (e.g.d_{N-O} 2.4-2.5 $\AA$) are similar to those found, e.g. for N_2 containing $Ba_2Ta_2O_7N_{0.62}$ compounds [237, 241].

The shortening of the N_2 bond length in configurations *a*-*d* is caused by the repulsive interaction between the WO_3 lattice and the N_2 molecule. The presence of N_2 exerts a stress on the WO_3 lattice and the lattice tends to distort and expand in order to release this chemical pressure; the stress compresses the N-N bond leading to a decrease of the bond length.

Fig. 3.3.2 shows the electron density difference ($\Delta\rho$) before and after N_2 was inserted at interstitial sites in monoclinic WO_3: $\Delta\rho = \rho(WO_3 + N_2) - \rho(WO_3) - \rho(N_2)$. In both $\langle 100 \rangle$ and $\langle 111 \rangle$ directions, the electron density decreases in the region between two N atoms and increases in the region close to each N atom but away from the N-N bond [242]. This indicates that the oxide lattice gains a small amount of electronic charge at the expenses of the nitrogen molecule. Thus N_2 is not completely inert inside the oxide lattices. In fact, N_2 has been shown to be weakly bonded to the oxide network [238] in several N_2 containing perovskite compounds. Charge density maps indicate that there is a larger charge overlap between N_2 and WO_3 in configuration *d* that weakens the N−N bonding; this may be responsible for a decrease in ν, in contrast to other N_2 orientations (see Table 3.12). These results explain the appearance of the red-shifted peak in the experimental Raman spectra [129], and the observed sharpness of this peak is consistent with the fact that

Table 3.12: Structural, bonding and vibrational properties of an interstitial N_2 molecule in monoclinic WO_3, oriented along different directions, at the "A" site in the "ABO_3" structure. Results are given for fully relaxed geometries. Configuration *e* denotes that of a N_2 molecule placed in a monoclinic cell in the absence of the WO_3 lattice [129]. *d*, ΔE and ν have the same meaning as in Table 3.11.

Configuration	Orientation	d_{N-N} (Å)	d_{N-W} (Å)	d_{N-O} (Å)	ΔE (eV)	ν (cm^{-1})
a	$\langle 100 \rangle$	1.091	3.037	2.464	1.669	2391
b	$\langle 010 \rangle$	1.090	2.982	2.451	1.722	2391
c	$\langle 001 \rangle$	1.091	3.045	2.457	1.631	2389
d	$\langle 111 \rangle$	1.092	2.251	2.326	1.865	2373
e		1.094			0	2382
Gas phase		1.094	–	–	–	2383

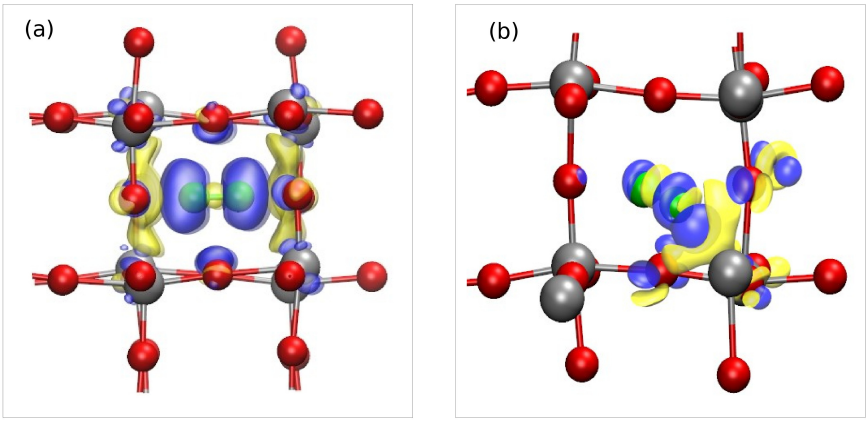

Figure 3.3.2: Electron density difference between pure monoclinic WO_3 and N_2 clathrates with N_2 oriented along the $\langle 100 \rangle$ (a) and $\langle 111 \rangle$ (b) directions. Yellow (blue) indicates electron depletion (accumulation). W and O atoms are represented by silver and red spheres, respectively; N atoms are represented by green spheres. The figures show isosurfaces of charge equal to 0.001 $e/{a_0}^3$

$\langle 111 \rangle$ is the only N_2 orientation that corresponds to a red-shifted ν.

Interestingly, a red shifted vibrational frequency is not found in simple cubic WO_3 (see Table 3.11), but it only occurs in monoclinic WO_3, likely because of the symmetry constraint in the cubic structure, preventing N_2 to approach W or O as much as in the monoclinic phase. In the latter, the lattice distortion and lower symmetry allow N_2 to get close (2.25 $\mathring{A}$) to one of the W atoms (configuration d), leading to a significant charge overlap between N_2 and W as shown in Fig. 3.3.2(b), and to a reduction in ν.

Our results show that the observed changes in vibrational frequency of interstitial N_2 may be explained by the presence of different orientations of the molecule within the host lattice. In some configurations, the repulsion between N_2 and WO_3 compresses the molecular bond and therefore leads to an increase of the molecular vibrational frequency; in other configurations the charge density redistribution between N_2 and WO_3 causes an electron density shifts from the bonding to the antibonding region of N_2, leading to a weakening of the N−N bonding and thus to a decrease of the vibrational frequency.

To further investigate whether the vibrational signatures observed experimentally are unique to intercalated N_2, we also examined the case of substitutional N_2 and computed its vibrational properties. We considered the case where one O atom in the unit cell of the monoclinic WO_3 is replaced by a N_2 molecule. The vibrational frequency of gas phase N_2 decreases to 1713 cm^{-1} and the bond length increases to 1.197 Å (gas phase: 2383 cm^{-1}, 1.094 Å). Therefore we concluded that the signal reported experimentally did not detect substitutional N_2 molecules.

3.3.1.2 Electronic Structure

Having analyzed the structural and vibrational properties of the N_2-WO_3 clathrate, which are in agreement with experiments [129], we now are in a position to investigate its electronic properties. We found that the LDA(vdW-DF2) band gap of fully optimized N_2-intercalated WO_3 decreased by 0.2 eV(0.35 eV) compared to that of pure WO_3 at $1N_2$:$8WO_3$, while the optimization of internal coordinates without volume variations led to a ≈0.05(0.16) eV decrease. This suggests that the volume expansion and the increased ∠W-O-W angle are largely responsible for the band gap reduction found in the fully optimized N_2-intercalated WO_3. We obtained very similar band gap reductions using the PBE0 functional [144] and the modified ΔSCF method [150] with the optimized LDA geometry. In particular the larger decrease in the gap obtained with the vdW-DF2 functional, which yields larger structural modifications upon insertion on N_2 in the lattice than any other functional, emphasizes the importance of structural changes in determining the gap reduction.

The gap decrease of 0.2-0.35 eV predicted by theory is smaller than that found experimentally (∼0.8 eV). However we note that by increasing the concentration of N_2 to 1:1, we obtained a band gap lowering of ∼0.7 eV at the LDA level, consistent with the value 0.8 eV reported experimentally. These results suggest that the N_2 molecules may be clustered in experimental samples.

Fig. 3.3.3 compares the band structure(LDA) of fully optimized monoclinic WO_3 intercalated by N_2 and pure WO_3. By aligning the W 5s,5p core states of the two systems, we found that the CBM of the doped oxide is lowered but the VBM position is almost unchanged (there is just a small positive shift of 0.05 eV). As discussed previously, this could be due to a change in the tilt angle of two octahedra, that

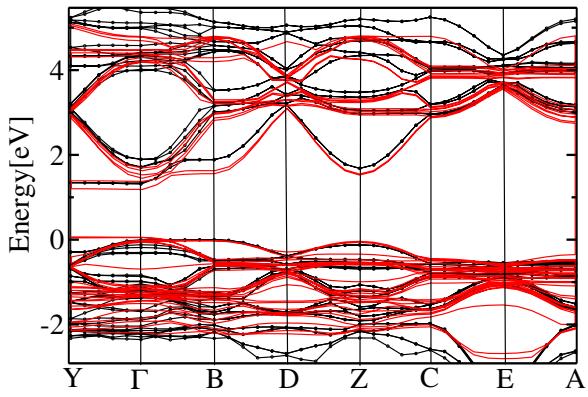

Figure 3.3.3: Band structure of N_2-intercalated monoclinic WO_3 (red) at $1N_2$:$8WO_3$ concentration as obtained by DFT-LDA calculations. For comparison, the band structure of pure monoclinic WO_3 obtained at the same level of theory is also shown (black).

Table 3.13: Equilibrium lattice parameters (a_0, b_0, c_0) of monoclinic $8WO_3$:$1N_2$ and its band gap (E_g) at the fully optimized geometry. α,β,γ are very close to 90°, which are not listed here. LDA/HGH denotes results of calculations carried out within the LDA with HGH pseudopotentials [158]; "PBE/HGH" denotes results of PBE calculations with HGH pseudopotentials, "vdW-DF2/HGH" denotes results of vdW-DF2 calculations [145, 146, 147, 148] with HGH pseudopotentials

Method	lattice parameters (Å)			E_g (eV)
	a_0	b_0	c_0	
LDA/HGH	7.57	7.57	7.72	1.13
PBE/HGH	7.51	7.67	7.92	1.42
vdW-DF2/HGH	7.57	7.75	8.09	1.45

becomes $\sim 180°$ and to an increase in overlap between the W 5d and O 2p orbitals at the CBM, enhancing 5d-2p hybridization and shifting downward the CBM. On the other hand, the VBM is composed by O nonbonding states which are less sensitive to the crystal geometry. In both cases, the CBM is at the Γ point while the VBM is along $Y(0, 0.5, 0) - B(0.5, 0, 0)$ where the band is nearly flat for the N_2 intercalated case. We found that the difference between direct and indirect band gap is less than 0.02 eV [243]. This is the case also for the band structures computed by PBE and vdW-DF2 functionals.

Table 3.13 shows the equilibrium lattice parameters and band gap of N_2 intercalated WO_3($8WO_3$:$1N_2$) optimized at LDA, PBE, vdW-DF2 functionals. Unlike pure monoclinic WO_3, the band gaps obtained at the PBE and vdW-DF2 level of theory are very close (they differ by less than 0.1 eV). This is consistent with the fact that the tilt angles of $8WO_3$:$1N_2$ obtained by PBE and vdW-DF2 all fall into the same range (between 165∼176°), and that the band structures obtained by PBE and vdW-DF2 are very similar (not shown), despite of differences in the optimized lattice constants (see Table 3.13).

3.3.2 CO intercalated WO_3

Inspired by N_2 intercalation, we studied other possible clathrates obtained by intercalating closed shell molecules and atoms, in particular CO and rare gases. These materials have not yet been realized experimentally, and similar to the case of N_2 we found that the formation of the clathrates is endothermic. Therefore the guest atoms or molecules will have to be kinetically trapped into the host oxide. Once trapping is achieved, large energy barriers (of the order of 2.9 eV for CO and 2.6 eV for N_2 in our nudged elastic band [239] calculations) will prevent escape of the guest species. Again similar to N_2 intercalation, the presence of CO and rare gas atoms does not

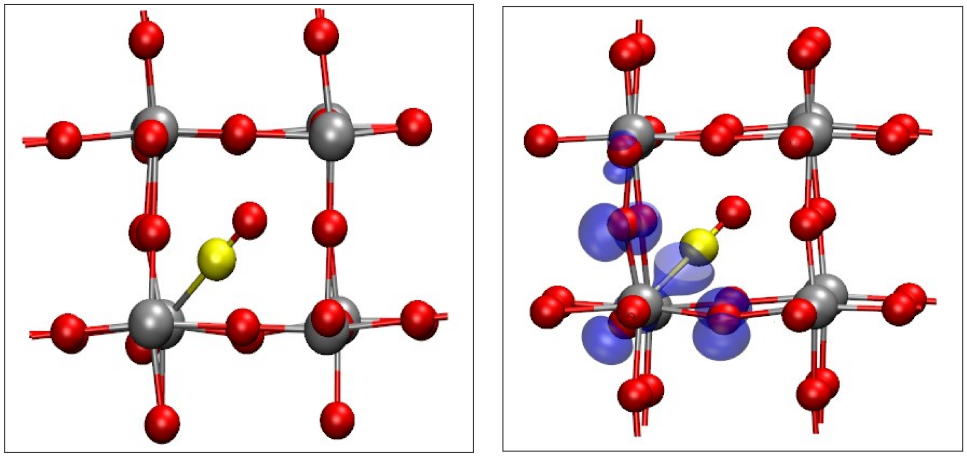

Figure 3.3.4: The geometry of CO intercalated in monoclinic WO_3 (left panel) at $1CO:8WO_3$ concentration and the squared modules of the wavefunction (right panel) at the VBM, at the high symmetric point A(-0.5,0.5,0).

induce any charged defects within the WO_3 crystal; thus one avoids the formation of electron-hole recombination centers found, e.g. in the case of N substitution and O vacancies.

Upon intercalation, CO binds to W along the <111> direction with a C−W atomic distance of 2.1 $\mathring{A}$ (see Fig. 3.3.4). This bonded configuration is more favorable than the one with CO inside an octahedral cavity and not bonded to the lattice: for instance, the configuration with CO along the <100> direction has a total energy 0.5 eV higher than the configuration of Fig. 3.3.4. Due to the Coulomb repulsion between carbon lone pair electrons and nearby O nonbonding p orbitals, the valence band edge of the oxide shifts upward in the presence of CO by ~ 0.15 eV, compared with that of pure monoclinic WO_3. The wavefunction at the VBM, reported in Fig. 3.3.4, shows the contribution from both O and C atoms. In addition, similar to N_2 intercalation, the tilt angle between two octahedra approaches towards 180°, leading to a better overlap of W 5d and O 2p orbitals at the bottom of the CB, which shifts downward by ~ 0.02 eV. The shifts of the VBM and CBM lead to a band gap reduction of $\sim$0.2 eV at the LDA level; the computed band gap of CO intercalated monoclinic WO_3 (1.13 eV) is direct at the Γ point. We note that the observed VBM upward shift is favorable for water splitting reactions, as the band alignment between monoclinic WO_3 and the H_2O redox potential [126] is improved.

As in the case of N_2, we computed the energy change for incorporation of CO into WO_3 and, using nudge elastic band calculations, the kinetic barrier for CO to diffuse from a hollow center of the WO_3 crystal to a neighboring hollow center; the energy change is +1.2 eV and the kinetic barrier is 2.9 eV, respectively, indicating that $CO.8WO_3$ is kinetically stable, as N_2, but not thermodynamically stable.

3.3.3 Rare gases intercalated WO_3

We now turn to the discussion of rare gas intercalation in WO_3. For rare gas atoms (e.g.Xe), we found the kinetic barrier for diffusing from a hollow center of the WO_3 crystal to a neighboring hollow center of the order of 2.5 eV in our nudged elastic band [239] calculations, indicating that these atoms may be kinetically trapped in the oxide crystal. The formation energy of Xe intercalated WO_3 is +3.3 eV, rather high compared with the thermal energy at room temperature. However, the formation energy per WO_3 unit, 0.4 eV, is similar to that reported for dinitrogen in La-Ti systems [238], 19-26 kJ mol^{-1} $LaTiO_{3.5}$ (0.2-0.3 eV per $LaTiO_{3.5}$ unit).

Table 3.14 shows that the computed band gap (E_g) of WO_3 monotonically decreases with increasing size of the intercalated rare gas atoms. For Ne, Ar and Kr, we observed a moderate reduction by about 0.1-0.2 eV, while in the case of Xe the gap substantially decreases, by about 0.9 eV. If the intercalated atoms are removed while keeping the WO_3 geometry fixed, the band gaps (E'_g) are reduced by 0.1-0.2 eV for all the rare gas atoms. The same trend as found with LDA calculations was also observed using the modified ΔSCF method [150]. This behavior can be explained by analyzing the two-fold effect of rare gas intercalation: induced structural modifications, i.e. lattice expansion and distortion of the WO_3 lattice, and orbital hybridization and weak charge overlap between rare gas atoms and WO_3. These effects are discussed below.

Similar to N_2 intercalation, the tilt angle between octahedra increases rapidly towards 180° for Ne, Ar and Kr intercalation: as expected, the bigger the atomic radius of the rare gas atoms, the larger the distortion induced in the lattice. The volume of intercalated WO_3 increases by 2.5%($8WO_3$:Ne) to 7.2%($8WO_3$:Xe) compared to that of pure WO_3. The expanded volume observed upon intercalation mainly comes

Table 3.14: Band gap (E_g) of monoclinic WO_3 with different rare gas intercalation at 1:8 ratio. Also listed are the energies of oxygen and rare gas atoms p orbitals evaluated [141] by all-electron LDA calculations. The third column (E'_g) gives the band gap of the pure WO_3 crystals with geometries fixed to those of the corresponding optimized intercalated structures. The difference between indirect and direct band gaps is within 0.01 eV. In the fourth column we report the band gap (Δ-sol E_g) obtained by the method of Ref.[150]. In the fifth column we report the formation energy denoted by ΔE defined as in Table 1. All energies are in eV.

	Atomic Orbital Energy	E_g	E'_g	Δ-sol E_g	ΔE
Pure WO_3	-9.20 [O 2p]	1.3	–	2.39	–
+Ne	-13.54 [Ne 2p]	1.17	1.17	2.29	0.140
+Ar	-10.40 [Ar 3p]	1.19	1.19	2.26	1.248
+Kr	-9.39 [Kr 4p]	1.12	1.09	2.17	2.136
+Xe	-8.39 [Xe 5p]	0.38	1.13	1.85	3.304

from the increased tilt angle between octahedra (∠W-O-W). When θ_t increases from 160° to 180°, the bottom of the CB (t_{2g}) is shifted downward, for the same reasons as those discussed in the case of N_2. (The relative position of the CB of the pure and intercalated solids has been obtained by aligning the W 5s core states. The 5s energy levels of W lie 70 eV below the VBM and are unaffected by the presence of intercalated atoms.)

While Ne and Ar weakly affect the band gap of the oxide, and Kr leads to a ∼0.2 eV decrease, Xe-intercalated monoclinic WO_3 has a significantly reduced band gap of 0.4 eV at the LDA level (see Table 3.14). This indicates the presence of a stronger interaction between Xe and the WO_3 lattice. This interaction arises thanks to the position of the 5p atomic orbitals of Xe, 0.8 eV higher in energy than the O 2p atomic orbitals. As previously discussed, the VBM of pure WO_3 is formed by the nonbonding O 2p states; therefore the hybridization between Xe 5p and O 2p states shifts upward the valence band edge and gives rise to mid-gap states (see Fig. 3.3.6) whose presence reduces the band gap. Note that, as in the case of CO intercalated WO_3, the upward shift of the VB edge is a desirable feature, improving the band alignment with H_2O redox potential.

As shown in Fig. 3.3.5, the VBM of Xe-intercalated WO_3 is mainly composed of O 2p nonbonding orbitals (perpendicular to the W-O bond) as in the case of pure WO_3; at the same time, the wave function is partially residing on the Xe p orbital. The CBM remains dominated by W 5d t_{2g} and O 2p as in the absence of Xe. We note that as in the case of N_2, Xe is unexpectedly not inert in the oxide matrix.

Finally we investigated the band gap dependence on the exchange-correlation functional, by replacing the LDA functional with the hybrid PBE0 functional at the LDA optimized geometry, and found a band gap of 2.0 eV for Xe-intercalated

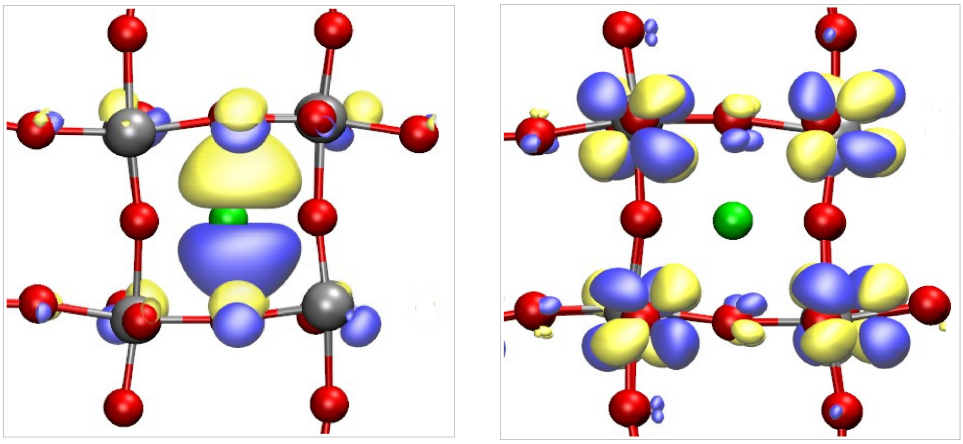

Figure 3.3.5: Isosurfaces of orbitals at the VBM (left panel) and CBM (right panel) of Xe-intercalated monoclinic WO_3 (Green: Xe, Red: O, Silver: W). Yellow/blue spheres indicate (-)/(+) signs of the wavefunction phases.

WO_3. The gap of pure WO_3 computed at the PBE0 level of theory is 3.28 eV, which, as noted earlier, is overestimated compared to the experimental value of 2.6 eV. Therefore PBE0 calculations most likely provide an upper bound for the band gap of Xe-intercalated monoclinic WO_3. One may expect the actual Xe intercalated band gap to be less than 2.0 eV (presumably of the order of 1.8 eV, as predicted at the ΔSCF level of theory) which would be ideal for water oxidation applications.

Effects similar to those observed for Xe, though weaker, were found in the case of Kr. In the case of Ne and Ar, no orbital coupling between the Ne 2p(Ar 3p) and the O 2p states occurs at the VB edge: the energy of the Ne 2p (Ar 3p) is 4 (1) eV lower than that of O 2p. The band structure (not shown) of Ne-intercalated monoclinic WO_3 is similar to that of pure WO_3 except that the CB shifts downward and the VB edge between Y (0, 0.5, 0) and B (0.5, 0,0) flattens out. Similar results are obtained also in the case of Ar. As a consequence for Ne and Ar intercalation the PDOS (not shown) is similar to that of pure WO_3: Ne and Ar p states are embedded deeply in the VB; the top of the VB is entirely composed of O p orbitals just as in pure WO_3.

In summary, in this section we investigated the structural and electronic properties of clathrates of tungsten oxide containing nitrogen, and carbon monoxide molecules, and rare gas atoms. We found that intercalation of closed shell species in the oxide is a promising way to modify the host lattice electronic properties for water oxidation: no charge defects and thus no potential charge recombination centers are introduced, and the band gap of the oxide may be substantially decreased.

Stable clathrates with host N_2 molecules were recently synthesized and our calculations provided an interpretation of the observed band gap reduction, as well as

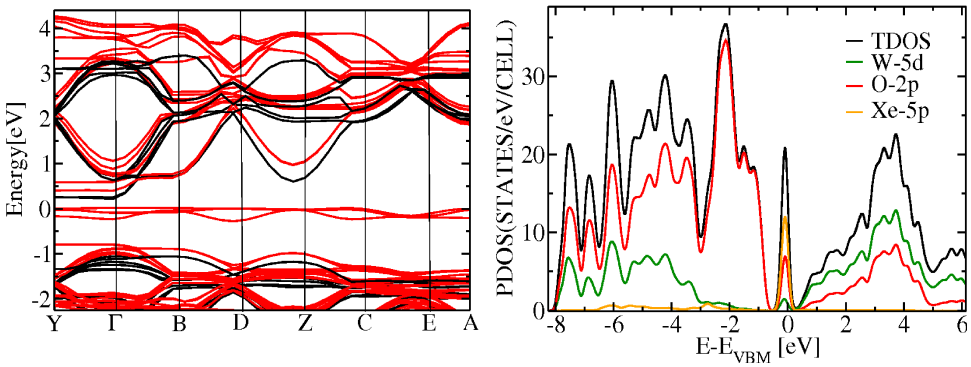

Figure 3.3.6: Left panel: Band structure of Xe-intercalated monoclinic WO_3 (red) as obtained with DFT-LDA calculations. For comparison, the band structure of pure monoclinic WO_3 obtained at the same level of theory is also shown (black). The two band structures are aligned at the energy of the W 5s core states. Right panel: projected density of states (PDOS) and total density of states (TDOS) of Xe-intercalated monoclinic WO_3 as obtained within DFT/LDA; the zero of energy has been chosen at the VBM (E_{VBM}).

of the measured lattice expansion and Raman spectra. In addition, we predicted the properties of WO_3 clathrates with CO and rare gas atoms inserted in the oxide lattice. We found that in all cases the band gap of intercalated WO_3 is reduced, due to the combined effect of structural and electronic changes occurring upon intercalation; however the magnitude of the reduction and the relative shift of the conduction and valence band edges depend on the host molecule or atom. While in the case of N_2 the position of the VBM is unaffected and the CBM moves downward, in the case of CO and Xe the VBM is moved upward, thus improving the alignment between the oxide VB and the water redox potential. However, in all clathrates of tungsten oxide investigated here, the hole mobility of the pure oxide is not improved by molecule or atom insertion, as shown by computed band structures, and improving hole mobilities remains an open issue.

For N_2 concentrations close to those reported experimentally ($xN_2.WO_3$, x=0.034-0.039), we found a band gap reduction smaller than the measured one (0.2-0.35 eV, depending on the level of theory, instead of ∼0.8 eV). Interestingly, by optimizing the geometry and cell parameters with a non local Van der Waals density functional, we obtained the largest structural changes upon N_2 insertion and the largest band gap reduction (0.35 eV). This indicates that the underestimate of band gap reduction with respect to experiment, might be caused by an underestimate of the lattice distortions occurring upon insertion of N_2 in the lattice. It is also possible that in the experimental samples, clustering of N_2 occurs, and this would lead to a larger reduction of the band gap.

3.4 First-principles calculations of $CuMo_xW_{1-x}O_4$ solid solutions

3.4.1 Review of synthetic methods

Stable oxide-based semiconductor electrodes that absorb visible light are highly desirable in various photoelectrochemical applications. To date only binary oxides have been mainly studied for solar energy conversion (e.g. WO_3 and Fe_2O_3) but there are many oxides with complex compositions and structures that can possess smaller bandgap energies [244, 132, 245, 246, 129, 247, 248, 249, 250]. However, making oxides with more complex compositions as high purity film-type electrodes can be difficult because corresponding binary oxides are often thermodynamically more stable and can readily form as impurities. This has limited the investigation of various multinary oxide-based photoelectrodes that can be more promising for solar energy conversion than binary oxide-based photoelectrodes.

Our experimental collaborators have developed a novel electrochemical route to prepare solid solutions of $CuWO_4$ and $CuMoO_4$ (i.e., $CuW_{1-x}Mo_xO_4$) as thin-film type electrodes to investigate their photoelectrochemical properties and we performed

ab initio calculations to interpret some of experimental measurements. $CuWO_4$ is an n-type semiconductor and has a smaller bandgap (2.3-2.4 eV) than n-type WO_3 (bandgap, 2.6-2.7 eV) that has been extensively studied for use as a photoanode in a water splitting photoelectrochemical cell [244, 132, 245, 246, 129]. $CuWO_4$ has a wolframite structure where both Cu^{2+} and W^{6+} ions are stabilized in octahedral sites (see Fig. 3.4.1). Both Cu and W octahedra form their own one dimensional chains along the c-axis by sharing edges. The resulting Cu octahedra chains and the W octahedra chains are connected by sharing corners of the octahedra to form a three dimensional structure. $CuMoO_4$ exists in multiple crystal structures. The one that is isostructural to wolframite $CuWO_4$ has been referred to as Type-III structure [251, 252]. However, the Type-III structure is not thermodynamically stable at room temperature and atmospheric pressure [252]. The most stable $CuMoO_4$ phase is known as α-$CuMoO_4$, and a phase known as γ-$CuMoO_4$ is reported to also be more stable than Type-III $CuMoO_4$ [252]. Due to the overwhelming stability of the α-$CuMoO_4$ and γ-$CuMoO_4$ over Type-III $CuMoO_4$, solid solutions of $CuWO_4$ and $CuMoO_4$ (or $CuW_{1-x}Mo_xO_4$) having a wolframite structure can form as a pure phase only when the Mo content remains low (x <ca. 0.30) [253]. A further increase in Mo content resulted in the formation of α-CuMoO4 or γ-CuMoO4 as the major impurity phase. Because of this reason Mo-rich solid solutions of $CuW_{1-x}Mo_xO_4$ having a wolframite structure have not been prepared and examined previously. Our experimental collaborators have prepared $CuWO_4$ and $CuW_{1-x}Mo_xO_4$ (x=0.45-0.65) films as thin-film type electrodes using a newly developed electrochemical synthesis route. Due to the solution-based, soft synthesis nature, electrochemical synthesis has the possibility of forming thermodynamically unstable structures or compositions that may not be easily accessed by other means.

In terms of theoretical studies, the electronic structures of $CuWO_4$, $CuMoO_4$, and W-rich $CuW_{1-x}Mo_xO_4$ have been calculated with focus on their magnetic properties as these compounds are antiferromagnetic [251, 253]. However, the theoretical studies of the band edge composition of $CuWO_4$ to date in the literature did not reach a consensus on the interpretation of experiments [254, 255, 256]. For example, Ref. [254] has predicted $CuWO_4$ a semiconductor with an energy gap of 1.9 eV at the LDA level, without considering the anti-ferromagnetization (AFM) and spin polarization. However, Ref. [255] obtained a metallic solid of $CuWO_4$ at the LDA level with a paramagnetic configuration (PM); and a semiconductor with a small gap of about 0.5 eV with its AFM configuration, which is computed to be energetic favorable than PM configuration.

Experimentally $CuWO_4$ is known to have an antiferromagnetic ground state with Neel temperature of 23K [257], indicating $CuWO_4$ is paramagnetic at the room temperature. The determination of magnetic ordering in $CuWO_4$ has been rather complicated: four decades ago a powder neutron diffraction study showed that $CuWO_4$ undergoes a phase transition to a long range antiferromagnetic (AF) state at low

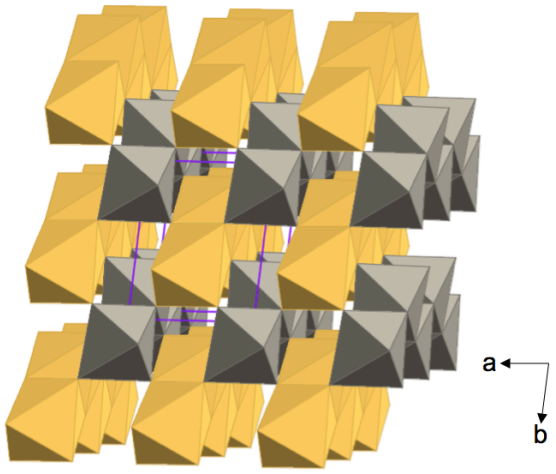

Figure 3.4.1: Wolframite structure of $CuWO_4$ showing the connectivity of Cu-centered (yellow) and W-centered (gray) octhedral.

temperature, accompanied by a doubling of its unit cell along the a-axis [258]. The three-dimensional (3D) AF ordering temperature of $CuWO_4$ was determined to be 23.0(2) K in the single-crystal neutron diffraction study, from the temperature dependence of the magnetic (1/2 0 0) reflection [257]. The low symmetry of this compound led to several models of magnetic ordering and to a large number of independent superexchange intrachain and super-superexchange interchain interaction parameters [259, 251].Similar to $CuWO_4$, $CuMoO_4$(III) is anti-ferromagnetic at zero temperature; with a unit cell doubled along the c-axis. The Neel temperature of $CuMoO_4$(III) is predicted to be 32K experimentally in Ref [260].

In addtion, calculations on Type-III $CuMoO_4$ and Mo-rich $CuW_{1-x}Mo_xO4$ have not previously explored the effect of Mo incorporation on band gap energies and band edge positions, which is critical to assess their potential for use in solar energy conversion. We report here, for the first time, the electronic band structures of Mo-rich $CuW_{1-x}Mo_xO_4$ electrodes with wolframite structure, and we show that they exhibit a significantly reduced band gap with respect to that of $CuWO_4$. We emphasize that the measured optical gaps and the computed DFT gaps are not directly comparable, quantitatively. The DFT gaps reported below are an approximation of the photoemission gap; to obtain the optical gap one should compute the exciton binding energy (E_b) and subtract it from the estimated photoemission gap. The value of E_b may be obtained, e.g., by solving the Bether-Salpeter Equation (BSE). However this approach is computationally very demanding, especially in the case of magnetic materials such as those considered here. Therefore we approximated E_b with the value we recently computed for RT-WO_3 [261], which turned out to be 0.15 eV. Thus the optical gap is expected to be at least 0.15 eV smaller than the photoemission gap

estimated by DFT. However in this study we are not interested in using theory to determine accurate values of photoemission or optical gaps but rather to give insights into how chemical doping (in particular Mo substitution of W) modifies the electronic properties of $CuWO_4$ (including its optical gap and band edge positions)

Recently, our experimental collaborators found that $CuW_xMo_{1-x}O_4$ solid solution (x=0.45-0.65) has a structure similar to that of $CuMoO_4$(III). Significant enhanced photocurrents have been observed compared with pure $CuWO_4$. The $CuW_xMo_{1-x}O_4$ solid solution has great potential as a photoanode material for water splitting solar cells.

3.4.2 Ab inito calculations of structral properties

We performed first-principles calculations within the framework of density functional theory (DFT) using the Quantum Espresso package [141] and different levels of theory (the spin polarized local density approximation (LDA),and the spin polarized generalized gradient approximation (GGA) using the PBE [143] functional, and the LDA+U approximation. Our LDA results (Table 3.15 and 3.16) for the structural properties of $CuWO_4$ and $CuMoO_4$ are in good agreement with experimental lattice constants with errors within 2%, whereas PBE overestimates the lattice constant by 2∼3%. Therefore, in our band structure and projected density of state calculations (PDOS), we primarily used the LDA. The lattice constants of $CuWO_4$ and $CuMoO_4$ optimized in the paramagnetic state have larger errors compared with experiments (3∼4%) than the ones optimized with anti-ferromagnetic ordering, consistent with theanti-ferromagnetic nature of $CuWO_4$ and $CuMoO_4$(III) found experimentally at low temperature. We used the lattice constants and geometries optimized with anti-ferromagnetic orderingin all calculations presented here, unless specified. The high symmetry points in the band structure plots are obtained from the online Bilbao Crystallographic Server [262] with space group $P\bar{1}$, because $CuWO_4$ and $CuMoO_4$ (III) lattices have triclinic symmetry. Norm-conversing Hartwigsen-Goedecker-Hutter (HGH) type pseudopotentials [158] were used in our calculations,including the 5s (4s) and 5p (4p) electrons of W (Mo) within the valence electrons; a kinetic energy cutoff of 140 Ry was used for the PW basis set. A (6x6x6) Monkhorst-Pack k-point grid was used for self-consistent ground state calculations and a (9x9x9) Monkhorst-Pack k-point grid was used for PDOS calculations.

We also found that the structure exhibiting AFM ordering has lower total energy than the PM ordered state: 0.36 eV/formula unit lower in the case of $CuWO_4$ and 0.27 eV/formula unit lower for $CuMoO_4$, in agreement with the experimental observation that $CuWO_4$ and $CuMoO_4$ exhibit AFM ordering at zero temperature.

Table 3.15: Equilibrium lattice parameters (a_0, b_0, c_0) of $CuWO_4$. LDA denotes results carried out within the Local Density Approximation [5] and anti-ferromagnetic ordering; LDA/noAFM denotes results carried out within the LDA without anti-ferromagnetic ordering; "PBE" denotes results carried out with the PBE [143] functional and anti-ferromagnetic ordering,"PBE/noAFM" denotes results carried out within the PBE without anti-ferromagnetic ordering; and "Exp1, Exp2, Exp3" denote experimental values from three different experimental papers [263, 257, 264]. β is the angle between the a and c axes, α is the angle between b and c, and γ is the angle between a and b.

Method	lattice parameters (Å)			Angles(°)		
	a_0	b_0	c_0	$\alpha(°)$	$\beta(°)$	$\gamma(°)$
LDA	4.614	5.751	4.855	92.12	92.05	84.49
LDA/noAF	4.529	5.636	4.890	90.33	90.51	88.91
PBE	4.807	5.981	4.909	91.94	93.30	81.74
PBE/noAF	4.815	6.038	4.942	92.77	94.37	80.27
Exp1. [263]	4.7095	5.8451	4.8849	88.30	92.50	97.20
Exp2. [257]	4.694	5.830	4.877	91.64	92.41	82.91
Exp3. [264]	4.7026	5.8389	4.8784	91.677	92.469	82.80

Table 3.16: Equilibrium lattice parameters (a_0, b_0, c_0) of $CuMoO_4$. LDA denotes results carried out within the Local Density Approximation and anti-ferromagnetic ordering; LDA/noAFM denotes results carried out within the LDA without anti-ferromagnetic ordering; "PBE" denotes results carried out with the PBE functional and anti-ferromagnetic ordering;"PBE/noAFM" denotes results carried out within the PBE without anti-ferromagnetic ordering; and "Exp" denotes experimental values [265]. β is the angle between the a and c axes, α is the angle between b and c, and γ is the angle between a and b.

Method	lattice parameters (Å)			Angles(°)		
	a_0	b_0	c_0	$\alpha(°)$	$\beta(°)$	$\gamma(°)$
LDA	4.581	5.753	4.844	91.45	91.37	84.01
LDA/noAF	4.535	5.650	4.855	90.65	90.65	87.03
PBE	4.861	6.031	4.939	91.66	93.78	79.27
PBE/noAF	4.818	6.044	4.947	92.28	94.21	79.52
Exp [265].	4.7152(2)	5.8399(2)	4.8583(2)	91.04(1)	92.43(1)	81.28(1)

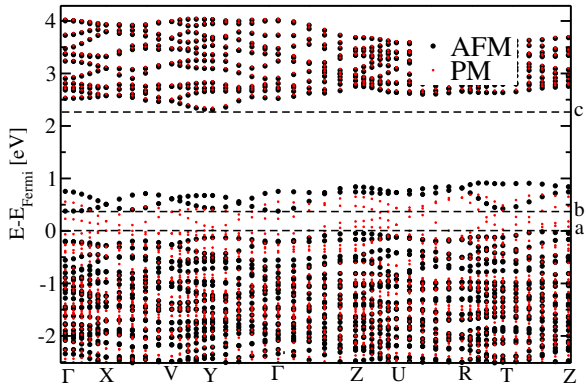

Figure 3.4.2: The band structure of $CuWO_4$ at the optimized geometry with a doubled unit cell along the a-axis. Black dot: anti-ferromagnetic (AFM); red star: paramagnetic (PM).

3.4.3 Electronic Structure of Pure $CuWO_4$

As mentioned earlier in the section, previous studies [254, 255] of the electronic structure of $CuWO_4$ present conflicting views. We have repeated calculations of the band structure of $CuWO_4$ at optimized geometry in an attempt to clarify exsiting discrepancies. Fig. 3.4.2 shows that the PM $CuWO_4$ band structure by LDA is slightly metallic -the top of the valence band maximum (VBM) is above the Fermi level. However, the AFM structure of $CuWO_4$ gives us a semiconductor with a small gap of about 0.4 eV. This result is in qualitative agreement with Ref [255], but not Ref [254]. Fig. 3.4.3 shows the PDOS of $CuWO_4$ with AFM ordering. A small gap appears between VBM and a sharp peak in proximity of the VBM. This peak will merge into the VB in the PM calculations (not shown). The top of valence bands as well as the sharp peak close to the VBM mainly consist of hybridized Cu 3d states and O 2p states; the states above 2.5 eV consist of hybridized W 5d states and O 2p states.

The small gap between states both having a mixed Cu 3d and O 2p character in PDOS (Fig. 3.4.3) of $CuWO_4$ with AFM corresponds to the small gap at AFM band structure(Fig. 3.4.2) between the few bands split from VB (the states labeled "b" in Fig. 3.4.2) and VBM (the states labeled "a" in Fig. 3.4.2). The small gap above VBM in the AFM band structure could be understood in a simple way by inspecting the crystal field splitting of d levels of Cu: as shown in Fig. 3.4.4, the octahedron crystal field first split the 5 d orbitals to double degenerate eg orbitals and triple degenerate t2g orbitals; then the JT effect splits the degeneracy of eg and t2g with elongated distortion of CuO_6. The splitting between two eg orbitals (one occupied and one half occupied) gives the gap between Cu d states. It was suggested that the

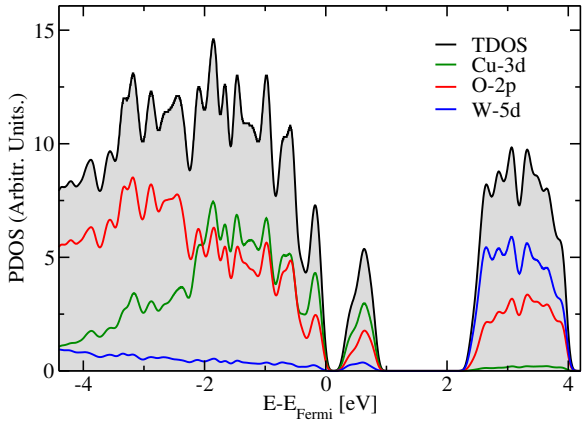

Figure 3.4.3: The Projected Density of States (PDOS) of $CuWO_4$ with AFM ordering as obtained at the optimized geometry with a doubled unit cell along the a-axis.

2.3 eV gap of $CuWO_4$ measured in Ref. [264] corresponds to the transition between Cu 3d-O 2p bonding and anti-bonding states [255, 256]. However we note that: (i) the position in energy of Cu-O states does not change with Mo doping (contrary to our experimental observation that Mo doping significantly decreases the optical gap of $CuWO_4$); (ii) the experimental flatband potential of $CuWO_4$ is very close to that of WO_3 [266], indicating that the CBM of $CuWO_4$ does have a substantial contribution from W 5d states; (iii) most importantly, experimental optical measurements reported the presence of a small absorption peak at 1.15 eV below the main absorption edge at 2.3 eV for $CuWO_4$, most likely due to Cu^{2+} d-d transition [267]. Our $CuWO_4$ and $CuMo_{0.65}W_{0.35}O_4$ electrodes also show this transition in the NIR-Vis absorption spectra measured by our experimental collaborators. Therefore we interpret the measured gap as corresponding to the transition from the Cu-O state labeled a in Fig. 3.4.2 and the state labeled c, originating predominantly from the hybrid W/Mo 5d/4d and O 2p states. The computed a $\rightarrow$ c gap (2.2 eV) is close to the measured one (2.3 eV).

following discussions This agreement with experiment may appear surprising due to the LDA tendency to underestimate band gaps. However we note that the minimum gap of the solid (usually underestimated within LDA) corresponds to the a $\rightarrow$ b transition, not to the a $\rightarrow$ c one. When we repeated our calculations using the LDA+U framework [109], we found that for both $CuWO_4$ and Type-III $CuMoO_4$ the Cu d-d gap is larger (0.8 eV at U=4 eV for Cu [255]) than that found at the LDA (0.4 eV) level of theory, in better agreement with experimental results (1.15 eV) [267], although the underestimate persisted. However, the position of the hybrid W/Mo d and O 2p states remained the same when using LDA +U ($\sim$2.2/1.6 eV). (We only applied a Hubbard U term to Cu because Cu^{2+} has unfilled 9 d electrons; U=4 eV

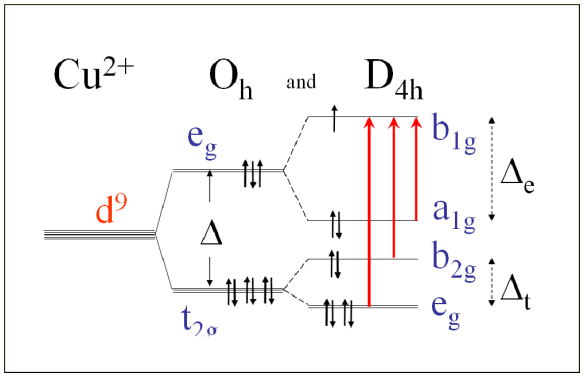

Figure 3.4.4: The 3d orbital splitting and electronic configuration of Cu^{+2} in $CuWO_4$ solid.

was chosen according to Ref. [255, 268]. We verified that increasing U to 7 eV did not significantly change the band structure.)

As measurements of absorption spectra and electric currents from electrochemical cells are mostly done at the room temperature which is above the Neel temperature of both $CuWO_4$ and $CuMoO_4$, the PM instead of AFM ordering should be considered in the calculations. However, the PM bandstructure shows metallicity at both LDA and LDA+U (not shown) level of theory, which seems to be in contradiction with the semiconductor properties of $CuWO_4$. This fact can be understood considering that both LDA and LDA+U are still static mean field theory, which can not handle PM insulators (such as V_2O_3 [269]); a higher level of theory such as dynamical mean field theory [269] is required which is a rather complicated many body method and out of the scope of this work. In addition, as DFT computes ground state properties at the zero temperature, this corresponds to the AFM ordering of $CuWO_4$ and $CuMoO_4$ experimentally at low temperature.

3.4.4 Electronic Strucutre of Pure $CuMoO_4$

Fig. 3.4.5 shows the AFM and PM bandstructures of $CuMoO_4$ at the fully optimized geometry. The anti-ferromagnetic band structure has a small gap ~0.4eV close to VBM; while the paramagnetic one is slightly metallic, with the top of valence residing slightly above the Fermi level, similar to the case of $CuWO_4$.

Similar to $CuWO_4$, we have also carried out LDA+U calculations for $CuMoO_4$ at U(Cu) = 4 eV as well as at U(Cu) = 7 eV. As shown in Fig. 3.4.6, by using LDA+U, the VBM decreased about 0.3 eV at U(Cu) = 4 eV compared with the LDA band structure (and the VBM decreased further with increasing the value of U), but the states above 1.5 eV stayed unchanged. This is because the VBM as well as the mid gap states at 0.5~1 eV above VBM are composed by hybrid Cu 3d and O 2p states,

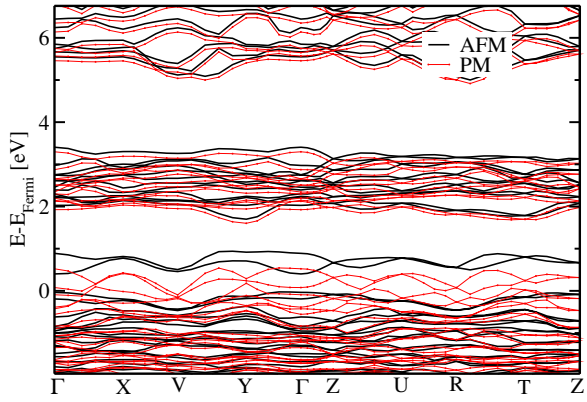

Figure 3.4.5: Band structure of $CuMoO_4$ with the fully optimized geometry at a doubled unit cell along the c-axis. Black curve: band structure computed with antiferromagnetization (AFM); red curve: band structure computed with paramagnetization (PM).

similar to the case of $CuWO_4$; and the states above 1.5 eV consist of Mo 4d and O 2p states. Since we applyed U to Cu only (which has unfilled d 9 electrons as Cu^{2+}, instead Mo has zero d electrons as Mo^{6+} in a simple ionic picture), Mo 4d and O 2p states are less affected by LDA+U calculations. The band structure has not been modified significantly by using LDA+U, which indicates LDA level of theory gives quanlitatively correct results for $CuWO_4$ and $CuMoO_4$ (the AFM ordering ground state and the insulating nature). As a result, the following discussions at section 3.4.5 are based on LDA.

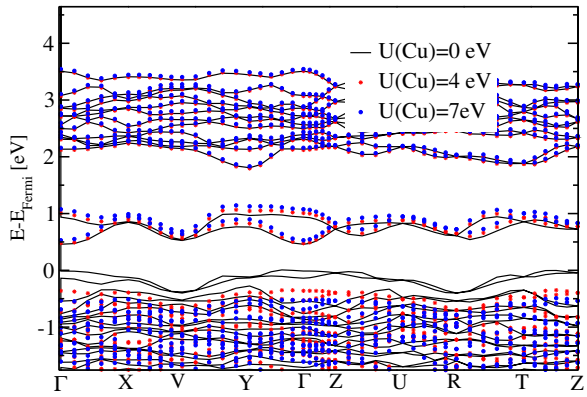

Figure 3.4.6: Band structure of Type-III CuMoO4, aligned by Mo 4s,4p core states, as obtained from LDA and LDA+U calculations (at U= 0, 4, 7 eV), respectively, with the fully optimized geometry at a doubled unit cell along the c-axis.

Table 3.17: Equilibrium lattice parameters (a_0, b_0, c_0) of $CuW_xMo_{1-x}O_4$ Solid Solutions (x=0.5 and 0.75), pure $CuWO_4$ and $CuMoO_4$. β is the angle between the a and c axes, α is the angle between b and c, and γ is the angle between a and b. PM denotes paramagnetic ordering; AFM denotes anti-ferromagnetic ordering.

Method	lattice parameters (Å)			Angles(°)		
	a_0	b_0	c_0	$\alpha(°)$	$\beta(°)$	$\gamma(°)$
$CuMo_{0.5}W_{0.5}O_4$-PM	4.529	5.601	4.892	89.97	90.06	90.77
$CuMo_{0.75}W_{0.25}O_4$-PM	4.559	5.683	4.854	91.26	91.12	85.92
$CuWO_4$-PM	4.529	5.636	4.890	90.33	90.51	88.91
$CuMoO_4$-PM	4.535	5.650	4.855	89.35	90.65	87.03
$CuMo_{0.5}W_{0.5}O_4$-AFM	4.605	5.739	4.844	91.80	91.68	84.23
$CuMo_{0.75}W_{0.25}O_4$-AFM	4.605	5.737	4.843	91.77	91.65	84.17
$CuWO_4$-AFM	4.614	5.751	4.855	92.12	92.05	84.49
$CuMoO_4$-AFM	4.581	5.753	4.844	91.45	91.37	84.01

3.4.5 Electronic Structure of $CuW_xMo_{1-x}O_4$ Solid Solutions

Our experimental collaborators have found that the gap of the $CuW_xMo_{1-x}O_4$ Solid Solution is significantly smaller than that of $CuWO_4$. In order to understand this experimental observation, we have performed first-principles calculations for $CuW_xMo_{1-x}O_4$ solid solution (x=0.5 and 0.75) similar to pure $CuWO_4$ and $CuMoO_4$. The lattice constants and internal geometry of the $CuW_xMo_{1-x}O_4$ solid solution (x=0.5 and 0.75) were fully optimized using the LDA functional at both PM and AFM configurations as shown in Table 3.17. It has been shown experimentally by the neutron powder diffraction that $CuW_xMo_{1-x}O_4$ solid solution is antiferromagnetic with a magnetic unit cell changing with respect to the Mo concentration. Its Neel temperature are determined to fall between 22.5 to 32.0 K [260]. We used the magnetic unit cell doubled along the c axis for $CuW_xMo_{1-x}O_4$ in our calculations similar to $CuMoO_4$ for simplicity, since the experimental magnetic structure of $CuW_xMo_{1-x}O_4$ is unknown. For comparison, the optimized lattice constants of $CuWO_4$ and $CuMoO_4$ are listed in Table 3.17 together with those of the solid solution. Our calculations show that the lattice parameters of $CuMo_xW_{1-x}O_4$ (x = 0.5) differ by less than 1% from those of $CuWO_4$ and Type-III $CuMoO_4$. This result is not unexpected, given the similarity between the $CuWO_4$ and Type-III $CuMoO_4$ crystal structures and between the atomic sizes of iso-electronic W and Mo. This result also indicates that the observed lowering of the optical bandgap of the solid solutions, with respect to that of the constituents, does not stem from geometrical changes of the $CuWO_4$ lattice upon Mo incorporation.

Fig. 3.4.7 shows the band structures of $CuWO_4$, Type-III $CuMoO_4$ and of the

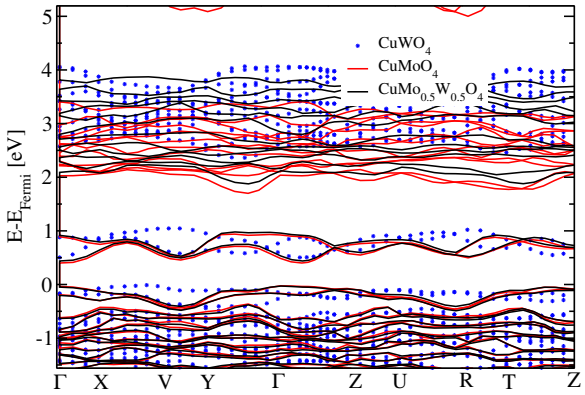

Figure 3.4.7: Band structures obtained from LDA calculations with the optimized geometries at AFM ordering for $CuW_{0.5}Mo_{0.5}O_4$ solid solution (black curve), $CuMoO_4$ (red curve) and $CuWO_4$ (blue dot), aligned by W(Mo) 5s,5p(4s,4p) core states.

$CuMo_{0.5}W_{0.5}O_4$ solid solution. The top of the valence band (VBM) is mainly composed of hybridized Cu 3d and O 2p states, as shown in Fig. 3.4.8, which displays the projected density of states (PDOS) of electrons. The VBM is at very similar energies in each of the three solids, although the band curvatures differ, mainly because of the different magnetic ordering of the Cu magnetic moments in $CuWO_4$ and Type-III $CuMoO_4$ (i.e. in the case of $CuWO_4$, the magnetic moments within one zig-zag chain and one layer are all parallel to each other, but antiparallel to those belonging to chains in an adjacent layer. On the other hand, in Type-III $CuMoO_4$ parallel and antiparallel spin pairs are alternating within one zig-zag chain) [265]. Although the band gaps of the three solids shown in Fig. 3.4.7 are all indirect, in Type-III $CuMoO_4$ the difference in energy between the indirect and direct band gaps [along T (0,0.5,0.5) to Z (0,0,0.5)] is smaller than in $CuWO_4$, which may explain the generally enhanced absorption of the Mo-rich $CuMo_xW_{1-x}O_4$ samples. We note that, at variance with the AFM ordering, in the case of PM ordering, both the position and the curvature of the VBM are the same in the three solids.

To understand the relationship between the band gap reduction and the Mo concentration, we analyzed the PDOS of the $CuW_{0.5}Mo_{0.5}O_4$ solid solution, shown in Fig. 3.4.8. The conduction band minimum is composed of Mo 4d states and O 2p states, while hybrid W 5d states and O 2p states are located higher in energy than hybrid Mo 4d and O 2p states. This indicates the Mo 4d states have lower energy than W 5d states. Since the CBM corresponding to the main absorption edge at 2.3 eV is composed by W 5d and O 2p hybrid states in $CuWO_4$ (Mo 4d and O 2p hybrid states in $CuMoO_4$), the molybdate exhibits the lowest CBM due to the lower energy of Mo 4d states, with respect to W 5d states; increasing the content of Mo in $CuMo_xW_{1-x}O_4$ lowers its CBM and decreases the optical gap, as observed ex-

perimentally. Comparing the band structure of the $CuW_xMo_{1-x}O_4$ solid solution at two different concentrations x=0.5 and x=0.75, we found the conduction band shifts down by ∼0.1 eV with increasing concentration of Mo, which is consistent with the experimental findings. We note the lower of CBM for $CuW_{0.25}Mo_{0.75}O_4$ solid solution (0.6 eV) is overestimated compared with the experimental gap reduction (0.3 eV). This difference mainly sterms from the difference between the optimized geometry and the corresponding experiment one i.e. at the experimental geometry the CBM between pure $CuWO_4$ and $CuMoO_4$ has a difference of 0.2 eV, smaller than the one at their corresponding optimized geometry. We note that the conduction bands of the three materials have rather similar curvatures(see Fig. 3.4.7), since both W and Mo are isoelectronic, they do not have magnetic moments and they have similar atomic sizes.

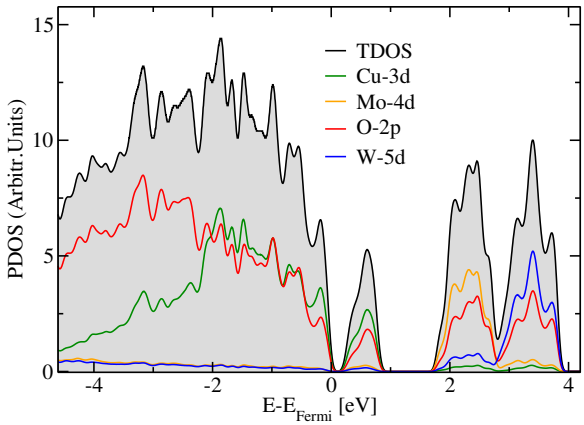

Figure 3.4.8: The Projected Density of States (PDOS) of the $CuW_{0.5}Mo_{0.5}O_4$ solid solution with the optimized LDA geometry at AFM ordering.

3.4.6 Incident photo-to-current conversion efficiencies of $CuWO_4$ and $CuW_{1-x}Mo_xO_4$

In order to confirm that the increase in photocurrent is due to the enhanced photon absorption, the incident photon-to-current conversion efficiencies (IPCEs) of $CuWO_4$ and $CuW_{0.35}Mo_{0.65}O_4$ were compared in Fig. 3.4.9, measured by our experimental collabrators. While the photocurrent onset of $CuWO_4$ appears at 560 nm, the photocurrent onset of $CuW_{0.35}Mo_{0.65}O_4$ was shifted to 620 nm. This shift agrees well with the bandgap reduction observed in the UV-vis absorption spectra. This result clearly demonstrates that the gain in photon absorption in the region of 560 nm-620 nm directly results in the gain in photocurrent. Fig. 3.4.9(c) also shows that in addition to the 560 nm - 620 nm region, $CuW_{0.35}Mo_{0.65}O_4$ exhibits much higher IPCEs

in the entire visible range. Since the IPCE is measured with back-side illumination (i.e., the light was illuminated through the FTO substrate), the observed difference in IPCE cannot be due to the difference in surface morphology of the $CuWO_4$ and $CuW_{0.35}Mo_{0.65}O_4$ electrodes, but due to the difference in optical properties of these electrodes.

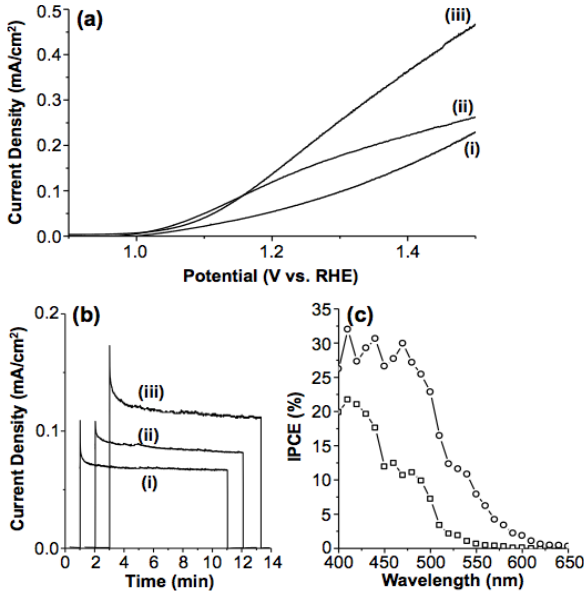

Figure 3.4.9: (a) J-V characteristics and (b) Photocurrent measurement at 1.21 V vs. RHE (0.6 V vs. Ag/AgCl) of (i) $CuWO_4$, (ii) $CuW_{0.55}Mo_{0.45}O_4$, and (iii) $CuW_{0.35}Mo_{0.65}O_4$ measured in a 0.1 M phosphate buffer (pH 7) under AM 1.5G, 100 mW/cm2 illumination. (c) IPCEs of $CuWO_4$ (square) and $CuW_{0.35}Mo_{0.65}O_4$ (circle) measured in in a 0.1 M phosphate buffer (pH 7) with an applied bias of 1.61 V vs. RHE (1.0 V vs. Ag/AgCl).

In summary, in this section we obtained experimental and theoretical result on $CuW_{1-x}Mo_xO_4$ [270]. The former were obtained by our collaborators in Prof. K-S.Choi's group. $CuWO_4$ and solid solutions of $CuWO_4$ and $CuMoO_4$ films were prepared by a new electrochemical route, which allowed for the formation of Mo-rich $CuW_{1-x}Mo_xO_4$ films ($x > 0.4$) for the first time. The incorporation of Mo to the $CuWO_4$ lattice decreased the bandgap energy and increased photon absorption in the visible light region, which resulted in a significant enhancement in photocurrent generation for water oxidation. The effect of Mo incorporation on the electronic band calculations were elucidated using first principles calculations, revealing that the bandgap reduction of $CuW_{1-x}Mo_xO_4$ is due to the shift of the main absorption edge CB position to the lower energy. This may not be entirely beneficial for overall solar water splitting since the difference between the water reduction potential and the main absorption edge CB position of the photoanode (i.e., $CuWO_4$ or

$CuW_{1-x}Mo_xO_4$) will have to be compensated by other mechanisms (e.g. applying an external bias). However, the enhanced photon absorption as well as inexpensive and facile synthesis of $CuW_{1-x}Mo_xO_4$ systems will be desirable for driving various other photoelectrochemical reactions (e.g. photoreduction or oxidation of inorganic or organic pollutants) in a much more efficient manner with further optimizations in their surface areas, carrier densities, and charge transport properties. Our study also suggests that there may be many unexplored new compositions that can achieve ideal bandgap energies for solar energy conversion in ternary oxide systems.

Chapter 4

Absorption spectra of semiconductor photoelectrodes

In this chapter we will discuss the computation of absorption spectra of semiconducting photoelectrode obtained by solving the Bethe-Salpeter Equation, and we separate our discussion into bulk systems and nanostructures. We studied WO_3 and silicon.

With a band gap of 1.12 eV, p-type Si (p-Si) is a desirable small band gap absorber for use as photocathode in dual band gap p/n-PEC water splitting configurations [271]. Several groups demonstrated that a p-Si photocathode, combined with metal catalysts, can be used to produce H_2 electrochemically with a reduced voltage [272, 273]. For example, photon to hydrogen conversion efficiencies as high as 6% was reported for p-Si decorated with Pt nanoparticles [273]. Other Earth abundant metal catalysts such as Ni or Ni-Mo can be alternatives to Pt [274] to provide similar photoelectrode efficiencies when deposited onto Si microwire arrays. BiPt alloys [275] was also shown to have improved catalytic activity to hydrogen evolution reaction performance compared with pure Pt. Nanostructured electrode morphologies can be used to address some of the intrinsic limitations of bulk materials for PEC applications [276]. The most obvious advantage of a nanostructured morphology is the increase of surface to volume ratio. The increase in the number of surface sites greatly enhances the overall charge transfer kinetics at the semiconductor/electrolyte interface and relaxes catalytic activity requirements. The second advantage is the shorter diffusion path lengths for the photogenerated charge carriers in one dimensional (1D) nanostructures. For example, in a traditional planar device, photogenerated carriers must cross the entire thickness of the cell in order to be collected before recombination. The cell thickness is dictated by how much material is necessary to absorb the incoming light. By using nanowires, the direction of light absorption and the direction of carrier collection is orthogonalized. For high-aspect ratio nanowires (i.e, wires having a high length/radius ratio), the length necessary for full optical absorption can be readily obtained, while the distance over which carriers are collected can be minimized, being only the radius of the nanowire; such a design offers the potential

for efficient charge-carrier collection from even very impure, low diffusion length materials [2]. Similar advantages are offered by nanostructures based on cauliflower-type morphologies or randomly packed spheres [277, 244]. The third possible advantage of using nanostructured materials is the so called quantum confinement effect. It is known [278] that spatial confinement of charge carriers to a volume that is less than their De Broglie wavelength results in a widening of the band gap. Even though the resulting blue shift of the absorption spectrum is usually not desirable for PEC absorbers, the widening of the band gap could be designed to shift the conduction or valence band edge toward ideal directions (band edge positions that straddle the water reduction and oxidation potentials) [279, 280], thus decreasing the required bias potential and increasing the solar to hydrogen conversion efficiency.

In the next section we describe calculations of absorption spectra starting from bulk systems and then we will focus on nanowires.

4.1 Absorption spectra of bulk systems

Two approaches widely used in the literature to compute *ab initio* optical absorption spectra are time-dependent functional theory (TDDFT) [12] and many-body perturbation theory (MBPT) [16]. When local or semi-local exchange-correlation functionals are used, time-dependent density functional theory may be applied to relatively large systems (up to thousands of electrons) and it has been proven to be accurate for several molecules. However, the most commonly used local approximations for the TDDFT kernel poorly describe the optical properties of extended periodic solids and nanostructures [16]. Within MBPT, the GW approximation (where G indicates the single-particle Green's function and W the screened Coulomb potential) has been used to compute quasi-particle energies and the Bethe-Salpeter equation (BSE) solved to compute optical spectra. The GW/BSE approach is computationally more expensive than TDDFT but it overcomes some of the limitations of local TDDFT, e.g., in the description of excitons in periodic systems [28, 281, 29, 16] and of charge transfer excitations in molecules [33]. Standard techniques to solve the BSE make use of an electron-hole basis set [29], that requires the explicit calculation of a large number of unoccupied electronic states, and the evaluation of a large number of exchange integrals between valence and conduction states.

In our group we proposed a method to solve the BSE that does not require the explicit calculation of empty states [33]. This has been obtained in chapter 2. This approach combines ideas proposed in the context of TDDFT [89, 66] and techniques to represent the dielectric matrix [60, 61] based on density functional perturbation theory [53]. The evaluation of the BSE kernel involves a number of orbitals equal to the number of occupied states (N_v) and numerically it scales as ground-state Hartree-Fock calculations (see Sec. 4.1.1). The approach developed in Ref. [33] makes efficient use of iterative solvers and matrix by vector multiplications are performed by using

fast Fourier transform techniques, without building and storing explicitly neither the BSE Hamiltonian nor dielectric matrices.

In this chapter we present a generalization of the formalism of Ref. [33] to periodic systems, and thus we include proper integrations over the first Brillouin zone. The method is then applied to the study of the optical properties of bulk silicon, carbon diamond and cubic silicon carbide. The convergence with respect to several numerical parameters and the comparison with previous results [281, 28, 29] are extensively discussed.

Below we review the BSE formalism presented for periodic systems and in Appendix 6.4 we give some details of the implementation of time-reversal symmetry operations.

4.1.1 Solution of the Bethe-Salpeter equation for periodic systems

The density matrix perturbation theory formulation of the BSE has been introduced in chapter 2. Here we present in detail its extension to periodic systems. Because of several formal analogies, the derivation given below can be easily extended to the TDDFT formulation presented in Refs. [89, 66, 101], including not only (semi-)local exchange-correlation functionals but also hybrid functionals.

As shown in chapter 2, the starting point of our derivation is the quantum-Liouville equation for density matrices written in the Coulomb-hole plus screened-exchange (COHSEX) approximation [42]:

$$i\frac{d\hat{\rho}_{\mathbf{k}}(t)}{dt} = \left[\hat{H}_{COHSEX}(t), \hat{\rho}_{\mathbf{k}}(t)\right], \tag{4.1.1}$$

where the square brackets indicate commutators and a hat denotes quantum-mechanical operators; within a real space representation, $\rho_{\mathbf{k}}(\mathbf{r},\mathbf{r}',t) = \sum_v \phi_{v\mathbf{k}}(\mathbf{r},t)\phi^*_{v\mathbf{k}}(\mathbf{r}',t)$ and the density matrix is given by:

$$\rho(\mathbf{r},\mathbf{r}',t) = \sum_{\mathbf{k}\in BZ} w_{\mathbf{k}}\rho_{\mathbf{k}}(\mathbf{r},\mathbf{r}',t) = \sum_v \sum_{\mathbf{k}\in BZ} w_{\mathbf{k}}\phi_{v\mathbf{k}}(\mathbf{r},t)\phi^*_{v\mathbf{k}}(\mathbf{r}',t), \tag{4.1.2}$$

$\mathbf{k}$ denotes a point in the Brillouin zone (BZ) and $\phi_{v\mathbf{k}}(\mathbf{r},t)$ are single particle occupied Bloch orbitals. In the following we will adopt the notation $\rho(\mathbf{r},t)$ to indicate $\rho(\mathbf{r},\mathbf{r},t)$. In Eq. 4.1.2 we have substituted the integral over the BZ with a summation over a discrete set of k-points:

$$\frac{1}{\Omega_{BZ}}\int_{\Omega_{BZ}} d\mathbf{k} \longrightarrow \sum_{\mathbf{k}\in BZ} w_{\mathbf{k}} \tag{4.1.3}$$

where $w_{\mathbf{k}}$ weighs the contribution of each k-point $\mathbf{k}$ and Ω_{BZ} is the BZ volume.

The time-dependent quasi-particle Hamiltonian operator applied to a valence

state, in Hartree atomic units and within the COHSEX approximation is:

$$\int \hat{H}_{COHSEX}(\mathbf{r},\mathbf{r}',t)\phi_{v\mathbf{k}}(\mathbf{r}',t)\,d\mathbf{r}' = \left(-\frac{1}{2}\nabla^2 + v_H(\mathbf{r},t) + v_{ext}(\mathbf{r},t)\right)\phi_{v\mathbf{k}}(\mathbf{r},t) + \int \Sigma_{COHSEX}(\mathbf{r},\mathbf{r}',t)\phi_{v\mathbf{k}}(\mathbf{r}',t)d\mathbf{r}', \quad (4.1.4)$$

where v_{ext} is an external time-dependent periodic potential,

$$v_H(\mathbf{r}) = \int \rho(\mathbf{r}',t)v(\mathbf{r},\mathbf{r}')d\mathbf{r}' \quad (4.1.5)$$

is the Hartree potential, and $\Sigma_{COHSEX} = \Sigma_{COH} + \Sigma_{SEX}$ is the self-energy in the COHSEX approximation

$$\int \Sigma_{COH}(\mathbf{r},\mathbf{r}')\phi_{v\mathbf{k}}(\mathbf{r}',t)d\mathbf{r}' = \frac{1}{2}\int \delta(\mathbf{r}-\mathbf{r}')W_p(\mathbf{r}',\mathbf{r};\mathbf{k})\phi_{v\mathbf{k}}(\mathbf{r}',t)d\mathbf{r}' \quad (4.1.6)$$

$$\int \Sigma_{SEX}(\mathbf{r},\mathbf{r}',t)\phi_{v\mathbf{k}}(\mathbf{r}',t)d\mathbf{r}' = -\sum_{v'}\sum_{\mathbf{k}'\in BZ}\int \phi_{v'\mathbf{k}'}(\mathbf{r},t)W(\mathbf{r}',\mathbf{r};\mathbf{k}-\mathbf{k}')\phi^*_{v'\mathbf{k}'}(\mathbf{r}',t)\phi_{v\mathbf{k}}(\mathbf{r}',t)d\mathbf{r}' \quad (4.1.7)$$

In Eqs. 4.1.5-4.1.7 $v(\mathbf{r},\mathbf{r}')$ is the Coulomb potential, $W(\mathbf{r}',\mathbf{r};\mathbf{k}-\mathbf{k}') = \int \epsilon^{-1}(\mathbf{r}',\mathbf{r}'';\mathbf{k}-\mathbf{k}')v(\mathbf{r}'',\mathbf{r})d\mathbf{r}''$ is the statically screened Coulomb interaction, and $W_p = W - v$. We note that, since the Hamiltonian (Eq. 4.1.4) depends on the density matrix $\hat{\rho}$, the set of equations 4.1.1 for different $\mathbf{k}$ points are coupled; this would be so also for DFT Hamiltonians in the (semi-)local approximation, that depend only on the charge density.

Linearization of Eq. (4.1.1) with respect to v_{ext} leads to

$$i\frac{d\hat{\rho}'_{\mathbf{k}}(t)}{dt} = \mathcal{L}\cdot\hat{\rho}'_{\mathbf{k}}(t) + [\hat{v}'_{ext}(t),\hat{\rho}^{\circ}_{\mathbf{k}}]\,, \quad (4.1.8)$$

$$\mathcal{L}\cdot\hat{\rho}'_{\mathbf{k}}(t) = \left[\hat{H}^{\circ}_{COHSEX},\hat{\rho}'_{\mathbf{k}}(t)\right] + [\hat{v}'_H[\hat{\rho}'](t),\hat{\rho}^{\circ}_{\mathbf{k}}] + \left[\hat{\Sigma}'[\hat{\rho}'](t),\hat{\rho}^{\circ}_{\mathbf{k}}\right], \quad (4.1.9)$$

where variables with superscript "$\circ$" represent unperturbed quantities, and those with prime denote linear variations. Within a real space representation, the charge response $\hat{\rho}' = \hat{\rho} - \hat{\rho}^{\circ}$ is given by

$$\rho'(\mathbf{r},\mathbf{r}',t) = \sum_{\mathbf{k}\in BZ} w_{\mathbf{k}}\rho'_{\mathbf{k}}(\mathbf{r},\mathbf{r}',t) = \sum_{v}\sum_{\mathbf{k}\in BZ} w_{\mathbf{k}}\left[\phi^{\circ}_{v\mathbf{k}}(\mathbf{r})\phi'^{*}_{v\mathbf{k}}(\mathbf{r}',t) + \phi'_{v\mathbf{k}}(\mathbf{r},t)\phi^{\circ *}_{v\mathbf{k}}(\mathbf{r}')\right]. \quad (4.1.10)$$

Eq. 4.1.10 denotes the linear variation of the density matrix and $\hat{\rho}'_{\mathbf{k}} = \hat{\rho}_{\mathbf{k}} - \hat{\rho}^{\circ}_{\mathbf{k}}$ is the contribution to $\hat{\rho}'$ of the k-point $\mathbf{k}$. We note that $\hat{v}'_H$ and $\hat{\Sigma}'$ depend on the perturbed density matrix $\hat{\rho}'$. In Eq. 4.1.9 a non-Hermitian operator $\mathcal{L}$ acting on $\hat{\rho}'_{\mathbf{k}}$ has been defined, which is known as Liouvillian super-operator [89, 66, 33], as its action is

defined on a space of operators. By Fourier transforming Eq. 4.1.8 into the frequency domain, one obtains

$$(\omega - \mathcal{L}) \cdot \hat{\rho}'_{\mathbf{k}}(\omega) = [\hat{v}'_{ext}(\omega), \hat{\rho}^{\circ}_{\mathbf{k}}] \,. \tag{4.1.11}$$

This equation, derived here in the context of the BSE, is formally the same within the density functional perturbation theory (DFPT) formulation of TDDFT (see e.g. Eq. (14) in Ref. [66]), but a different definition of the Liouvillian $\mathcal{L}$ is used in the two cases.

The solution of Eq. 4.1.11 yields the perturbed density matrix in the frequency domain:

$$\rho'(\mathbf{r}, \mathbf{r}', \omega) = \sum_{\mathbf{k} \in BZ} w_{\mathbf{k}} \rho'_{\mathbf{k}}(\mathbf{r}, \mathbf{r}', \omega) = \sum_{v} \sum_{\mathbf{k} \in BZ} w_{\mathbf{k}} \left[\phi^{\circ}_{v\mathbf{k}}(\mathbf{r}) \phi'^{*}_{v\mathbf{k}}(\mathbf{r}', -\omega) + \phi'_{v\mathbf{k}}(\mathbf{r}, \omega) \phi^{\circ *}_{v\mathbf{k}}(\mathbf{r}') \right] . \tag{4.1.12}$$

Eq. 4.1.12 shows that $\rho'(\omega)$ is fully determined by the set of the N_v unperturbed occupied states $\phi^{\circ *}_{v\mathbf{k}}$ and by the two sets of N_v perturbed orbitals $\phi'^{*}_{v\mathbf{k}}(\mathbf{r}', -\omega)$ and $\phi'_{v\mathbf{k}}(\mathbf{r}, \omega)$, orthogonal to the occupied state subspace. We note that $\rho'(\omega)$, unlike $\rho'(t)$ in Eq. 4.1.10, is a non-Hermitian operator. In order to simplify the numerical implementation, we assume time-reversal symmetry holds by imposing $v'_{ext}(\mathbf{r}, t) = v'_{ext}(\mathbf{r}, -t)$ in Eq. 4.1.9. As a consequence $v'_{ext}(\mathbf{r}, \omega)$ is a real function and $\phi'_{v-\mathbf{k}}(\mathbf{r}, t) = \phi'^{*}_{v\mathbf{k}}(\mathbf{r}, -t)$, implying $\phi'_{v-\mathbf{k}}(\mathbf{r}, \omega) = \phi'^{*}_{v\mathbf{k}}(\mathbf{r}, \omega)$ and $\phi'_{v-\mathbf{k}}(\mathbf{r}, -\omega) = \phi'^{*}_{v\mathbf{k}}(\mathbf{r}, -\omega)$. Therefore, assuming $v'_{ext}(\mathbf{r}, t) = v'_{ext}(\mathbf{r}, -t)$ yields a real $\rho'(\omega)$. This assumption does not limit the generality of our approach, since we are interested in computing the macroscopic dielectric function of bulk systems (see Eqs. 4.1.13-4.1.16 below); the latter is an intrinsic property of the system and does not depend on the specific time or ω dependence of the applied electric field. Furthermore since we can perform the $\mathbf{k} \leftrightarrow -\mathbf{k}$ transformation by a complex conjugate operation, the total number of k-points included in Eqs. 4.1.11-4.1.12 can be significantly reduced. Details on the time-reversal symmetry operations are given in Appendix 6.4.

The absorption spectrum of a solid is related to the imaginary part of the *macroscopic dielectric function* ε_M defined by the equation (see also [53]):

$$E_{0i}(\omega) = E_i(\omega) + 4\pi P_i(\omega) = \Sigma_j \varepsilon^{ij}_M(\omega) E_j(\omega) \tag{4.1.13}$$

where the indexes i and j indicate Cartesian components, $\mathbf{E}_0$ is the applied external electric field, $\mathbf{E}$ is the screened field and $\mathbf{P}$ is the electronic polarization induced by $\mathbf{E}$. In order to compute ε_M, it is convenient to start by setting the value of the screened electric field $\mathbf{E}$ [53]. By introducing the potential

$$v'_{ext} = -\mathbf{E}(\omega) \cdot \mathbf{r} \tag{4.1.14}$$

in Eq. 4.1.11, and expressing the polarization in terms of the density operator,

$$P_i(\omega) = -\frac{1}{V}\sum_{\mathbf{k}\in BZ} w_{\mathbf{k}} Tr(\hat{r}_i\hat{\rho}'_{\mathbf{k}}) = -\frac{1}{V}Tr(\hat{r}_i\hat{\rho}'), \tag{4.1.15}$$

from Eq. 4.1.13 one has

$$\varepsilon_M^{ij}(\omega) = \delta_{ij} - \frac{4\pi}{V}\sum_{\mathbf{k}\in BZ} w_{\mathbf{k}} \left\langle \hat{r}_i|(\omega - \mathcal{L} + i\eta)^{-1}\cdot[\hat{r}_j, \hat{\rho}^{\circ}_{\mathbf{k}}]\right\rangle, \tag{4.1.16}$$

where V is the crystal volume, η is a positive infinitesimal, and we have written the scalar product of two operators A and B as $\langle\hat{A}|\hat{B}\rangle \equiv Tr(\hat{A}^{\dagger}\hat{B})$. As already discussed in the Appendix of Ref. [33], the definition of ϵ_M in Eq. 4.1.16 is equivalent to the definition of the BSE macroscopic dielectric function given in Ref. [16] (Eqs. 2.23 and B26). However the formulation of Ref. [33] was so far applicable only to molecules. In addition, the position operator in Eq. 4.1.14 is ill defined in periodic boundary conditions; this problem can be overcome within perturbation theory, following Refs. [53, 282].

The numerical solution of Eq. 4.1.11 and Eq. 4.1.16 requires a basis set for $\hat{\rho}'$. From Eq. 4.1.12 it follows that only the elements of $\hat{\rho}'$ between unperturbed occupied and empty orbitals are different from zero. The use of those orbitals as a basis set leads to the so called electron-hole (e-h) representation, widely used in the literature to solve the BSE [28, 281, 29]. This approach requires the explicit calculation of empty electronic states and convergence with respect to their number has to be carefully checked. By using the projector operators $\hat{Q}_{\mathbf{k}}$ onto the unperturbed empty state subspace, explicit calculations of empty states may be avoided [33]: $\hat{Q}_{\mathbf{k}} = \hat{I} - \hat{P}_{\mathbf{k}} = \hat{I} - \sum_v |\phi^{\circ}_{v\mathbf{k}}\rangle\langle\phi^{\circ}_{v\mathbf{k}}|$, where $\hat{P}_{\mathbf{k}}$ is the projector onto the occupied state subspace for a fixed $\mathbf{k}$ in the first BZ and $\hat{I}$ is the identity operator. The evaluation of $\hat{Q}_{\mathbf{k}}$ does not require the explicit calculation of empty states. Since Bloch states corresponding to different k-points are orthogonal, the projection can be preformed independently for each k-point. Within this formalism a generic operator $\hat{A}$ can be represented by a set of $2\times \mathrm{N}_v \times \mathrm{N}_{\mathbf{k}}$ orbitals that are defined in the following way:

$$|a_{v\mathbf{k}}\rangle = \hat{Q}_{\mathbf{k}}\,\hat{A}\,|\phi^{\circ}_{v\mathbf{k}}\rangle, \tag{4.1.17}$$

$$\langle b_{v\mathbf{k}}| = \langle\phi^{\circ}_{v\mathbf{k}}|\,\hat{A}\,\hat{Q}_{\mathbf{k}}, \tag{4.1.18}$$

where the index v runs from 1 to the number of occupied bands N_v, while $\mathbf{k}$ is a point of the discrete mesh used to perform the integral in the first BZ. If $\hat{A} = \hat{\rho}'$ we have $a_{v\mathbf{k}}(\mathbf{r}) = \phi'_{v\mathbf{k}}(\mathbf{r},\omega)$ and $b_{v\mathbf{k}}(\mathbf{r}) = \phi'_{v\mathbf{k}}(\mathbf{r},-\omega)$. Within this representation the operator $\mathcal{L}$ takes the form:

$$\mathcal{L} = \begin{pmatrix} \mathcal{D} + 2\mathcal{K}^{1x} - \mathcal{K}^{1d} & 2\mathcal{K}^{2x} - \mathcal{K}^{2d} \\ -2\mathcal{K}^{2x} + \mathcal{K}^{2d} & -\mathcal{D} - 2\mathcal{K}^{1x} + \mathcal{K}^{1d} \end{pmatrix}, \tag{4.1.19}$$

where $\mathcal{D}$, the exchange terms $\mathcal{K}^{1x}$ and $\mathcal{K}^{2x}$ and the direct terms $\mathcal{K}^{1d}$ and $\mathcal{K}^{2d}$ are defined as:

$$\sum_{v'}\sum_{\mathbf{k}'\in BZ}\mathcal{D}_{v\mathbf{k},v'\mathbf{k}'}\,|a_{v'\mathbf{k}'}\rangle = \sum_{v'}\sum_{\mathbf{k}'\in BZ}(\hat{H}^{\circ}_{COHSEX}-\epsilon_{v'\mathbf{k}'})\,\delta_{vv'}\,\delta_{\mathbf{k}\mathbf{k}'}|a_{v'\mathbf{k}'}\rangle, \tag{4.1.20}$$

$$\sum_{v'}\sum_{\mathbf{k}'\in BZ}\mathcal{K}^{1x}_{v\mathbf{k},v'\mathbf{k}'}\,|a_{v'\mathbf{k}'}\rangle = \sum_{v'}\sum_{\mathbf{k}'\in BZ}w_{\mathbf{k}'}\hat{Q}_{\mathbf{k}}\left(\int\frac{1}{|\mathbf{r}-\mathbf{r}'|}\phi^{\circ *}_{v'\mathbf{k}'}(\mathbf{r}')a_{v'\mathbf{k}'}(\mathbf{r}')d\mathbf{r}'\right)|\phi^{\circ}_{v\mathbf{k}}\rangle, \tag{4.1.21}$$

$$\sum_{v'}\sum_{\mathbf{k}'\in BZ}\mathcal{K}^{2x}_{v\mathbf{k},v'\mathbf{k}'}\,|b_{v'\mathbf{k}'}\rangle = \sum_{v'}\sum_{\mathbf{k}'\in BZ}w_{\mathbf{k}'}\hat{Q}_{\mathbf{k}}\left(\int\frac{1}{|\mathbf{r}-\mathbf{r}'|}b^{*}_{v'\mathbf{k}'}(\mathbf{r}')\phi^{\circ}_{v'\mathbf{k}'}(\mathbf{r}')d\mathbf{r}'\right)|\phi^{\circ}_{v\mathbf{k}}\rangle, \tag{4.1.22}$$

$$\sum_{v'}\sum_{\mathbf{k}'\in BZ}\mathcal{K}^{1d}_{v\mathbf{k},v'\mathbf{k}'}\,|a_{v'\mathbf{k}'}\rangle = \sum_{v'}\sum_{\mathbf{k}'\in BZ}w_{\mathbf{k}'}\hat{Q}_{\mathbf{k}}\left(\int W(\mathbf{r},\mathbf{r}';\mathbf{k}-\mathbf{k}')\phi^{\circ *}_{v'\mathbf{k}'}(\mathbf{r}')\phi^{\circ}_{v\mathbf{k}}(\mathbf{r}')d\mathbf{r}'\right)|a_{v'\mathbf{k}'}\rangle, \tag{4.1.23}$$

$$\sum_{v'}\sum_{\mathbf{k}'\in BZ}\mathcal{K}^{2d}_{v\mathbf{k},v'\mathbf{k}'}\,|b_{v'\mathbf{k}'}\rangle = \sum_{v'}\sum_{\mathbf{k}'\in BZ}w_{\mathbf{k}'}\hat{Q}_{\mathbf{k}}\left(\int W(\mathbf{r},\mathbf{r}';\mathbf{k}-\mathbf{k}')b^{*}_{v'\mathbf{k}'}(\mathbf{r}')\phi^{\circ}_{v\mathbf{k}}(\mathbf{r}')d\mathbf{r}'\right)|b_{v'\mathbf{k}'}\rangle \tag{4.1.24}$$

The operator $\mathcal{D}$ describes bare single particle ground-state excitations, the $\mathcal{K}^{1x}$ and $\mathcal{K}^{2x}$ terms include so-called local field effects and the $\mathcal{K}^{1d}$ and $\mathcal{K}^{2d}$ terms describe electron-hole interactions. The integrals entering the definition of $\mathcal{K}^{1d}$ and $\mathcal{K}^{2d}$ include divergent terms in reciprocal space; in our implementation these divergences are integrated by using the method proposed in Refs. [69, 62].

The formalism described here to solve the BSE is equivalent to a time-dependent COHSEX within linear response; the COHSEX self-energy enters both in the definition of the bare independent quasi-particle (QP) ground-state excitations in $\mathcal{D}$ and in the $\mathcal{K}^{1d}$ and $\mathcal{K}^{2d}$ components of the kernel. In the linearization procedure used in Eqs. 4.1.8-4.1.9, the dependence of W (which enters Σ_{COHSEX}) on the density matrix is neglected [40]; this implies that only the linearized Σ_{SEX} contributes to $\mathcal{K}^{1d}$ and $\mathcal{K}^{2d}$. The COHSEX approximation is known to overestimate quasi-particle gaps [18], and single particle states and eigenvalues obtained within the GW approximation are usually preferred as starting points for BSE calculations. Within our current implementation $\hat{H}^{\circ}_{QP}$ ($\hat{H}^{\circ}_{COHSEX}$) is approximated either by the Kohn-Sham (KS) Hamiltonian whose gap is corrected by the use of a scissor shift Δ ($\hat{H}^{\circ}_{QP}=\hat{H}^{\circ}_{LDA}+\Delta\hat{Q}_{\mathbf{k}}$) or by including several GW corrected eigenvalues using Eqs. $24-25$ in Ref. [33]; the scissor approximation is accurate for the s-p bonded solids considered in this work [20]. The introduction of a more general scheme to include quasi-particle corrections within our formulation of the BSE will be the subject of future work. For example, the use in Eq. 4.1.20 of the enhanced COHSEX approximation presented in Ref. [45] may yield quasi-particle corrections of accuracy similar to that of the GW approximation, in a way fully consistent with our formulation.

The evaluation of the integrals defined by Eqs. 4.1.23-4.1.24 is the most expensive part in a BSE calculation. We note that the number of orbitals involved in the definition of $\mathcal{K}^{1d}$ and $\mathcal{K}^{2d}$ is equal to the number of occupied states. Hence the scala-

bility of our approach is the same as that of a ground state Hartree-Fock calculation (assuming $W = v$ for simplicity; the scalability of the calculation of the dielectric matrix is discussed in detail in Ref. [60]). Specifically, in a plane-wave (PW) implementation the evaluation of $\mathcal{K}^{1d}$ and $\mathcal{K}^{2d}$ scales as $\alpha[N_v^2 \times N_{\mathbf{k}}^2 \times N_{PW} \times \log N_{PW}]$, where N_{PW} is the size of the plane-wave basis set and α is constant with respect to system size; this is exactly the same scaling as that of calculations of the Hartree-Fock exact-exchange; as shown in the next section the computational complexity can be further decreased to $\alpha[N_v^2 \times N_{\mathbf{k}} \times N_{\mathbf{k}_I} \times N_{PW} \times \log N_{PW}]$, where $N_{\mathbf{k}_I}$ is the number of k-points in the irreducible Brillouin zone, by exploiting the symmetry operations of the system point group. In general the constant (or pre-factor) α of a BSE calculation is much larger than that of a ground state Hartree-Fock calculation. For example for the systems studied in this work, a number of Lanczos iterations between 1000 and 2000 is necessary to achieve convergence and for each iteration four operations are performed, with the same complexity of Hartree-Fock exact-exchange calculations (only one of such operations is required within the Tamm-Dancoff approximation). Within a electron-hole approach, the evaluation of $\mathcal{K}^{1d}$ and $\mathcal{K}^{2d}$ scales as $[N_v \times N_c \times N_{\mathbf{k}}^2 \times N_{PW} \times \log N_{PW}]$. Since in general N_c is much larger than N_v, the approach presented in this work is more efficient than an electron-hole approach and increasingly so for large systems. Within a matrix representation, the dimension of $\mathcal{L}$ (Eq. 4.1.19) is $2 \times N_v \times N_c \times N_{\mathbf{k}}$ in an e-h approach. Only in cases where N_c and $N_{\mathbf{k}}$ can be chosen small enough, the matrix $\mathcal{L}$ can be built explicitly and kept in memory for subsequent use (such as, i.e., the calculation of the dielectric tensor using the Lanczos algorithm). Storing $\mathcal{L}$ clearly allows for a large decrease in the pre-factor α of e-h BSE calculations, with respect to those presented here. However explicit calculation and storage of $\mathcal{L}$ are possible only for relatively small systems, as the required memory becomes rapidly unaffordable for large values of N_c and $N_{\mathbf{k}}$. Within the density matrix perturbation theory approach of this work, the dimension of $\mathcal{L}$ is $2 \times N_v \times N_{PW} \times N_{\mathbf{k}}$; if one chooses N_c to be the total number of conduction states, since $N_c \gg N_v$ and $N_{PW} = N_c + N_v \approx N_c$, the matrices representing $\mathcal{L}$ in the density matrix perturbation theory approach and in the e-h approach have similar dimensions [101]. N_{PW} is usually a large number, and thus within our method the matrix $\mathcal{L}$ is never built explicitly. Our approach is instead based on iterative calculations, where the application of $\mathcal{L}$ to a generic vector is performed by taking advantage of procedures analogous to those used in applying the Hamiltonian to wavefunctions in ground state calculations.

In the evaluation of $\mathcal{K}^{1d}$ and $\mathcal{K}^{2d}$, one needs to evaluate the inverse dielectric matrix ϵ^{-1} entering the definition of the screened Coulomb interaction $W(\mathbf{r}', \mathbf{r}; \mathbf{q}) = \int \epsilon^{-1}(\mathbf{r}', \mathbf{r}''; \mathbf{q}) v(\mathbf{r}'', \mathbf{r}) d\mathbf{r}''$ (where $\mathbf{q}$ is a generic wave vector). Also in this case the explicit calculation of empty electronic states can be avoided by using DFPT. In particular, following Refs. [[60, 61]], we use an eigenvalue decomposition of the symmetrized dielectric matrix [65] $\widetilde{\epsilon}$ in the random-phase approximation (RPA), and an

iterative algorithm to obtain eigenvalues and eigenvectors: such algorithm involves the evaluation of the action of $\widetilde{\epsilon}$ on trial potentials. Finally no inversion of the dielectric matrix is necessary as a spectral decomposition of $\widetilde{\epsilon}^{-1}$ is easily obtained from the eigenvalues (λ_i) and eigenvectors ($\widetilde{\mathbf{v}}_i$) of $\widetilde{\epsilon}$:

$$\widetilde{\epsilon}^{\,-1}(\mathbf{q}) = \hat{I} + \sum_{i=1}^{N} |\widetilde{\mathbf{v}}_i(\mathbf{q})\rangle(\lambda_i^{-1}(\mathbf{q}) - 1)\langle\widetilde{\mathbf{v}}_i(\mathbf{q})|, \tag{4.1.25}$$

As shown in Ref. [33] and in Sec. 4.1.4 below, convergence of computed spectra can be achieved with a small number N of eigenpairs included in Eq. 4.1.25. Indeed it has been shown that the eigenvalues λ_i are always greater than or equal to 1 [65] and that for a variety of systems $(\lambda_i^{-1} - 1)$ decays rapidly to zero, as the eigenvalue index increases [60, 61].

4.1.2 Use of symmetries in the solution of the Bethe-Salpeter equation

As shown in the previous section, the solution of the BSE for crystalline materials (and in general for periodic systems) involves the evaluation of integrals over a grid in the first Brillouin zone. Our implementation exploits the symmetry of the system to reduce the computational time and the memory requirements of the calculations. In a crystal the most general symmetry operation is given by a combination of a rotation R and a fractional translation $\mathbf{f}$ (denoted by $\{R|\mathbf{f}\}$). The set of symmetry operations $\{R|\mathbf{f}\}$ constitute the space group of the crystal. By using rotations R, we can express a generic point in the BZ as $\mathbf{k} = R\mathbf{k}_I$, where $\mathbf{k}_I$ belongs to the irreducible BZ (IBZ). The unperturbed Bloch wavefunctions satisfy the following equation [283]:

$$\phi^{\circ}_{v\mathbf{k}}(\mathbf{r}) = \phi^{\circ}_{vR\mathbf{k}_I}(\mathbf{r}) = \phi^{\circ}_{v\mathbf{k}_I}(R^{-1}\mathbf{r} - \mathbf{f}). \tag{4.1.26}$$

The perturbed orbitals implicitly depend on the direction of the electric field (Eq. 4.1.14). For this reason they satisfy the relationship:

$$\phi'^{i}_{v\mathbf{k}}(\mathbf{r},\omega) = \phi'^{i}_{vR\mathbf{k}_I}(\mathbf{r},\omega) = \sum_j R_{ij}\phi'^{j}_{v\mathbf{k}_I}(R^{-1}\mathbf{r} - \mathbf{f},\omega) \tag{4.1.27}$$

where i and j indicate Cartesian coordinates; the same relationship holds for the $\phi'^{*}_{v\mathbf{k}}(\mathbf{r},-\omega)$ perturbed orbitals. These properties can be used to improve the efficiency of the numerical solution of the equations described in the previous section. We first consider the calculation of P_i in Eq. 4.1.15. From the definition of $\hat{\rho}'(\omega)$ in Eq. 4.1.12 we have

$$P_{ij}(\omega) = -\frac{1}{V}\sum_{\mathbf{k}\in BZ} w_{\mathbf{k}} Tr(\hat{r}_i\hat{\rho}'^{j}_{\mathbf{k}}) = -\frac{1}{V}\int r_i\rho'^{j}(\mathbf{r},\omega)d\mathbf{r}, \tag{4.1.28}$$

where we have emphasized the dependence of P_i and $\hat{\rho}'_{\mathbf{k}}$ on the direction of the electric field, corresponding to the j-th Cartesian coordinate. By defining

$$\varrho'^{j}(\mathbf{r},\omega) = \sum_{\mathbf{k_I}\in IBZ} w_{\mathbf{k_I}} \rho'^{j}_{\mathbf{k_I}}(\mathbf{r},\omega) \tag{4.1.29}$$

from Eqs. 4.1.26-4.1.27 and Eq. 4.1.12, we have

$$\rho'^{j}(\mathbf{r},\omega) = \frac{1}{N_S}\sum_R \sum_l R_{jl}\varrho'^{l}(R^{-1}\mathbf{r}-\mathbf{f},\omega) \tag{4.1.30}$$

where N_S indicates the number of symmetry operations of the space group of the system; finally one has:

$$\begin{aligned} P_{ij} &= -\frac{1}{V}\frac{1}{N_S}\sum_R\sum_l R_{jl}\int r_i \varrho'^{l}(R^{-1}\mathbf{r}-\mathbf{f},\omega)d\mathbf{r} \\ &= -\frac{1}{V}\frac{1}{N_S}\sum_R\sum_{l,m} R_{im}R_{jl}\int r_m \varrho'^{l}(\mathbf{r},\omega)d\mathbf{r}. \end{aligned} \tag{4.1.31}$$

The set of Eqs. 4.1.29-4.1.31 shows that the perturbed density matrix $\hat{\rho}'$ (and consequently the macroscopic dielectric function) can be computed by solving Eq. 4.1.11 only for the k-points in the irreducible Brillouin zone instead of the full Brillouin zone. Symmetry operations can be further exploited in the calculation of the $\mathcal{K}^{1x}$ and $\mathcal{K}^{2x}$ components of the kernel defined in Eqs. 4.1.21-4.1.22. To this end in Eq. 4.1.21 we define:

$$n'^{j}(\mathbf{r}') = \sum_{v'}\sum_{\mathbf{k}'\in BZ} w_{\mathbf{k}'}\phi^{\circ *}_{v'\mathbf{k}'}(\mathbf{r}')a^{j}_{v'\mathbf{k}'}(\mathbf{r}') = \sum_{\mathbf{k}'\in BZ} w_{\mathbf{k}'} n'^{j}_{\mathbf{k}'}(\mathbf{r}'), \tag{4.1.32}$$

where the orbitals $a^{j}_{v\mathbf{k}}(\mathbf{r})$ satisfy Eq. 4.1.27 (where for simplicity we have omitted the implicit dependence on the j-th Cartesian coordinate). Likewise in Eq. 4.1.29, we define

$$\widetilde{n}'^{j}(\mathbf{r}') = \sum_{\mathbf{k_I}\in IBZ} w_{\mathbf{k_I}} n'^{j}_{\mathbf{k_I}}(\mathbf{r}') \tag{4.1.33}$$

and finally we have

$$n'^{j}(\mathbf{r}') = \frac{1}{N_S}\sum_R\sum_l R_{jl}\widetilde{n}'^{l}(R^{-1}\mathbf{r}'-\mathbf{f}). \tag{4.1.34}$$

Eq. 4.1.33 implies that, in order to evaluate the term in parentheses in Eq. 4.1.21 (and in Eq. 4.1.22), it is necessary to consider only the orbitals corresponding to $\mathbf{k}'$ points inside the irreducible BZ. Such simplification cannot be exploited in a straightforward

manner for the calculation of $\mathcal{K}^{1d}$ and $\mathcal{K}^{2d}$ as defined in Eqs. 4.1.23-4.1.24, where one needs to sum $\mathbf{k}'$ over the full BZ.

In order to calculate $\rho'^{j}(\mathbf{r},\omega)$, the linear system of Eq. 4.1.11 is iteratively solved using the non-Hermitian Lanczos algorithm introduced in Ref. [66]. To apply the required symmetrization operations (i.e. Eq. 4.1.34), three simultaneous iterative chains are performed at the same time, corresponding to the three directions of the perturbing electric field.

4.1.3 Absorption spectra of bulk silicon, carbon diamond and silicon carbide

The formalism presented in the previous sections has been implemented in the framework of the Quantum Espresso (QE) package, that uses plane-waves as a basis set and pseudopotentials [141]. The quasi-particle Hamiltonian $\hat{H}^{\circ}$ in Eq. 4.1.20 is approximated by $\hat{H}_{KS} + \Delta\hat{Q}_{\mathbf{k}}$, where $\hat{H}_{KS}$ is the Kohn-Sham (KS) Hamiltonian and Δ is the difference between the quasi-particle gap and the KS gap (scissor approximation). From quasi-particle (QP) calculations at the GW level of theory [42] it is known that the scissor approximation is accurate for the description of the band structure of several sp-bonded bulk systems [20].

We computed the absorption spectra of solids as the imaginary part of the macroscopic dielectric function ε_M (Eq. 4.1.16). In general ε_M is a tensor but in the specific cases studied here this tensor is diagonal and the diagonal elements all have the same value.

We first discuss the absorption spectrum of bulk silicon. The ground state calculation has been performed using the local density approximation (LDA) in the Perdew-Zunger [284] parametrization and the pseudopotential was taken from the Quantum Espresso library [285]. We used a lattice constant optimized at the LDA level of theory (10.20 a_0), as given in Ref. [286]. The value of the scissor shift Δ is determined as the difference of the experimental value of the minimum direct QP gap at the Γ point (3.4 eV) [287] and the LDA gap at the same point (2.57 eV). The use of a computed G_0W_0 quasi-particle gap would not significantly affect our results, since the G_0W_0 approximation reproduces the experimental value within 0.1 eV [20]. A cutoff of 18 Ry was used to expand the ground-state wavefunctions as well as the dielectric matrix (in Eq. 4.1.25); all the empty bands described by this cut-off are implicitly included in our calculation, corresponding to at least 328 empty bands per k-point. In Refs. [28, 29], as few as 4 conduction states were considered sufficient to reasonably converge the spectrum of bulk silicon. However, even in this case, our approach has a few advantages over the traditional e-h approach: the convergence with respect to the number of empty states does not need to be tested; the number of perturbed orbitals included in our calculations is equal to $N_v(=4)$; due to the large amount of e-h pairs included implicitly in our approach the spectrum can be com-

puted up to high energy and the validity of the f-sum rule can be easily verified (see below).

As shown in Ref. [52] the convergence of the static macroscopic dielectric constant (head of the dielectric matrix) is rather slow with respect to the k-points included in the first BZ. In order to integrate the BSE we use Monkhorst-Pack (M-P) grids of special k-points as implemented in QE [288, 289]. As shown in the early work of Benedict *et al.* [281], in order to improve the convergence of computed spectra it is useful to shift the grid from the origin (Γ point). In the QE implementation, automatically generated k-point grids centered at Γ may be shifted by $\left(\frac{1}{2n}\mathbf{b}_1 + \frac{1}{2n}\mathbf{b}_2 + \frac{1}{2n}\mathbf{b}_3\right)$, where n is the grid dimension and $\mathbf{b}_1$, $\mathbf{b}_2$ and $\mathbf{b}_3$ are reciprocal lattice primitive vectors. Since in the face-centered cubic lattice after such shift the k-point grid does not have the full symmetry of the crystal, additional points are generated, leading to a mesh with four times the number of k-points as in the original grid. This fact can be understood in the simple case of a single k-point $1 \times 1 \times 1$ mesh shifted in $\left(\frac{1}{2}\mathbf{b}_1 + \frac{1}{2}\mathbf{b}_2 + \frac{1}{2}\mathbf{b}_3\right)$. By applying all the symmetry operations (48 for the systems considered in this work) we can generate additional k-points $\frac{1}{2}\mathbf{b}_1$, $\frac{1}{2}\mathbf{b}_2$, $\frac{1}{2}\mathbf{b}_3$ equivalent by symmetry. This leads to a mesh with four times the k-points as the original $1 \times 1 \times 1$ mesh. Of course only the k-point $\left(\frac{1}{2}\mathbf{b}_1 + \frac{1}{2}\mathbf{b}_2 + \frac{1}{2}\mathbf{b}_3\right)$ is included in the IBZ and this property is exploited to accelerate the calculations, as discussed in Sec. 4.1.2. If the single k-point is shifted by a random vector in the BZ, the application of the symmetry operations may lead up to 48 different k-points in the full BZ (this is the number of symmetry operations of the point group of the diamond lattice). Similar arguments can be applied to the case of a k-point mesh of larger dimensions. The convergence with respect to the dimension of the grid is discussed below.

In order to test the computational parameters and approximations entering the solution of the BSE, we have first performed calculations for Si with a $4 \times 4 \times 4$ mesh with the origin shifted by $\left(\frac{1}{8}\mathbf{b}_1 + \frac{1}{8}\mathbf{b}_2 + \frac{1}{8}\mathbf{b}_3\right)$. This grid is then symmetrized, leading to 256 k-points in the full BZ and 10 in the IBZ. This mesh is sufficient to obtain accurate ground state properties but does not yield converged results for absorption spectra; nevertheless it is sufficiently accurate for the purpose of testing additional numerical parameters and approximations involved in the solution of the BSE. In Fig. 4.1.1 we show the convergence of the absorption spectrum of bulk silicon as a function of the number of eigenvalues and eigenvectors used in Eq. 4.1.25. The convergence is rapid and no difference is present between the spectra obtained using 16 and 48 eigenvalues. We note that the dimension of the full matrix is 2733, that is much bigger than the small number of eigenpotentials used here for its representation. In Fig. 4.1.2 we compare results obtained with and without the Tamm-Dancoff approximation (TDA). Minor differences are observed only in the high energy part of the spectrum. We have also computed the f-sum rule for these spectra and found that the full BSE fulfills 97% of the f-sum rule while the TDA spectrum yields 107%. The TDA appears to be reliable for the optical properties of bulk systems, as widely

accepted since the early use of the BSE [29]. However the TDA may break down for the optical spectra of molecules and nanostructures [99, 33] and for the electron energy loss spectra of bulk systems [290]. In the following, calculations on larger k-point grids are carried out within the TDA approximation.

We now consider the convergence of the spectrum of bulk silicon as a function of the dimension of the k-point grid used in the calculations. In Fig. 4.1.3 we show the results for three different Monkhorst-Pack (M-P) grids [288] of dimension $n \times n \times n$ with $n = 8, 10$, and 12, respectively, and we compare them with the experimental spectrum [291]. In order to improve the convergence, the origin of those grids is shifted by $\left(\frac{1}{2n}\mathbf{b}_1 + \frac{1}{2n}\mathbf{b}_2 + \frac{1}{2n}\mathbf{b}_3\right)$. After symmetrization the total number of k-points in the grid is $4 \times n \times n \times n$. Our calculations give accurate results for the position and intensity of the two main peaks, compared to experiment, with an error of at most 0.12 eV for the first (E_1) transition. However in the computed spectra we obtain a weak additional peak between the two main transitions which has a strong dependence on the k-point mesh used in the calculation. This extra peak was already present in some of the earlier BSE calculations of the optical spectrum of bulk silicon [28, 29] and in recent publications [292], as shown in Fig. 4.1.4. When the same k-point mesh is used, our approach reproduces the same result of a well converged electron-hole calculation (see panel b of Fig. 4.1.4).

Since the early applications of the BSE to the calculation of spectra of bulk systems, it was suggested that the use of M-P grids was likely responsible for the appearance of spurious peaks in the spectra [293]. It was also suggested that the use of grids shifted off the high symmetry directions [281] or randomly distributed k-points may help avoid the appearance of spurious spectral features. For example in Ref. [293] the example of an independent particle spectrum computed with 400000 k-points was presented, showing improved accuracy. However such a large mesh is not affordable in the solution of the BSE for realistic solids. For the sake of completeness, in this work we have also considered the use of a k-point grid off symmetry, obtained by shifting the origin of a regular grid at $\frac{1}{64}\mathbf{b}_1 + \frac{1}{32}\mathbf{b}_2 + \frac{3}{64}\mathbf{b}_3$, as suggested in Refs [281, 293]; in this case the grid is not symmetrized and the formalism described in Sec. 4.1.2 to accelerate the calculations cannot be applied (only the time-reversal symmetry is used, as explained in Appendix 6.4). The results are shown in Fig. 4.1.5 for some of the components of the dielectric tensor. Since the grid does not have the full symmetry of the crystal, the diagonal components of ε_M are different from each other, and the off-diagonal components of the tensor are different from zero. In Ref. [281] the perturbation was applied along the $(1, 1, 1)$ direction, amounting to an average of all the components of the tensor. This average eliminates the spurious peaks, which, however, are still present on the xx and yy diagonal components of the tensor (see Fig. 4.1.5). In this work, we have not considered random k-points in the integration of the BSE. In the literature, the BSE spectrum of silicon has already been computed using 1000 k-points randomly distributed over the BZ, finding a shoulder instead of

a peak between the two main transitions (see Fig.2 of Ref. [100]). Since a random distribution of k-points does not have the lattice symmetry, an effect analogous to the one shown in Fig. 4.1.5 might occur also in this case, especially for a small set of k-points. We note that a systematic test of the convergence of random distributions of k points or grids shifted off-symmetry can not take advantage of the symmetry to simplify the calculations and would become rapidly impractical when increasing the size of the sampling.

As a further application of our technique we have computed the absorption spectrum of carbon diamond. Also in this case the ground state calculation was performed using the local density approximation (LDA) and the pseudopotentials were taken from the Quantum Espresso library [285]. The lattice parameter was set to the experimental value of 6.74 a_0 [294]. A cutoff of 40 Ry was used to expand the wavefunctions and more than 300 empty band are implicitly included in our calculation. The value of the scissor shift Δ is obtained as the difference between the value of the experimental minimum direct gap (7.3 eV) [295] and the LDA minimum direct gap (5.66 eV). As shown in Ref. [20] the G_0W_0 quasi-particle and the experimental gap differ by 0.2 eV. As suggested in Ref. [281] a 6.4% stretch of the valence band was applied, to correct for the underestimate of the valence band width given by the LDA.

We tested the convergence of our results with respect to the number of eigenpairs included in Eq. 4.1.25 and the accuracy of the Tamm-Dancoff approximation. The conclusions are similar to the case of bulk silicon. In Fig. 4.1.6 we show the results for the calculated absorption spectrum of carbon diamond for two different k-point grids and we compare them with the experimental curve (from Ref. [296]). In this case the convergence with respect to the dimension of the k-point grid is faster than for bulk silicon; however, following Ref. [297] a larger Lorentzian broadening than in bulk Si was used for the computed spectrum (0.57 eV), which overall has less features than that of Si. The comparison with the experimental data is satisfactory, with a shift in the main peak of about 0.1 eV.

As a final example we consider the absorption spectrum of silicon carbide in the zincblende structure. The calculation was performed in the local density approximation with the lattice parameter set to the experimental value of 8.24 a_0 [294]. A cutoff of 40 Ry was used to expand the wavefunctions, corresponding to the implicit inclusion of more than 580 empty states. The value of the scissor shift is obtained as the difference between the experimental gap of 2.39 eV [294] and the LDA gap of 1.30 eV. In Fig. 4.1.7 we show the BSE spectrum computed for a $8 \times 8 \times 8$ shifted k-point mesh and the experimental curve from Ref. [298]. Overall the agreement between theory and experiment is good and the main peak position is reproduced with an error of about 0.15 eV. If a Lorentzian broadening of 0.57 is used, as in the case of diamond, a good agreement between the computed and experimental intensity is found, but the first shoulder of the experimental spectrum is not visible. This shoulder becomes detectable in the spectrum computed using a 0.27 eV broadening.

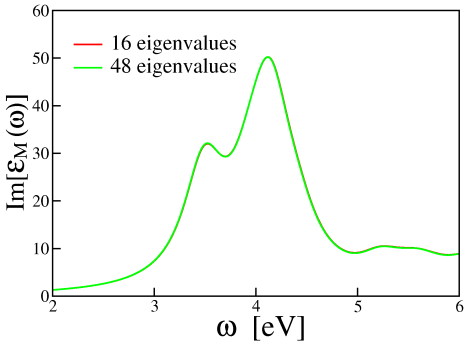

Figure 4.1.1: Absorption spectrum of bulk silicon computed as a function of the number of eigenvalues and eigenvectors used in the spectral decomposition of the dielectric matrix (Eq. 4.1.25). A mesh of 256 k-points in the BZ corresponding to 10 k-points in the IBZ has been used. A Lorentzian broadening of 0.24 eV was added to the curves.

In this case the intensity of the main peak is overestimated; overall our computed spectra are similar to previous results in the literature [299, 100].

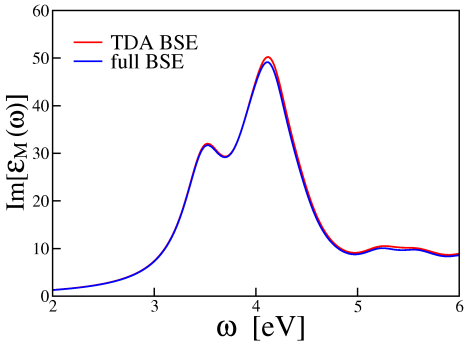

Figure 4.1.2: Absorption spectrum of bulk silicon computed with and without the Tamm-Dancoff approximation (TDA). A mesh of 256 k-points in the BZ corresponding to 10 k-points in the IBZ has been used. A Lorentzian broadening of 0.24 eV was added to the curves. We used 16 eigenvalues in Eq. 4.1.25 (see Fig. 4.1.1).

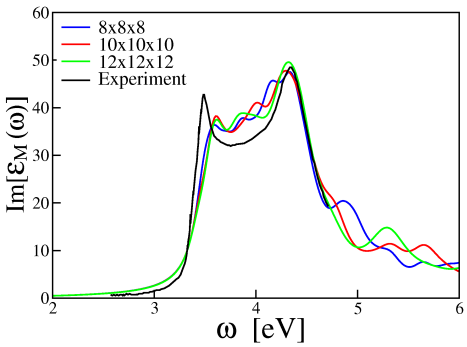

Figure 4.1.3: Absorption spectrum of bulk silicon computed with different Monkhorst-Pack k-point grids, compared to the experimental results [291]. A Lorentzian broadening of 0.11 eV has been added to the computed curves.

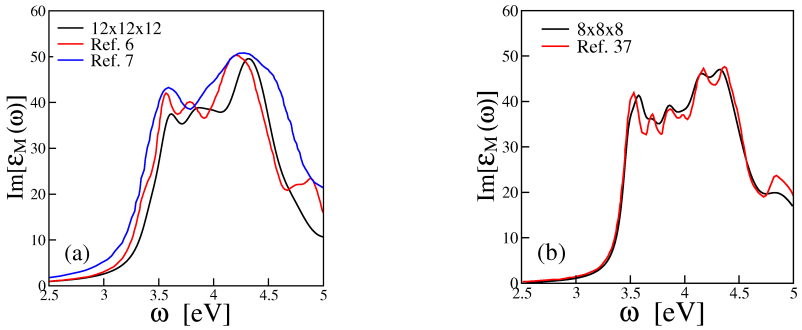

Figure 4.1.4: (a) Comparison of the bulk silicon spectrum (computed with a $12\times12\times12$ shifted k-grid) with some of the early BSE calculations (Ref. [28] and Ref. [29]). In Ref. [28] a grid containing 2048 k-points in the BZ was used while in Ref. [29] a 32 k-point grid was extrapolated up to 500 k-points. (b) Comparison of the bulk silicon spectrum computed using an $8\times8\times8$ shifted k-grid using our method and the electron-hole implementation of the Yambo code [292]; in this case an energy dependent broadening was used in order to compare with Ref. [292] (in the energy range shown in the figure the broadening increases linearly from 0.02 eV to 0.15 eV as a function of ω).

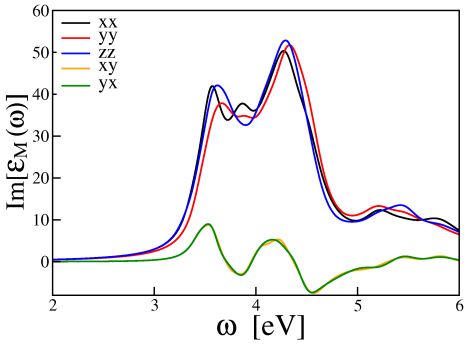

Figure 4.1.5: Absorption spectrum of bulk silicon computed with the nonsymmetric k-point mesh proposed in Ref. [281]. A Lorentzian broadening of 0.11 eV has been added to the curves. The different components of ε_M are represented by different colors.

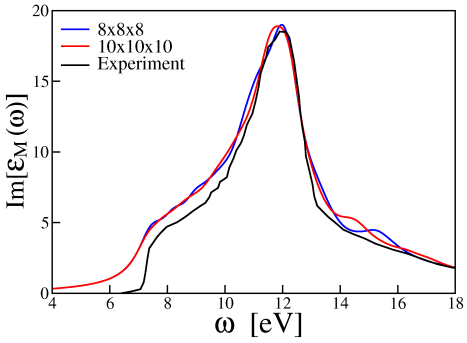

Figure 4.1.6: Absorption spectrum of carbon diamond as computed with different Monkhorst-Pack k-point grids, compared to the experimental results from Ref. [296]. We used 16 eigenvalues in Eq. 4.1.25. A Lorentzian broadening of 0.57 eV has been added to the computed curves.

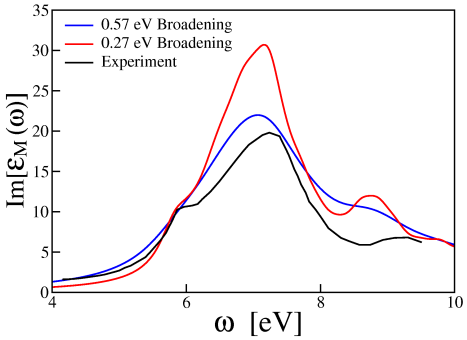

Figure 4.1.7: Absorption spectrum of silicon carbide as computed with an $8 \times 8 \times 8$ shifted Monkhorst-Pack k-point grid compared to the experimental results from Ref. [298]. The results are shown for two different values of the Lorentzian broadening.

4.1.4 Absorption spectra of WO_3 and N_2 intercalated WO_3

Having found a good agreement between theory and experiment for the optical spectra of several simple semiconductors, we proceeded to analyze the optical spectrum of bulk WO_3 first and then of N_2 doped WO_3. Most UV-vis spectra of WO_3 [235, 300] were measured over a narrow energy range nearby the fundamental absorption edge, and they are likely to be very sensitive to optical transitions with small intensity. Instead, measurements of reflectivity (e.g. with synchrotron radiation or by using ellipsometry) over a large energy range far from the absorption edge are less sensitive to the details of the edge, e.g. phonon-assisted transitions. Our spectra were computed using the implementation of Refs [33, 30], at the BSE level of theory, and then did not include phonon-assisted transitions and it is therefore meaningful to compare them with ellipsometry data. However, the latter are limited for pure single crystal RT-monoclinic WO_3 [301], and rather uncertain. To the best of our knowledge, they were reported only in Ref [301], where it was noted that the ellipsometry measurements may have been influenced by contributions from domains with different crystallographic orientations. Therefore we choose to compare the spectrum of simple cubic WO_3 with that of sodium bronze ($Na_{0.65}WO_3$) (see Fig. 4.1.8), which has a band structure similar to that of simple cubic WO_3: the extra electrons from Na fill the conduction bands of the simple cubic lattice [154] without modifying its original band structure. We note that even though simple cubic WO_3 has a smaller band gap than that of the RT-monoclinic phase, since the energy of the Fermi level increases with increasing electron concentration from Na, and the Coulomb repulsion increases within the filled states, the onset of inter band transitions shifts to higher energies as sodium is added to the system [301]. This results in a similar O2p-W5d gap in RT-monoclinic WO_3 and in $Na_{0.65}WO_3$. Therefore, in order to compare with experiment, the computed BSE absorption spectrum of simple cubic WO_3 was shifted to the blue by the difference of the simple cubic WO_3 and RT-monoclinic WO_3 band gaps, both obtained at the G_0W_0 level. The overall shape of the computed spectrum (Fig. 4.1.8) is in very good agreement with experiment.

To understand the influence of many body effects on the computed spectrum, we compared calculations at the BSE and Random Phase Approximation (RPA) level of theory (see Fig. 4.1.9). The RPA spectrum (including local field effects) using the LDA band gap presents two characteristic features: the band edge is red shifted due to the underestimate of the electronic gap by LDA, and the first peak has smaller intensity compared with the BSE spectrum, due to the lack of excitonic effects; as expected the RPA spectrum computed using the GW quasiparticle gap is shifted to higher energy, compared to that with the LDA gap. The BSE spectrum, which includes both quasiparticle corrections and excitonic effects is at lower energies, and the excitonic effects lead to an enhancement of the oscillator strength of the first peak, which compares well with experiment.

As mentioned in the introduction, for solar applications it is desirable to lower the

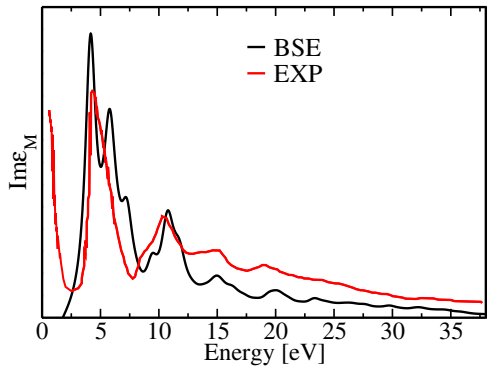

Figure 4.1.8: Absorption spectrum (Imε_M) of WO_3 computed by solving the Bethe-Salpeter Equation (BSE) and that of $Na_{0.65}WO_3$ obtained by reflectivity experiments [302](EXP). A Lorentzian broadening of 0.04 Ry was added to the computed curve. The low energy rise of the experimental spectra is due to extra electrons from Na filling the bottom of the conduction band (see text).

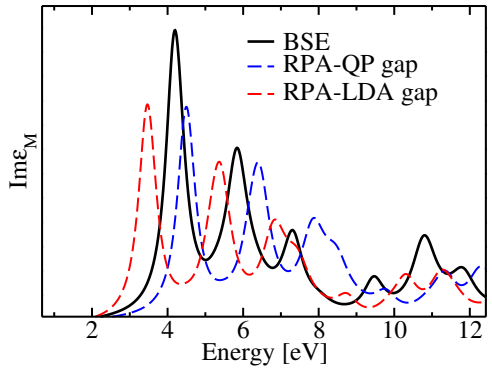

Figure 4.1.9: Absorption spectrum (Imε_M) of WO_3 computed at different levels of theory: by solving the Bethe-Salpeter Equation (BSE); using the Random Phase Approximation (RPA) with quasiparticle (QP) G_0W_0 gap; and the RPA with LDA band gap. A Lorentzian broadening of 0.027 Ry was added to the computed curves.

absorption gap of RT-monoclinic WO_3 towards the visible range, and it was recently suggested that insertion of closed shell molecules in the oxide lattice may lead to a gap decrease. In particular, Refs. [129, 130] showed that RT-monoclinic WO_3 intercalated with nitrogen molecules (N_2@WO_3) has a substantially smaller band gap than pure WO_3 (by about 0.8 eV), without exhibiting charged defects. Therefore we also examined the modifications of the absorption spectrum of the oxide upon insertion of N_2, although for computational convenience we considered a concentration higher than

in experiments (We carried out calculations of N_2 in SC WO_3, with a di-nitrogen concentration of $1N_2$:$1WO_3$. The latter is higher than reported experimentally [129] and was chosen for computational convenience, and because we were interested in probing a qualitative effect of N_2 intercalation in WO_3). The computed GW-BSE spectrum of N_2@WO_3 in Fig. 4.1.10 shows two main features: the absorption edge is red shifted compared with that of pure WO_3, consistent with the experimental observation; the oscillator strength of the first two peaks is redistributed to higher energy. This indicates that the N_2 presence increases the screening of the electron hole interaction and hence it decreases the exciton binding between electron and hole pairs. Indeed, we found that the lowest exciton binding energy decreased by 0.05 eV upon N_2 intercalation. The redistribution of the oscillator strength to higher energy is not desirable for solar applications; however, the presence of N_2 is mostly beneficial as the light absorption within the visible spectrum is enhanced by the presence of the molecule.

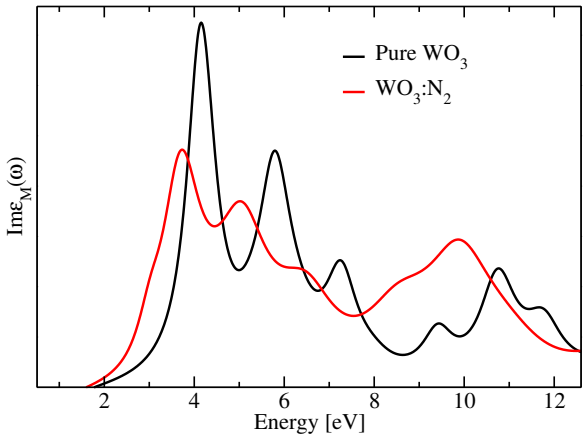

Figure 4.1.10: Absorption spectrum of WO_3 and dinitrogen intercalated WO_3. A Lorentzian broadening of 0.027 Ry was added to the computed curves.

In summary, in the section we have presented the extension to periodic systems of the density matrix perturbation theory formalism [33] for the calculation of optical absorption spectra. Within this approach the explicit calculation of empty electronic states and the storage and inversion of the dielectric matrix for the calculation of the screened Coulomb interaction are avoided. The use of both spatial and time-reversal symmetries leads to a significant reduction of the computational workload. As a proof of principle, we have applied our approach to the calculation of the optical absorption spectra of bulk silicon, carbon diamond, silicon carbide and WO_3. The convergence of numerical parameters, such as the dimension of the k-point grid and the number of eigenpairs used to expand the dielectric screening, have been carefully discussed. The accuracy of the Tamm-Dancoff approximation for bulk systems has been confirmed by the explicit calculation of absorption spectra and sum rules. Our

results exhibit good agreement with previously published data [28, 281, 29] and with experimental spectra [291, 296].

4.2 Absorption spectra of Si nanowires

Two main theoretical frameworks have been adopted in recent years to study absorption spectra of nanostructures: time dependent density functional theory (TDDFT) [12] and many body perturbation theory (MBPT) [16, 29] (see chapter 2). In many calculations using TDDFT appeared to date, local or semi-local approximations of the exchange-correlation energy have been used, either at the local density approximation (LDA) or gradient corrected approximation (GGA) levels of theory. Within these frameworks, a number of results in good or satisfactory agreement with experiment have been reported for finite systems, but the theory fails to describe excitons in solids [13] and charge transfer excitations in molecules [15, 14] as discussed in chapter 2.2.3.3. The failure of TDLDA for extended systems has motivated active researches on non local exchange correlation kernels, which may decribe bound excitons[102, 104, 103, 107]. Within MBPT, the solution of the Bethe-Salpeter equation (BSE) [16, 29, 303, 304, 305, 306] may yield a correct description of excitations in both solids and molecules, including charge transfer excitations. However we have seen that the techniques used to solve the BSE are much more demanding, from a computational standpoint, than those adopted to solve the time dependent Kohn-Sham equations in the adiabatic approximation; thus the application of MBPT has so far been limited to few, relatively small systems. In addition, fully converged numerical results have been difficult to obtain, and this may have hampered a robust assessment of the performance of the theory. Such an assessment is clearly important, as the theory is approximate, and possibly not applicable with the same degree of reliability to all classes of systems.

In this section we focus on semiconducting nanowires, and Si in particular, and we present calculations of absorption spectra as obtained by solving the BSE in the static approximation. We discuss the numerical accuracy of our calculations for semi-infinite systems (section 4.2.2) and we demonstrate the need to evaluate error bars of computed spectra, in order to carry out meaningful comparisons with results obtained at the same level of theory, but with different algorithms and numerical parameters. We then use our results to investigate absorption spectra as a function of surface structure and we compare our findings with those obtained within TDLDA (section 4.2.3). Section 4.2.5 contains a discussion of the efficiency of the approach adopted here.

4.2.1 Numerical accuracy of the solution of the Bethe-Salpeter equation for semi-infinite systems

We solved the BSE using pseudopotentials (PP) and plane wave basis sets and thus periodic supercells. In order to assess the numerical accuracy achieved in the solutions of Bethe-Salpeter equation, one needs to control the effect, on computed spectra, of the following parameters: 1) kinetic energy cutoff (E_{cut}) used to represent ground state wavefunctions; 2) number of eigenvalues and eigenvectors included in the decomposition of the dielectric matrix (Eq. 2.2.5); 3) accuracy of the technique adopted to integrate the divergence of the Fock operator; 4) number of k points used for integrals over the Brillouin zone (BZ); 5) size of the supercell. We now proceed to analyze each of these parameters, one at a time, for the case of a 0.4 nm Si nanowire grown along the [100] direction. The core atomic structure was constructed from bulk silicon. Both the cell dimension along the periodic direction and the internal geometry were fully optimized using the QUANTUM ESPRESSO package [141].

4.2.1.1 Basis set for ground state wavefunctions

Ground state calculations have been carried out within the LDA using a norm conserving, von Barth-Car type PP [307] for both hydrogen and Si. We did not address the accuracy of pseudopotential versus all electron (AE) calculations for excited state spectra and all the results reported below have been obtained with the same PP as in the ground state calculations. Comparisons between PP and AE calculations will be discussed elsewhere[308].

The convergence of computed spectra as a function of E_{cut} has been investigated at the TDLDA level and we established that $E_{cut} = 12$ Ry yields spectra converged within 0.05 eV, as shown in Fig. 4.2.1. This is the value of the cutoff used throughout the paper for Si NWs.

4.2.1.2 Eigenvalue decomposition of the dielectric matrix

As discussed in section 4.1.2 (see Eq. 4.1.25), we represent the inverse dielectric matrix by an eigenvalue decomposition and thus the convergence of our calculations as a function of the number N_{eig} of eigenvalues and eigenvectors included in Eq. 4.1.25 need to be tested.The same number of N_{eig} is used for all k points included in the BZ integration. As seen in Fig. 4.2.2, the sum in Eq. 4.1.25 can be truncated to a relatively small N_{eig} : spectra computed with $N_{eig} = 72$ and 88 are essentially identical and they differ by a minimal amount with respect to that obtained with $N_{eig} = 56$. All calculations for wires reported below have been carried out by truncating the summation to $N_{eig} = 72$, which appears to be a rather conservative choice. We note that the shape of the spectrum is preserved when N_{eig} is further decreased to 28 and that the difference of peak positions with respect to converged spectra is about

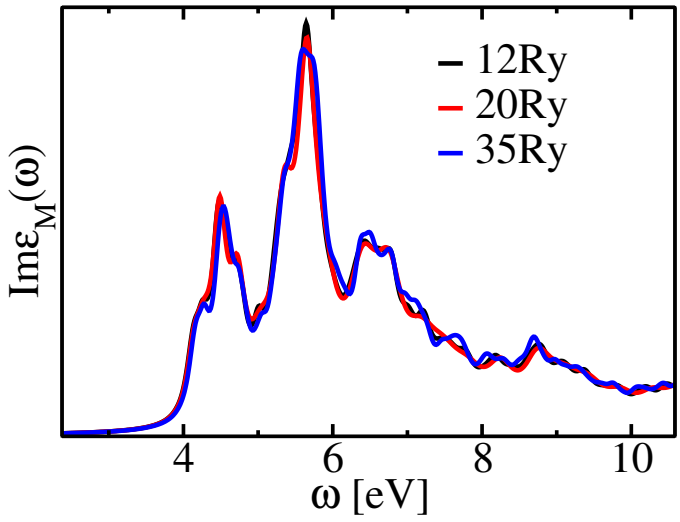

Figure 4.2.1: Convergence of the spectrum of a 0.4 nm Si nanowire grown in the [001] direction, as a function of the kinetic energy cutoff used for the solution of the Kohn-Sham equation. Calculations were carried out at the TDLDA level, with a cubic cell of lateral dimension equal to 37 a.u. and 16 k-points.

0.3-0.4 eV.

4.2.1.3 Integration of the divergence of the Fock operator for semi-infinite systems and Brillouin zone sampling

The evaluation of the screened Coulomb interaction amounts to evaluating the following term (following Eq.4.1.23):

$$\begin{aligned}
&\sum_{v'}\sum_{\mathbf{k}'\in BZ}\frac{1}{N_{\mathbf{k}'}}\mathcal{K}^{1d}_{v\mathbf{k},v'\mathbf{k}'}|a_{v'\mathbf{k}'}\rangle = \\
&\sum_{v'}\sum_{\mathbf{k}'\in BZ}\frac{1}{N_{\mathbf{k}'}}\hat{Q}_{\mathbf{k}}\left(\int W(\mathbf{r},\mathbf{r}';\mathbf{q})\phi^{o*}_{v'\mathbf{k}'}(\mathbf{r}')\phi^{o}_{v\mathbf{k}}(\mathbf{r}')d\mathbf{r}'\right)|a_{v'\mathbf{k}'}\rangle \\
&=\sum_{v'}\sum_{\mathbf{k}'\in BZ}\frac{1}{N_{\mathbf{k}'}}\hat{Q}_{\mathbf{k}}\left(\int \upsilon(\mathbf{r},\mathbf{r}')\phi^{o*}_{v'\mathbf{k}'}(\mathbf{r}')\phi^{o}_{v\mathbf{k}}(\mathbf{r}')d\mathbf{r}'\right)|a_{v'\mathbf{k}'}\rangle \\
&+\sum_{v'}\sum_{\mathbf{k}'\in BZ}\frac{1}{N_{\mathbf{k}'}}\hat{Q}_{\mathbf{k}}\left(\int (\varepsilon^{-1}(\mathbf{r},\mathbf{r}'',\mathbf{q})-\delta(\mathbf{r}-\mathbf{r}''))\upsilon(\mathbf{r},\mathbf{r}'')d\mathbf{r}''\phi^{o*}_{v'\mathbf{k}'}(\mathbf{r}')\phi^{o}_{v\mathbf{k}}(\mathbf{r}')d\mathbf{r}'\right)|a_{v'\mathbf{k}'}\rangle
\end{aligned} \tag{4.2.1}$$

where we have defined $\mathbf{q}=\mathbf{k}-\mathbf{k}'$. The first term on the right hand side includes the integrable divergence of the Fock operator; the second term does not include any

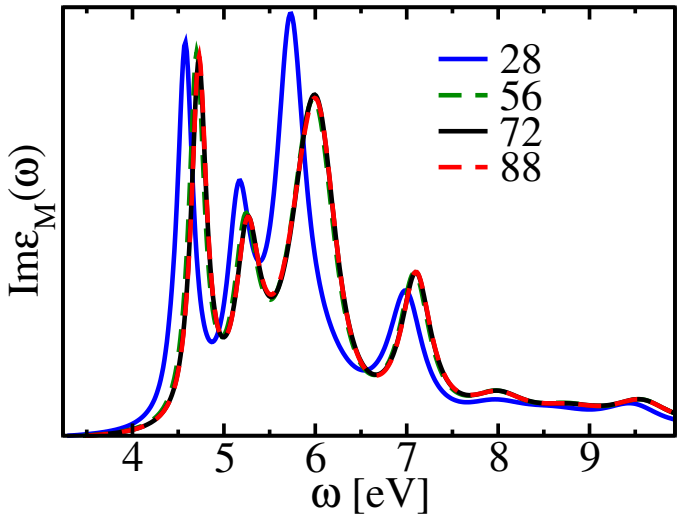

Figure 4.2.2: Convergence of the spectrum of a 0.4 nm Si nanowire grown in the [001] direction, as a function of the number of eigenvectors included in the decomposition of the dielectric matrix (see Eq.8). Calculations were carried by solving the BSE, with a kinetic energy cutoff of 12 Ry for the Kohn-Sham orbitals, a cubic cell of 37 a.u. linear dimensions and 7 k-points. The divergence of the Fock operator was integrated using the scheme of Ref. [69] and the head of the dielectric matrix was obtained from the inverse of the dielectric constant. A scissor operator was used, by adjusting the value of the band gap to that obtained within the G_0W_0 approximation.

divergence. We introduce the co-densities $\rho_{v,\mathbf{k}}^{v',\mathbf{k}'}(\mathbf{r}') = \phi_{v',\mathbf{k}'}^{o*}(\mathbf{r}')\phi_{v,\mathbf{k}}^{o}(\mathbf{r}')$, with Fourier transform $\rho_{v,\mathbf{k}}^{v',\mathbf{k}'}(G)$. A Fourier transform of the first term of the right hand side of Eq. 4.2.1 yields:

$$\begin{aligned}
&\sum_{v'}\sum_{\mathbf{k}'\in BZ}\frac{1}{N_{\mathbf{k}'}}\hat{Q}_{\mathbf{k}}\left(\int \upsilon(\mathbf{r},\mathbf{r}')\phi_{v'\mathbf{k}'}^{o*}(\mathbf{r}')\phi_{v\mathbf{k}}^{o}(\mathbf{r}')d\mathbf{r}'\right)|a_{v'\mathbf{k}'}\rangle \\
&=\sum_{v'}\sum_{\mathbf{k}'\in BZ}\frac{1}{N_{\mathbf{k}'}}\hat{Q}_{\mathbf{k}}\frac{1}{\Omega}\left(\int \upsilon(\mathbf{r},\mathbf{r}')\sum_{\mathbf{G}}\rho_{v,\mathbf{k}}^{v',\mathbf{k}'}(\mathbf{G})e^{i(\mathbf{q}+\mathbf{G})\cdot\mathbf{r}'}d\mathbf{r}'\right)|a_{v'\mathbf{k}'}\rangle \\
&=\sum_{v'}\sum_{\mathbf{k}'\in BZ}\frac{1}{N_{\mathbf{k}'}}\hat{Q}_{\mathbf{k}}\frac{1}{\Omega}\sum_{\mathbf{G}}\rho_{v,\mathbf{k}}^{v',\mathbf{k}'}(\mathbf{G})\frac{4\pi}{(\mathbf{q}+\mathbf{G})^2}e^{i(\mathbf{q}+\mathbf{G})\cdot\mathbf{r}}|a_{v'\mathbf{k}'}\rangle
\end{aligned} \tag{4.2.2}$$

By substituting $\hat{Q}_{\mathbf{k}} = \hat{I} - \hat{P}_{\mathbf{k}} = \hat{I} - \sum_v |\phi^o_{v\mathbf{k}}\rangle\langle\phi^o_{v\mathbf{k}}|$, Eq. 4.2.2 becomes:

$$\frac{1}{\Omega}\sum_{v'}\sum_{\mathbf{q}\in BZ}\frac{1}{N_{\mathbf{q}}}\sum_{\mathbf{G}}\rho^{v',\mathbf{k}'}_{v,\mathbf{k}}(\mathbf{G})\frac{4\pi}{(\mathbf{q}+\mathbf{G})^2}e^{i(\mathbf{q}+\mathbf{G}).\mathbf{r}}a_{v'\mathbf{k}'}(\mathbf{r})$$
$$-\frac{1}{\Omega}\sum_{v'}\sum_{\mathbf{q}\in BZ}\frac{1}{N_{\mathbf{q}}}\phi^o_{v\mathbf{k}}(\mathbf{r}'')\int\phi^{o*}_{v\mathbf{k}}(\mathbf{r})\sum_{\mathbf{G}}\rho^{v',\mathbf{k}'}_{v,\mathbf{k}}(\mathbf{G})\frac{4\pi}{(\mathbf{q}+\mathbf{G})^2}e^{i(\mathbf{q}+\mathbf{G}).\mathbf{r}}a_{v'\mathbf{k}'}(\mathbf{r})d\mathbf{r} \tag{4.2.3}$$

The second term in Eq. 4.2.3 vanishes at $\mathbf{q}+\mathbf{G}=0$ because the Fourier component of $\phi^{o*}_{v\mathbf{k}}(\mathbf{r})a_{v'\mathbf{k}'}(\mathbf{r})$ at $\mathbf{q}+\mathbf{G}=0$ is zero due to the orthogonality of $|\phi^o_{v\mathbf{k}}\rangle$ and $|a_{v'\mathbf{k}'}\rangle$. The summation in the first term of Eq. 4.2.3 exhibits an integrable divergence for $(\mathbf{q}+\mathbf{G})=0$ and cannot be performed by using a special point integration technique. We considered two approaches to tackle the divergence in the Fock operator: (i) the use of the integration technique proposed by Gygi and Baldereschi (GB) [69] and (ii) the use of a cylindrical cutoff for the Coulomb interaction [309, 310, 311]. We briefly summarize the two techniques below and present results obtained with both of them.

Following Ref. [69], we add to and subtract from Eq. 4.2.3 a term with a known analytic form, that exhibits the same divergent behavior as the one of the sum in Eq. 4.2.3. We also add a correction term, as suggested in Ref. [62], to properly account for the spherically averaged limit at $q=0$. If we define $A_{v,\mathbf{k}}(\mathbf{q}+\mathbf{G}) = \sum_{v'}\rho^{v',\mathbf{k}-\mathbf{q}}_{v,\mathbf{k}}(\mathbf{G})e^{i(\mathbf{q}+\mathbf{G}).\mathbf{r}}a_{v'\mathbf{k}-\mathbf{q}}(\mathbf{r})$, the first term of Eq. 4.2.3 is then given by:

$$\frac{4\pi}{\Omega N_{\mathbf{q}}}\sum_{\mathbf{G},\mathbf{q}}\frac{A_{v,\mathbf{k}}(\mathbf{q}+\mathbf{G})}{|\mathbf{q}+\mathbf{G}|^2} = \frac{4\pi}{\Omega N_{\mathbf{q}}}[\sum_{\mathbf{G},\mathbf{q}}{}'\frac{A_{v,\mathbf{k}}(\mathbf{q}+\mathbf{G})}{|\mathbf{q}+\mathbf{G}|^2}+\langle\langle\lim_{\mathbf{q}\to 0}\frac{A_{v,\mathbf{k}}(\mathbf{q})-A_{v,\mathbf{k}}(0)}{\mathbf{q}^2}\rangle\rangle]+DA_{v,\mathbf{k}}(0) \tag{4.2.4}$$

$$D = \frac{4\pi}{\Omega N_{\mathbf{q}}}[-\sum_{\mathbf{q},\mathbf{G}}{}'\frac{e^{-\alpha|\mathbf{q}+\mathbf{G}|^2}}{|\mathbf{q}+\mathbf{G}|^2}+\alpha]+\frac{1}{\pi}\sqrt{\frac{\pi}{\alpha}} \tag{4.2.5}$$

$N_{\mathbf{q}}$ is the number of $\mathbf{q}$ points and Ω is the unit cell volume, $\alpha = \frac{C}{E_{cut}}$ is a parameter, where C is a constant; the prime in the summation ($\sum'$) indicates that the term $\mathbf{q}+\mathbf{G}=0$ is excluded. We have verified that the computed value of the exact exchange energy is independent on the choice of α. As pointed out in Ref. [62], the term $\langle\langle\lim_{\mathbf{q}\to 0}\frac{A(\mathbf{q})-A(0)}{\mathbf{q}^2}\rangle\rangle$ is related to the gauge invariant spread of the occupied electronic orbital manifold, as defined in the theory of maximally localized Wannier Functions [312]. We note that neglecting such term in the evaluation of the summation of Eq. 4.2.4 amounts to an error inversely proportional to the cell volume times the number of q points included in the BZ sampling.

We first tested the accuracy of the GB integration scheme by performing time dependent Hartree-Fock (TDHF) calculations as a function of the cell size and as a

function of the number of k-points used for the BZ integration. Fig. 4.2.3a shows an example for a 0.4 nm Si NW: when 16 k pts are used , nearly identical results are obtained for cells with edges 37 and 55 a.u.; in addition, the difference with respect to the spectrum computed with a cell of 27 a.u. is small. We also repeated a calculation with 21 k pts and cell edge = 37 a.u., and found the same results as those shown in Fig. 4.2.3b for 16 k pts.

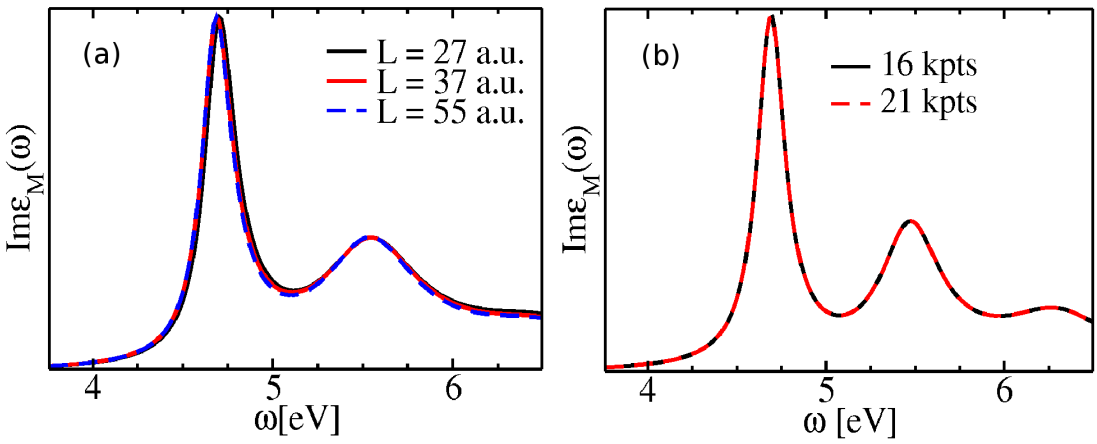

Figure 4.2.3: Convergence of the spectrum of a 0.4 nm Si nanowire grown in the [001] direction, as a function of the cell size (L) (a) and the number of k-points (kpts) used in the BZ sampling (b). Calculations were carried out at the time dependent Hartree Fock (HF) level, with a kinetic energy cutoff of 12 Ry for the Kohn-Sham orbitals, and a scissor operator obtained by computing the difference between the lowest LDA and HF energy gaps. The divergence of the Fock operator was integrated with the techniques proposed in Refs. [62, 69]. In (a) we used 16 kpts and in (b) L=37 a.u.

An alternative way to evaluate the summation in Eq. 4.2.3 is to use a Coulomb cutoff to truncate the long range Coulomb interaction in the direction perpendicular to the wire growth direction, and thus avoid fictitious interactions between periodic replica. Following Ref. [309], we define a region $\mathcal{C}$ of real space, outside which the Coulomb interaction is assumed to be zero:

$$\tilde{v}(r) = \begin{cases} \frac{1}{r} & if\ r \in \mathcal{C} \\ 0 & if\ r \notin \mathcal{C} \end{cases} \tag{4.2.6}$$

For a cluster (0-dimension), $\mathcal{C}$ is a sphere; in the case of a wire $\mathcal{C}$ is an infinitely long cylinder with a given radius R. A sharp cutoff in real space yields a rapidly oscillating function in Fourier space; therefore care must be exercised in the choice of the plane

wave cutoff, as in principle a value of E_{cut} larger than the one chosen for the charge density is needed to represent the truncated Coulomb potential in G space.

After performing a Fourier transformation of the Coulomb potential in cylindrical coordinates, one obtains [309]:

$$\tilde{v}^{1D}(G_\parallel, G_\perp) = \frac{4\pi}{G^2}[1 + G_\perp R J_1(G_\perp R) K_0(G_\parallel R) - G_\parallel R J_0(G_\perp R) K_1(G_\parallel R)] \quad (4.2.7)$$

The term $\mathcal{K}_0(G)$ diverges logarithmically for $G \to 0$ and so does the truncated Coulomb potential:

$$\tilde{v}^{1D}(G_\parallel, G_\perp) \sim -log(G_\parallel R) \ for \ G_\perp > 0, G_\parallel \to 0^+ \quad (4.2.8)$$

In ground state calculations this divergence can be canceled by a divergence of the same kind present in the Coulomb interaction between nuclear charges, that is the *sum* of the interaction of electronic and nuclear charges gives rise to a non divergent contribution to the total energy. However in calculations involving excited states, no cancellation occurs. In most papers using a Coulomb cutoff (see, e.g. Ref. [309, 310]), a finite cylinder of radius R and length h was considered. The cutoff length h was usually chosen larger than the estimated exciton Bohr radius in the system, and smaller than an effective supercell size [310]. An effective linear size of the supercell is defined by the product of the unit cell size along the periodic direction and the number of k points. We note that the use of a Coulomb cutoff in the periodic direction is a mathematical tool to avoid the divergence at $G_\parallel \to 0^+$. It may be a reasonable procedure for several systems, however if excitons turn out to be rather extended, with respect to the chosen cell size, the use of a cutoff may become impractical or lead to very slow convergence as a function of the number of k points used for the BZ integration.

One may avoid the use of a cutoff in the periodic direction by using the scheme proposed in Ref. [311] where the Coulomb interaction is truncated outside one Wigner-Seitz cell centered on the wire, in the xy plane. In this case the divergence at $\mathbf{q} \to 0$ is still present, although it is a logarithmic divergence instead of a $1/\mathbf{q}^2$ divergence. In Fig. 4.2.4 we compare TDHF calculations carried out using a Coulomb cutoff[309] with those reported in Fig. 4.2.3 with the GB integration scheme. The radius R was chosen equal to half the cell size and h equal to the number of k points times the cell size, following the prescription [1] of Ref. [309],[310]. It is seen that a much larger number of k pts (larger than 50) is needed to converge the spectrum computed with

[1] As long as R is large enough (.ie. it defines a region including more than 99% of the charge density of the system), the computed spectra do not depend on R. However, results are very sensitive to the choice of h. As noted in Refs. [309, 310], h has to be larger than the exciton length and shorter than the number of k points times the cell size. In practice, it is hard to predict the exciton length and different choices of h with the same number of k points may yield different results.

a cylindrical Coulomb cutoff than with the GB technique. Similar results have been obtained also for other systems, e.g. hydrogen chains. In the latter case, 180 k pts were not sufficient to converge the spectrum computed with a cylindrical Coulomb cutoff; instead 51 k pts are enough to converge the spectra by using the GB technique.

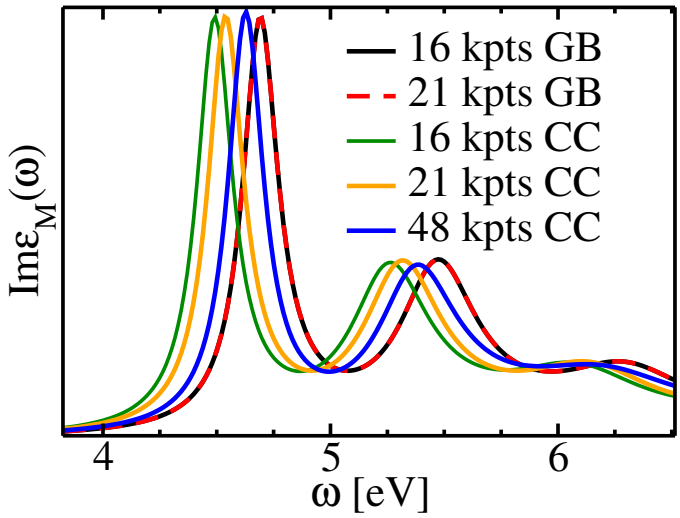

Figure 4.2.4: Convergence of the spectrum of a 0.4 nm Si nanowire grown in the [001] direction, as a function of the number of k-points (kpts) used in the BZ sampling, using two different techniques for the evaluation of the Fock operator: the one proposed in Refs. [62, 69] (GB) and a Coulomb cutoff (CC). Calculations were carried out at the time dependent Hartree Fock (HF) level, with a kinetic energy cutoff of 12 Ry for the Kohn-Sham orbitals, a cell edge of 37 a.u. and a scissor operator obtained by computing the difference between the lowest energy LDA and HF gaps.

4.2.1.4 Convergence of computed absorption spectra as a function of cell size

Fig. 4.2.5 shows the convergence of computed spectra as a function of cell size for a 0.4nm Si wire. Calculations were carried out using the GB integration scheme and 16 k-pts for the BZ integration. Although one may obtain well converged TDHF spectra with 37 a.u. cells (see Fig. 4.2.3), cells as large as 60 a.u. are required to fully converge BSE spectra. As a function of cell size, the spectra are rigidly shifted in energy, with respect to each other and the peak positions scale as the inverse of the square of the cell size (L), as shown in Fig. 4.2.6a. This linear dependance on $\frac{1}{L^2}$ is the same as that of the head of the dielectric matrix, reported in Fig. 4.2.6b, and it is largely responsible for the slow convergence of computed BSE spectra as a

function of cell sizes. However also the elements of the wing of the dielectric matrix have long range contributions and are partly responsible for the slow convergence. In order to overcome such slow convergence, we used a Coulomb cutoff[311] to compute the eigenpotentials of the dielectric matrix and to evaluate the difference between bare and screened Coulomb interaction (See second term of Eq. 4.2.1). Within such scheme, we obtain a fast convergence of the BSE spectra within 0.1 eV as a function of both cell size and k-pts (see Fig. 4.2.7). We note that the Fourier components of the Coulomb potential truncated with a cylindrical Coulomb cutoff exhibits strong oscillations as $q_{\|} \to 0$ which may cause numerical instabilities; instead the truncation procedure proposed in Ref. [311] appears to be much more stable and the potentials exhibit smaller oscillations in Fourier space for a given cutoff.

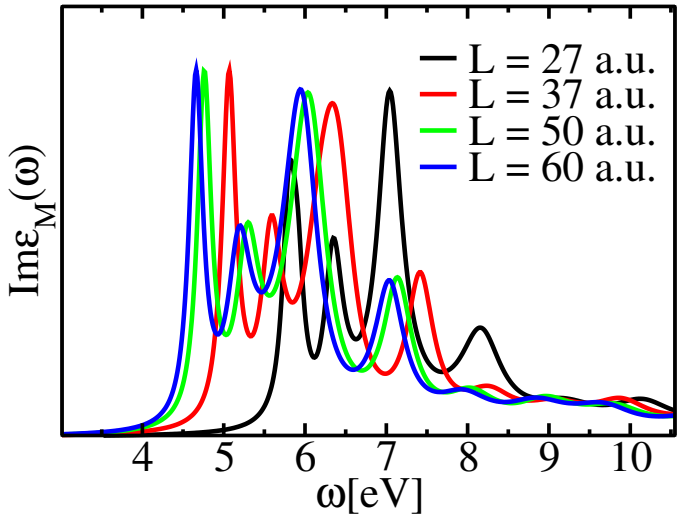

Figure 4.2.5: Convergence of the spectrum of a 0.4 nm Si nanowire grown in the [001] direction, computed by solving the BSE, as a function of the cell lateral dimension (L) . We included 72 eigenvectors in the decomposition of the dielectric matrix (see Eq. 4.1.25); we used 16 k points for the BZ integration, the technique of Refs. [62, 69] to compute the Fock operator and the head of the dielectric matrix was computed from the inverse dielectric constant.

4.2.2 Comparison between spectra obtained with different levels of theory and with different numerical techniques

In this section we first discuss differences between our computed spectra, at the BSE level of theory, and previously published ones, calculated with different algorithms and numerical parameters. We then compare BSE spectra with those obtained by carrying out TDLDA calculations.

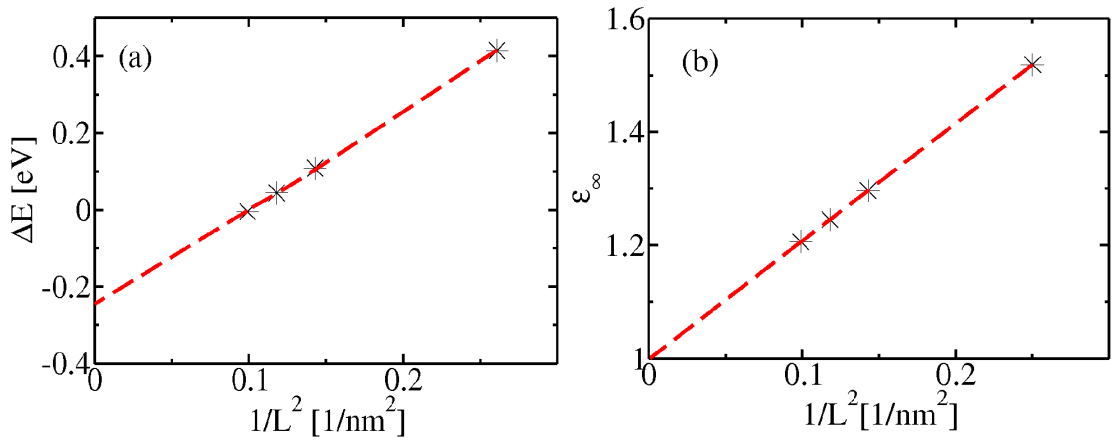

Figure 4.2.6: (a) Position of the first peak (ΔE) of spectra of a 0.4 nm Si nanowire grown in the [001] direction, computed by solving the BSE, as a function of the square of the cell lateral dimension (L) . ΔE is defined as the energy difference between the main peak position at a given L and the peak position at L = 60 a.u. We included 72 eigenvectors in the decomposition of the dielectric matrix (see Eq. 4.1.25); we used 12 Ry for the Kohn-Sham orbitals, 16 k points for the BZ integration, the technique of Refs. [62, 69] to compute the Fock operator and the head of the dielectric matrix was obtained from the inverse dielectric constant. (b) Macroscopic dielectric constant (ε_∞) as a function of the square of the cell lateral dimension (L), obtained from density functional perturbation theory (DFPT) using the QUANTUM ESPRESSO package [141].

Fig. 4.2.8 compares our computed spectrum for a 0.4 nm Si NW with that reported in Ref. [313]. The agreement between number of peaks and peak positions is satisfactory, although differences in intensities are present, probably due to the use of different numerical techniques. We have also tested the accuracy of the TDA approximation; only small differences in the high energy part of the spectra are observed, when using the TDA. A comparison of our results obtained with and without the TDA is shown in Fig. 4.2.9.

Fig. 4.2.10 shows a comparison with existing results for a wire with bigger diameter (0.8 nm), grown in the [110] direction. The curve [b] was obtained by linearly extrapolating the position of the BSE spectra as a function of the inverse of the cell size, similar to the case of Fig. 4.2.6. The curve [a] was obtained by using a Coulomb cutoff to evaluate the dielectric matrix[311] and shows very good agreement with the extrapolated results of [b]. Our results are in very good agreement with those of Ref. [313] but exhibit a shift of about 0.3-0.5 eV with respect to those of Ref. [316]. The use of G_0W_0 corrections in Ref. [316], instead of a scissor operator (as done here) may be partially responsible for this difference; the orgin of the discrepancy may also

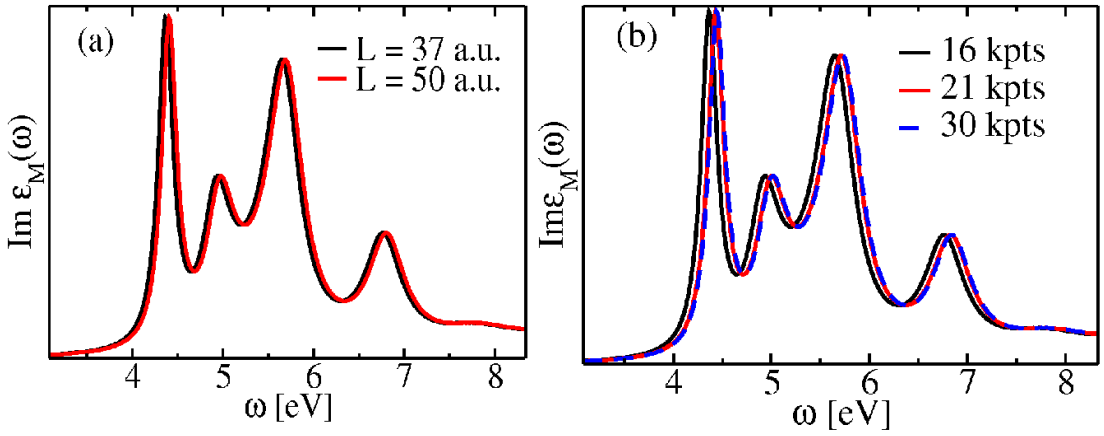

Figure 4.2.7: Convergence of the BSE spectrum of a 0.4 nm Si nanowire grown in the [001] direction, as a function of the cell size (L) (a) and k-points (kpts) used in the BZ sampling (b). Calculations were carried out with a kinetic energy cutoff of 12 Ry. The technique of Refs. [62, 69] was used to evaluate the Fock operator and we employed a Coulomb cutoff to evaluate the dielectric matrix (see text). The scissor operator was obtained by computing the difference between the lowest energy gap within LDA and G_0W_0. We included 72 eigenvectors to evaluate the dielectric matrix. In (a) we used 16 kpts and in (b) L=37a.u.

come from the use of different geometries for the surface of the NW. As discussed in the next section, even a small difference in the chosen geometry of the surface may lead to differences in the computed spectra.

In Fig. 4.2.11 we compare spectra obtained within MBPT and TDLDA, which turn out to be rather different, in the case of the two thin wires investigated here. In the case of the smallest wire the main identifiable peaks are the same, although the relative intensity and positions of the two lowest energy ones differ substantially. In the case of the 0.8 nm wire, the differences are much more substantial, including peak positions and the overall width of the spectrum main peak. The TDLDA approximation does not describe properly bound excitons and thus the spectrum turns out to be broader than the one obtained at the BSE level, with a larger number of peaks. TDLDA has been known to fail for the description of the optical absorption spectra of solids [13, 16]. The absence of long range interactions, that is of a $1/q^2$ term in the exchange-correlation kernel is responsible for the error of TDLDA in extended systems. We note that the RPA ($f_{xc} = 0$) and TDLDA SiNW spectra are almost identical except for a slight lower intensity in the RPA spectra.

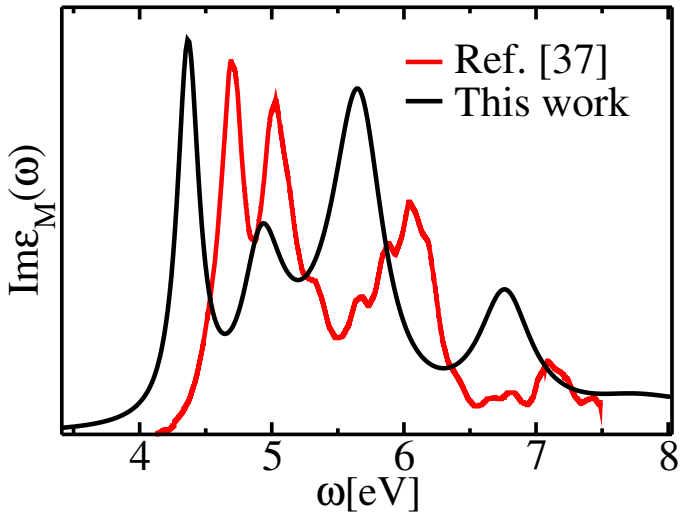

Figure 4.2.8: Spectra of a 0.4 nm Si nanowire grown in the [001] direction, as obtained in this work and in Ref. [313], where an electron-hole approach was used to solve the BSE. We used a cell size of 37 a.u. (40 a.u. in Ref. [313]), 16 k points (as in Ref. [313]) for the BZ sampling , a kinetic energy cutoff of 12 Ry to solve the Kohn Sham equations (30 Ry in Ref. [313] with norm-conserving pseudopotentials[314, 315]), the technique of Refs. [62, 69] to evaluate the Fock operator (the Random Integration Method was used in Ref. [313]) and a Coulomb cutoff for the dielectric matrix (no Coulomb cutoff was used in Ref. [313]). We included 72 eigenvectors in the evaluation of dielectric matrix. The scissor operator was obtained by computing the difference between the lowest energy gap within LDA and G_0W_0 (A scissor operator obtained by computing the difference between the lowest energy gap within LDA and G_0W_0 was also used in Ref. [313]).

4.2.3 Effect of surface structure on absorption spectra of thin Si nanowires

Fig. 4.2.12a shows the BSE spectrum for a 0.8 nm Si NW grown in the [110] direction for two different surface geometries. Both surfaces are hydrogen terminated. It is seen that in a broad energy range, the spectrum is very sensitive to the surface structure. This indicates that care must be used when comparing theoretical and experimental results, as apparently small differences in the atomic arrangement may give rise to substantial differences in the band structure close to the Fermi level, and also to substantial differences in the matrix elements entering the definition of absorption spectra. Differences are also visible at the TDLDA level (see Fig. 4.2.12c), especially at low energy space, where transitions between levels close to the top of the valence bands and bottom of the conduction bands are involved. An analysis of the band

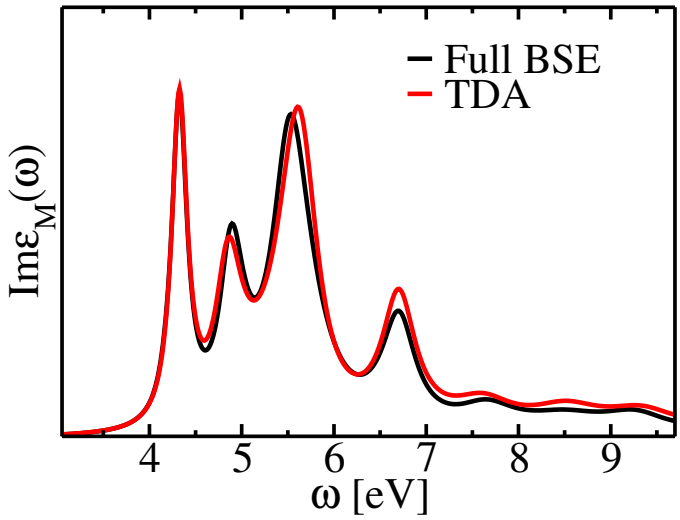

Figure 4.2.9: Spectra of 0.4 nm Si nanowire grown in the [001] direction compuated by solving the BSE with and without the Tamm Dancoff approximation (TDA). Calculations were carried out with a kinetic energy cutoff of 12 Ry. The technique of Refs. [62, 69] was used to evaluate the Fock operator and we adopted a Coulomb cutoff for the dielectric matrix. The scissor operator was obtained by computing the difference between the lowest energy gap within LDA and G_0W_0. We included 72 eigenvectors to evaluate the dielectric matrix, 16 k-points (kpts) in the BZ sampling, and the cell lateral dimension (L) is 37 a.u.

structure for the two geometries (not shown) reveals that the position of levels close to the top of the valence bands is greatly influenced by the surface structure (e.g. the HOMO of the wire with a canted surface is 0.2 eV lower than the one of the wire with a symmetric surface). The first peak to which the HOMO has a large contribution is blue shifted in the wire with a canted surface. However, in the wire with a canted surface the main excitonic peak is red shifted and merged with the first peak, indicating a stronger exciton binding. Before summarizing our results in section 4.2.6, we briefly discuss the efficiency of our technique, in the next section.

4.2.4 Efficiency of calculations of absorption spectra within density matrix perturbation theory

The scaling and overall efficiency of the technique used here to solve the BSE have been discussed in Ref. [33]. In this section we point out additional advantages of the approach and present ways to further speed up the calculations by taking advantage of the localization of dielectric eigenvectors in Fourier space.

As shown by Eq. 4.2.1, the evaluation of the screened Coulomb interaction involves

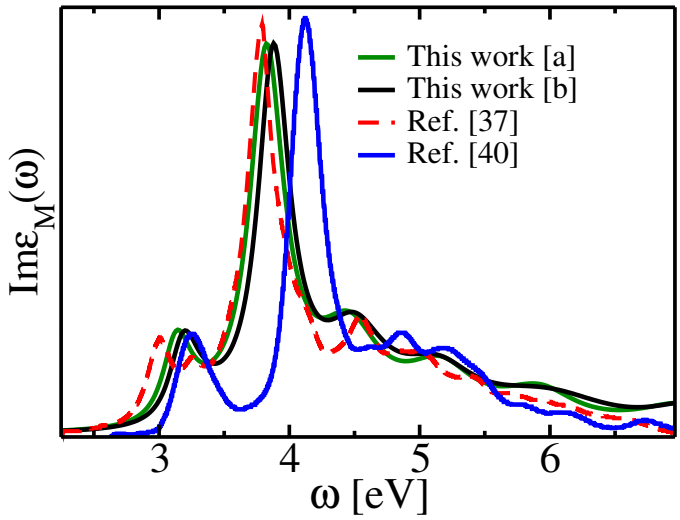

Figure 4.2.10: Spectra of a 0.8 nm Si nanowire grown in the [110] direction, as obtained in this work and in Ref. [313] and Ref. [316]. In both [a] and [b] we used a kinetic energy cutoff of 12 Ry to solve the Kohn Sham equations (30 Ry in Ref. [313], 12 Ry in Ref. [316]), the technique of Refs. [62, 69] to evaluate the Fock operator (the Random Integration Method was used in Ref. [313], a cylindrical Coulomb cutoff was used in Ref. [316]). In [a] we used a cell size of 50 a.u. (same as Refs. [313, 316]), and 16 k points, (16 k points in Ref. [313], 192 k points in Ref. [316]) for the BZ sampling and a Coulomb cutoff[311] to evaluate the dielectric matrix (see text). In [b] we did not use any cutoff for the dielectric matrix but extrapolated the spectrum as a function of cell size, by performing calculations with cells of 50, 60 and 70 a.u. In this case, the head of the dielectric matrix was computed from the inverse dielectric constant. In both [a] and [b] we included 114 eigenvectors in the evaluation of dielectric matrix. The scissor operator was obtained by computing the difference between the lowest energy gap within LDA and G_0W_0 (A scissor operator was also used in Ref. [313], G_0W_0 quasi particel energies were instead used in Ref. [316]).

the calculations of the following integral:

$$\int (\varepsilon^{-1}(\mathbf{r},\mathbf{r}'';\mathbf{q}) - \delta(\mathbf{r},\mathbf{r}''))v(\mathbf{r}'',\mathbf{r}')d\mathbf{r}''\rho_{v,\mathbf{k}}^{v',\mathbf{k}'}(\mathbf{r}')d\mathbf{r}'$$
$$= \frac{4\pi}{\Omega^2}\sum_i(\lambda_i^{-1}-1)\sum_{\mathbf{G}'}\frac{\mathbf{v}_i(\mathbf{G}'+\mathbf{q}')}{\mathbf{q}'+\mathbf{G}'}.e^{i(\mathbf{G}'+\mathbf{q}').r}.\sum_{\mathbf{G}}\frac{\mathbf{v}_i^+(\mathbf{G}+\mathbf{q})}{\mathbf{q}+\mathbf{G}}.\rho_{v,\mathbf{k}}^{v',\mathbf{k}'}(\mathbf{G}) \tag{4.2.9}$$

We found that the summation over G vectors can be carried out using a much smaller cutoff than that used for the charge density and even the wavefunctions. In

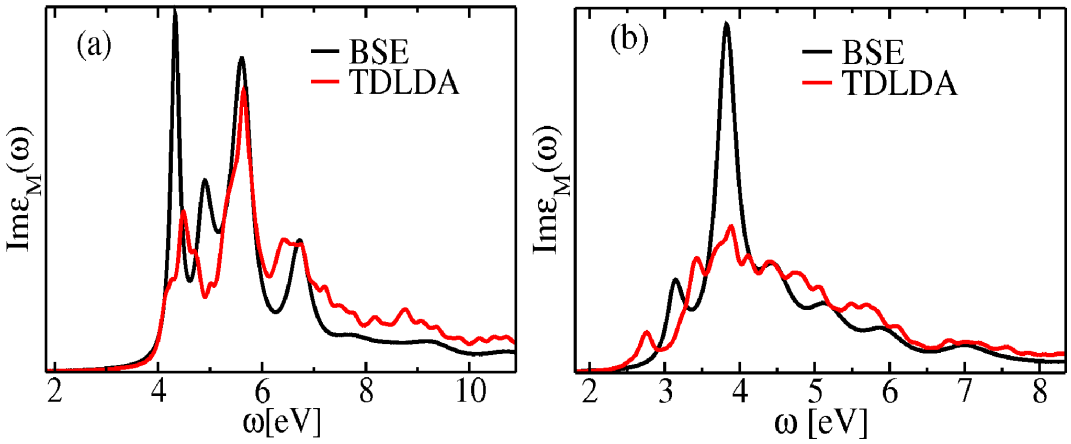

Figure 4.2.11: Spectra of Si nanowires compuated by solving the BSE and obtained within TDLDA. (a) 0.4 nm Si nanowire grown in the [001] direction; (b) 0.8 nm Si nanowire grown in the [110] direction. The numerical parameters used in the calculations are the same as those of Fig. 4.2.10 and Fig 4.2.8.

Fig. 4.2.13 we show for which cutoff ($\bar{E}_{cut}$) one may recover 90, 99 and 99.9 % of their norm. We find that a cutoff of $\simeq 6$ (3) Ry yields an error in the evaluation of the norm that is less than 1 (10) %. It turns out that even by allowing an error of about 10% in the norm one obtains spectra that are well converged. Fig. 4.2.14 shows the BSE spectra of a SiNW in the [001] growth direction, with 0.4nm diameter, computed by truncating the sums over G vectors in Eq.4.2.9 to 3, 6 and 48 Ry, respectively. Results obtained with 6 and 48 Ry (the cutoff used for the charge density in these calculations) are nearly identical, with relatively small differences with respect to those obtained with only 3 Ry. Our findings imply that the calculation of the screened Coulomb interaction may be considerably sped up by performing all Fourier transforms on grids that are much smaller than those used for the wavefunctions and charge density.

In summary, in this section we have presented calculations of absorption spectra of thin Si NWs using a technique to solve the BSE based on density matrix perturbation theory[33, 30]. Within this approach, the static BSE equation is derived from the linearized quantum Liouville equation, and solved in the frequency domain by employing the iterative algorithm proposed in Refs. [66, 317]. The dielectric matrix ϵ entering the definition of the screened Coulomb interaction is not explicitly diagonalized; rather we use a spectral decomposition[60, 61, 62]of ϵ and iteratively compute its eigenvalues and eigenvectors, using density functional perturbation theory[53].

We have shown that it is sufficient to compute a small number of eigenvalues and eigenvectors of ϵ to obtain fully converged spectra of nanowires. Similar results have been found for small molecules and Si nanoclusters[33]. An additional advantage of the spectral decomposition of ϵ regards the control of convergence of

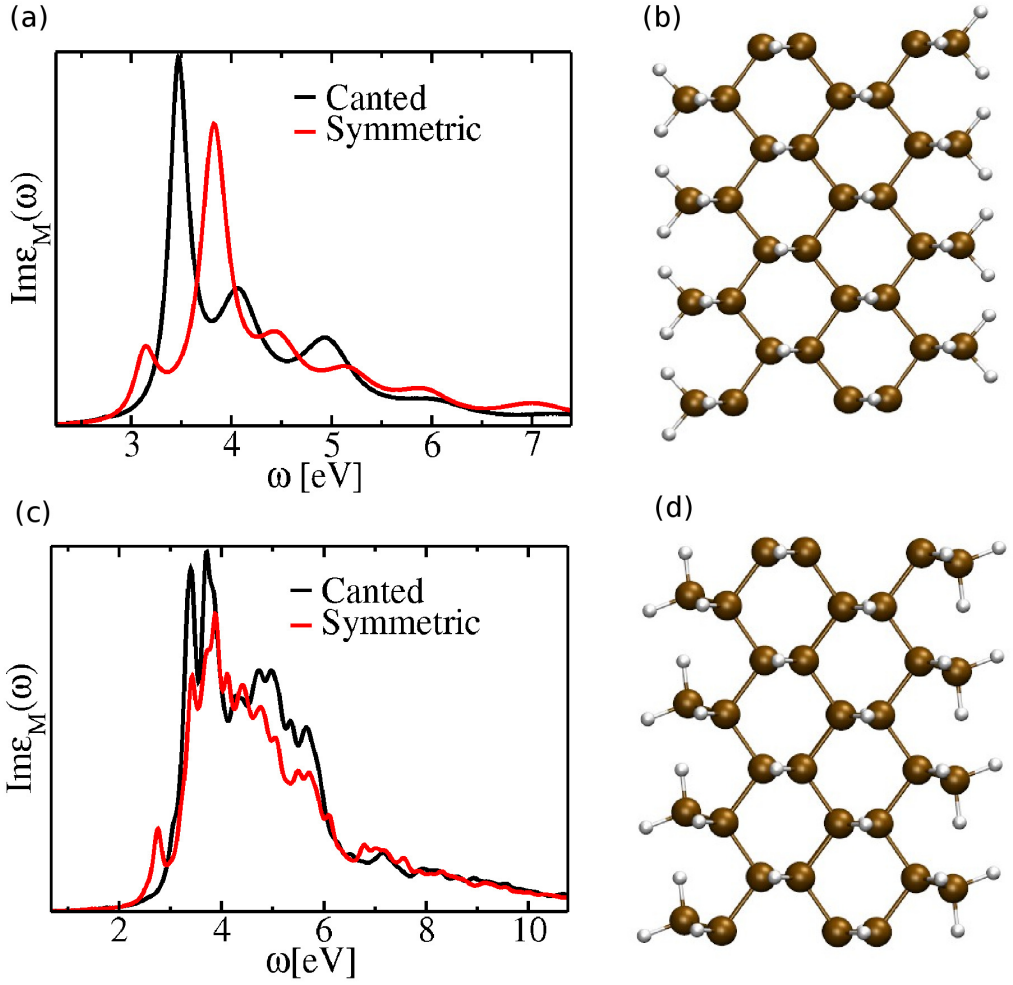

Figure 4.2.12: Spectra of a 0.8 nm Si nanowire grown in the [110] direction with canted (d) and symmetric (b) surface geometries. (a) BSE spectra for Si NWs with different surface geometries. We used a cell size of 50 a.u., 16 k points for the BZ sampling , a kinetic energy cutoff of 12 Ry to solve the Kohn Sham equations, the technique of Refs. [62, 69] to evaluate the Fock operator, and a Coulomb cutoff[311] to evaluate the dielectric matrix. We included 114 eigenvectors in the evaluation of dielectric matrix. A scissor operator was obtained by computing the difference between the lowest energy gap within LDA and G_0W_0. (c) TDLDA spectra for Si NWs with different surface geomentries, obtained with a cubic cell of lateral dimension equal to 50 a.u. and 16 k-points for the BZ sampling.

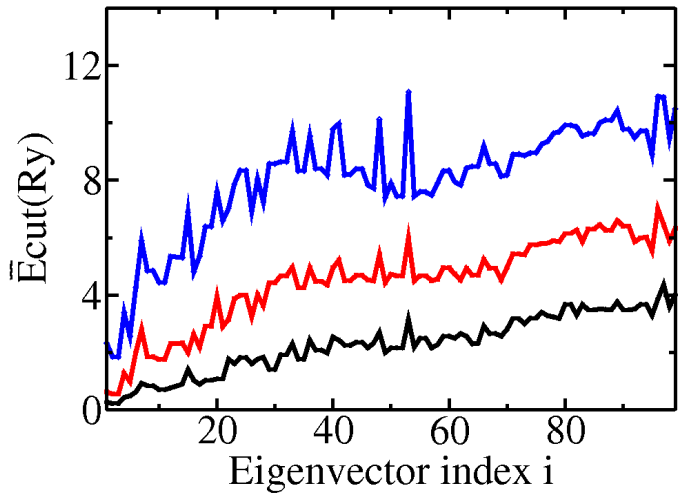

Figure 4.2.13: The cutoff used to represent the square moduli of the dielectric eigenvectors as a function of the number of eigenvectors for a 0.4 nm Si nanowire grown in the [100] direction. $\bar{E}_{cut}$ is the kinetic energy cutoff such that $\sum_{\mathbf{G}}^{\bar{\mathbf{G}}_{max}} \frac{|\mathbf{v}_i(\mathbf{G}+\mathbf{q})|}{|\mathbf{G}+\mathbf{q}|} = C * \sum_{\mathbf{G}}^{\mathbf{G}_{max}} \frac{|\mathbf{v}_i(\mathbf{G}+\mathbf{q})|}{|\mathbf{G}+\mathbf{q}|}$ where $C = 0.9, 0.99, 0.999$ for the black, red and blue curves, respectively, and $\bar{E}_{cut} = \frac{1}{2m_e}|\mathbf{k}+\bar{\mathbf{G}}_{max}|^2$. $\mathbf{G}_{max}$ corresponds to the maximum G vectors used to represent the charge density.

the calculations of spectra, which can be achieved in a straightforward manner by systematically increasing the number of eigenvalues and eigenvectors included in the spectral decomposition (Eq. 4.1.25). We have also found that the eigenvectors of the dielectric matrix exhibit good localization properties in Fourier space, and thus they can be represented with a cutoff much smaller than that used for the single particle electronic orbitals, leading to a substantial computational saving.

In addition, we have shown that the divergence in the Fock operator can be accurately and efficiently integrated by using the scheme proposed by Gygi and Baldereschi [69, 62] also in the case of wires. Such a scheme is superior to the one employing a Coulomb cutoff, in terms of both efficiency and control of convergence as a function of k points and cell size. The convergence of absorption spectra as a function of cell size is much more delicate at the BSE level of theory than within TDHF. This originates from the slow convergence of the head of the dielectric matrix as a function of cell sizes. In the BSE case we have found that the most accurate and computationally efficient approach consists in using the cutoff procedure proposed in Ref. [311] to compute the dielectric matrix.

Our analysis of the solutions of the BSE for semi-infinite systems has shown how to control all the numerical parameters entering the calculation and thus how to evaluate error bars on computed spectra. It is key to take into account numerical

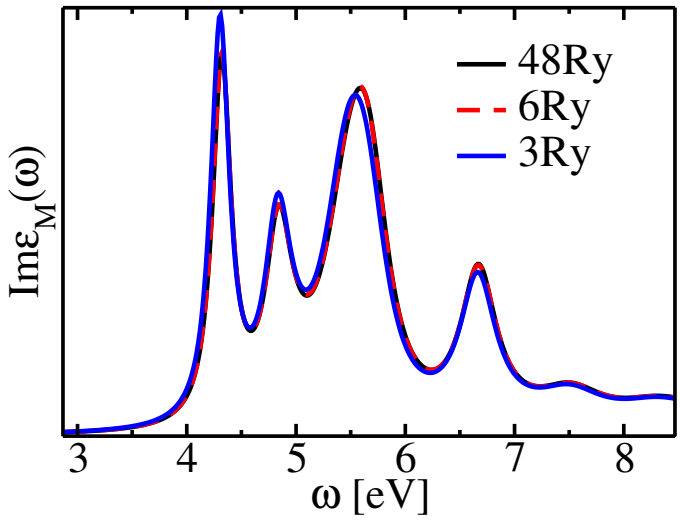

Figure 4.2.14: Convergence of the BSE spectrum of a 0.4 nm Si nanowire grown in the [001] direction, as a function of the cutoff used to represent the square moduli of the dielectric eigenvectors. Calculations were carried out with a kinetic energy cutoff of 12 Ry for the solution of the Kohn-Sham equations, and a cell edge of 37 a.u. We used the technique of Refs. [62, 69] to evaluate the Fock operator and a Coulomb cutoff[311] for the dielectric matrix (see text). A scissor operator was obtained by computing the difference between the lowest energy gap within LDA and G_0W_0.

errors and the convergence criteria used in the calculation, when comparing with experiments and with results obtained using the same level of theory but different algorithms.

The workload of the algorithm used here to compute absorption spectra scales as that of Hartree-Fock ground state calculations, and therefore our approach is suitable for computations using large basis sets (e.g. plane wave calculations) and it is scalable to systems with hundreds of electrons.

Finally we have presented calculations of absorption spectra of wires with different surface geometries, indicating that even small differences in atomic configurations may lead to substantial changes in the spectrum.

Chapter 5

Summary and conclusions

This dissertation focused on the study of electronic excited state properties of bulk systems and nanostructured materials by using advanced theoretical and computational techniques based on first principles, encompassing Density Functional Theory (DFT), many body perturbation theory (MBPT) and time-dependent DFT. We both developed post-DFT methods and computer codes for accurate predictions of photoemission and absorption of light by semiconducting and insulating materials, and we applied these techniques to promising systems for use as photocathode and photoanode in water splitting devices.

The many body perturbation theory techniques include the GW approximation for the study of photoemission processes and the Bethe-Salpeter Equation for the calculation of absorption spectra including excitonic effects. We also used first-principles calculation to predict the best alignment between the valence and conduction bands of oxides and the redox potential of water.

MBPT was applied to study semiconducting solids , semiconducting nanowires, tungsten oxide solids and $CuW_{1-x}Mo_xO_4$ solid solutions. The choice of these materials was motivated by a collaboration with two experimental groups: that of Prof. N.S.Lewis at Caltech, where silicon wires and tungsten oxide based materials are being explored as promising, cheap and abundant light absorbers, for water reduction and oxidation respectively; and the group of Prof. K-S.Choi at University of Wisconsin, Madison where several promising solid solutions for water oxidation were synthesized.

Below we summarize in more details each of the chapters. The theory and the numerical methods were presented in Section 2 and the examples of band edge calculations and absorption spectra were given in Sections 3 and 4, respectively.

In particular, we presented the basic definitions of Green's function theory and introduced the equations satisfied by single and two-particle Green's functions, the Dyson's equation [35, 17] and the Bethe Salpeter Equation [26](BSE), respectively. The poles of the single particle Green's function represent the energies necessary to add or remove an electron from a given solid or molecule. These energies are directly

comparable to those measured, e.g. in photoemission experiments. The poles of the correlation function defined from the two-particle Green's functions correspond to neutral excitation energies of interacting electrons. These neutral excitations may be, for example, an electron and a hole in a semiconductor, created by the interaction with incident light, and they are directly related to those measured in absorption experiments.

The Dyson's equation relates the single-particle Green's function to the effective many body potential of interacting electrons. Such complex interaction potential is called self-energy, and one may define a Schrödinger-like equation where the self-energy enters as a mean field potential acting on single-particle states. Those, among such states, with a long lifetime are called quasi-particles. The concepts of self-energy and quasi-particles are central concepts in MBPT, and in the interpretation of spectroscopic measurements of solids and molecules.

While the single-particle Green's function satisfies the Dyson's equation, the two body correlation function satisfies the BSE. The self-energy enters the Dyson's equation, while the derivative of the self-energy with respect to the single-particle Green's function enters the BSE . In the recent literature, solving the BSE to obtain absorption spectra has been the strategy of choice for most solids [27, 28, 29, 30]; in the case of molecules many calculations of absorption spectra are carried out using time dependent DFT [66, 318, 319, 320]. We emphasize that the BSE may be used for both molecules and solids and, in principle, for any material, irrespective of its morphology.

After introducing the basic concepts of Green's function theory, we discussed their relation to the key concepts entering linear response theory, including reducible and irreducible polarizabilities and the dielectric matrix. We used linear response theory to describe optical absorption experiments because the electric field of the incident light (the perturbation) is small compared to the internal field of the system. One of the key quantities of linear response theory and MBPT is the dielectric matrix, which describes how an external perturbing potential is screened within a solid and a molecule, by the presence of interacting electrons. The dielectric matrix is also used to define an effective, screened Coulomb potential (W) acting among the electrons. Using a perturbative series in terms of the screened Coulomb potential and an approximation of the self-energy in terms of such potential, we introduced the GW approximation [42] to compute quasiparticle energies. Calculations at the GW level of theory represent the most advanced computations of band structures and band edges carried out at present for complex materials, including photoelectrodes.

Having established the basic concepts of Green's function, many body perturbation and linear response theories, we turned from theory to computation. We discussed numerical techniques to compute quasi-particle energies and optical spectra, with emphasis on algorithms that do not require the explicit calculation of empty (virtual) single particle states. Such algorithms are instrumental in making possible

calculations of large systems and thus of realistic materials. We emphasize that in order to assess the accuracy of the theory, numerical parameters need to be controlled with great care. The same level of theory implemented with different levels of accuracy, from a numerical standpoint, may lead to qualitatively different predictions or interpretation of experiments. An example of such differences was presented for the optical gaps of WO_3.

In our discussion of specific calculations, we chose representative photoanode and photocathode materials and we summarized first-principles results of band edges and absorption spectra. We mostly focused on two oxide materials for the photoanode, WO_3 and $CuMo_xW_{1-x}O_4$ and on silicon for the photocathode including bulk silicon and silicon nanowires. We have proposed methods to modify the structural and electronic properties of oxides in order to improve their light absorption and band edge alignments with H_2O redox potential: for example, by small molecule intercalation for WO_3 and by Mo doping of $CuMo_xW_{1-x}O_4$ solid solution.

Although much progress was made in recent years to compute the electronic properties of molecules and solids from first principles, beyond approximate DFT theories, outstanding challenges remain in the theoretical and computational description of materials for photoelectrochemical energy conversion. An accurate determination of band alignments of photoeletrodes with water redox potentials requires the explicit calculation of the electronic properties of semiconductor-liquid interfaces. This remains a challenging task, as it encompasses the determination of the interface structural properties, and GW calculations of systems with possibly thousands of electrons. Although GW calculations for systems containing several hundreds of electrons [24, 23] are now feasible, they are not yet routine tasks: they require substantial computational resources and are thus difficult to carry out for multiple samples at a time (and multiple samples may be required, e.g. to investigate different types of defects at the interface). In addition simulations of liquid water themselves, even in the absence of interfaces, are challenging [321, 322], as the level of theory necessary to obtain, at the same time, reasonably good structural and electronic properties is yet unclear. Furthermore, one would need to simulate water with dissolved ions under different pH conditions, interfaced with a semiconductor, not just pure water. An accurate description of certain solvated ions (e.g. most of the anions) requires the use of hybrid functionals [323], as semi-local ones often yield an incorrect localization of charge around the anion, and hybrid functional calculations of liquid water are still computationally demanding [321] for large samples. As for absorption spectra, even with methods that avoid the explicit calculation of empty single particle states, the solution of the BSE for several hundreds of electrons is a heavy computational task. In addition improvements of the theory are necessary to include indirect transitions at the absorption onset and electron-phonon interaction.

We note in closing that here we only dealt with light absorbers for water splitting and thus with electronic structure calculations; clearly one will need to go beyond

static electronic properties and acquire capabilities to describe charge transport, in order to fully understand water splitting processes.

Chapter 6

Appendices

6.1 Appendix I: Structrual properties of WO_3

Computational Details

In most of our calculations we treated the exchange-correlation potential within either the local-density approximation (LDA) or the generalized gradient approximation (GGA) using the parameterization proposed by Perdew-Burke-Ernzerhof (PBE) [324]. In some cases we performed calculations using the hybrid functional PBE0 [144], the non local van der Waals functional DF2 [145, 146, 147, 148, 149], and the modified self-consistent field method proposed in Ref. [150]. We used norm-conversing Hartwigsen-Goedecker-Hutter (HGH) type [325] pseudopotentials. The pseudopotentials were extensively tested by comparing the computed lattice constant of WO_3 with experimental data, as well as with results obtained with the projected augmented wave (PAW) technique (see Tables 6.1 and 6.2). To optimize the cell parameters and the internal geometry of all crystal structures (variable cell calculations), we used a smooth kinetic-energy cutoff scheme [326]. We employed a $(3 \times 3 \times 3)$ Monkhorst-Pack k-point grid [166] for self-consistent ground state calculations for most phases other than simple cubic $(6 \times 6 \times 6)$ and a refined $(6 \times 6 \times 6)$ k-point grid for the projected density of states (PDOS) analysis for most phases other than simple cubic $(12 \times 12 \times 12)$.

Table 6.1: Equilibrium lattice constant (a_0) and band gap (E_g) of simple cubic WO_3 as obtained using the local density (LDA) and the gradient corrected approximation (PBE). Results obtained in Ref. [155] using the PBE functional are given within brackets for comparison.

	LDA	PBE
a_0 (Å)	3.79	3.81 [3.80]
E_g (eV)	0.54	0.63 [0.69]

Table 6.2: Equilibrium lattice parameters (a_0, b_0, c_0) of monoclinic WO_3 and its band gap (E_g) at both the experimental geometry $(V_{\rm exp})$ and the geometry optimized within density functional theory $(V_{\rm DFT,0})$. LDA/HGH (PAW) denotes results of calculations carried out within the LDA with HGH pseudopotentials [158],(PAW results with PAW pseudopotentials from the Ref. [153]); "PBE/HGH" denotes results of PBE calculations with HGH pseudopotentials, "vdW-DF2/HGH" denotes results of vdW-DF2 calculations [145, 146, 147, 148] with HGH pseudopotentials derived using the PBE approximation; and "Exp" experimental values from Ref [161]. "Δ-sol" denotes results of the modified self-consistent field (SCF) approach for solids (Ref.[150]). β is the angle between the a and c axes, and ΔV is the relative difference between the computed and the experimental volumes.

Method	lattice parameters (Å)			β (°)	ΔV (%)	E_g (eV)		E_g-Δ-sol (eV)	
	a_0	b_0	c_0			$V_{\rm exp}$	$V_{\rm DFT,0}$	$V_{\rm exp}$	$V_{\rm DFT,0}$
LDA/HGH	7.35	7.45	7.66	90.6	-0.9	1.87	1.30	2.90	2.39
LDA/PAW [153]	7.38	7.47	7.63	–	–		1.31		
PBE/HGH	7.44	7.67	7.77	90.6	4.5	1.97	1.53		
vdW-DF2/HGH	7.54	7.56	7.77	90.8	4.6	2.04	1.80		
Exp.	7.306	7.540	7.692	90.88		2.62			

Table 6.1 and Table 6.2 show the equilibrium lattice parameters and band gap of simple cubic WO_3 and of room temperature (RT) monoclinic WO_3, respectively. Due to a second order Jahn-Teller distortion, the simple cubic WO_3 structure is not stable at atmospheric pressure. However, a cubic phase of WO_3 was prepared at 0.66 Gpa and 700℃ [136]. For the simple cubic structure considered here, we found good agreement between our results and those obtained with ultrasoft pseudopotentials by Chatten et al [155]. In the case of monoclinic WO_3, we evaluated the band gap both at the experimental and at the DFT-optimized geometry (including cell parameter optimization). We denote the corresponding unit cell parameters as $V_{\rm exp}$ and $V_{\rm DFT,0}$ respectively, where the subscript "0" in $V_{\rm DFT,0}$ refers to the case of the pure WO_3 crystal. Our LDA results are in good agreement with previous PAW calculations [153] and the predicted equilibrium volume deviates from experiment by less than 1%, whereas PBE overestimates the equilibrium volume by 5%.

6.2 Appendix II: Band edges of WO_3

In appendix 6.2.1 and 6.2.2, we report the computational details of ΔSCF and G_0W_0 calculations, respectively.

6.2.1 Computational details of ΔSCF calculations

We computed the band gap of WO_3 using the ΔSCF method proposed in Ref [11] as $E_g = [E(N_0 + n) + E(N_0 - n) - 2E(N_0)]/n$, where N_0 is the number of valence electrons in the unit cell and $n = N_0/N^*$, where N^* is the number of electrons assumed to belong to the exchange and correlation (XC) hole; N^* was parametrized for hundreds of compounds in Ref [11]. For our WO_3 calculations (LDA XC functional and spd valence electrons), $N^* = 63$. The band gap was computed at the room temperature experimental lattice constants. In the equation defining E_g, E is the total energy of the solid. The calculations were performed for charged periodic cells with neutralizing backgrounds. We note that the ΔSCF method of Ref [11] only yields the smallest band gap of the solid and it can not be used to compute the direct band gap for materials with indirect fundamental gaps. The results of ΔSCF calculations are reported in Table 3.7 and Table 3.8 for simple cubic and RT-monoclinic WO_3, respectively.

6.2.2 Computational details of G_0W_0 calculations

In our G_0W_0 calculations we used the plasmon pole approximation(PPA) [327] to represent the frequency dependence of the dielectric matrix. PP models have proven to be relatively accurate for some energy bands of semiconductors and insulators, such as Si, Ge and LiCl [20]. However, Ref [197] found that the use of the Hybertsen-Louie PPA [20] leads to an overestimate of the gap of TiO_2 by 0.7-0.9 eV [197]. In addition, in Ref [59], the Hybertsen-Louie (HL) and von der LindenHorsch (vdLH) PP models were shown to strongly overestimate the band gap of ZnO compared with the full frequency integration, e.g. the contour-deformation (CD) approach [328]. Interestingly, the Godby-Needs (GN) [327] PP model gave results close to the CD approach for ZnO, and the convergence of GW calculations utilizing this model, with respect to the number of empty bands, was faster than that of the CD approach. Therefore we adopted the GN PP model and, for the case of the simple cubic structure, we compared the results with those of direct real frequency integration [329, 330] (RA, see Fig. 6.2.1), as implemented in the YAMBO package [90]. At the Γ point, the difference between G_0W_0 eigenvalues obtained with RA and the PPA (GN) was found to be less than 0.1 eV, while the difference between the direct band gap values is 0.14.

We also tested the convergence of the G_0W_0 direct band gap at Γ with respect to the number of bands included in the calculation (see Fig. 6.2.2), when using the GN model. For the simple cubic phase, the G_0W_0 direct gap extrapolated using the fitted function $E(N) = E_0 - b.exp(-N/c)$ is 2.76 eV (see Fig. 6.2.2 (left), where in the fit we used 6 points corresponding to the inclusion of 200 to 700 bands); the extrapolated value differs by only 0.05 eV from the one obtained with 300 bands. For the RT-monoclinic phase, the convergence was found to be slightly slower than

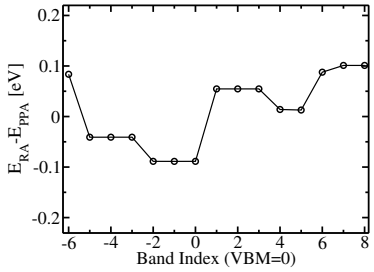

Figure 6.2.1: The difference between G_0W_0 eigenvalues at Γ for simple cubic WO_3, obtained using a plasmon pole approximation (E_{PPA}) and integration along the real axis (E_{RA}).

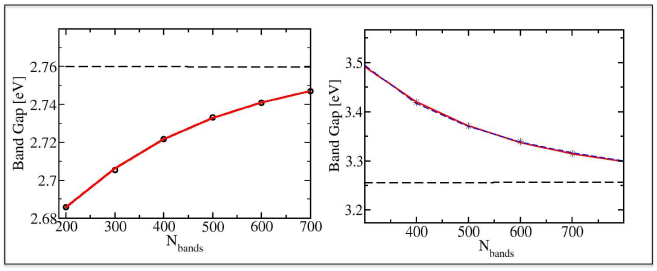

Figure 6.2.2: G_0W_0 direct band gap at Γ as a function of the number of bands (N_{bands}) included in the calculation, for simple cubic WO_3 (left panel) and RT-monoclinic WO_3 (right panel). Spheres and stars represent the calculated G_0W_0 gaps using the PPA [327] for simple cubic and RT-monoclinic WO_3, respectively. The results are fitted using two different functional forms described in the text, and displayed as red ($E(N) = E_0 - b.exp(-N/c)$) solid line and blue dotted line($E(N) = E_0 - b/N$).

for the simple cubic phase; we applied two different empirical fitting functions (see Fig. 6.2.2 right panel, where in the fit we used 6 points corresponding to the inclusion of 300 to 800 bands): $E(N) = E_0 - b/N$ and $E(N) = E_0 - b.exp(-N/c)$ which gave extrapolated values of 3.18 and 3.26 eV, respectively. The latter has a smaller root-mean-square relative error, therefore we retained this value as the best computed one. It differs by less than 0.05 eV from the band gap computed with 800 bands (3.30 eV). The numerical parameters entering our G_0W_0 calculations are: 37.5 Ry(16 Ry) for the size of the dielectric matrix and screened Coulomb potential of simple cubic (RT-monoclinic) WO_3, which yielded converged eigenvalues within 0.1 eV compared to 60 Ry energy cutoff for the dielectric matrix; we used 6×6×6 (3×3×3) kpts sampling for simple cubic (RT-monoclinic) WO_3 and 120 Ry for the ground state wavefunctions.

We also computed G_0W_0 eigenvalues for band edges at different k points (Ta-

ble 6.3).

Table 6.3: Valence band maximum (VBM), conduction band minimum (CBM) and fundamental gap computed using DFT/LDA and G_0W_0 methods for RT-monoclinic WO_3 at different k points.

	Γ	B	Z	D	Y	A	C	E
VBM								
LDA	0	-0.21	-0.024	-0.36	-0.14	-0.33	-0.48	-0.47
G_0W_0	0.29	0.025	0.26	-0.11	0.094	-0.12	-0.25	-0.24
CBM								
LDA	1.81	2.65	1.84	3.11	2.16	3.53	3.08	3.75
G_0W_0	3.59	4.49	3.62	4.98	3.98	5.42	4.93	5.67
Gap								
LDA	1.81	2.92	1.87	3.47	2.30	3.86	3.57	4.22
G_0W_0	3.30	4.46	3.36	5.09	3.88	5.54	5.18	5.91

The smallest LDA and G_0W_0 band gaps are direct at Γ(see Table 6.3), although the VBM and CBM at Z (0,0,1) are very close (within 0.05 eV) to respective eigenvalues at Γ (see Table 6.3). In fact, the lowest conduction state is between Γ to Z with a G_0W_0 eigenvalue of 3.58 eV, which indicates that the difference between direct and indirect gaps is negligible in RT-monoclinic WO_3. As shown in Table 6.3, the G_0W_0 correction to the LDA gap is nearly the same at different k points, with variations less than 0.2 eV.

6.3 Appendix III: First-principles calculations of WO_3 clathrates

6.3.1 Computational Details

In the calculations of the intercalated systems, we primarily used the LDA. For N_2 intercalated RT-monoclinic WO_3, we used a $(1 \times 1 \times 1)$ unit cell containing 8 WO_3. Some calculations were performed with a $(3 \times 1 \times 1)$ unit cell containing 24 WO_3. The cell parameters optimized upon intercalation are denoted as $V_{\mathrm{DFT,doped}}$.We calculated the vibrational properties of inserted N_2 using density functional perturbation theory (DFPT), in the harmonic approximation and at the LDA level. We found that a plane wave cutoff of 140 Ry is sufficient to converge the vibrational frequencies within 5 cm^{-1} and bond lengths within 10^{-4} Å. For comparison, we performed calculations for gas phase N_2 in a cubic supercell with a lattice parameter of 15.9 Å.

For rare gas intercalated RT-monoclinic WO_3, similar to the case of N_2 intercalation, we used a $(1 \times 1 \times 1)$ unit cell containing 8 WO_3, and we obtained results for

structures relaxed with the optimized cell parameters found upon intercalation, and corresponding to the volume $V_{\mathrm{DFT,doped}}$.

We tested the accuracy of local DFT to describe the interaction and electronic coupling between WO_3 and the rare gas atoms, in the case of a simple molecule. The tetrahedral structure of the XeO_4 molecule is experimentally known and we computed the Xe-O bond length (d(Xe-O)) to validate our calculations. d(Xe-O) predicted by DFT/LDA (1.800 Å) is in satisfactory agreement with experiments [331] (1.736 Å) and with that obtained using the CCSD(T) method [332](1.758 Å). Our DFT/LDA result is in close agreement with the GGA results of Ref. [333] (1.82 Å)

6.3.2 Electronic Structure of N_2-Intercalated Simple Cubic WO_3

To separate structural effects from those of charge overlap between the molecule and the host lattice, we investigated the changes in the electronic structure of N_2 intercalated in simple cubic WO_3, as a function of N_2 concentration. We fixed the volume to that of pure simple cubic WO_3. The band gap of the oxide vanishes and the system becomes metallic with 1:1 (N_2:WO_3) ratio, at the LDA level (Fig. 6.3.1). However, a finite band gap (1.18 eV) was obtained by applying a modified ΔSCF method [150] corresponding to a reduction of 0.4 eV with respect to pure simple cubic WO_3. When one decreases the N_2 concentration to 1:8 (Fig. 6.3.2), the coupling between the N $2p$ states with those of WO_3 becomes weaker. The calculated LDA band gap is 0.52 eV which is only 0.02 eV lower than that of pure WO_3. The charge density maps (Fig. 6.3.3) show that the charge overlap at 1:8 N_2 intercalation is much smaller than that at 1:1 N_2 intercalation, consistent with the different magnitude of gap reduction observed in the two cases. N_2-intercalated RT-monoclinic WO_3 crystal ($1N_2$:$8WO_3$) exhibits a charge overlap of a similar magnitude as N_2 intercalated in simple cubic WO_3 at 1:8 ratio, indicating that the electronic effect of N_2 intercalation may lead to a similar band gap reduction (<0.1eV) in monoclinic and simple cubic WO_3.

6.3.3 Oxygen Vacancy and Nitrogen Substitution in Monoclinic WO_3

Here we compare the electronic structure of the crystal with O vacancies to that of N and N_2 substitutional crystals. The presence of oxygen vacancies in WO_3 has been extensively studied [155, 334, 335]. An oxygen vacancy per unit cell of room temperature monoclinic WO_3 leads to a decrease in the gap by 0.50 eV and to a shift of the absorption coefficient to lower energies. The PDOS of monoclinic WO_3 with two O vacancies in a unit cell (not shown) shows that the conduction band shifts downward, and the band gap is reduced to 0.9 eV, consistent with the results of

Ref. [334] and [335]. In addition, a small peak appears at the conduction band edge in the PDOS (not shown), which is not present in the PDOS of pure WO_3. This peak is mainly composed of W 5d states which can contribute to visible light absorption; however these states can also act as electron-hole recombination centers, leading to a decrease in the photocatalytic activity of WO_3. Similar results have been reported in Ref. [336] and [337] for an O vacancy in TiO_2.

In the presence of two substitutional N atoms, a sharp peak contributed by hybridized O and N 2p states appear near the VBM in the PDOS (not shown). The valence band is shifted upward, thus reducing the band gap by about 0.5 eV compared to that of pure WO_3. The band gap reduction by N substitution is consistent with that found in previous studies [221, 153]. Although the band gap reduction is a desired property, the sharp peak near the VBM suggests that localized p states have very low mobility and may act as carrier recombination centers, an undesired effect.

When an O atom is substituted with a N_2 molecule in one monoclinic WO_3 unit cell, a mid-gap impurity band appears in the band structure (not shown). Due to the small width of impurity bands, the absorption edge at low energy is not significantly enhanced. Overall our calculations showed that the most promising way of reducing the gap of WO_3 is by N_2 intercalation, as shown experimentally [129] and not by N or N_2 substitution.

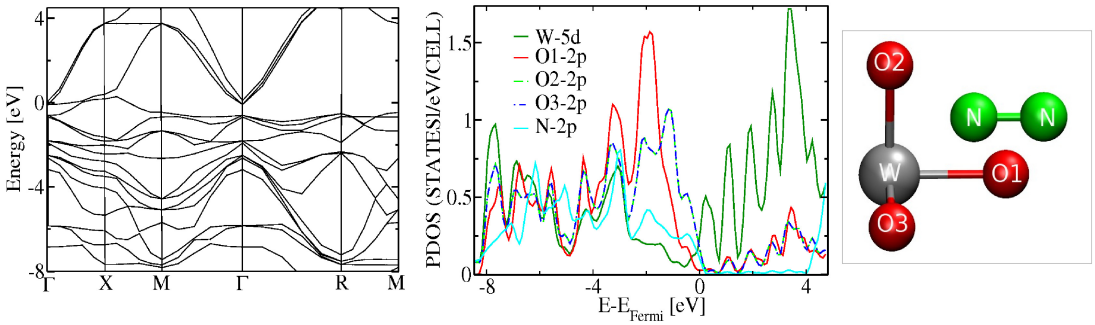

Figure 6.3.1: Band structure (left panel) and projected density of states (PDOS) (right panel) of N_2 intercalated simple cubic WO_3 ($1N_2$:$1WO_3$) as obtained by DFT/LDA calculations. In the right panel, the zero of energy has been chosen at the Fermi level (E_{Fermi}).

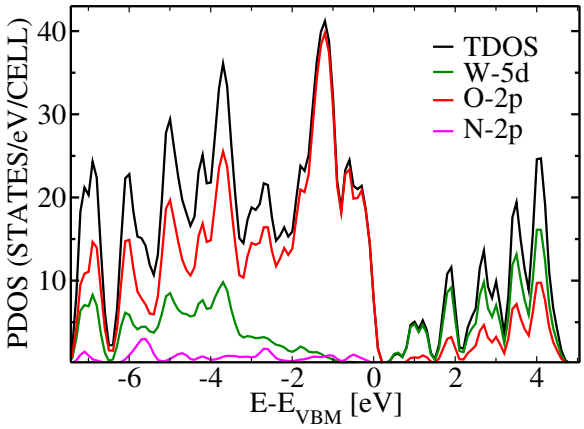

Figure 6.3.2: Projected density of states (PDOS) and total density of states (TDOS) of N_2 intercalated in simple cubic WO_3 at 1:8 ratio, as obtained by DFT/LDA calculations. The zero of energy has been chosen at the VBM (E_{VBM}).

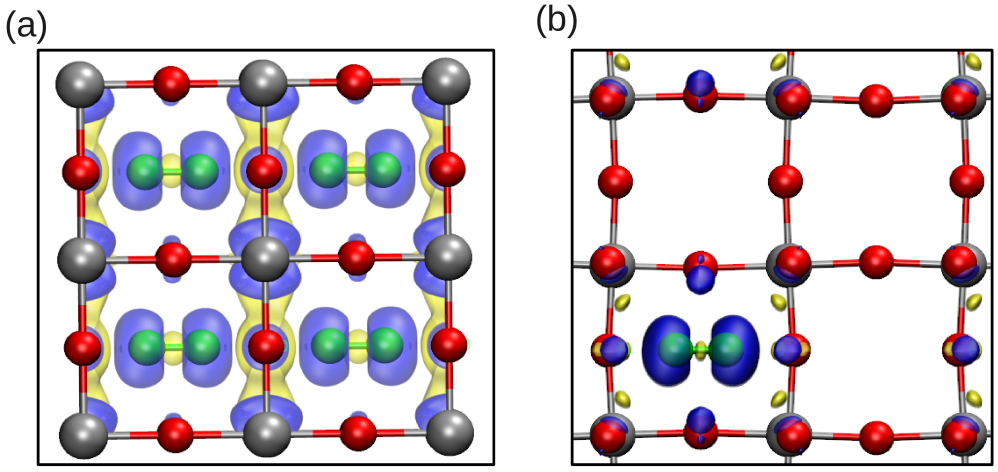

Figure 6.3.3: Electron density difference between pure simple cubic WO_3 and N_2 clathrates with concentration $1N_2$:$1WO_3$ (a) and $1N_2$:$8WO_3$ (b). Yellow (blue) indicates electron depletion (accumulation). W and O atoms are represented by silver and red spheres, respectively; N atoms are represented by green spheres. The figures show isosurfaces of charge 0.0015 e/a_0^3

6.4 Appendix IV: Absorption spectra of bulk systems

Time-reversal symmetry

In order to simplify the implementation described in Sec. 4.1.1, it is useful to exploit the time-reversal symmetry in the solution of the Bethe-Salpeter equation, which consists in assuming $v_{ext}(\mathbf{r},t) = v_{ext}(\mathbf{r},-t)$ in Eq. 4.1.4. The use of this symmetry yields a real perturbed density matrix in the frequency domain (Eq. 4.1.12), and the actual number of k-points needed in Eqs. 4.1.11-4.1.12 is decrease by about 50%. For the sake of simplicity we will first illustrate the time-reversal symmetry result for a generic real non-local Hamiltonian which satisfies the property $\hat{H}(\mathbf{r},\mathbf{r}',t) = \hat{H}(\mathbf{r},\mathbf{r}',-t)$. We consider the corresponding time-dependent Schrödinger equation

$$i\frac{d\phi_{v\mathbf{k}}(\mathbf{r},t)}{dt} = \int \hat{H}(\mathbf{r},\mathbf{r}',t)\phi_{v\mathbf{k}}(\mathbf{r}',t)d\mathbf{r}'. \tag{6.4.1}$$

By time inversion one has:

$$-i\frac{d\phi_{v\mathbf{k}}(\mathbf{r},-t)}{dt} = \int \hat{H}(\mathbf{r},\mathbf{r}',t)\phi_{v\mathbf{k}}(\mathbf{r},-t)d\mathbf{r}' \tag{6.4.2}$$

and the complex conjugate of this equation is:

$$i\frac{d\phi^*_{v\mathbf{k}}(\mathbf{r},-t)}{dt} = \int \hat{H}(\mathbf{r},\mathbf{r}',t)\phi^*_{v\mathbf{k}}(\mathbf{r},-t)d\mathbf{r}'. \tag{6.4.3}$$

By comparing Eq. 6.4.3 with the time-dependent Schrödinger equation corresponding to $-\mathbf{k}$

$$i\frac{d\phi_{v-\mathbf{k}}(\mathbf{r},t)}{dt} = \int \hat{H}(\mathbf{r},\mathbf{r}',t)\phi_{v-\mathbf{k}}(\mathbf{r},t)d\mathbf{r}' \tag{6.4.4}$$

we have that

$$\phi_{v-\mathbf{k}}(\mathbf{r},t) = \phi^*_{v\mathbf{k}}(\mathbf{r},-t); \tag{6.4.5}$$

by Fourier transforming Eq. 6.4.5 one has:

$$\phi_{v-\mathbf{k}}(\mathbf{r},\omega) = \phi^*_{v\mathbf{k}}(\mathbf{r},\omega). \tag{6.4.6}$$

It is important to note that $\hat{H}_{COHSEX}$ in Eq. 4.1.4 is a self-consistent Hamiltonian, namely it depends on the solution of the time-dependent Schrödinger equation. Under the assumption of Eq. 6.4.5, it is easy to see that the COHSEX Hamiltonian under

time-reversal symmetry transforms as $\hat{H}_{COHSEX}(\mathbf{r},\mathbf{r}',t) = \hat{H}^*_{COHSEX}(\mathbf{r},\mathbf{r}',-t)$. This property is consistent with the derivation of this appendix. Indeed for the COHSEX Hamiltonian Eq. 6.4.2 would become

$$-i\frac{d\phi_{v\mathbf{k}}(\mathbf{r},-t)}{dt} = \int \hat{H}_{COHSEX}(\mathbf{r},\mathbf{r}',-t)\phi_{v\mathbf{k}}(\mathbf{r},-t)d\mathbf{r}' = \int \hat{H}^*_{COHSEX}(\mathbf{r},\mathbf{r}',t)\phi_{v\mathbf{k}}(\mathbf{r},-t)d\mathbf{r}' \quad (6.4.7)$$

and Eq. 6.4.3 remains unchanged, when a complex conjugate operation is applied. Since $\phi_{v\mathbf{k}}(\mathbf{r},t) = \phi^{\circ}_{v\mathbf{k}}(\mathbf{r}) + \phi'_{v\mathbf{k}}(\mathbf{r},t)$ the properties in Eqs. 6.4.5-6.4.6 are still valid for perturbed orbitals, namely $\phi'_{v-\mathbf{k}}(\mathbf{r},t) = \phi'^*_{v\mathbf{k}}(\mathbf{r},-t)$ and $\phi'_{v-\mathbf{k}}(\mathbf{r},\omega) = \phi'^*_{v\mathbf{k}}(\mathbf{r},\omega)$. For this reason, assuming the time-reversal symmetry in the external time-dependent potential, the perturbed density matrix in Eq. 4.1.12 can be considered as real. Furthermore, since for every perturbed orbital at $\mathbf{k}$ we can obtain the corresponding $-\mathbf{k}$ by a simple complex conjugate operation, the total cost of the calculation is significantly decreased (except of the Γ point and the k-points at the boundaries).

Bibliography

[1] Lewis, Nathan S. and Nocera, Daniel G., "Powering the planet: Chemical challenges in solar energy utilization," *Proc Natl Acad Sci*, volume 103, no. 43, pp. 15729–15735, 2006

[2] Walter, Michael G., Warren, Emily L., McKone, James R., Boettcher, Shannon W., Mi, Qixi, Santori, Elizabeth A., and Lewis, Nathan S., "Solar Water Splitting Cells," *Chem Rev*, volume 110, no. 11, pp. 6446–6473, 2010

[3] Hohenberg, P. and Kohn, W., "Inhomogeneous Electron Gas," *Phys Rev*, volume 136, pp. B864–B871, Nov 1964

[4] Martin, Richard M., *Electronic Structure Basic Theory and Pratical Methods*, Cambridge University Press, 2004

[5] Kohn, W. and Sham, L. J., "Self-Consistent Equations Including Exchange and Correlation Effects," *Phys Rev*, volume 140, pp. A1133–A1138, 1965

[6] Herman, Frank, Van Dyke, John P., and Ortenburger, Irene B., "Improved Statistical Exchange Approximation for Inhomogeneous Many-Electron Systems," *Phys Rev Lett*, volume 22, pp. 807–811, Apr 1969

[7] Becke, A. D., "Density-functional exchange-energy approximation with correct asymptotic behavior," *Phys Rev A*, volume 38, pp. 3098–3100, Sep 1988

[8] Perdew, John P., Burke, Kieron, and Ernzerhof, Matthias, "Generalized Gradient Approximation Made Simple," *Phys Rev Lett*, volume 77, pp. 3865–3868, Oct 1996

[9] Koopmans, T, "ber die Zuordnung von Wellenfunktionen und Eigenwerten zu den Einzelnen Elektronen Eines Atoms," *Physica*, volume 1, no. 16, pp. 104 – 113, ISSN 0031-8914, 1934

[10] Jones, R. O. and Gunnarsson, O., "The density functional formalism, its applications and prospects," *Rev Mod Phys*, volume 61, pp. 689–746, Jul 1989

[11] Chan, M. K. Y. and Ceder, G., "Efficient Band Gap Prediction for Solids," *Phys Rev Lett*, volume 105, p. 196403, Nov 2010

[12] Runge, Erich and Gross, E. K. U., "Density-Functional Theory for Time-Dependent Systems," *Phys Rev Lett*, volume 52, no. 12, p. 997, 1984

[13] Botti, Silvana, Schindlmayr, Arno, Sole, Rodolfo Del, and Reining, Lucia, "Time-dependent density-functional theory for extended systems," *Reports on Progress in Physics*, volume 70, no. 3, p. 357, 2007

[14] Dreuw, A., Weisman, J. L., and Head-Gordon, M., "Long-range charge-transfer excited states in time-dependent density functional theory require non-local exchange," *J Chem Phys*, volume 119, pp. 2943–2946, August 2003

[15] Dreuw, A. and Head-Gordon, M., "Failure of Time-Dependent Density Functional Theory for Long-Range Charge-Transfer Excited States: The Zincbacteriochlorin Bacteriochlorin and eriochlorophyll Spheroidene Complexes," *J Am Chem Soc*, volume 126, p. 4007, 2004

[16] Onida, Giovanni, Reining, Lucia, and Rubio, Angel, "Electronic excitations: density-functional versus many-body Green's-function approaches," *Rev Mod Phys*, volume 74, no. 2, pp. 601–659, 2002

[17] Fetter, Alexander L. and Walecka, John Dirk, *Quantum Theory of Many-Particle Systems*, Dover, New York, 2003

[18] Hybertsen, Mark S. and Louie, Steven G., "First-Principles Theory of Quasiparticles: Calculation of Band Gaps in Semiconductors and Insulators," *Phys Rev Lett*, volume 55, pp. 1418–1421, 1985

[19] Godby, R. W., Schlüter, M., and Sham, L. J., "Accurate Exchange-Correlation Potential for Silicon and Its Discontinuity on Addition of an Electron," *Phys Rev Lett*, volume 56, pp. 2415–2418, Jun 1986

[20] Hybertsen, Mark S. and Louie, Steven G., "Electron correlation in semiconductors and insulators: Band gaps and quasiparticle energies," *Phys Rev B*, volume 34, pp. 5390–5413, Oct 1986

[21] Shaltaf, R., Rignanese, G.-M., Gonze, X., Giustino, Feliciano, and Pasquarello, Alfredo, "Band Offsets at the Si/SiO_2 Interface from Many-Body Perturbation Theory," *Phys Rev Lett*, volume 100, p. 186401, May 2008

[22] van Setten, M. J., Weigend, F., and Evers, F., "The GW-Method for Quantum Chemistry Applications: Theory and Implementation," *J Chem Theory Comput*, volume 9, no. 1, pp. 232–246, 2013

[23] Nguyen, Huy-Viet, Pham, T. Anh, Rocca, Dario, and Galli, Giulia, "Improving accuracy and efficiency of calculations of photoemission spectra within the many-body perturbation theory," *Phys Rev B*, volume 85, p. 081101, Feb 2012

[24] Umari, P., Stenuit, Geoffrey, and Baroni, Stefano, "Optimal representation of the polarization propagator for large-scale *GW* calculations," *Phys Rev B*, volume 79, p. 201104, May 2009

[25] Umari, P., Stenuit, Geoffrey, and Baroni, Stefano, "GW quasiparticle spectra from occupied states only," *Phys Rev B*, volume 81, p. 115104, Mar 2010

[26] Salpeter, E. E. and Bethe, H. A., "A Relativistic Equation for Bound-State Problems," *Phys Rev*, volume 84, pp. 1232–1242, Dec 1951

[27] Albrecht, Stefan, Onida, Giovanni, and Reining, Lucia, "Ab initio calculation of the quasiparticle spectrum and excitonic effects in *Li*2O," *Phys Rev B*, volume 55, no. 16, pp. 10278–10281, Apr 1997

[28] Albrecht, Stefan, Reining, Lucia, Del Sole, Rodolfo, and Onida, Giovanni, "Ab Initio Calculation of Excitonic Effects in the Optical Spectra of Semiconductors," *Phys Rev Lett*, volume 80, no. 20, pp. 4510–4513, 1998

[29] Rohlfing, M. and Louie, S. G., "Electron-hole excitations and optical spectra from first principles," *Phys Rev B*, volume 62, pp. 4927–4944, August 2000

[30] Rocca, Dario, Ping, Yuan, Gebauer, Ralph, and Galli, Giulia, "Solution of the Bethe-Salpeter equation without empty electronic states: Application to the absorption spectra of bulk systems," *Phys Rev B*, volume 85, p. 045116, Jan 2012

[31] Ramos, L. E., Paier, J., Kresse, G., and Bechstedt, F., "Optical spectra of Si nanocrystallites: Bethe-Salpeter approach versus time-dependent density-functional theory," *Phys Rev B*, volume 78, no. 19, p. 195423, November 2008

[32] Benedict, L. X., Puzder, A., Williamson, A. J., Grossman, J. C., Galli, G., Klepeis, J. E., Raty, J.-Y., and Pankratov, O., "Calculation of optical absorption spectra of hydrogenated Si clusters: Bethe-Salpeter equation versus time-dependent local-density approximation," *Phys Rev B*, volume 68, no. 8, p. 085310, August 2003

[33] Rocca, D., Lu, D., and Galli, G., "Ab initio calculations of optical absorption spectra: Solution of the Bethe-Salpeter equation within density matrix perturbation theory," *J Chem Phys*, volume 133, no. 16, p. 164109, October 2010

[34] Galitskii, V. M. and Migdal, A. B., *Soviet Phys JETP*, volume 7, p. 96, 1958

[35] Dyson, F. J., "The S Matrix in Quantum Electrodynamics," *Phys Rev*, volume 75, pp. 1736–1755, Jun 1949

[36] Hedin, Lars and Lundqvist, Stig, "Effects of Electron-Electron and Electron-Phonon Interactions on the One-Electron States of Solids," *Solid State Physics*, volume 23, pp. 1 – 181, 1970

[37] Tassi, M., Theophilou, Iris, and Thanos, S., "HartreeFock calculation for excited states," *International Journal of Quantum Chemistry*, volume 113, no. 5, pp. 690–693, ISSN 1097-461X, 2013

[38] Hirata, S., Podeszwa, R., Tobita, M., and Bartlett, R. J., "Coupled-cluster singles and doubles for extended systems," *J Chem Phys*, volume 120, p. 2581, 2004

[39] Dagens, L. and Perrot, F., "Hartree-Fock Band Structure and Optical Gap in Solid Neon and Argon," *Phys Rev B*, volume 5, pp. 641–648, Jan 1972

[40] Strinati, G., "Effects of dynamical screening on resonances at inner-shell thresholds in semiconductors," *Phys Rev B*, volume 29, no. 10, pp. 5718–5726, May 1984

[41] McLachlan, A. D. and Ball, M. A., "Time-Dependent Hartree-Fock Theory for Molecules," *Rev Mod Phys*, volume 36, no. 3, pp. 844–855, 1964

[42] Hedin, Lars, "New Method for Calculating the One-Particle Green's Function with Application to the Electron-Gas Problem," *Phys Rev*, volume 139, pp. A796–A823, 1965

[43] Schwinger, J., "On the Green's Functions of Quantized Fields. I," *Proc Natl Acad Sci*, volume 37, pp. 452–455, July 1951

[44] Inkson, John. C., *Many-body theory of solids: an introduction*, Plenum Press, New York, 1984

[45] Kang, Wei and Hybertsen, Mark S., "Enhanced static approximation to the electron self-energy operator for efficient calculation of quasiparticle energies," *Phys Rev B*, volume 82, p. 195108, Nov 2010

[46] Benedict, L. X., Shirley, E. L., and Bohn, R. B., "Optical Absorption of Insulators and the Electron-Hole Interaction: An Ab Initio Calculation," *Phys Rev Lett*, volume 80, pp. 4514–4517, May 1998

[47] Godby, R. W., Schlüter, M., and Sham, L. J., "Self-energy operators and exchange-correlation potentials in semiconductors," *Phys Rev B*, volume 37, pp. 10159–10175, Jun 1988

[48] Rohlfing, Michael and Louie, Steven G., "Electron-Hole Excitations in Semiconductors and Insulators," *Phys Rev Lett*, volume 81, no. 11, pp. 2312–2315, 1998

[49] Hybertsen, Mark S. and Louie, Steven G., "*Ab initio* static dielectric matrices from the density-functional approach. I. Formulation and application to semiconductors and insulators," *Phys Rev B*, volume 35, pp. 5585–5601, Apr 1987

[50] Godby, R. W. and Needs, R. J., "Metal-insulator transition in Kohn-Sham theory and quasiparticle theory," *Phys Rev Lett*, volume 62, pp. 1169–1172, Mar 1989

[51] Bauernschmitt, R. and Ahlrichs, R., "Treatment of electronic excitations within the adiabatic approximation of time dependent density functional theory," *Chem Phys Lett*, volume 256, pp. 454–464, 1996

[52] Baroni, Stefano and Resta, Raffaele, "*Ab initio* calculation of the macroscopic dielectric constant in silicon," *Phys Rev B*, volume 33, pp. 7017–7021, May 1986

[53] Baroni, Stefano, de Gironcoli, Stefano, Dal Corso, Andrea, and Giannozzi, Paolo, "Phonons and related crystal properties from density-functional perturbation theory," *Rev Mod Phys*, volume 73, no. 2, pp. 515–562, 2001

[54] Rohlfing, Michael, Krüger, Peter, and Pollmann, Johannes, "Efficient scheme for GW quasiparticle band-structure calculations with applications to bulk Si and to the Si(001)-(2×1) surface," *Phys Rev B*, volume 52, pp. 1905–1917, Jul 1995

[55] Blase, X., Attaccalite, C., and Olevano, V., "First-principles GW calculations for fullerenes, porphyrins, phtalocyanine, and other molecules of interest for organic photovoltaic applications," *Phys Rev B*, volume 83, p. 115103, Mar 2011

[56] Bruneval, F., "Ionization energy of atoms obtained from GW self-energy or from random phase approximation total energies," *J Chem Phys*, volume 136, no. 19, p. 194107, May 2012

[57] Adler, Stephen L., "Quantum Theory of the Dielectric Constant in Real Solids," *Phys Rev*, volume 126, pp. 413–420, Apr 1962

[58] Wiser, Nathan, "Dielectric Constant with Local Field Effects Included," *Phys Rev*, volume 129, pp. 62–69, Jan 1963

[59] Stankovski, M., Antonius, G., Waroquiers, D., Miglio, A., Dixit, H., Sankaran, K., Giantomassi, M., Gonze, X., Côté, M., and Rignanese, G.-M., "G^0W^0 band gap of ZnO: Effects of plasmon-pole models," *Phys Rev B*, volume 84, p. 241201, Dec 2011

[60] Wilson, H. F., Gygi, F., and Galli, G., "Efficient iterative method for calculations of dielectric matrices," *Phys Rev B*, volume 78, no. 11, p. 113303, September 2008

[61] Wilson, H. F., Lu, D., Gygi, F., and Galli, G., "Iterative calculations of dielectric eigenvalue spectra," *Phys Rev B*, volume 79, p. 245106, 2009

[62] Nguyen, Huy-Viet and de Gironcoli, Stefano, "Efficient calculation of exact exchange and RPA correlation energies in the adiabatic-connection fluctuation-dissipation theory," *Phys Rev B*, volume 79, p. 205114, May 2009

[63] Lu, Deyu, Li, Yan, Rocca, Dario, and Galli, Giulia, "*Ab initio* Calculation of van der Waals Bonded Molecular Crystals," *Phys Rev Lett*, volume 102, p. 206411, May 2009

[64] Davidson, E. R., *J Comput Phys*, volume 17, p. 87, 1975

[65] Car, R., Tosatti, E., Baroni, S., and Leelaprute, S., "Dielectric band structure of crystals: General properties and calculations for silicon," *Phys Rev B*, volume 24, no. 2, pp. 985–999, 1981

[66] Rocca, D., Gebauer, R., Saad, Y., and Baroni, S., "Turbo charging time-dependent density-functional theory with Lanczos chains," *J Chem Phys*, volume 128, no. 15, p. 154105, April 2008

[67] Rojas, H. N., Godby, R. W., and Needs, R. J., *Phys Rev Lett*, volume 74, pp. 1827–1830, Mar 1995

[68] Rostgaard, C., Jacobsen, K. W., and Thygesen, K. S., "Fully self-consistent GW calculations for molecules," *Phys Rev B*, volume 81, p. 085103, Feb 2010

[69] Gygi, F. and Baldereschi, A., "Self-consistent Hartree-Fock and screened-exchange calculations in solids: Application to silicon," *Phys Rev B*, volume 34, pp. 4405–4408, Sep 1986

[70] Friedrich, Christoph, Müller, Mathias C., and Blügel, Stefan, "Band convergence and linearization error correction of all-electron GW calculations: The extreme case of zinc oxide," *Phys Rev B*, volume 83, p. 081101, Feb 2011

[71] Giustino, Feliciano, Cohen, Marvin L., and Louie, Steven G., "GW method with the self-consistent Sternheimer equation," *Phys Rev B*, volume 81, p. 115105, Mar 2010

[72] Hübener, Hannes, Pérez-Osorio, Miguel A., Ordejón, Pablo, and Giustino, Feliciano, "Dielectric screening in extended systems using the self-consistent Sternheimer equation and localized basis sets," *Phys Rev B*, volume 85, p. 245125, Jun 2012

[73] Berger, J. A., Reining, Lucia, and Sottile, Francesco, "*Ab initio* calculations of electronic excitations: Collapsing spectral sums," *Phys Rev B*, volume 82, p. 041103, Jul 2010

[74] Berger, J. A., Reining, Lucia, and Sottile, Francesco, "Efficient *GW* calculations for SnO_2, ZnO, and rubrene: The effective-energy technique," *Phys Rev B*, volume 85, p. 085126, Feb 2012

[75] Bruneval, Fabien and Gonze, Xavier, "Accurate *GW* self-energies in a plane-wave basis using only a few empty states: Towards large systems," *Phys Rev B*, volume 78, p. 085125, Aug 2008

[76] Samsonidze, Georgy, Jain, Manish, Deslippe, Jack, Cohen, Marvin L., and Louie, Steven G., "Simple Approximate Physical Orbitals for *GW* Quasiparticle Calculations," *Phys Rev Lett*, volume 107, p. 186404, Oct 2011

[77] Stan, Adrian, Dahlen, Nils Erik, and van Leeuwen, Robert, "Levels of self-consistency in the GW approximation," *J Chem Phys*, volume 130, no. 11, p. 114105, 2009

[78] Kotani, Takao, van Schilfgaarde, Mark, and Faleev, Sergey V., "Quasiparticle self-consistent GW method: A basis for the independent-particle approximation," *Phys Rev B*, volume 76, p. 165106, Oct 2007

[79] van Schilfgaarde, M., Kotani, Takao, and Faleev, S., "Quasiparticle Self-Consistent *GW* Theory," *Phys Rev Lett*, volume 96, no. 22, p. 226402, Jun 2006

[80] Tamblyn, Isaac, Darancet, Pierre, Quek, Su Ying, Bonev, Stanimir A., and Neaton, Jeffrey B., "Electronic energy level alignment at metal-molecule interfaces with a *GW* approach," *Phys Rev B*, volume 84, p. 201402, Nov 2011

[81] Shishkin, M. and Kresse, G., "Self-consistent *GW* calculations for semiconductors and insulators," *Phys Rev B*, volume 75, p. 235102, Jun 2007

[82] Bruneval, Fabien, Vast, Nathalie, and Reining, Lucia, "Effect of self-consistency on quasiparticles in solids," *Phys Rev B*, volume 74, p. 045102, 2006

[83] Holm, B. and von Barth, U., "Fully self-consistent GW self-energy of the electron gas," *Phys Rev B*, volume 57, pp. 2108–2117, Jan 1998

[84] Del Sole, R., Reining, Lucia, and Godby, R. W., "GW Γ approximation for electron self-energies in semiconductors and insulators," *Phys Rev B*, volume 49, pp. 8024–8028, Mar 1994

[85] Bruneval, Fabien, Sottile, Francesco, Olevano, Valerio, Del Sole, Rodolfo, and Reining, Lucia, "Many-Body Perturbation Theory Using the Density-Functional Concept: Beyond the GW Approximation," *Phys Rev Lett*, volume 94, p. 186402, May 2005

[86] Tiago, M. L. and Chelikowsky, J. R., "Optical excitations in organic molecules, clusters, and defects studied by first-principles Green's function methods," *Phys Rev B*, volume 73, no. 20, p. 205334, May 2006

[87] Onida, G., Reining, L., Godby, R. W., del Sole, R., and Andreoni, W., "Ab Initio Calculations of the Quasiparticle and Absorption Spectra of Clusters: The Sodium Tetramer," *Phys Rev Lett*, volume 75, pp. 818–821, July 1995

[88] Rohlfing, M. and Louie, S. G., "Excitonic Effects and the Optical Absorption Spectrum of Hydrogenated Si Clusters," *Phys Rev Lett*, volume 80, pp. 3320–3323, April 1998

[89] Walker, Brent, Saitta, A. Marco, Gebauer, Ralph, and Baroni, Stefano, "Efficient Approach to Time-Dependent Density-Functional Perturbation Theory for Optical Spectroscopy," *Phys Rev Lett*, volume 96, no. 11, p. 113001, 2006

[90] Marini, Andrea, Hogan, Conor, Grning, Myrta, and Varsano, Daniele, "yambo: An ab initio tool for excited state calculations," *Comput Phys Commun*, volume 180, no. 8, pp. 1392 – 1403, ISSN 0010-4655, 2009

[91] Deslippe, J., Samsonidze, G., Strubbe, D. A., Jain, M., Cohen, M. L., and Louie, S. G., "BerkeleyGW: A massively parallel computer package for the calculation of the quasiparticle and optical properties of materials and nanostructures," *Comput Phys Commun*, volume 183, pp. 1269–1289, June 2012

[92] Martin-Samos, L. and Bussi, G., "SaX: An open source package for electronic-structure and optical-properties calculations in the GW approximation," *Comput Phys Commun*, volume 180, pp. 1416–1425, August 2009

[93] Tamm, I., *J Phys Moscow*, volume 78, p. 382, 1945

[94] Benedict, Lorin X., Shirley, Eric L., and Bohn, Robert B., "Theory of optical absorption in diamond, Si, Ge, and GaAs," *Phys Rev B*, volume 57, no. 16, pp. R9385–R9387, 1998

[95] Benedict, L. X. and Shirley, E. L., "Ab initio calculation of $\epsilon_2(\omega)$ including the electron-hole interaction: Application to GaN and CaF_2," *Phys Rev B*, volume 59, pp. 5441–5451, February 1999

[96] Hahn, P. H., Schmidt, W. G., Seino, K., Preuss, M., Bechstedt, F., and Bernholc, J., "Optical Absorption of Water: Coulomb Effects versus Hydrogen Bonding," *Phys Rev Lett*, volume 94, p. 037404, Jan 2005

[97] Olevano, Valerio and Reining, Lucia, "Excitonic Effects on the Silicon Plasmon Resonance," *Phys Rev Lett*, volume 86, no. 26, pp. 5962–5965, Jun 2001

[98] Ma, Yuchen, Rohlfing, Michael, and Molteni, Carla, "Excited states of biological chromophores studied using many-body perturbation theory: Effects of resonant-antiresonant coupling and dynamical screening," *Phys Rev B*, volume 80, p. 241405, 2009

[99] Gruning, M., Marini, A., and Gonze, X., "Exciton-plasmon states in nanoscale materials: breakdown of the Tamm-Dancoff approximation," *Nano lett*, volume 9, pp. 2820–2824, 2009

[100] Hahn, P. H., Schmidt, W. G., and Bechstedt, F., "Molecular electronic excitations calculated from a solid-state approach: Methodology and numerics," *Phys Rev B*, volume 72, no. 24, p. 245425, December 2005

[101] Rocca, D., Bai, Z., Li, R.-C., and Galli, G., "A block variational procedure for the iterative diagonalization of non-Hermitian random-phase approximation matrices," *J Chem Phys*, volume 136, no. 3, p. 034111, January 2012

[102] Reining, Lucia, Olevano, Valerio, Rubio, Angel, and Onida, Giovanni, "Excitonic Effects in Solids Described by Time-Dependent Density-Functional Theory," *Phys Rev Lett*, volume 88, p. 066404, Jan 2002

[103] Botti, Silvana, Fourreau, Armel, Nguyen, Francois, Renault, Yves-Olivier, Sottile, Francesco, and Reining, Lucia, "Energy dependence of the exchange-correlation kernel of time-dependent density functional theory: A simple model for solids," *Phys Rev B*, volume 72, p. 125203, Sep 2005

[104] Sottile, Francesco, Olevano, Valerio, and Reining, Lucia, "Parameter-Free Calculation of Response Functions in Time-Dependent Density-Functional Theory," *Phys Rev Lett*, volume 91, p. 056402, Jul 2003

[105] Adragna, Gianni, Del Sole, Rodolfo, and Marini, Andrea, "*Ab initio* calculation of the exchange-correlation kernel in extended systems," *Phys Rev B*, volume 68, p. 165108, Oct 2003

[106] Marini, Andrea, Del Sole, Rodolfo, and Rubio, Angel, "Bound Excitons in Time-Dependent Density-Functional Theory: Optical and Energy-Loss Spectra," *Phys Rev Lett*, volume 91, p. 256402, Dec 2003

[107] Sharma, S., Dewhurst, J. K., Sanna, A., and Gross, E. K. U., "Bootstrap Approximation for the Exchange-Correlation Kernel of Time-Dependent Density-Functional Theory," *Phys Rev Lett*, volume 107, p. 186401, Oct 2011

[108] Anisimov, Vladimir I., Zaanen, Jan, and Andersen, Ole K., "Band theory and Mott insulators: Hubbard U instead of Stoner I," *Phys Rev B*, volume 44, pp. 943–954, Jul 1991

[109] Anisimov, V. I., Aryasetiawan, F., and Lichtenstein, A. I., "REVIEW ARTICLE: First-principles calculations of the electronic structure and spectra of strongly correlated systems: the LDA+ U method," *J Phys Condens Matter*, volume 9, pp. 767–808, January 1997

[110] Cococcioni, Matteo and de Gironcoli, Stefano, "Linear response approach to the calculation of the effective interaction parameters in the LDA + U method," *Phys Rev B*, volume 71, p. 035105, Jan 2005

[111] Currao, Antonio, "Photoelectrochemical Water Splitting," *Chimia*, volume 61, no. 12, pp. 815–819, 2007

[112] Turner, John A., "A Realizable Renewable Energy Future," *Science*, volume 285, no. 5428, pp. 687–689, 1999

[113] Heller, Adam, "Conversion of sunlight into electrical power and photoassisted electrolysis of water in photoelectrochemical cells," *Acc Chem Res*, volume 14, no. 5, pp. 154–162, 1981

[114] van de Krol, Roel, Liang, Yongqi, and Schoonman, Joop, "Solar hydrogen production with nanostructured metal oxides," *J Mater Chem*, volume 18, pp. 2311–2320, 2008

[115] Weber, M.F. and Dignam, M.J., "Splitting water with semiconducting photoelectrodesEfficiency considerations," *Int J Hydrogen Energy*, volume 11, no. 4, pp. 225 – 232, ISSN 0360-3199, 1986

[116] Bolton, James R., Strickler, Stewart J., and Connolly, John S., "Limiting and realizable efficiencies of solar photolysis of water," *Nature*, volume 316, pp. 495–500, 1985

[117] Murphy, A.B., Barnes, P.R.F., Randeniya, L.K., Plumb, I.C., Grey, I.E., Horne, M.D., and Glasscock, J.A., "Efficiency of solar water splitting using semiconductor electrodes," *Int J Hydrogen Energy*, volume 31, no. 14, pp. 1999 – 2017, ISSN 0360-3199, 2006

[118] Wu, Yabi, Chan, M. K. Y., and Ceder, G., "Prediction of semiconductor band edge positions in aqueous environments from first principles," *Phys Rev B*, volume 83, p. 235301, Jun 2011

[119] Cheng, Jun and Sprik, Michiel, "Aligning electronic energy levels at the TiO_2/H_2O interface," *Phys Rev B*, volume 82, p. 081406, Aug 2010

[120] Cheng, Jun and Sprik, Michiel, "Alignment of electronic energy levels at electrochemical interfaces," *Phys Chem Chem Phys*, volume 14, pp. 11245–11267, 2012

[121] Chen, Shiyou and Wang, Lin-Wang, "Thermodynamic Oxidation and Reduction Potentials of Photocatalytic Semiconductors in Aqueous Solution," *Chem Mater*, volume 24, no. 18, pp. 3659–3666, 2012

[122] Bak, T, Nowotny, J, Rekas, M, and Sorrell, C.C, "Photo-electrochemical hydrogen generation from water using solar energy. Materials-related aspects," *Int J Hydrogen Energy*, volume 27, no. 10, pp. 991 – 1022, ISSN 0360-3199, 2002

[123] de Walle, Van, G., Chris, and Neugebauer, J., "Universal alignment of hydrogen levels in semiconductors, insulators and solutions," *Nature*, volume 423, pp. 626–628, 2003

[124] Chun, Wang-Jae, Ishikawa, Akio, Fujisawa, Hideki, Takata, Tsuyoshi, Kondo, Junko N., Hara, Michikazu, Kawai, Maki, Matsumoto, Yasumichi, and Domen, Kazunari, "Conduction and Valence Band Positions of Ta2O5, TaON, and Ta3N5 by UPS and Electrochemical Methods," *J Phys Chem B*, volume 107, no. 8, pp. 1798–1803, 2003

[125] Trasatti, Sergio, "The absolute electrode potential: an explanatory note. Recommendations 1986," *Pure Appl Chem*, volume 58, pp. 955–66, 1986

[126] Weinhardt, L., Blum, M., Bar, M., Heske, C., Cole, B., Marsen, B., and Miller, E. L., "Electronic Surface Level Positions of WO3 Thin Films for Photoelectrochemical Hydrogen Production," *J Phys Chem B*, volume 112, no. 8, pp. 3078–3082, 2008

[127] Toroker, Maytal Caspary, Kanan, Dalal K., Alidoust, Nima, Isseroff, Leah Y., Liao, Peilin, and Carter, Emily A., "First principles scheme to evaluate band edge positions in potential transition metal oxide photocatalysts and photoelectrodes," *Phys Chem Chem Phys*, volume 13, pp. 16644–16654, 2011

[128] Hodes, Gary, Cahen, David, and Manassen, Joost, "Tungsten trioxide as a photoanode for a photoelectrochemical cell(PEC)," *Nature*, volume 260, pp. 312–313, 1976

[129] Mi, Qixi, Ping, Yuan, Li, Yan, Cao, Bingfei, Brunschwig, Bruce S., Khalifah, Peter G., Galli, Giulia A., Gray, Harry B., and Lewis, Nathan S., "Thermally Stable N2-Intercalated WO3 Photoanodes for Water Oxidation," *J Am Chem Soc*, volume 134, no. 44, pp. 18318–18324, 2012

[130] Ping, Yuan, Li, Yan, Gygi, Francois, and Galli, Giulia, "Tungsten Oxide Clathrates for Water Oxidation: A First Principles Study," *Chemistry of Materials*, volume 24, no. 21, pp. 4252–4260, 2012

[131] Seabold, Jason A. and Choi, Kyoung-Shin, "Effect of a Cobalt-Based Oxygen Evolution Catalyst on the Stability and the Selectivity of Photo-Oxidation Reactions of a WO3 Photoanode," *Chem Mater*, volume 23, no. 5, pp. 1105–1112, 2011

[132] Hill, James C. and Choi, Kyoung-Shin, "Effect of Electrolytes on the Selectivity and Stability of n-type WO3 Photoelectrodes for Use in Solar Water Oxidation," *J Phys Chem C*, volume 116, no. 14, pp. 7612–7620, 2012

[133] Deb, Satyen K., "Opportunities and challenges in science and technology of WO3 for electrochromic and related applications," *Solar Energy Materials and Solar Cells*, volume 92, no. 2, pp. 245 – 258, ISSN 0927-0248, 2008

[134] Granqvist, C.G, "Electrochromic tungsten oxide films: Review of progress 1993-1998," *Solar Energy Materials and Solar Cells*, volume 60, no. 3, pp. 201 – 262, ISSN 0927-0248, 2000

[135] Granqvist, C.G, "Progress in electrochromics: tungsten oxide revisited," *Electrochimica Acta*, volume 44, no. 18, pp. 3005 – 3015, ISSN 0013-4686, 1999

[136] Crichton, Wilson A., Bouvier, Pierre, and Grzechnik, Andrzej, "The first bulk synthesis of ReO3-type tungsten trioxide, WO3, from nanometric precursors," *Mater Res Bull*, volume 38, no. 2, pp. 289 – 296, ISSN 0025-5408, 2003

[137] Woodward, P.M., Sleight, A.W., and Vogt, T., "Ferroelectric Tungsten Trioxide," *Journal of Solid State Chemistry*, volume 131, no. 1, pp. 9 – 17, ISSN 0022-4596, 1997

[138] Woodward, P. M., "Octahedral Tilting in Perovskites. I. Geometrical Considerations," *Acta Crystallographica Section B*, volume 53, no. 1, pp. 32–43, Feb 1997

[139] Lefkowitz, I., Dowell, M.B., and Shields, M.A., "Phase transitions in tungsten trioxide at low temperatures," *J Solid State Chem*, volume 15, no. 1, pp. 24 – 39, ISSN 0022-4596, 1975

[140] Hirose, Toshikazu and Furukawa, Kazuo, "Dielectric anomaly of tungsten trioxide WO3 with giant dielectric constant," *Phys Status Solidi A*, volume 203, no. 3, pp. 608–615, ISSN 1862-6319, 2006

[141] Giannozzi, P., Baroni, S., Bonini, N., Calandra, M., Car, R., Cavazzoni, C., Ceresoli, D., Chiarotti, G. L., Cococcioni, M., Dabo, I., Dal Corso, A., de Gironcoli, S., Fabris, S., Fratesi, G., Gebauer, R., Gerstmann, U., Gougoussis, C., Kokalj, A., Lazzeri, M., Martin-Samos, L., Marzari, N., Mauri, F., Mazzarello, R., Paolini, S., Pasquarello, A., Paulatto, L., Sbraccia, C., Scandolo, S., Sclauzero, G., Seitsonen, A. P., Smogunov, A., Umari, P., and Wentzcovitch, R. M., "QUANTUM ESPRESSO: a modular and open-source software project for quantum simulations of materials," *J Phys Condens Mat*, volume 21, p. 5502, September 2009

[142] Http://eslab.ucdavis.edu/software/qbox

[143] Perdew, John P., Burke, Kieron, and Ernzerhof, Matthias, "Generalized Gradient Approximation Made Simple," *Phys Rev Lett*, volume 77, pp. 3865–3868, Oct 1996

[144] Perdew, John P., Ernzerhof, Matthias, and Burke, Kieron, "Rationale for mixing exact exchange with density functional approximations," *J Chem Phys*, volume 105, no. 22, pp. 9982–9985, 1996

[145] Dion, M., Rydberg, H., Schröder, E., Langreth, D. C., and Lundqvist, B. I., "Van der Waals Density Functional for General Geometries," *Phys Rev Lett*, volume 92, p. 246401, Jun 2004

[146] Thonhauser, T., Cooper, Valentino R., Li, Shen, Puzder, Aaron, Hyldgaard, Per, and Langreth, David C., "Van der Waals density functional: Self-consistent potential and the nature of the van der Waals bond," *Phys Rev B*, volume 76, p. 125112, Sep 2007

[147] Román-Pérez, Guillermo and Soler, José M., "Efficient Implementation of a van der Waals Density Functional: Application to Double-Wall Carbon Nanotubes," *Phys Rev Lett*, volume 103, p. 096102, Aug 2009

[148] Lee, Kyuho, Murray, Éamonn D., Kong, Lingzhu, Lundqvist, Bengt I., and Langreth, David C., "Higher-accuracy van der Waals density functional," *Phys Rev B*, volume 82, p. 081101, Aug 2010

[149] Murray, Éamonn D. and Galli, Giulia, "Dispersion Interactions and Vibrational Effects in Ice as a Function of Pressure: A First Principles Study," *Phys Rev Lett*, volume 108, p. 105502, Mar 2012

[150] Chan, M. K. Y. and Ceder, G., "Efficient Band Gap Prediction for Solids," *Phys Rev Lett*, volume 105, p. 196403, Nov 2010

[151] Wijs, G. A. de, Boer, P. K. de, Groot, R. A. de, and Kresse, G., "Anomalous behavior of the semiconducting gap in WO_3 from first-principles calculations," *Phys Rev B*, volume 59, pp. 2684–2693, Jan 1999

[152] Hjelm, Anders, Granqvist, Claes G., and Wills, John M., "Electronic structure and optical properties of $WO3$, $LiWO3$, $NaWO3$, and $HWO3$," *Phys Rev B*, volume 54, no. 4, pp. 2436–2445, Jul 1996

[153] Huda, Muhammad N., Yan, Yanfa, Moon, Chang-Yoon, Wei, Su-Huai, and Al-Jassim, Mowafak M., "Density-functional theory study of the effects of atomic impurity on the band edges of monoclinic $WO3$," *Phys Rev B*, volume 77, no. 19, p. 195102, May 2008

[154] Cora, F., Stachiotti, M. G., Catlow, C. R. A., and Rodriguez, C. O., "Transition Metal Oxide Chemistry: Electronic Structure Study of WO3, ReO3, and NaWO3," *J Phys Chem B*, volume 101, no. 20, pp. 3945–3952, May 1997

[155] Chatten, Ryan, Chadwick, Alan V., Rougier, Aline, and Lindan, Philip J. D., "The Oxygen Vacancy in Crystal Phases of WO3," *J Phys Chem B*, volume 109, no. 8, pp. 3146–3156, March 2005

[156] Wang, Fenggong, Di Valentin, Cristiana, and Pacchioni, Gianfranco, "Electronic and Structural Properties of WO3: A Systematic Hybrid DFT Study," *J Phys Chem C*, volume 115, no. 16, pp. 8345–8353, 2011

[157] The difference between our results and those of Ref. [156] may be due to the use of different basis sets (Gaussian basis sets in Ref. [156] and plane waves in the present work) and different geometries (optimized at the LDA level here, but at the PBE0 level in Ref. [156]).

[158] Hartwigsen, C., Goedecker, S., and Hutter, J., "Relativistic separable dual-space Gaussian pseudopotentials from H to Rn," *Phys Rev B*, volume 58, pp. 3641–3662, Aug 1998

[159] Kehl, W. L., Hay, R. G., and Wahl, D., "The Structure of Tetragonal Tungsten Trioxide," *Journal of Applied Physics*, volume 23, no. 2, pp. 212–215, 1952

[160] Salje, E., "The orthorhombic phase of WO_3," *Acta Crystallographica Section B*, volume 33, no. 2, pp. 574–577, Feb 1977

[161] Loopstra, B. O. and Rietveld, H. M., "Further refinement of the structure of WO_3," *Acta Crystallogr Sect B*, volume 25, no. 7, pp. 1420–1421, Jul 1969

[162] Woodward, P. M., Sleight, A. W., and Vogt, T, "Structure refinement of triclinic tungsten trioxide," *Journal of Physics and Chemistry of Solids*, volume 56, p. 1305, 1995

[163] In the band structure of a (2×2×2) simple cubic unit cell, the high symmetry points Y, B, Z are equivalent, while they are slightly inequivalent in the monoclinic phase (see Fig.2(b))

[164] Ackermann, R. J. and Sorrell, C. A., "Thermal expansion and the high–low transformation in quartz. I. High-temperature X-ray studies," *J Appl Crystallogr*, volume 7, no. 5, pp. 461–467, Oct 1974

[165] Iwai, Tsuruji, "Temperature Dependence of the Optical Absorption Edge of Tungsten Trioxide Single Crystal," *J Phys Soc Jpn*, volume 15, no. 9, pp. 1596–1600, 1960

[166] Monkhorst, Hendrik J. and Pack, James D., "Special points for Brillouin-zone integrations," *Phys Rev B*, volume 13, pp. 5188–5192, Jun 1976

[167] Salje, E., "Lattice dynamics of WO_3," *Acta Crystallographica Section A*, volume 31, no. 3, pp. 360–363, May 1975

[168] Zhong, W., King-Smith, R. D., and Vanderbilt, David, "Giant LO-TO splittings in perovskite ferroelectrics," *Phys Rev Lett*, volume 72, pp. 3618–3621, May 1994

[169] Kawaminami, Masaru and Hirose, Toshikazu, "Condensed Phonon Modes in Successive Phases of WO_3," *Journal of the Physical Society of Japan*, volume 46, no. 3, pp. 864–870, 1979

[170] Kleperis, Janis, Zubkans, Juris, and Lusis, Andrejs R., "Nature of fundamental absorption edge of WO3," *Proc SPIE 2968*, pp. 186–191, 1997

[171] Koffyberg, F.P., Dwight, K., and Wold, A., "Interband transitions of semiconducting oxides determined from photoelectrolysis spectra," *Solid State Commun*, volume 30, no. 7, pp. 433 – 437, ISSN 0038-1098, 1979

[172] Salje, E., "A new type of electro-optic effect in semiconducting WO_3," *J Appl Crystallogr*, volume 7, no. 6, pp. 615–617, Dec 1974

[173] Amtout, A. and Leonelli, R., "Optical properties of rutile near its fundamental band gap," *Phys Rev B*, volume 51, pp. 6842–6851, Mar 1995

[174] Tezuka, Yasuhisa, Shin, Shik, Ishii, Takehiko, Ejima, Takeo, Suzuki, Shoji, and Sato, Shigeru, "Photoemission and Bremsstrahlung Isochromat Spectroscopy Studies of TiO_2 (Rutile) and $SrTiO_3$," *J Phys Soc Jpn*, volume 63, no. 1, pp. 347–357, 1994

[175] Rangan, Sylvie, Katalinic, Senia, Thorpe, Ryan, Bartynski, Robert Allen, Rochford, Jonathan, and Galoppini, Elena, "Energy Level Alignment of a Zinc(II) Tetraphenylporphyrin Dye Adsorbed onto TiO2(110) and ZnO(1120) Surfaces," *J Phys Chem C*, volume 114, no. 2, pp. 1139–1147, 2010

[176] Meyer, J., Kroger, M., Hamwi, S., Gnam, F., Riedl, T., Kowalsky, W., and Kahn, A., "Charge generation layers comprising transition metal-oxide/organic interfaces: Electronic structure and charge generation mechanism," *Appl Phys Lett*, volume 96, no. 19, p. 193302, 2010

[177] Ping, Yuan, Rocca, Dario, and Galli, Giulia, "Electronic excitations in light absorbers for photoelectrochemical energy conversion: first principles calculations based on many body perturbation theory," *Chem Soc Rev*, volume 42, pp. 2437–2469, 2013

[178] Mahan, Gerald D., *Many-Particle Physics*, Kuwer Academic, 2000

[179] Marder, Michael P., *Condensed Matter Physics*, A Wiley-Interscience Publication, 2000

[180] C.G.Kuper and G.D.Whitfield, *Polarons and Excitons*, Plenum Press, 1962

[181] Gonze, Xavier, "A brief introduction to the ABINIT software package," *Z Kristallogr*, volume 220, pp. 558–562, 2005

[182] Gonze, X., Amadon, B., Anglade, P.-M., Beuken, J.-M., Bottin, F., Boulanger, P., Bruneval, F., Caliste, D., Caracas, R., Cote, M., Deutsch, T., Genovese, L., Ghosez, Ph., Giantomassi, M., Goedecker, S., Hamann, D.R., Hermet, P., Jollet, F., Jomard, G., Leroux, S., Mancini, M., Mazevet, S., Oliveira, M.J.T., Onida, G., Pouillon, Y., Rangel, T., Rignanese, G.-M., Sangalli, D., Shaltaf, R., Torrent, M., Verstraete, M.J., Zerah, G., and Zwanziger, J.W., "ABINIT: First-principles approach to material and nanosystem properties," *Comput Phys Commun*, volume 180, no. 12, pp. 2582 – 2615, ISSN 0010-4655, 2009

[183] Kohn, W. and Sham, L. J., "Self-Consistent Equations Including Exchange and Correlation Effects," *Phys Rev*, volume 140, pp. A1133–A1138, Nov 1965

[184] Mermin, N. David, "Thermal Properties of the Inhomogeneous Electron Gas," *Phys Rev*, volume 137, pp. A1441–A1443, Mar 1965

[185] Paier, J., Marsman, M., Hummer, K., Kresse, G., Gerber, I. C., and Angyan, J. G., "Screened hybrid density functionals applied to solids," *J Chem Phys*, volume 124, no. 15, p. 154709, 2006

[186] Krukau, Aliaksandr V., Vydrov, Oleg A., Izmaylov, Artur F., and Scuseria, Gustavo E., "Influence of the exchange screening parameter on the performance of screened hybrid functionals," *J Chem Phys*, volume 125, no. 22, p. 224106, 2006

[187] Janotti, A., Varley, J. B., Rinke, P., Umezawa, N., Kresse, G., and Van de Walle, C. G., "Hybrid functional studies of the oxygen vacancy in TiO_2," *Phys Rev B*, volume 81, p. 085212, Feb 2010

[188] Iwai, Tsuruji, "Temperature Dependence of the Optical Absorption Edge of Tungsten Trioxide Single Crystal," *J Phys Soc Jpn*, volume 15, no. 9, pp. 1596–1600, 1960

[189] Bylander, D. M. and Kleinman, Leonard, "Self-consistent relativistic calculation of the energy bands and cohesive energy of W," *Phys Rev B*, volume 29, pp. 1534–1539, Feb 1984

[190] Svane, A., Christensen, N. E., Cardona, M., Chantis, A. N., van Schilfgaarde, M., and Kotani, T., "Quasiparticle self-consistent *GW* calculations for PbS, PbSe, and PbTe: Band structure and pressure coefficients," *Phys Rev B*, volume 81, p. 245120, Jun 2010

[191] Sakuma, R., Friedrich, C., Miyake, T., Blügel, S., and Aryasetiawan, F., "*GW* calculations including spin-orbit coupling: Application to Hg chalcogenides," *Phys Rev B*, volume 84, p. 085144, Aug 2011

[192] Cardona, Manuel, "Electron-phonon interaction in tetrahedral semiconductors," *Solid State Commun*, volume 133, no. 1, pp. 3 – 18, ISSN 0038-1098, 2005

[193] Giustino, Feliciano, Louie, Steven G., and Cohen, Marvin L., "Electron-Phonon Renormalization of the Direct Band Gap of Diamond," *Phys Rev Lett*, volume 105, p. 265501, Dec 2010

[194] Cannuccia, Elena and Marini, Andrea, "Effect of the Quantum Zero-Point Atomic Motion on the Optical and Electronic Properties of Diamond and Trans-Polyacetylene," *Phys Rev Lett*, volume 107, p. 255501, Dec 2011

[195] Cardona, Manuel and Thewalt, M. L. W., "Isotope effects on the optical spectra of semiconductors," *Rev Mod Phys*, volume 77, pp. 1173–1224, Nov 2005

[196] Perebeinos, Vasili, Tersoff, J., and Avouris, Phaedon, "Electron-Phonon Interaction and Transport in Semiconducting Carbon Nanotubes," *Phys Rev Lett*, volume 94, p. 086802, Mar 2005

[197] Kang, Wei and Hybertsen, Mark S., "Quasiparticle and optical properties of rutile and anatase TiO_2," *Phys Rev B*, volume 82, p. 085203, Aug 2010

[198] Lee, B. C., Kim, K. W., Dutta, M., and Stroscio, M. A., "Electron˘optical-phonon scattering in wurtzite crystals," *Phys Rev B*, volume 56, pp. 997–1000, Jul 1997

[199] Mora-Ramos, M E, Rodrguez, F J, and Quiroga, L, "Polaron properties of III-V nitride compounds: second-order effects," *J Phys Condens Matter*, volume 11, no. 42, p. 8223, 1999

[200] Riera, R., Comas, F., Ramos, M.E. Mora, and Trallero-Giner, C., "Polaron effective mass and binding energy in a semiconductor heterostructure," *Physica B*, volume 168, no. 3, pp. 211 – 218, ISSN 0921-4526, 1991

[201] Schirmer, O F and Salje, E, "Conduction bipolarons in low-temperature crystalline WO 3-x," *J Phys C*, volume 13, no. 36, p. L1067, 1980

[202] Schirmer, O.F. and Salje, E., "The W5+ polaron in crystalline low temperature WO3 ESR and optical absorption," *Solid State Commun*, volume 33, no. 3, pp. 333 – 336, ISSN 0038-1098, 1980

[203] Smondyrev, M. A., "Diagrams in the polaron model," *Theor Math Phys*, volume 68, pp. 653–664, ISSN 0040-5779, 1986

[204] Berak, James M. and Sienko, M.J., "Effect of oxygen-deficiency on electrical transport properties of tungsten trioxide crystals," *J Solid State Chem*, volume 2, no. 1, pp. 109 – 133, ISSN 0022-4596, 1970

[205] Larsson, Anna-Lena, Sernelius, Bo E., and Niklasson, Gunnar A., "Optical absorption of Li-intercalated polycrystalline tungsten oxide films: comparison to large polaron theory," *Solid State Ionics*, volume 165, no. 1-4, pp. 35 – 41, ISSN 0167-2738, 2003

[206] Niklasson, Gunnar A., Berggren, Lars, and Larsson, Anna-Lena, "Electrochromic tungsten oxide: the role of defects," *Sol Energy Mater Sol Cells*, volume 84, no. 1-4, pp. 315 – 328, international Solar Energy Society World Congress 2003, 2004

[207] Granqvist, C. G., *Handbook of Inorganic Electrochromic Materials*, Elsevier, Amsterdam, 1995

[208] DeVries, Michael J., Trimble, Chris, Tiwald, Thomas E., Thompson, Daniel W., Woollam, John A., and Hale, Jeffrey S., "Optical constants of crystalline WO3 deposited by magnetron sputtering," *J Vac Sci Technol A*, volume 17, no. 5, pp. 2906–2910, 1999

[209] Iguchi, E and Miyagi, H, "A study on the stability of polarons in monoclinic WO3," *J Phys Chem Solids*, volume 54, no. 4, pp. 403 – 409, ISSN 0022-3697, 1993

[210] Gray, A. X., Papp, C., Ueda, S., Balk e, B., Yamashita, Y., Yamashita, Y., Plucinski, L., Minr, J., Braun, J., Ylvisaker, E. R., Schneider, C. M., Pickett, W. E., Ebert, H., Kobayashi, K., and Fadley, C. S., "Probing bulk electronic structure with hard X-ray angle-resolved photoemission," *Nat Mater*, volume 10, pp. 759–764, 2011

[211] Morkel, M., Weinhardt, L., Lohmuller, B., Heske, C., Umbach, E., Riedl, W., Zweigart, S., and Karg, F., "Flat conduction-band alignment at the CdS/CuInSe2 thin-film solar-cell heterojunction," *Appl Phys Lett*, volume 79, no. 27, pp. 4482–4484, 2001

[212] Wood, D. L. and Tauc, J., "Weak Absorption Tails in Amorphous Semiconductors," *Phys Rev B*, volume 5, pp. 3144–3151, Apr 1972

[213] Yu, Peter Y. and Cardona, Manuel, *Fundamentals of Semiconductors: Physics and Material Properties*, Springer, New York, 1996

[214] Ping, Yuan and Galli, Giulia, in preparation, 2013

[215] Butler, M.A., Nasby, R.D., and Quinn, Rod K., "Tungsten trioxide as an electrode for photoelectrolysis of water," *Solid State Commun*, volume 19, no. 10, pp. 1011 – 1014, ISSN 0038-1098, 1976

[216] Miller, Eric L., Paluselli, Daniela, Marsen, Bjorn, and Rocheleau, Richard E., "Development of reactively sputtered metal oxide films for hydrogen-producing hybrid multijunction photoelectrodes," *Sol Energy Mater Sol Cells*, volume 88, no. 2, pp. 131 – 144, ISSN 0927-0248, 2005

[217] Miller, Eric L., Marsen, Bjorn, Cole, Brian, and Lum, Misti, "Low-Temperature Reactively Sputtered Tungsten Oxide Films for Solar-Powered Water Splitting Applications," *Electrochem Solid State Lett*, volume 9, no. 7, pp. G248–G250, 2006

[218] Zheng, Haidong, Tachibana, Yasuhiro, and Kalantar-zadeh, Kourosh, "Dye-Sensitized Solar Cells Based on WO3," *Langmuir*, volume 26, no. 24, pp. 19148–19152, 2010

[219] Su, Jinzhan, Guo, Liejin, Bao, Ningzhong, and Grimes, Craig A., "Nanostructured WO3/BiVO4 Heterojunction Films for Efficient Photoelectrochemical Water Splitting," *Nano Lett*, volume 11, no. 5, pp. 1928–1933, 2011

[220] Park, Hyunwoong, Kim, Kyoo Young, and Choi, Wonyong, "Photoelectrochemical Approach for Metal Corrosion Prevention Using a Semiconductor Photoanode," *J Phys Chem B*, volume 106, no. 18, pp. 4775–4781, 2002

[221] Paluselli, Daniela, Marsen, Bjorn, Miller, Eric L., and Rocheleau, Richard E., "Nitrogen Doping of Reactively Sputtered Tungsten Oxide Films," *Electrochem Solid State Lett*, volume 8, no. 11, pp. G301–G303, 2005

[222] Tang, Junwang and Ye, Jinhua, "Correlation of crystal structures and electronic structures and photocatalytic properties of the W-containing oxides," *J Mater Chem*, volume 15, pp. 4246–4251, 2005

[223] Maruthamuthu, P., Ashokkumar, M., Gurunathan, K., Subramanian, E., and Sastri, M.V.C., "Hydrogen evolution from water with visible radiation in presence of Cu(II)/WO3 and electron relay," *Int J Hydrogen Energy*, volume 14, no. 8, pp. 525 – 528, ISSN 0360-3199, 1989

[224] Wang, Fenggong, Di Valentin, Cristiana, and Pacchioni, Gianfranco, "Doping of WO3 for Photocatalytic Water Splitting: Hints from Density Functional Theory," *J Phys Chem C*, volume 116, no. 16, pp. 8901–8909, 2012

[225] Wang, Fenggong, Di Valentin, Cristiana, and Pacchioni, Gianfranco, "Semiconductor-to-metal transition in WO_{3-x}: Nature of the oxygen vacancy," *Phys Rev B*, volume 84, p. 073103, Aug 2011

[226] Goodenough, John B., "Metallic oxides," *Prog Solid State Chem*, volume 5, pp. 145 – 399, ISSN 0079-6786, 1971

[227] Brown, B. W. and Banks, E., "The Sodium Tungsten Bronzes1,2," *J Am Chem Soc*, volume 76, no. 4, pp. 963–966, 1954

[228] Stachiotti, M. G., Cor'a, F., Catlow, C. R. A., and Rodriguez, C. O., "First-principles investigation of ReO3 and related oxides," *Phys Rev B*, volume 55, no. 12, pp. 7508–7514, Mar 1997

[229] Asahi, R., Morikawa, T., Ohwaki, T., Aoki, K., and Taga, Y., "Visible-Light Photocatalysis in Nitrogen-Doped Titanium Oxides," *Science*, volume 293, no. 5528, pp. 269–271, 2001

[230] Wang, Jin, Tafen, De Nyago, Lewis, James P., Hong, Zhanglian, Manivannan, Ayyakkannu, Zhi, Mingjia, Li, Ming, and Wu, Nianqiang, "Origin of Photocatalytic Activity of Nitrogen-Doped TiO2 Nanobelts," *J Am Chem Soc*, volume 131, no. 34, pp. 12290–12297, 2009

[231] Livraghi, Stefano, Paganini, Maria Cristina, Giamello, Elio, Selloni, Annabella, Di Valentin, Cristiana, and Pacchioni, Gianfranco, "Origin of Photoactivity of Nitrogen-Doped Titanium Dioxide under Visible Light," *J Am Chem Soc*, volume 128, no. 49, pp. 15666–15671, 2006

[232] Batzill, Matthias, Morales, Erie H., and Diebold, Ulrike, "Influence of Nitrogen Doping on the Defect Formation and Surface Properties of TiO_2 Rutile and Anatase," *Phys Rev Lett*, volume 96, p. 026103, Jan 2006

[233] Nakamura, Ryuhei, Tanaka, Tomoaki, and Nakato, Yoshihiro, "Mechanism for Visible Light Responses in Anodic Photocurrents at N-Doped TiO2 Film Electrodes," *J Phys Chem B*, volume 108, no. 30, pp. 10617–10620, 2004

[234] Hoang, Son, Guo, Siwei, Hahn, Nathan T., Bard, Allen J., and Mullins, C. Buddie, "Visible Light Driven Photoelectrochemical Water Oxidation on Nitrogen-Modified TiO2 Nanowires," *Nano Lett*, volume 12, no. 1, pp. 26–32, 2012

[235] Cole, Brian, Marsen, Bjorn, Miller, Eric, Yan, Yanfa, To, Bobby, Jones, Kim, and Al-Jassim, Mowafak, "Evaluation of Nitrogen Doping of Tungsten Oxide for Photoelectrochemical Water Splitting," *J Phys Chem C*, volume 112, no. 13, pp. 5213–5220, 2008

[236] Yin, Wan-Jian, Tang, Houwen, Wei, Su-Huai, Al-Jassim, Mowafak M., Turner, John, and Yan, Yanfa, "Band structure engineering of semiconductors for enhanced photoelectrochemical water splitting: The case of TiO_2," *Phys Rev B*, volume 82, p. 045106, Jul 2010

[237] Gendre, L. Le, Marchand, R., and Laurent, Y., "A new class of inorganic compounds containing dinitrogen-metal bonds," *J Eur Ceram Soc*, volume 17, no. 1516, pp. 1813 – 1818, ISSN 0955-2219, 1997

[238] Tessier, Franck, Le Gendre, Laurent, Chevire, Franois, Marchand, Roger, and Navrotsky, Alexandra, "Thermochemistry of a New Class of Materials Containing Dinitrogen Pairs in an Oxide Matrix," *Chem Mater*, volume 17, no. 13, pp. 3570–3574, 2005

[239] Henkelman, Graeme, Uberuaga, Blas P., and Jonsson, Hannes, "A climbing image nudged elastic band method for finding saddle points and minimum energy paths," *J Chem Phys*, volume 113, no. 22, pp. 9901–9904, 2000

[240] Li, Yan and Galli, Giulia, "Vibrational properties of alkyl monolayers on Si(111) surfaces: Predictions from ab-initio calculations," *Appl Phys Lett*, volume 100, no. 7, p. 071605, 2012

[241] Fang, C.M., de Wijs, G.A., Orhan, E., de With, G., de Groot, R.A., Hintzen, H.T., and Marchand, R., "Local structure and electronic properties of BaTaO2N with perovskite-type structure," *J Phys Chem Solids*, volume 64, no. 2, pp. 281 – 286, ISSN 0022-3697, 2003

[242] We obtained the same results for $\Delta\rho$ at the LDA and PBE0 level of theory.

[243] The Y(0,0.5,0) point corresponds to the (0,0,0.5) point in Refs [155] and [153], because the y and z coordinates are switched in our calculations with respect to those adopted in Ref [155].

[244] Santato, Clara, Odziemkowski, Marek, Ulmann, Martine, and Augustynski, Jan, "Crystallographically Oriented Mesoporous WO3 Films: Synthesis, Characterization, and Applications," *J Am Chem Soc*, volume 123, no. 43, pp. 10639–10649, pMID: 11673995, 2001

[245] Seabold, Jason A. and Choi, Kyoung-Shin, "Efficient and Stable Photo-Oxidation of Water by a Bismuth Vanadate Photoanode Coupled with an Iron Oxyhydroxide Oxygen Evolution Catalyst," *Journal of the American Chemical Society*, volume 134, no. 4, pp. 2186–2192, 2012

[246] Mi, Qixi, Zhanaidarova, Almagul, Brunschwig, Bruce S., Gray, Harry B., and Lewis, Nathan S., "A quantitative assessment of the competition between water and anion oxidation at WO3 photoanodes in acidic aqueous electrolytes," *Energy Environ Sci*, volume 5, pp. 5694–5700, 2012

[247] Sivula, Kevin, Le Formal, Florian, and Gratzel, Michael, "Cover Picture: Solar Water Splitting: Progress Using Hematite (Fe2O3) Photoelectrodes (ChemSusChem 4/2011)," *ChemSusChem*, volume 4, no. 4, pp. 417–417, ISSN 1864-564X, 2011

[248] Spray, Ryan L., McDonald, Kenneth J., and Choi, Kyoung-Shin, "Enhancing Photoresponse of Nanoparticulate Fe2O3 Electrodes by Surface Composition Tuning," *The Journal of Physical Chemistry C*, volume 115, no. 8, pp. 3497–3506, 2011

[249] Cummings, Charles Y., Marken, Frank, Peter, Laurence M., Tahir, Asif A., and Wijayantha, K. G. Upul, "Kinetics and mechanism of light-driven oxygen evolution at thin film Fe2O3 electrodes," *Chem Commun*, volume 48, pp. 2027–2029, 2012

[250] Liang, Yongqi and van de Krol, Roel, "Influence of Si dopant and SnO2 interfacial layer on the structure of the spray-deposited Fe2O3 films," *Chemical Physics Letters*, volume 479, pp. 86 – 90, ISSN 0009-2614, 2009

[251] Koo, Hyun-Joo and Whangbo, Myung-Hwan, "Spin Dimer Analysis of the Anisotropic Spin Exchange Interactions in the Distorted Wolframite-Type Oxides CuWO4, CuMoO4-III, and Cu(Mo0.25W0.75)O4," *Inorganic Chemistry*, volume 40, no. 9, pp. 2161–2169, 2001

[252] M., Wiesmann, H., Ehrenberg, G., Miehe, T., Peun, H., Weitzel, and H., Fuess, "p-T Phase Diagram of CuMoO4," *Journal of Solid State Chemistry*, volume 132, no. 1, pp. 88–97, 1997

[253] Schwarz, BC., Ehrenberg, Helmut, Weitzel, Hans, and Fuess, Hartmut, "Investigation on the Influence of Particular Structure Parameters on the Anisotropic Spin-Exchange Interactions in the Distorted Wolframite-Type Oxides Cu(MoxW1-x)O4," *Inorganic Chemistry*, volume 46, no. 2, pp. 378–380, 2007

[254] Khyzhun, O.Yu., Bekenev, V.L., and Solonin, Yu.M., "First-principles calculations and X-ray spectroscopy studies of the electronic structure of CuWO4," *Journal of Alloys and Compounds*, volume 480, no. 2, pp. 184 – 189, ISSN 0925-8388, 2009

[255] Lali, M.V., Popovi, Z.S., and Vukajlovi, F.R., "Ab initio study of electronic, magnetic and optical properties of CuWO4 tungstate," *Computational Materials Science*, volume 50, no. 3, pp. 1179 – 1186, ISSN 0927-0256, 2011

[256] Kuzmin, A., Kalinko, A., and Evarestov, R.A., "Ab initio {LCAO} study of the atomic, electronic and magnetic structures and the lattice dynamics of triclinic CuWO4," *Acta Materialia*, volume 61, no. 1, pp. 371 – 378, ISSN 1359-6454, 2013

[257] Forsyth, J B, Wilkinson, C, and Zvyagin, A I, "The antiferromagnetic structure of copper tungstate, CuWO4," *Journal of Physics Condensed Matter*, volume 3, no. 43, p. 8433, 1991

[258] Anders, A G, Zvyagin, A I, Kobets, M I, Pelikh, L N, Khatsko, E N, and Yurko, V G, *Zh Eksp Theor Phys*, volume 62, p. 1798, (in russian), 1972

[259] Lake, B, Tennant, D A, Cowley, R A, Axe, J D, and Chen, C K, "Magnetic excitations in the ordered phase of the antiferromagnetic alternating chain compound," *Journal of Physics Condensed Matter*, volume 8, no. 44, p. 8613, 1996

[260] Ehrenberg, Helmut, Theissmann, Ralf, Gassenbauer, Yvonne, Knapp, Michael, Wltschek, Gernot, Weitzel, Hans, Fuess, Hartmut, Herrmannsdorfer, Thilo, and Sheptyakov, Denis, "The crystal and magnetic structure relationship in CuW(1-x)MoxO4 compounds with wolframite-type structure," *Journal of Physics Condensed Matter*, volume 14, no. 36, p. 8573, 2002

[261] Ping, Yuan, Rocca, Dario, and Galli, Giulia, "Optical properties of tungsten trioxide from first-principles calculations," *Phys Rev B*, volume 87, p. 165203, Apr 2013

[262] Aroyo, Mois I., Kirov, Asen, Capillas, Cesar, Perez-Mato, J. M., and Wondratschek, Hans, "Bilbao Crystallographic Server. II. Representations of crystallographic point groups and space groups," *Acta Crystallographica Section A*, volume 62, no. 2, pp. 115–128, Mar 2006

[263] Kihlborg, L. and Gebert, E., *Acta Crystallogr B*, volume 26, pp. 1020–1025, 1970

[264] Ruiz-Fuertes, J., Errandonea, D., Segura, A., Manjn, F. J., Zhu, Zh., and Tu, C. Y., "Growth, characterization, and high-pressure optical studies of CuWO4," *High Pressure Research*, volume 28, no. 4, pp. 565–570, 2008

[265] Ehrenberg, H., Wiesmann, M., Garcia-Jaca, J., Weitzel, H., and Fuess, H., "Magnetic structures of the high-pressure modifications of CoMoO4 and CuMoO4," *Journal of Magnetism and Magnetic Materials*, volume 182, no. 1-2, pp. 152 – 160, ISSN 0304-8853, 1998

[266] Yourey, Joseph E. and Bartlett, Bart M., "Electrochemical deposition and photoelectrochemistry of CuWO4, a promising photoanode for water oxidation," *J Mater Chem*, volume 21, pp. 7651–7660, 2011

[267] Ruiz-Fuertes, J, Sanz-Ortiz, M N, Gonzalez, J, Rodriguez, F, Segura, A, and Errandonea, D, "Optical absorption and Raman spectroscopy of CuWO4," *Journal of Physics Conference Series*, volume 215, no. 1, p. 012048, 2010

[268] Cox, B N, Coulthard, M A, and Lloyd, P, "A calculation of the Coulomb correlation energy, U, for transition metals in Hubbard's model," *Journal of Physics F Metal Physics*, volume 4, no. 6, p. 807, 1974

[269] Held, K., Keller, G., Eyert, V., Vollhardt, D., and Anisimov, V. I., "Mott-Hubbard Metal-Insulator Transition in Paramagnetic V_2O_3: An $LDA + DMFT$(QMC) Study," *Phys Rev Lett*, volume 86, pp. 5345–5348, Jun 2001

[270] James C. Hill, Yuan Ping, Giulia A. Galli and Choi, Kyoung-Shin, "Synthesis, photoeletrochemical properties, and first principle study of n-type CuWxMo(1-x)O4 electrodes showing enhanced visible light absorption," Submitted, 2013

[271] Hamann, Thomas W. and Lewis, Nathan S., "Control of the Stability, Electron-Transfer Kinetics, and pH-Dependent Energetics of Si/H2O Interfaces through Methyl Termination of Si(111) Surfaces," *J Phys Chem B*, volume 110, no. 45, pp. 22291–22294, 2006

[272] Nakato, Yoshihiro, Yano, Hiroyuki, Nishiura, Shinji, Ueda, Tetsuya, and Tsubomura, Hiroshi, "Hydrogen photoevolution at p-type silicon electrodes coated with discontinuous metal layers," *J Electroanal Chem*, volume 228, no. 12, pp. 97 – 108, ISSN 0022-0728, 1987

[273] Dominey, Raymond N., Lewis, Nathan S., Bruce, James A., Bookbinder, Dana C., and Wrighton, Mark S., "Improvement of photoelectrochemical hydrogen generation by surface modification of p-type silicon semiconductor photocathodes," *J Am Chem Soc*, volume 104, no. 2, pp. 467–482, 1982

[274] McKone, James R., Warren, Emily L., Bierman, Matthew J., Boettcher, Shannon W., Brunschwig, Bruce S., Lewis, Nathan S., and Gray, Harry B., "Evaluation of Pt, Ni, and Ni-Mo electrocatalysts for hydrogen evolution on crystalline Si electrodes," *Energy Environ Sci*, volume 4, pp. 3573–3583, 2011

[275] Greeley, Jeff, Jaramillo, Thomas F., Bonde, Jacob, Chorkendorff, Ib, and Norskov, Jens K., "Computational high-throughput screening of electrocatalytic materials for hydrogen evolution," *Nat Mate*, volume 5, pp. 909–913, 2006

[276] Lin, Yongjing, Yuan, Guangbi, Liu, Rui, Zhou, Sa, Sheehan, Stafford W., and Wang, Dunwei, "Semiconductor nanostructure-based photoelectrochemical water splitting: A brief review," *Chem Phys Lett*, volume 507, no. 46, pp. 209 – 215, ISSN 0009-2614, 2011

[277] Kay, Andreas, Cesar, Ilkay, and Grtzel, Michael, "New Benchmark for Water Photooxidation by Nanostructured -Fe2O3 Films," *J Am Chem Soc*, volume 128, no. 49, pp. 15714–15721, pMID: 17147381, 2006

[278] Brus, L. E., "Electron–electron and electron-hole interactions in small semiconductor crystallites: The size dependence of the lowest excited electronic state," *J Chem Phys*, volume 80, no. 9, pp. 4403–4409, 1984

[279] van de Kol, R. and Gratzel, M., *Photoelectrochemical Hydrogen Production*, Springer, 2012

[280] Osterloh, Frank E., "Inorganic nanostructures for photoelectrochemical and photocatalytic water splitting," *Chem Soc Rev*, 2013

[281] Benedict, L. X., Shirley, E. L., and Bohn, R. B., "Theory of optical absorption in diamond, Si, Ge, and GaAs," *prb*, volume 57, pp. R9385–+, April 1998

[282] Malcıoğlu, O. B., Gebauer, R., Rocca, D., and Baroni, S., "turboTDDFT A code for the simulation of molecular spectra using the Liouville Lanczos approach to time-dependent density-functional perturbation theory," *Comput Phys Commun*, volume 182, pp. 1744–1754, August 2011

[283] Bassani, F. and Pastori Parravicini, G., *Electronic States and Optical Transitions in Solids*, Pergamon, Oxford, 1975

[284] Perdew, J. P. and Zunger, Alex, "Self-interaction correction to density-functional approximations for many-electron systems," *Phys Rev B*, volume 23, no. 10, pp. 5048–5079, 1981

[285] The Quantum Espresso pseudopotential library is available online at the URL `http://www.quantum-espresso.org/pseudo.php`. In this work the pseudopotential file `Si.pz-vbc.UPF` was used for silicon and `C.pz-vbc.UPF` for carbon

[286] Dal Corso, Andrea, Baroni, Stefano, and Resta, Raffaele, "Density-functional theory of the dielectric constant: Gradient-corrected calculation for silicon," *Phys Rev B*, volume 49, no. 8, pp. 5323–5328, Feb 1994

[287] Zucca, Ricardo R. L. and Shen, Y. R., "Wavelength-Modulation Spectra of Some Semiconductors," *Phys Rev B*, volume 1, pp. 2668–2676, Mar 1970

[288] Monkhorst, Hendrik J. and Pack, James D., "Special points for Brillouin-zone integrations," *Phys Rev B*, volume 13, no. 12, pp. 5188–5192, Jun 1976

[289] Dal Corso, Andrea, "Reciprocal Space Integration and Special-Point Techniques," *Quantum-Mechanical Ab-initio Calculation of the Properties of Crystalline Materials*, edited by Cesare Pisani, Springer Verlag, Berlin, 1996

[290] Olevano, Valerio and Reining, Lucia, "Excitonic Effects on the Silicon Plasmon Resonance," *Phys Rev Lett*, volume 86, pp. 5962–5965, Jun 2001

[291] Lautenschlager, P., Garriga, M., Vina, L., and Cardona, M., "Temperature dependence of the dielectric function and interband critical points in silicon," *Phys Rev B*, volume 36, pp. 4821–4830, Sep 1987

[292] Marini, A., Hogan, C., Grüning, M., and Varsano, D., "yambo: An ab initio tool for excited state calculations," *Comput Phys Commun*, volume 180, pp. 1392–1403, August 2009

[293] Albrecht, Stefan, Reining, Lucia, Onida, Giovanni, Olevano, Valerio, and Del Sole, Rodolfo, "Albrecht *et al.* Reply:," *Phys Rev Lett*, volume 83, pp. 3971–3971, Nov 1999

[294] Hellwege, K. H. and Madelung, O., editors, *Numerical Data and Functional Relationships in Science and Technology*, volume 17a and 22a of Landolt-Börnstein, New Series, Group III, Springer Verlag, Berlin, 1982

[295] Roberts, R. A. and Walker, W. C., "Optical Study of the Electronic Structure of Diamond," *Phys Rev*, volume 161, pp. 730–735, Sep 1967

[296] Phillip, H. R. and Taft, E. A., "Kramers-Kronig Analysis of Reflectance Data for Diamond," *Phys Rev*, volume 136, pp. A1445–A1448, Nov 1964

[297] Botti, Silvana, Sottile, Francesco, Vast, Nathalie, Olevano, Valerio, Reining, Lucia, Weissker, Hans-Christian, Rubio, Angel, Onida, Giovanni, Del Sole, Rodolfo, and Godby, R. W., "Long-range contribution to the exchange-correlation kernel of time-dependent density functional theory," *Phys Rev B*, volume 69, p. 155112, Apr 2004

[298] Logothetidis, S. and Petalas, J., "Dielectric function and reflectivity of 3C-silicon carbide and the component perpendicular to the c axis of 6H-silicon carbide in the energy region 1.5-9.5 eV," *Journal of Applied Physics*, volume 80, pp. 1768–1772, August 1996

[299] Rohlfing, Michael and Pollmann, Johannes, "Dielectric function and reflectivity spectrum of SiC polytypes," *Phys Rev B*, volume 63, p. 125201, Mar 2001

[300] Hussain, Zahid, "Dopant-Dependent Reflectivity and Refractive Index of Microcrystalline HxWO3 and LixWO3 Bronze Thin Films," *Appl Opt*, volume 41, no. 31, pp. 6708–6724, Nov 2002

[301] Owen, J. F., Teegarden, K. J., and Shanks, H. R., "Optical properties of the sodium-tungsten bronzes and tungsten trioxide," *Phys Rev B*, volume 18, pp. 3827–3837, Oct 1978

[302] Lynch, D.W., Rosei, R., Weaver, J.H., and Olson, C.G., "The optical properties of some alkali metal tungsten bronzes from 0.1 to 38 eV," *J Solid State Chem*, volume 8, no. 3, pp. 242 – 252, ISSN 0022-4596, 1973

[303] Garbuio, V., Cascella, M., Reining, L., Sole, R. Del, and Pulci, O., "*Ab Initio* Calculation of Optical Spectra of Liquids: Many-Body Effects in the Electronic Excitations of Water," *Phys Rev Lett*, volume 97, p. 137402, Sep 2006

[304] Spataru, Catalin D., Ismail-Beigi, Sohrab, Benedict, Lorin X., and Louie, Steven G., "Excitonic Effects and Optical Spectra of Single-Walled Carbon Nanotubes," *Phys Rev Lett*, volume 92, p. 077402, Feb 2004

[305] Wirtz, Ludger, Marini, Andrea, and Rubio, Angel, "Excitons in Boron Nitride Nanotubes: Dimensionality Effects," *Phys Rev Lett*, volume 96, p. 126104, Mar 2006

[306] Onida, Giovanni, Reining, Lucia, Godby, R. W., Del Sole, R., and Andreoni, Wanda, "*Ab Initio* Calculations of the Quasiparticle and Absorption Spectra of Clusters: The Sodium Tetramer," *Phys Rev Lett*, volume 75, pp. 818–821, Jul 1995

[307] von Barth, U. and Car, R., *unpublished*, poseudopotentials were obtained through a nonlinear fit of the atomic pseudoorbitals and energies to their all electron counterparts.

[308] Kaur, Amandeep, Ylvisaker, Erik R., Lu, Deyu, Pham, Tuan Anh, Galli, Giulia, and Pickett, Warren E., "Spectral representation analysis of dielectric screening in solids and molecules," *Phys Rev B*, volume 87, p. 155144, Apr 2013

[309] Rozzi, Carlo A., Varsano, Daniele, Marini, Andrea, Gross, Eberhard K. U., and Rubio, Angel, "Exact Coulomb cutoff technique for supercell calculations," *Phys Rev B*, volume 73, p. 205119, May 2006

[310] Spataru, C.D., Ismail-Beigi, S., Benedict, L.X., and Louie, S.G., "Quasiparticle energies, excitonic effects and optical absorption spectra of small-diameter single-walled carbon nanotubes," *Applied Physics A Materials Science Processing*, volume 78, pp. 1129–1136, ISSN 0947-8396, 2004

[311] Ismail-Beigi, Sohrab, "Truncation of periodic image interactions for confined systems," *Phys Rev B*, volume 73, p. 233103, Jun 2006

[312] Marzari, Nicola and Vanderbilt, David, "Maximally localized generalized Wannier functions for composite energy bands," *Phys Rev B*, volume 56, pp. 12847–12865, Nov 1997

[313] Bruno, Mauro, Palummo, Maurizia, Marini, Andrea, Del Sole, Rodolfo, and Ossicini, Stefano, "From Si Nanowires to Porous Silicon: The Role of Excitonic Effects," *Phys Rev Lett*, volume 98, p. 036807, Jan 2007

[314] Hamann, D. R., "Generalized norm-conserving pseudopotentials," *Phys Rev B*, volume 40, pp. 2980–2987, Aug 1989

[315] Fuchs, Martin and Scheffler, Matthias, "Ab initio pseudopotentials for electronic structure calculations of poly-atomic systems using density-functional theory," *Computer Physics Communications*, volume 119, no. 1, pp. 67 – 98, ISSN 0010-4655, 1999

[316] Yang, Li, Spataru, Catalin D., Louie, Steven G., and Chou, M. Y., "Enhanced electron-hole interaction and optical absorption in a silicon nanowire," *Phys Rev B*, volume 75, p. 201304, May 2007

[317] Walker, Brent, Saitta, A. Marco, Gebauer, Ralph, and Baroni, Stefano, "Efficient Approach to Time-Dependent Density-Functional Perturbation Theory for Optical Spectroscopy," *Phys Rev Lett*, volume 96, p. 113001, Mar 2006

[318] Yabana, K. and Bertsch, G. F., "Time-dependent local-density approximation in real time: Application to conjugated molecules," *Int J Quantum Chem*, volume 75, no. 1, pp. 55–66, ISSN 1097-461X, 1999

[319] Marques, Miguel A. L., López, Xabier, Varsano, Daniele, Castro, Alberto, and Rubio, Angel, "Time-Dependent Density-Functional Approach for Biological Chromophores: The Case of the Green Fluorescent Protein," *Phys Rev Lett*, volume 90, p. 258101, Jun 2003

[320] Marques, Miguel A. L. and Botti, Silvana, "The planar-to-tubular structural transition in boron clusters from optical absorption," *J Chem Phys*, volume 123, no. 1, p. 014310, 2005

[321] Zhang, Cui, Donadio, Davide, Gygi, Francois, and Galli, Giulia, "First Principles Simulations of the Infrared Spectrum of Liquid Water Using Hybrid Density Functionals," *J Chem Theory Comput*, volume 7, no. 5, pp. 1443–1449, 2011

[322] Zhang, Cui, Wu, Jun, Galli, Giulia, and Gygi, Franois, "Structural and Vibrational Properties of Liquid Water from van der Waals Density Functionals," *J Chem Theory Comput*, volume 7, no. 10, pp. 3054–3061, 2011

[323] Cohen, Aron J., Mori-Snchez, Paula, and Yang, Weitao, "Insights into Current Limitations of Density Functional Theory," *Science*, volume 321, no. 5890, pp. 792–794, 2008

[324] Perdew, John P., Burke, Kieron, and Ernzerhof, Matthias, "Generalized Gradient Approximation Made Simple," *Phys Rev Lett*, volume 77, no. 18, pp. 3865–3868, 1996

[325] Hartwigsen, C., Goedecker, S., and Hutter, J., "Relativistic separable dual-space Gaussian pseudopotentials from H to Rn," *Phys Rev B*, volume 58, no. 7, pp. 3641–3662, Aug 1998

[326] Bernasconi, M., Chiarotti, G. L., Focher, P., Scandolo, S., Tosatti, E., and Parrinello, M., "First-principle-constant pressure molecular dynamics," *J Phys Chem Solids*, volume 56, no. 3-4, pp. 501 – 505, 1995

[327] Godby, R. W. and Needs, R. J., "Metal-insulator transition in Kohn-Sham theory and quasiparticle theory," *Phys Rev Lett*, volume 62, pp. 1169–1172, Mar 1989

[328] Giantomassi, M., Stankovski, M., Shaltaf, R., Gruning, M., Bruneval, F., Rinke, P., and Rignanese, G.-M., "Electronic properties of interfaces and defects from many-body perturbation theory: Recent developments and applications," *phys status solidi b*, volume 248, no. 2, pp. 275–289, ISSN 1521-3951, 2011

[329] Marini, Andrea, Del Sole, Rodolfo, Rubio, Angel, and Onida, Giovanni, "Quasiparticle band-structure effects on the d hole lifetimes of copper within the GW approximation," *Phys Rev B*, volume 66, p. 161104, Oct 2002

[330] Rostgaard, C., Jacobsen, K. W., and Thygesen, K. S., "Fully self-consistent GW calculations for molecules," *Phys Rev B*, volume 81, p. 085103, Feb 2010

[331] Gundersen, Grete, Hedberg, Kenneth, and Huston, John L., "Molecular Structure of Xenon Tetroxide, XeO4," *J Chem Phys*, volume 52, no. 2, pp. 812–815, 1970

[332] Pyykko, Pekka and Tamm, Toomas, "Calculations for XeOn (n = 2-4): Could the Xenon Dioxide Molecule Exist?" *J Phys Chem A*, volume 104, no. 16, pp. 3826–3828, 2000

[333] Probert, M I J, "An ab initio study of xenon retention in -quartz," *J Phys Condens Matter*, volume 22, no. 2, p. 025501, 2010

[334] Lambert-Mauriat, C and Oison, V, "Density-functional study of oxygen vacancies in monoclinic tungsten oxide," *J Phys Condens Matter*, volume 18, no. 31, p. 7361, 2006

[335] Migas, D. B., Shaposhnikov, V. L., Rodin, V. N., and Borisenko, V. E., "Tungsten oxides. I. Effects of oxygen vacancies and doping on electronic and optical properties of different phases of WO[sub 3]," *J Appl Phys*, volume 108, no. 9, p. 093713, 2010

[336] Ikeda, Shigeru, Sugiyama, Noboru, Murakami, Shin-ya, Kominami, Hiroshi, Kera, Yoshiya, Noguchi, Hidenori, Uosaki, Kohei, Torimoto, Tsukasa, and Ohtani, Bunsho, "Quantitative analysis of defective sites in titanium(IV) oxide photocatalyst powders," *Phys Chem Chem Phys*, volume 5, pp. 778–783, 2003

[337] Takeda, Satoshi, Suzuki, Susumu, Odaka, Hidefumi, and Hosono, Hideo, "Photocatalytic TiO2 thin film deposited onto glass by DC magnetron sputtering," *Thin Solid Films*, volume 392, no. 2, pp. 338 – 344, ISSN 0040-6090, 2001